



HAL
open science

Sound Directivity Control in a 3-D Space by a Compact Spherical Loudspeaker Array

Alexander Mattioli Pasqual

► **To cite this version:**

Alexander Mattioli Pasqual. Sound Directivity Control in a 3-D Space by a Compact Spherical Loudspeaker Array. Mechanics [physics.med-ph]. Universidade Estadual de Campinas, 2010. English. NNT: . tel-00530855

HAL Id: tel-00530855

<https://theses.hal.science/tel-00530855>

Submitted on 30 Oct 2010

HAL is a multi-disciplinary open access archive for the deposit and dissemination of scientific research documents, whether they are published or not. The documents may come from teaching and research institutions in France or abroad, or from public or private research centers.

L'archive ouverte pluridisciplinaire **HAL**, est destinée au dépôt et à la diffusion de documents scientifiques de niveau recherche, publiés ou non, émanant des établissements d'enseignement et de recherche français ou étrangers, des laboratoires publics ou privés.

STATE UNIVERSITY OF CAMPINAS
FACULTY OF MECHANICAL ENGINEERING
PhD PROGRAM IN MECHANICAL ENGINEERING

**Sound Directivity Control in a 3-D Space by a
Compact Spherical Loudspeaker Array**

Author: Alexander Mattioli Pasqual

Advisor: Professor José Roberto de França Arruda

Co-advisor: Professor Philippe Herzog

24/2010

**STATE UNIVERSITY OF CAMPINAS
FACULTY OF MECHANICAL ENGINEERING
PhD PROGRAM IN MECHANICAL ENGINEERING
DEPARTMENT OF COMPUTATIONAL MECHANICS**

Sound Directivity Control in a 3-D Space by a Compact Spherical Loudspeaker Array

Author: Alexander Mattioli Pasqual

Advisor: Professor José Roberto de França Arruda (Unicamp, Campinas/Brazil)

Co-advisor: Professor Philippe Herzog (LMA, UPR 7051, Marseille/France)

Program: Mechanical Engineering

Area of Concentration: Solid Mechanics and Mechanical Design

A dissertation submitted to the Faculty of Mechanical Engineering in partial fulfillment of the requirements for the degree of Doctor of Philosophy in Mechanical Engineering.

Campinas, 2010

S.P. — Brazil

STATE UNIVERSITY OF CAMPINAS
FACULTY OF MECHANICAL ENGINEERING
PhD PROGRAM IN MECHANICAL ENGINEERING
DEPARTMENT OF COMPUTATIONAL MECHANICS

PhD DISSERTATION

**Sound Directivity Control in a 3-D Space by a
Compact Spherical Loudspeaker Array**

Author: Alexander Mattioli Pasqual

Advisor: Professor José Roberto de França Arruda

Co-advisor: Professor Philippe Herzog

Committee in charge:

Professor José Roberto de França Arruda, Chair
Unicamp — Faculty of Mechanical Engineering

Professor José Maria Campos dos Santos
Unicamp — Faculty of Mechanical Engineering

Professor Rafael Santos Mendes
Unicamp — School of Electrical and Computer Engineering

Professor Sylvio Reynaldo Bistafa
USP — Polytechnic School

Professor Adolfo Maia Jr.
Unicamp — Mathematics, Statistics and Scientific Computing Institute

Campinas, february 22, 2010

Acknowledgments

First of all, I would like to express my deep gratitude to my advisor José Roberto de França Arruda for his very positive influence and confidence in my work. The discussions and opportunities he provided me have proven invaluable to my personal and scientific development.

I am very grateful to my co-advisor Philippe Herzog for his enthusiastic technical assistance and kind support during my stays at the Laboratory of Mechanics and Acoustics (LMA, CNRS, UPR 7051, Marseille, France).

Special thanks to members of the SACADS team from the LMA and to all staff at Department of Computational Mechanics (DMC, Unicamp, Campinas, Brazil). I am particularly in debt to Cédric Pinhède from LMA — the experimental work could not be done without his invaluable help and dedication. Also, I would like to thank the undergraduate and graduate students Samuel Pinson, Victor Bécard and Lucas Cóser for their contribution to this work with complementary simulations and experiments.

Thanks to people from Interdisciplinary Nucleus for Sound Studies (NICS, Unicamp, Campinas, Brazil) for the interesting discussions concerning the musical and practical implementation aspects of directivity controlled sound sources, especially Jônatas Manzolli, Adolfo Maia Jr., Tuti Fornari and José Augusto Mannis.

For having kindly built the mechanical frame of the Unicamp dodecahedral loudspeaker prototype, I thank Jorge Vicente Lopes da Silva, Marcelo Oliveira and their colleagues of the 3-D Technology Division from the Renato Archer Information Technology Center (CTI, Campinas, Brazil).

I am grateful to Franz Zotter (Institute of Electronic Music and Acoustics, Graz, Austria) for the technical discussions on spherical acoustics and tips that helped me to improve this manuscript.

I would like to acknowledge the grant sponsored by *Coordenação de Aperfeiçoamento de Pessoal de Nível Superior* (CAPES, Brazil) and the financial support of National Center for Scien-

tific Research (CNRS, France).

I am in debt to my funny uncle Carlos Henrique Mattioli and his son Enzo for their great hospitality and support. Special thanks to my cousin Vivian G. Mattioli who allowed me to occupy her room during her absence and trusted me to take care of her frogs.

Last but not least, I would like to warmly thank my parents, brother, sister, grandparents and friends who have encouraged me along this amazing journey in one way or another: Lucas Lima, Flávio Bianchini, Igor Chalfoun, Katlen Allganer, Lúcia Cambraia, Alberto Caeiro, Constance Meiners, Camila Boscariol, Karen Paulino, Riccardo Mariani, Fabiano Bianchini, Liliana Leonardi, Bruno Costa, Fernanda Calegari, Samer Hamandi, Kailing Zhu... thank you all!

*“The greatest challenge to any thinker is stating the
problem in a way that will allow a solution.”*

Bertrand Russel

Abstract

PASQUAL, Alexander Mattioli, *Sound Directivity Control in a 3-D Space by a Compact Spherical Loudspeaker Array*. 2010. 171 p. Thesis (PhD in Mechanical Engineering): Faculty of Mechanical Engineering, State University of Campinas, Campinas.

Angular control of the sound radiation can be achieved by using a compact array of independently programmable loudspeakers operating at the same frequency range. The drivers are usually distributed over a sphere-like frame according to a Platonic solid geometry to obtain a highly symmetrical configuration. Prototypes of compact spherical loudspeaker arrays have been recently developed and applied in room acoustics measurements, electroacoustic music performance and synthesis of directivity patterns of acoustical sources such as musical instruments. However, many aspects concerning their control, design, electromechanical behavior and ability to provide a more realistic sound experience than conventional audio systems remain unclear.

This work concerns the analysis and synthesis of sound fields by a compact spherical loudspeaker array and aims to contribute to clarifying some aspects mentioned above. A control strategy based on the acoustic radiation modes of the spherical array is proposed, which presents several advantages over the usual strategy based on the spherical harmonics. A theoretical and experimental analysis of the electromechanical behavior of compact loudspeaker arrays is also presented, in which the acoustic coupling between drivers inside the array frame is taken into account. In addition, optimum driver signals corresponding to a given target directivity pattern are derived using two different cost functions, indicating that the realism of the synthesized pattern may be significantly increased by neglecting the phase of the target directivity pattern. Finally, the proposed theoretical models are validated through measurements of electrical impedance, loudspeaker diaphragm velocity and directivity patterns.

List of Figures

1.1	Principal radiation directions for a violin in the horizontal plane [1].	3
1.2	Synthesis of the temporal and spatial signature of an acoustical source by a compact loudspeaker array.	5
1.3	Spherical loudspeaker array prototypes based on the Platonic solids.	7
2.1	Spherical coordinates.	16
2.2	Acoustic dipole arbitrarily oriented modeled by two monopoles with source-strengths $+Q_s$ and $-Q_s$	17
2.3	Longitudinal (on the left) and lateral (on the right) quadrupoles arbitrarily oriented modeled by two dipoles with moments \mathbf{d}_m and $-\mathbf{d}_m$	18
2.4	Directivity patterns of a monopole, a dipole and a lateral quadrupole. The figure shape indicates the magnitude of a normalized sound pressure, and the dark and light portions indicate a 180° phase difference.	20
2.5	Directivity patterns of a longitudinal quadrupole evaluated at $kr = 0.2$, $kr = 2$, $kr = 20$ and under farfield condition. The figure shape indicates the magnitude of a normalized sound pressure and the color gradient indicates its phase.	20
2.6	Complex-valued spherical harmonics up to order $n = 3$	25
2.7	Real-valued spherical harmonics up to order $n = 3$	27
2.8	An acoustic domain (“listening area”), V , bounded by Γ_o and Γ_i , free of sound sources and scatterers.	32

2.9	Boundary value problems: a) Interior problem: sound sources and scatterers outside the listening area; b) Exterior problem: free-field sound radiation.	35
2.10	Synthesis or playback of an acoustic field: a) Irradiation reproduction: Ambisonics and Wave Field Synthesis; b) Radiation reproduction: compact loudspeaker array.	35
3.1	Radiation efficiencies of the first 49 acoustic radiation modes of the continuous sphere (spherical harmonics).	40
3.2	Spherical cap with aperture angle θ_0 mounted on a rigid sphere at \mathbf{r}_c	41
3.3	Convex regular polyhedra (Platonic solids) and their midspheres.	45
3.4	Radiation efficiency of the ARM # 1 of the continuous sphere and the discrete spheres based on the Platonic solids (linear scale on the left; logarithmic scale on the right).	46
3.5	Radiation efficiency of the ARM # 2 to 4 of the continuous sphere and the discrete spheres based on the Platonic solids (linear scale on the left; logarithmic scale on the right).	46
3.6	Radiation efficiency of the ARM # 5 to 9 of the continuous sphere, the dodecahedron-like sphere and the icosahedron-like sphere, as well as the ARM # 5 to 6 of the hexahedron-like sphere and the ARM # 5 to 7 of the octahedron-like sphere (linear scale on the left; logarithmic scale on the right).	47
3.7	Radiation efficiency of the ARM # 10 to 16 of the continuous sphere, the ARM # 8 of the octahedron-like sphere, the ARM # 10 to 12 of the dodecahedron-like sphere and the ARM # 10 to 16 of the icosahedron-like sphere (linear scale on the left; logarithmic scale on the right).	47
3.8	Radiation efficiency of the ARM # 17 to 25 of the continuous sphere and the ARM # 17 to 20 of the icosahedron-like sphere (linear scale on the left; logarithmic scale on the right).	48
3.9	Sound pressure patterns corresponding to the ARM # 1 of the discrete spheres based on the five Platonic solids. Patterns obtained for $ka = 0.1$ at a distance $r = 10a$ from the sphere center.	49

3.10	Sound pressure patterns corresponding to the ARM # 2 of the discrete spheres based on the five Platonic solids. Patterns obtained for $ka = 0.1$ at a distance $r = 10a$ from the sphere center.	49
3.11	Sound pressure patterns corresponding to the ARM # 6 of the hexahedron-like, octahedron-like and dodecahedron-like spheres, as well as the ARM # 9 of the icosahedron-like sphere. Patterns obtained for $ka = 0.1$ at a distance $r = 10a$ from the sphere center.	50
3.12	Sound pressure patterns corresponding to the ARM # 8 of the octahedron-like sphere, the ARM # 12 of the dodecahedron-like sphere and the ARM # 10 of the icosahedron-like sphere. Patterns obtained for $ka = 0.1$ at a distance $r = 10a$ from the sphere center.	50
3.13	Sound pressure patterns corresponding to the ARM # 1 of the discrete spheres based on the five Platonic solids. Patterns obtained for $ka = 5$ at a distance $r = 10a$ from the sphere center.	51
3.14	Frequency response functions between input diaphragm velocity and output voltage.	57
3.15	Ratio between the voltage magnitude that feeds the most solicited driver of the array (driver # 1) and the resulting sound power. Simulation results obtained for the acoustic radiation modes # 1, 2, 5 and 12.	59
4.1	Upper and lower bounds of the normalized root mean square error (RMSE) achieved in the synthesis of functions in the subspaces spanned by spherical harmonics of orders 0, 1, 2 and 3. $\theta_0 = 15.1^\circ$ has been used for the tetrahedron, hexahedron, octahedron, dodecahedron and icosahedron.	64
4.2	Upper and lower bounds of the normalized root mean square error (RMSE) achieved in the synthesis of functions in the subspaces spanned by spherical harmonics of orders 0, 1, 2 and 3. $\theta_0 = 54.7^\circ, 45.0^\circ, 35.2^\circ, 31.7^\circ$ and 20.9° have been used for the tetrahedron, hexahedron, octahedron, dodecahedron and icosahedron, respectively.	65
4.3	Normalized ARM weights for a dodecahedral source with $\theta_0 = 15.1^\circ$. These curves arise from the synthesis of a function in the subspace spanned by spherical harmonics of order n chosen so that it leads to the lowest RMSE.	67

4.4 Synthesis of the farfield directivity of a spherical cap oriented according to the Euler angles $(0^0, 37.38^0, 0^0)$ by a dodecahedral source with $\theta_0 = 15.1^0$. Comparison between the normalized magnitude RMSE obtained by solving the standard weighted least-squares problem (phase concerned) and the magnitude least-squares problem (phase not concerned). 71

4.5 Synthesis of the farfield directivity of a spherical cap oriented according to the Euler angles $(0^0, 37.38^0, 0^0)$ by a dodecahedral source with $\theta_0 = 15.1^0$. Comparison between the target directivity pattern and the synthesized patterns obtained by solving the standard weighted least-squares problem (phase concerned) and the magnitude least-squares problem (phase not concerned) for $ka = 2$ 72

4.6 Synthesis of the farfield directivity of a spherical cap oriented according to the Euler angles $(0^0, 37.38^0, 0^0)$ by a dodecahedral source with $\theta_0 = 15.1^0$. Comparison between the target directivity pattern and the synthesized patterns obtained by solving the standard weighted least-squares problem (phase concerned) and the magnitude least-squares problem (phase not concerned) for $ka = 3$ 72

4.7 Synthesis of the farfield directivity of a spherical cap oriented according to the Euler angles $(0^0, 37.38^0, 0^0)$ by a dodecahedral source with $\theta_0 = 15.1^0$. Comparison between the target directivity pattern and the synthesized patterns obtained by solving the standard weighted least-squares problem (phase concerned) and the magnitude least-squares problem (phase not concerned) for $ka = 5$ 73

4.8 Synthesis of the farfield directivity of a spherical cap oriented according to the Euler angles $(0^0, 37.38^0, 0^0)$ by a dodecahedral source with $\theta_0 = 15.1^0$. Usual norm of \mathbf{c}_{opt} obtained by the standard and the magnitude least-squares, and of the vector difference between them. 73

4.9 Synthesis of the farfield directivity of a spherical cap oriented according to the Euler angles $(0^0, 37.38^0, 0^0)$ by a dodecahedral source with $\theta_0 = 15.1^0$. Directivity patterns corresponding to the vector difference between the optimum weights \mathbf{c}_{opt} obtained by the standard and the magnitude least-squares. 74

5.1 Block diagram representing the synthesis of the l -th acoustic radiation mode of a L -driver loudspeaker array. 78

5.2	Block diagram representing the sound pressure field produced by the l -th acoustic radiation mode of a L -driver loudspeaker array after equalization.	79
5.3	Filter $\mu_l(\omega)$, $l = 1, 2, \dots, 12$, that compensates for the non-flat frequency response of the electromechanical transducers of a hollow loudspeaker array with 12 identical drivers. The transducer features are given in the row “mean value” of Tab. 6.1.	83
5.4	Radiation efficiency of the acoustic radiation modes of a dodecahedral source with $\theta_0 = 15.1^0$ (linear scale on the left; logarithmic scale on the right).	83
5.5	Frequency response (log magnitude) of the sound pressure equalizers for the acoustic radiation modes of a dodecahedral source.	84
5.6	Radiation patterns at $1000Hz$ and $4750Hz$ corresponding to the ARM # 2 of a dodecahedral source with $a = 0.075m$ and $\theta_0 = 15.1^0$	84
5.7	Frequency response (log magnitude) of the sound power equalizers for the acoustic radiation modes of a dodecahedral source.	85
5.8	Frequency response (log magnitude) of the sound power equalizers for the acoustic radiation modes of a dodecahedral source. Solid curves: ideal theoretical filters; dashed curves: approximated IIR filters with $B = D = 9$	87
5.9	Sound power level of the equalized acoustic radiation modes of a dodecahedral source. The ideal sound power equalization filters have been approximated by IIR filters with $B = D = 9$	88
5.10	Sound pressure response at $(\hat{r}, \hat{\theta}, \hat{\phi})$ for some acoustic radiation modes of the dodecahedral array with IIR sound power equalizers.	88
6.1	Spherical array prototype with $L = 12$ independently programmable transducers mounted on a hollow sphere with outer radius $a = 0.075m$ and inner radius $a_i = 0.060m$	90
6.2	Experimental set-up for the electrical impedance measurements.	92
6.3	Theoretical and experimental electrical impedance of the driver #11 under the following operation conditions: suspended driver, driver mounted at open-closed tubes of volumes $V_{t1} = 1.5 \times 10^{-4}m^3$ and $V_{t2} = 3.3 \times 10^{-4}m^3$, suspended driver with attached masses of $(M_{t1}, M_{t2}, M_{t3}, M_{t4}) = (0.9, 1.4, 2.3, 2.8) \times 10^{-3}kg$	93

6.4	Theoretical and experimental electrical impedance of a suspended driver unit (driver #08) for use in the spherical array prototype.	94
6.5	Laser scanning grid points on the driver vibrating surface. On the left, driver is suspended and both diaphragm and suspension velocities are measured. On the right, driver is mounted on the spherical array prototype and only the diaphragm velocity is measured.	96
6.6	Measured vibration pattern of the diaphragm (first 7 inner circles) and suspension (circles 8 to 16) of a suspended driver for use in the spherical array prototype. This pattern has been measured at the frequency of $1616Hz$ and the grid points are illustrated on the left of Fig. 6.5. The results have been normalized and averaged over the circumferences shown in such a figure.	98
6.7	Theoretical and experimental FRFs corresponding to the config. 1 described in Tab. 6.2 and to a "suspended" driver. Each experimental FRF is the area-weighted average of FRFs measured on the driver diaphragm surface.	100
6.8	Theoretical and experimental FRFs corresponding to the config. 2 described in Tab. 6.2. The experimental FRF is the area-weighted average of FRFs measured on the driver diaphragm surface.	101
6.9	Theoretical and experimental FRFs corresponding to the config. 3 described in Tab. 6.2. The experimental FRF is the area-weighted average of FRFs measured on the driver diaphragm surface.	102
6.10	Theoretical and experimental FRFs corresponding to the config. 4 described in Tab. 6.2. The experimental FRF is the area-weighted average of FRFs measured on the driver diaphragm surface.	103
6.11	Experimental set-up for the directivity measurements at the large anechoic chamber of the Laboratory of Mechanics and Acoustics of the National Center for Scientific Research (UPR-7051, CNRS, Marseille, France).	105
6.12	Experimental set-up for the directivity measurements with the driver and microphone labels indicated.	106
6.13	Theoretical and experimental FRFs corresponding to the configurations #1 to #4 shown in Tab. 6.4.	108

6.14	Theoretical and experimental FRFs corresponding to the configurations #5 to #7 shown in Tab. 6.4.	109
6.15	Theoretical and experimental directivity pattern for the ARM #01 at $400Hz$	110
6.16	Theoretical and experimental directivity pattern for the ARM #02 at $400Hz$	111
6.17	Theoretical and experimental directivity pattern for the ARM #02 at $1000Hz$	111
6.18	Theoretical and experimental directivity pattern for the ARM #02 at $1500Hz$	112
6.19	Theoretical and experimental directivity pattern for the ARM #03 at $400Hz$	112
6.20	Theoretical and experimental directivity pattern for the ARM #03 at $1000Hz$	113
6.21	Theoretical and experimental directivity pattern for the ARM #04 at $400Hz$	113
6.22	Theoretical and experimental directivity pattern for the ARM #04 at $2000Hz$	114
6.23	Theoretical and experimental directivity pattern for the ARM #05 at $600Hz$	114
6.24	Theoretical and experimental directivity pattern for the ARM #06 at $600Hz$	115
6.25	Theoretical and experimental directivity pattern for the ARM #07 at $600Hz$	115
6.26	Theoretical and experimental directivity pattern for the ARM #07 at $2000Hz$	116
6.27	Theoretical and experimental directivity pattern for the ARM #10 at $1000Hz$	116
6.28	Theoretical and experimental directivity pattern for the ARM #10 at $2000Hz$	117
6.29	Theoretical and experimental directivity pattern at $400Hz$ corresponding to a rotated dipole obtained from a linear combination of the ARM #02 to #04.	117
6.30	Theoretical and experimental directivity pattern at $600Hz$ corresponding to a rotated lateral quadrupole obtained from a linear combination of the ARM #05 to #09.	118
D.1	Block diagram representation of a discrete-time SISO system.	143

List of Tables

4.1	Iterative variable exchange procedure to solve the magnitude least-squares problem.	70
6.1	Estimated parameters of the 12 Aurasound [®] NSW2-326-8A drivers used in the spherical array prototype.	93
6.2	Measurement configurations for evaluating the interaction between drivers mounted on the spherical array prototype. Each driver number corresponds to a position in the array shown in Fig. 6.1.	96
6.3	Sensitivities of the electret microphones used in the directivity measurements; calibration performed in january 2010.	107
6.4	Measurement configurations for evaluating some FRFs between an input driver voltage and an output sound pressure taken at the mic #10. The antenna is positioned so that mic #10 is approximately in front of the driver #01.	107
C.1	Basic properties of Platonic solids.	140
C.2	Cartesian coordinates and Euler angles of the center of the polyhedrons' faces. . . .	141
C.3	Modal matrix (Ψ) of the tetrahedron.	142
C.4	Modal matrix (Ψ) of the hexahedron.	142
C.5	Modal matrix (Ψ) of the octahedron.	142
C.6	Modal matrix (Ψ) of the dodecahedron.	142
C.7	Modal matrix (Ψ) of the icosahedron.	142

List of Symbols and Abbreviations

Latin Letters

a	- Outer sphere radius
a_i	- Inner sphere radius
b	- Clamped electromagnetic force, filter coefficient
B	- Magnetic flux density
\mathbf{B}	- $(N + 1)^2 \times L$ complex matrix
c	- Sound speed
C	- Mechanical compliance of the driver suspension
\mathbf{C}	- $L \times L$ matrix that couples the power radiated by the elements of \mathbf{u}
CF	- Correction factor
d	- Filter coefficient
\mathbf{d}_m	- Dipole moment
$D_{m'm}^n(\alpha, \beta, \gamma)$	- Rotation matrices for complex-valued spherical harmonics
\mathbf{E}	- $(N + 1)^2 \times L$ complex matrix
$F^{(a)}$	- Net acoustic force acting on a driver diaphragm
$G(\mathbf{x}, \mathbf{x}_s)$	- 3-D free-space Green's function
k	- Wave number
$h_n^{(1)}(\cdot)$	- Spherical Hankel function of the first kind
$h_n^{(2)}(\cdot)$	- Spherical Hankel function of the second kind
$H_1(\cdot)$	- Struve function of order 1
i	- Electrical current
\mathbf{I}	- Identity matrix
$j_n(\cdot)$	- Spherical Bessel function of the first kind
$J_n(\cdot)$	- Bessel function of first kind
$J_n^{(m',m)}(\cdot)$	- Jacobi polynomial
K	- Parameter of the lossy inductor model
l_e	- Length of the voice-coil conductor

L	- Number of degrees of freedom, number of loudspeakers
M	- Mass of the driver diaphragm assembly
n	- Parameter of the lossy inductor model
\mathbf{n}	- Unit normal
N	- Truncation order
N_p	- Number of samples in the azimuth angle direction
N_s	- Total number of samples over a sphere
N_t	- Number of samples in the zenith angle direction
$p(\mathbf{x}, t)$	- Sound pressure
$\bar{p}(\mathbf{x}, \omega)$	- Complex magnitude spectrum of the sound pressure
$P_n(\cdot)$	- Legendre polynomial
$P_n^m(\cdot)$	- Associated Legendre function of the first kind
Q_s	- Volume velocity of a pulsating sphere, monopole source-strength
r	- Radial coordinate
R	- Mechanical resistance of the driver suspension
$R^{(e)}$	- Voice-coil resistance
s	- Mono audio signal
S	- Area of a vibrating surface
\mathbb{S}	- Vibrating surface
\hat{S}	- Net surface area of a driver membrane
t	- Time
T_s	- Sampling period
$\mathbf{T}(\omega)$	- Transduction matrix
\mathbf{u}	- Column vector of velocity amplitude coefficients
v	- Voltage
V	- Volume, listening area
\mathbf{x}	- Position vector
\mathbf{x}_s	- Position vector of an elementary radiator, point on a given surface
W	- Acoustic power
\mathbf{W}	- Diagonal matrix containing non-dimensional area weight factors
$y_n^m(\cdot)$	- Real-valued spherical harmonic function
$Y_n^m(\cdot)$	- Complex-valued spherical harmonic function
\mathbf{Y}	- Vector containing complex-valued spherical harmonics up to order N
\mathbf{Z}	- Acoustic-impedance matrix
$Z^{(e)}$	- Clamped electrical impedance

Greek Letters

α	-	First zyz Euler angle
β	-	Second zyz Euler angle
γ	-	Third zyz Euler angle
Γ	-	Smooth closed surface
δ	-	Dirac delta
δ_{mn}	-	Kronecker delta
$\Delta(\cdot)$	-	Laplace operator, variation
ϵ	-	Compensation filter
θ	-	Zenith angle
ι	\equiv	$\sqrt{-1}$
$\mu(\omega)$	-	Eigenvalue of $\mathbf{T}(\omega)$
ν	$=$	$-\omega$
$\xi(\mathbf{x}_s)$	-	Set of orthogonal functions defined on a vibrating surface
ρ	-	Fluid density in the absence of acoustic perturbation
σ	-	Radiation efficiency
$\mathbf{v}(\mathbf{x}, t)$	-	Acoustic velocity
$\bar{\mathbf{v}}(\mathbf{x}, \omega)$	-	Complex magnitude spectrum of the acoustic velocity
$v(\mathbf{x}, t)$	-	Radial acoustic velocity
v_n	-	Acoustic velocity normal to a vibrating surface
ϕ	-	Azimuth angle
ψ	-	Acoustic radiation mode
Ψ	-	Modal matrix
ω	-	Angular frequency

Superscripts

*	-	Complex conjugate
<i>ap</i>	-	All pass
H	-	Complex conjugate transpose
<i>min</i>	-	Minimum phase
T	-	Matrix transpose
-	-	Frequency domain

Subscripts

- ap - All pass
- c - Continuous-time
- l - Acoustic radiation mode or transducer of the loudspeaker array
- min - Minimum phase
- opt - Optimum
- ref - Reference

Abbreviations and Acronyms

- ARM - Acoustic Radiation Mode
- BIBO - Bounded-Input Bounded-Output
- CLF - Common Loudspeaker Format
- CNMAT - Center for New Music and Audio Technologies
- DSP - Digital Signal Processing
- FIR - Finite-duration Impulse Response
- FRF - Frequency Response Function
- HOA - Higher Order Ambisonics
- IEM - Institute of Electronic Music and Acoustics
- IIR - Infinite-duration Impulse Response
- IRCAM - *Institut de Recherche et Coordination Acoustique/Musique*
- ITA - Institute of Technical Acoustics
- LDV - Laser Doppler Vibrometry
- LMS - Least Mean Squares
- LTI - Linear Time-Invariant
- MIMO - Multiple Inputs Multiple Outputs
- RMSE - Root Mean Square Error
- SISO - Single Input Single Output
- WFS - Wave Field Synthesis

Symbols

- $\Re \{ \cdot \}$ - Real part of a complex number
- $\mathbf{1}$ - Matrix of all 1's

Contents

1	Introduction	1
1.1	Directional characteristics of sound sources	2
1.2	Compact spherical loudspeaker arrays	4
1.3	Thesis main contributions and organization	7
1.3.1	Directivity representation	7
1.3.2	Electromechanical behavior of spherical loudspeaker arrays	9
1.3.3	Optimization criteria	11
1.3.4	Thesis organization	12
2	Sound Radiation and 3-D Sound Field Rendering	14
2.1	Wave equation	14
2.2	Directivity patterns	16
2.2.1	Simple multipole sources	16
2.2.2	Nearfield and farfield propagation	21
2.3	Subspaces for directivity representation	22
2.3.1	Spherical harmonics	23
2.3.2	Acoustic radiation modes (ARMs)	28

2.4	Spatial sound rendering using loudspeaker arrays	32
2.4.1	Theory	32
2.4.2	Spatial audio systems	36
3	Spherical Loudspeaker Array Modeling	38
3.1	Sound radiation	38
3.1.1	Continuous sphere	38
3.1.2	Discrete sphere	40
3.1.2.1	Convex regular polyhedra	44
3.2	Electromechanical behavior	51
3.2.1	Electrodynamic loudspeakers	51
3.2.2	Acoustical coupling	53
3.2.2.1	Lumped-parameter model	54
3.2.2.2	Distributed-parameter model	54
3.3	Enclosure design	55
4	Synthesis and Reproduction of Directivity Patterns	60
4.1	Synthesis of an arbitrary function	60
4.2	Synthesis of a spherical harmonic function	62
4.3	Synthesis with desired magnitude response	68
5	Equalization Filtering	75
5.1	The electroacoustical modeling of spherical loudspeaker arrays revisited	75
5.2	Signal processing chain of a spherical loudspeaker array	77

5.2.1	Sound pressure equalization	80
5.2.2	Sound power equalization	81
5.3	Numerical example: a dodecahedral loudspeaker array	82
6	Experimental Evaluation	89
6.1	Prototype description	89
6.2	Parameter estimation of the electrodynamic loudspeaker model	91
6.3	Electromechanical behavior	95
6.3.1	Experimental procedures	95
6.3.2	Results and discussion	97
6.4	Sound radiation	104
6.4.1	Experimental procedures	104
6.4.2	Results and discussion	107
7	Conclusion	119
7.1	Directivity representation	119
7.2	Electromechanical behavior of spherical loudspeaker arrays	121
7.3	Optimization criteria	122
7.4	Further research	123
A	Wave Equation in Spherical Coordinates	133
A.1	General solution	133
A.2	Exterior and interior problems	136
B	Properties of the Coupling Matrix for the Discrete Sphere	138

C Convex Regular Polyhedra	140
D Discrete-Time LTI Systems	143
E Author's Publications	147

Chapter 1

Introduction

The spatial properties of sound fields are important for human sound source localization in daily life and greatly affect the perceived sound quality and intelligibility, which has been explored in audio applications since the early days of the two-channel stereophonic reproduction, remaining an active field of research and development. In the aesthetics context, spatial control of sound has been widely used in contemporary electroacoustic music, in which not only the projection space, but also the composed space (integral to the composition itself) are dealt with [2, 3].

Most of the spatial audio systems such as conventional surround, WFS (Wave Field Synthesis) [4] and Ambisonics [5] provide the listeners with spatial sensations by surrounding them with many loudspeakers. Nevertheless, the difficulties in predicting the interaction between the electroacoustic sources and the room they are placed in make the problem extremely complex to address and massive computation is necessary to deal with the large number of loudspeakers used in sophisticated spatialization systems like WFS.

In this work a different approach is adopted. Instead of placing loudspeakers around the listener to produce spatial sound effects, a multi-channel electroacoustic source is used in order to reproduce the sound field generated by an acoustical source or to synthesize a desired sound field. Thus, the interaction of the source with the room it is placed in is naturally felt and understood by the listener, making the problem much simpler to treat. Unlike the WFS loudspeaker array, a multi-channel source is a compact array of loudspeakers designed to simulate complicated sound radiators such as musical instruments.

In the following, the directional characteristics of sound sources are briefly described. Next, an overview of the state of the art concerning compact spherical loudspeaker arrays for radiation

control is presented. Finally, the thesis main contributions are highlighted.

1.1 Directional characteristics of sound sources

A sound source can be characterized by the temporal and spatial properties of the sound field that it produces under free-field conditions, i.e., in the absence of any reflected waves¹. The interaction with both the room the source is placed in and the listener's hearing system determines the perceived auditory event. The temporal structure of the audio signals reaching the eardrums plays a major role in the human perception, which is categorized in musical and psychoacoustical attributes such as pitch, duration, dynamics, timbre, loudness and localization [6, 7].

The temporal signature of a sound source can be captured and analyzed by well-established techniques, like Fourier analysis [8]. The source spatial signature is characterized by the so-called sound directivity or directionality, which depends on frequency and can be obtained through measurements in an anechoic chamber. Unfortunately, the corresponding experimental procedures are complex, time-consuming and require expensive facilities which are not readily available in many acoustics laboratories. Therefore, little directivity data can be found in literature. The overall directional characteristics of several musical instruments are presented in [1], which is perhaps the most comprehensive and referenced work on this subject. Since the excitation mechanism of a loudspeaker unit is merely an electrical signal that can be easily controlled and processed, the directivity characterization is simpler than for musical instruments. Many loudspeaker manufacturers provide directivity data of their products in a file format called CLF (Common Loudspeaker Format), which can be downloaded in the CLF group website (<http://www.clfgroup.org/>).

As said above, the directivity pattern of a sound source is relevant for human perception. This statement can be qualitatively checked by rotating a given sound source around its axis. It is not expected that this will change the directional characteristics of the source, but will rather lead to a directivity pattern that is a rotated version of the original one relatively to the room the source is placed in and to the listener's position, so that he or she should be able to experience a different sound sensation. However, a directivity pattern contains lots of information and the scientific community has not yet found out what features of it are important for human perception. In addition, as far as the 3-D sound field simulation and synthesis is concerned, listening tests and

¹There is a mechano-acoustic coupling between the radiating body and the sound field it produces. Strictly speaking, this coupling depends on the characteristics of the room the source is placed in, so that the room affects the acoustical properties of the sound source. However, since most of the sound sources placed in ordinary rooms present a mechanical impedance much higher than the sound field (impedance mismatch), the room has just a minor effect on the source dynamics, so that it can be neglected.

room acoustics simulation results have shown that the choice of the directivity representation for the actual source has an influence on the perceived sound and on room acoustical parameters such as the clarity factor, the lateral energy fraction and the early decay time [9, 10, 11].

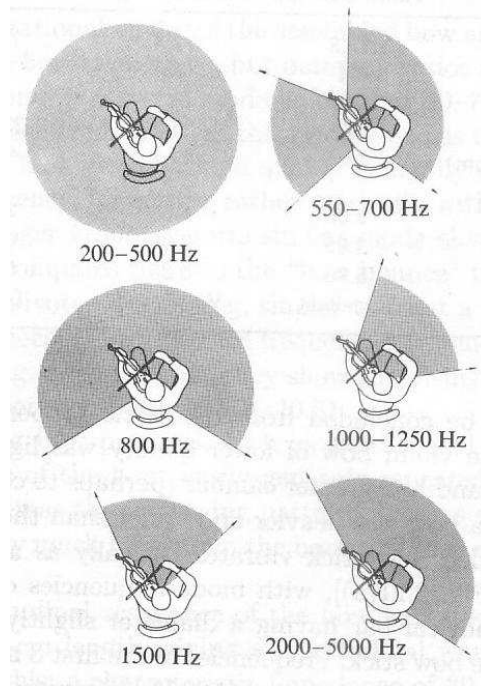


Figure 1.1: Principal radiation directions for a violin in the horizontal plane [1].

Figure 1.1 depicts the essential characteristics of the directivity pattern of a violin in the horizontal plane according to [1]. The shaded areas represent the directions in which the sound pressure level is within 3 dB of its maximum value averaged over a given frequency range in the horizontal plane. Most simulation and auralization of room acoustics use the averaged directivity data of musical instruments presented in that work. However, the angular radiation pattern of a violin varies strongly with frequency above about 1 kHz, changing drastically from one semitone to the next, so that averaged directivity patterns give rise to a poor representation of the violin spatial signature [12, 13]. This behavior is important for the violin sound quality and it has been called “directional tone color”, which makes it very difficult to produce a realistic violin sound with a single ordinary loudspeaker because it imposes its own directivity on all sounds it generates [14, 13]. The violin example illustrates the shortcomings of averaged directivity patterns and how complex the directional characteristic of a sound source may be.

1.2 Compact spherical loudspeaker arrays

Modern loudspeaker systems provide satisfactory control over the temporal signature of the sound field they generate, so that the current audio technologies can be used to reproduce these characteristics of acoustical sources. On the other hand, the commercially available loudspeaker systems are not able to reproduce the directivity pattern of an arbitrary sound source. As stated before, the loudspeakers impose their own spatial signature on the resulting 3-D sound field, which is generally quite different from the spatial signature of the original source that the electroacoustical device aims to reproduce.

In order to overcome the limitations of conventional audio systems concerning directivity reproduction, a compact spherical array of independently programmable loudspeaker units can be used. This electroacoustic device consists of several drivers mounted on a rigid sphere-like frame, which are generally distributed according to a convex regular polyhedron (Platonic solid) geometry to obtain a highly symmetrical configuration, so that the occurrence of preferred regions in the three-dimensional rendition space is reduced. The main objective is to control the directivity pattern of the loudspeaker array by acting on the signals that feed the transducers. Unlike conventional loudspeaker systems, the array drivers operate at the same frequency range, so that the sound fields produced by the individual loudspeaker units interact in a controllable way. Hence, the compact loudspeaker array should ideally be able to reproduce both the temporal and spatial signature of an acoustical source, i.e., the sound field produced by a given source at a given position in a room would be entirely reproduced by replacing the original source with the electroacoustical device, as depicted in Fig. 1.2, where V is the rendition space and Γ is a surface enclosing the source.

It is worth mentioning that the spherical loudspeaker arrays largely employed to obtain an approximate omnidirectional source² in room acoustics measurements constitute a simple special case of directivity controlled loudspeaker arrays. The drivers of omnidirectional sources are usually mounted on the faces of a rigid Platonic solid [15, 16, 17, 18], so that the desired directivity is approximately obtained by driving the array elements with the same electrical signal. These devices are simple mono-channel sources whose acoustical behavior is well-known. In contrast, this work focuses rather on the general case of multi-channel sources for directivity control.

Researchers from IRCAM (*Institut de Recherche et Coordination Acoustique/Musique*, Paris) introduced the concept of using a compact array of independently programmable electrodynamic loudspeakers in 1992 [19]. The first IRCAM prototype was a four-channel dodecahedral source

²Strictly speaking, an omnidirectional source is that one able to radiate sound energy to all directions. However, in this work, a source will be called omnidirectional if it radiates sound energy equally to all directions.

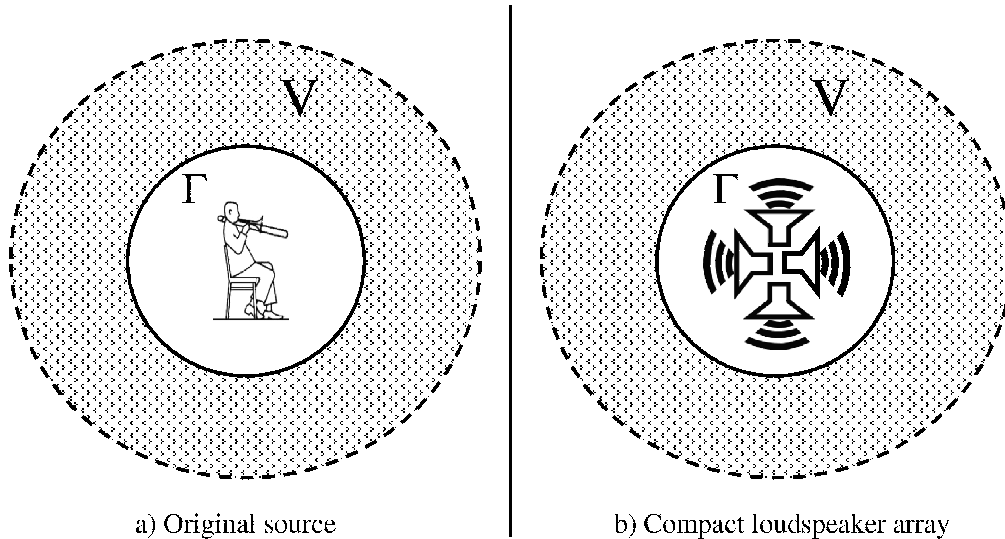


Figure 1.2: Synthesis of the temporal and spatial signature of an acoustical source by a compact loudspeaker array.

(twelve drivers, one per face) used to synthesize some simple directivity patterns [20]. Later, they built a set of three cubic shaped loudspeaker arrays of different sizes in order to increase the frequency bandwidth: a 25-cm cube with six 7-in (17.78-cm) drivers for the mid frequencies, an 8-cm cube with six tweeters for the high frequencies and a larger cube with four horizontal drivers for the low frequencies. These devices were conceived to provide electroacoustic music composers with a new spatialization tool and to partially reproduce the directivity of musical instruments [21].

Since a given directivity pattern can be decomposed over a basis of the so-called spherical harmonic functions (these are treated in detail in section 2.3.1), the IRCAM sources were programmed to reproduce such functions. This method leads to a set of filters for each spherical harmonic, so that a desired pattern can be obtained only by changing the gain associated with each set of filters. Due to its relatively small number of loudspeakers, the cubic source is able to reproduce only spherical harmonics of lower orders, that are the monopole (order $n = 0$), the dipole (order $n = 1$) in any spatial direction and partially the spherical harmonics of order $n = 2$ but with angular restrictions.

Kassakian and Wessel from CNMAT (Center for New Music and Audio Technologies, University of California Berkeley) presented further theoretical developments and simulated some spherical source configurations with different sizes and number of drivers [22]. The mean square error was used to evaluate the spherical array performance in reproducing spherical harmonic functions. However, loudspeaker constraints were not considered and their directivities were supposed to be frequency independent. These researchers also constructed a dodecahedral array with twelve

independent 4-in (10.16-cm) drivers, each provided with its own sealed enclosure in order to avoid the acoustical coupling inside of the array cavity [23]. Simulation results showed that the prototype can reproduce spherical harmonics up to order $n = 2$ and partially harmonics of order $n = 3$ in specific combinations, but only in the low-frequency range because of the relatively large source diameter (37 cm approximately).

In order to increase the operating range of the spherical source, researchers from CNMAT in collaboration with the Meyer Sound Laboratories built a compact spherical loudspeaker array with 120 independent 1.25-in (3.175-cm) drivers (an icosahedron with six drivers per face with 25.4cm in diameter) [24]. The geometric and engineering challenges that were overcome to create it are described in [25]. Simulation results were also presented and showed that the source can potentially reproduce spherical harmonics up to order $n = 8$ over a large frequency range (up to 7 kHz approximately). However, details of the directivity control software and measurements of the array have not been provided so far. It is worth mentioning that relevant driver constraints such as limited excursion, distortion and overheating were not taken into account in the simulations.

Zotter *et al.* from IEM (Institute of Electronic Music and Acoustics, Graz, Austria) presented an analytical model that describes the radiated sound field of a spherical array and is dedicated to the synthesis of spherical harmonic patterns [26, 27]. The source is modeled as a rigid sphere with several vibrating caps corresponding to the loudspeakers. The optimum cap velocities are obtained by the least-squares method. They also constructed an icosahedral source with 20 independent drivers sharing a common enclosure [28, 29, 30].

Behler and Pollow from ITA (Institute of Technical Acoustics, Aachen, Germany) built dodecahedral arrays to be used in room acoustics measurements in order to obtain improved room impulse responses for auralization purposes [31, 32, 33].

Figure 1.3 shows the spherical loudspeaker array prototypes developed at the laboratories mentioned above. The researches concerning the application of compact loudspeaker arrays to electroacoustic music performance that were conducted at Princeton University are also worth mention (see [34, 35, 36]). In contrast to all works cited up to now, which consider only electrodynamic transducers, a loudspeaker array of four piezoelectric transducers that provides directivity control in the horizontal plane at high frequencies (5 – 20 kHz) has recently been proposed [37].

It is worth noting that, besides room acoustics measurements, electroacoustic music performance and synthesis of directivity patterns of acoustical sources, other applications for spherical loudspeaker arrays can be sought, such as information diffusion in privileged adjustable directions, microphone feedback control in sound reinforcement applications [38] and active control of

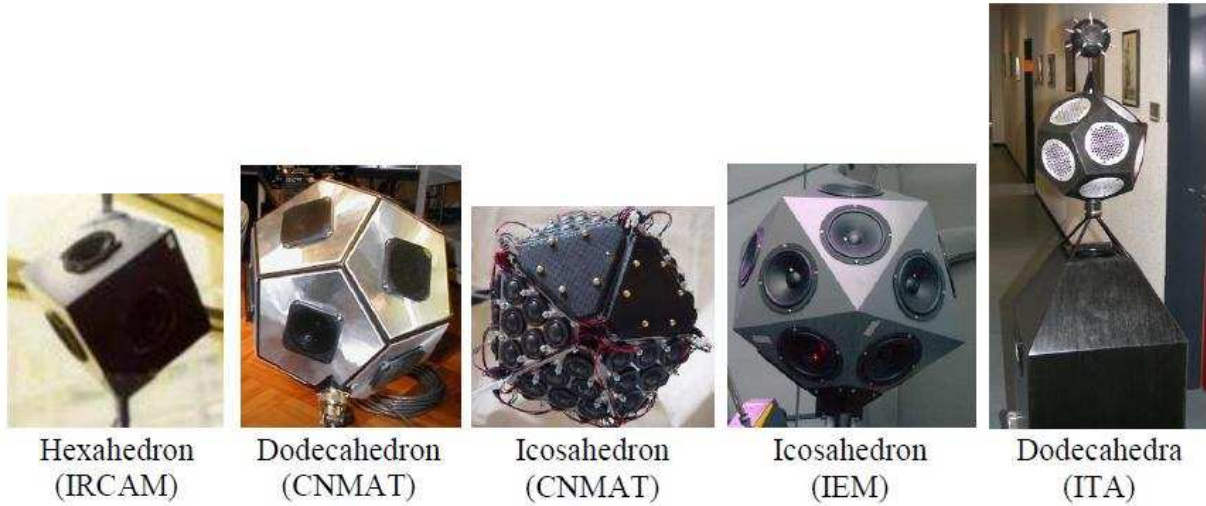


Figure 1.3: Spherical loudspeaker array prototypes based on the Platonic solids.

sound [39].

1.3 Thesis main contributions and organization

This work concerns the analysis and synthesis of directivity patterns by a compact spherical loudspeaker array. As explained throughout this section, the thesis main contributions are: the characterization of an improved basis for directivity representation, the investigation of the electromechanical behavior of compact loudspeaker arrays and the comparative analysis of distinct optimization criteria to derive the signals that must feed the drivers in order to reproduce a given directivity pattern.

1.3.1 Directivity representation

Spherical harmonics have been playing an important role in spherical array research. These functions constitute a natural basis for representation of sound source directivities, since they emerge from the solution of the Helmholtz equation in spherical coordinates (refer to appendix A). Therefore, as said before, the control strategy generally adopted is to provide the spherical array with some preprogrammed basic directivities corresponding to spherical harmonic patterns. The number of these elementary directivities is limited to the number of loudspeakers in the array. Then, different radiation patterns can be achieved simply by changing the gains associated with the ba-

sic directivities, so that it is not necessary to redesign the filters when a different target directivity pattern is desired.

However, it is known that spatial aliasing degrades the spherical array capability in synthesizing spherical harmonics as frequency increases [22, 21, 26] so that the control strategy based on these functions becomes inaccurate. In fact, although spherical harmonics are suitable basis elements in describing arbitrary directivity patterns, they cannot be expected to correspond to efficient radiation patterns of a spherical loudspeaker array at all frequencies.

At low frequencies, since higher order spherical harmonics exhibit very low radiation efficiencies [40], spatial aliasing does not affect the radiation pattern in the farfield³. However, as frequency increases, the radiation efficiencies of higher order spherical harmonics increase as well and they start to propagate to the farfield. Thus, the spherical array can no longer radiate pure spherical harmonics, like the monopole or dipoles. Moreover, at high frequencies the shape and vibration pattern of each loudspeaker lead to numerous radiating higher order spherical harmonics, which are combined and interact in the nearfield when multiple loudspeakers are driven. Then, in order to obtain an accurate sound field representation, the truncated spherical harmonic expansion must retain a number of terms much higher than the number of independent degrees of freedom of the array. Such terms can be grouped in a finite number of subsets corresponding to the so-called “acoustic radiation modes” (these are treated in detail in section 2.3.2) of the array.

Acoustic radiation modes are an alternative way to describe the sound field that a vibrating structure radiates. Such a modal approach is based on how efficiently a given velocity distribution on the structure surface radiates sound energy and it has been used since the 1990’s (cf. [42, 43, 44, 45, 46]). Radiation modes are commonly used to describe the structural vibration of primary sources in active noise control applications (see, for example, [47]). However, they have not been applied to secondary sources or to compact loudspeaker arrays for directivity control. The author has found only one work by Wen *et al.* [48] which applies such a modal approach to sound field synthesis by planar loudspeaker arrays, where the array elements were assumed to be simple omnidirectional point sources.

As far as a vibration system with a finite number of degrees of freedom is concerned (as is the case for a spherical loudspeaker array), its radiation modes span an equally finite dimension subspace on which any radiation pattern that such a system is able to generate can be projected. Such a useful property does not hold for the spherical harmonic representation of the sound field pro-

³If a given field point is sufficiently far from the source so that the sound pressure decreases linearly with distance along a radial line connecting the point with the source, the former is said to be in the farfield [41]. For further details, refer to section 2.2.2.

duced by the same radiator. Actually, the real-valued spherical harmonics are the radiation modes of the continuous sphere [40], i.e., the sphere which is able to assume any surface velocity pattern (infinite number of degrees of freedom). Therefore, spherical harmonics span an infinite dimension subspace so that truncation error generally arises from the spherical harmonic decomposition.

In this work, instead of using a finite set of spherical harmonics as preprogrammed basic directivities, an approach based on the acoustic radiation modes of the spherical loudspeaker array is proposed. Unlike the usual spherical harmonic strategy, any radiation pattern that the array is able to reproduce can be decomposed into its radiation modes with no approximation error. Since radiation modes are closely related to radiation efficiencies, this approach leads also to a quantitative description of the low-frequency constraints in the directivity synthesis, which have only been qualitatively discussed in previous works. Moreover, radiation modes allow to rank the expansion terms by their radiation efficiencies, so that a reduced number of active channels can be obtained because it is useless to drive inefficient modes. Finally, radiation modes are not restricted to spherical shapes. So, it is expected that most of the ideas presented here can be extended to non-spherical loudspeaker arrays and will allow to take into account the actual vibration pattern and shape of the loudspeakers.

1.3.2 Electromechanical behavior of spherical loudspeaker arrays

Unlike omnidirectional sources, the interaction of the sound fields produced by the independent drivers of a directivity controlled source is not intuitive and some attempts have been made to predict the radiation pattern of a spherical array [22, 26, 33, 39]. For the moment, the spherical caps approach proposed in [26] is the most elaborate radiation prediction model for a compact spherical loudspeaker array, in which the drivers of the array are modeled as convex spherical caps, each oscillating with a constant radial velocity amplitude over its surface. This model presents the advantage of having an analytical solution (which will be presented in section 3.1.2) and is inspired in a previous work dealing with a single driver mounted on a rigid sphere [49]. However, it cannot predict the non-rigid body behavior of real drivers and neglects their actual geometry, which is known to affect the radiation pattern, especially at high frequencies [50, 51].

A comparison of the theoretical predictions by the spherical cap model and measured directivity data in an anechoic chamber for a single driver mounted on a rigid sphere (a 3-in, 7.62-cm, cone woofer mounted on a sphere with a 10-in, 25.4-cm, radius) is presented in [49]. It was observed that, in general, the theoretical predictions match the experimental results closely, indicating that the spherical cap approach can be extended to spherical loudspeaker arrays. However, the cap

size used in the simulations presented in [49] was made frequency-dependent in order to match the experimental data. This was explained as being probably a result of the driver suspension behavior, which can be hardly modeled as a rigid body. This can be investigated by measuring the vibration of the driver membrane and suspension.

For a spherical loudspeaker array, theoretical results have not been explicitly compared to directivity measurements in anechoic chamber so far. As a matter of fact, directivity measurements of the IEM icosahedral array are described in [28, 29]. These works do not directly compare the measured radiation patterns to theoretical predictions, but ref. [29] does provide an indirect comparison which indicates a deviation between experimental and theoretical results. Nevertheless, the used measurement setup is not satisfactory for directivity measurements, for example, the experiments were not conducted in an anechoic chamber. Therefore, it is not possible to determine whether the prediction radiation model or the experimental setup (or both) should be improved.

The directivity control by a spherical loudspeaker array is achieved by setting the relative voltages, rather than velocities, of the array elements. Hence, the electromechanical behavior of such a device must be known in order to evaluate its surface vibration pattern which, in turn, leads to the sound field. In this direction, similar electromechanical models for spherical arrays were proposed in [27] — which was later improved in [29, 52] — and [32]. Surface velocity measurements by LDV (Laser Doppler Vibrometry) of the IEM icosahedral array revealed a good match between theoretical and experimental results in the low-frequency range [27, 29, 52], while some discrepancies were observed at high frequencies. However, only a single point on the membrane of each driver was measured, so that the rigid body assumption could not be explicitly and rigorously validated. Nevertheless, since researchers have been mainly concerned about the relation between an idealized vibration pattern of the loudspeaker array and the resulting acoustic radiation pattern, there is still a lack in the accurate description of the electromechanics of spherical loudspeaker arrays for radiation control.

The enclosure design is a controversial issue that is also related to the electromechanical behavior of spherical arrays. Two different approaches have been reported in literature (cf. [23, 29, 30, 31, 32, 52]). In the first approach, the drivers share a common hollow enclosure and, in the second, they have their own independent sealed cavities. The former leads to an easier to build mechanical frame and to a larger cabinet volume that potentially gives rise to lower voltages in the low-frequency range [31, 52, 53]. However, to let the drivers share an empty cavity produces undesirable acoustic cavity resonances in the operation frequency range of the array [32, 52] and leads to acoustic coupling effects that cannot be easily predicted. The electromechanical model proposed in [32] takes the acoustic coupling into account by modeling the common array cavity as

a lumped-parameter element (acoustic compliance). On the other hand, the model presented in [27] applies the spherical caps approach also to the interior sound field, so that the resulting boundary-value problem has an analytical solution and the higher-order cavity modes can be considered (distributed-parameter model); as a drawback, this model assumes that the array cavity is a perfect sphere.

This work presents a detailed theoretical and experimental investigation of the compact loudspeaker array electromechanics. An improved electromechanical model which takes into account the inductance losses of the driver voice-coil is proposed and experimentally validated through LDV measurements of a dodecahedral source prototype, as shown in chapter 6. Unlike the previous works mentioned before, many points on the surface of the diaphragm suspension assembly of the drivers are measured by using a scanning laser Doppler vibrometer, so that uneven deformation can be characterized. The cited lumped- and distributed-parameter modeling of the acoustic coupling between the drivers inside the array frame are compared. In addition, directivity measurements were carried out in an anechoic chamber in order to study the limitations and applications of the spherical caps model proposed in [26].

As it will be shown in section 3.3, the effect of the internal acoustic coupling on the sound power can be evaluated in a simple way by combining the electromechanical model with the acoustic radiation mode approach, on which the enclosure design discussion presented in this work is based. Furthermore, this combination leads to an unexpected result, namely, the acoustic radiation modes of a Platonic loudspeaker are the eigenvectors of the transduction matrix obtained using the electromechanical model for drivers sharing a common cabinet. This result greatly simplifies the equalization filter design and is discussed in chapter 5.

1.3.3 Optimization criteria

As said before, compact spherical loudspeaker arrays are used to reproduce or to synthesize desired directivity patterns. To accomplish this, an inverse problem must be addressed, i.e., the signals that must feed the drivers in order to reproduce the target directivity pattern must be derived from an optimization criterion.

Most of the published works about spherical loudspeaker arrays minimize the Euclidean norm of the difference between the target pattern and the synthesized pattern in order to obtain the velocity of each driver (cf. [22, 26, 54]). This is a well-known convex optimization problem (least-squares) that can be easily solved and whose solution is unique. However, the least-squares

method may lead to a suboptimal solution due to the fact that the cost function is based on the physical characteristics of the sound field rather than on a psychoacoustic measure. For example, in the least-squares formulation, magnitude error and phase error are treated equally, although the importance of these errors may not be equal as far as the human perception is concerned.

Modern room acoustic simulation and auralization tools permit to evaluate the influence of source directivity on the sound field in a room. For this purpose, only the magnitude of the farfield directivity data is used [10, 32, 33, 55]. Therefore, the literature on room acoustics suggests that the phase of the farfield directivity pattern plays a minor role in the human perception compared to its magnitude. Hence, it is expected that a spherical loudspeaker array will be able to better synthesize the perceptually relevant attributes of the sound field if the phase of the target pattern is excluded from the cost function.

Unlike the usual least-squares method, the optimization problem with desired magnitude response (phase not concerned) is non-convex and therefore more difficult to solve. The so-called “magnitude least-squares” problem and several solution methods are described in detail in [56]. In addition, its application to directivity synthesis by spherical arrays is briefly presented in some recent works [33, 37, 56, 57]. However, a comparison between the standard least-squares and the magnitude least-squares applied to directivity synthesis has not been satisfactorily presented and discussed so far, so that the advantages and the shortcomings of the latter remain unclear. This is carried out in chapter 4.

1.3.4 Thesis organization

This thesis is organized as follows:

- Chapter 2: this chapter presents an overview of advanced topics in acoustics that are not collected in books, but which are essential (except for section 2.2, which is rather complementary) to the comprehension of the thesis content;
- Chapter 3: the theoretical models used to predict the sound radiation and the electromechanical behavior of spherical loudspeaker arrays are described. In addition, a discussion on the enclosure design and simulation results are presented;
- Chapter 4: this chapter addresses the inverse problem, namely, given the target directivity pattern and the radiation model described in chapter 3, optimization criteria are applied to

compute the velocity of each driver of the spherical array. Numerical simulation results are also presented;

- Chapter 5: the problem of equalization filtering is addressed. Two different equalization approaches for a spherical loudspeaker array are presented and compared. A numerical example is provided;
- Chapter 6: the theoretical models presented in chapter 3 are experimentally validated. Results of electrical impedance, loudspeaker vibration and directivity measurements of a 12-driver array prototype are presented and discussed;
- Chapter 7: conclusions and suggestions for further work are presented.

Chapter 2

Sound Radiation and 3-D Sound Field Rendering

This chapter reviews some topics related to sound radiation and spatial audio as they are required for the comprehension of the thesis. First, the basic wave propagation model used throughout this work — which is described by the well-known Helmholtz equation — is presented in section 2.1. Next, section 2.2 introduces fundamental concepts on sound source directivity through the development of elementary radiators such as monopoles and dipoles, which may be skipped by advanced readers. The subspaces for directivity representation (spherical harmonics and acoustic radiation modes) mentioned in chapter 1 are considered in detail in section 2.3, whose content is essential and widely used in the next chapters. Finally, the theory of spatial sound rendering through loudspeaker arrays is presented in section 2.4, as well as some promising audio technologies.

2.1 Wave equation

This work concerns linear acoustic phenomena in a perfect homogeneous quiescent gas, i.e., only low energy waves not subjected to dissipative effects and heat exchange are considered; in addition, there is no mean flow and the medium properties are constant and uniform through the acoustic domain. Therefore, in the absence of sound sources in the domain, the following well-known linearized wave equation governs the sound propagation [58]:

$$\Delta p(\mathbf{x}, t) - \frac{1}{c^2} \frac{\partial^2 p(\mathbf{x}, t)}{\partial t^2} = 0 \quad (2.1)$$

where $p(\mathbf{x}, t)$ is the sound pressure, c is the sound speed, \mathbf{x} is the position vector, t is time and $\Delta(\cdot)$ is the Laplace operator.

The acoustic velocity $\mathbf{v}(\mathbf{x}, t)$ is related with the acoustic pressure $p(\mathbf{x}, t)$ by the linearized Euler equation [58]

$$\rho \frac{\partial \mathbf{v}(\mathbf{x}, t)}{\partial t} = -\nabla p(\mathbf{x}, t) \quad (2.2)$$

where ρ is the fluid density when the acoustic perturbation is absent. Throughout this work, unless otherwise specified, lower case bold letters indicate vectors, while upper case bold letters indicate matrices.

Now assume a harmonic time dependence of the form $e^{-i\omega t}$ (classical choice in theoretical acoustics) for $p(\mathbf{x}, t)$, where $i = \sqrt{-1}$ and ω is the angular frequency. This yields the wave and Euler equations in the frequency domain, respectively,

$$\Delta \bar{p}(\mathbf{x}, \omega) + k^2 \bar{p}(\mathbf{x}, \omega) = 0 \quad (2.3)$$

and

$$i\omega \rho \bar{\mathbf{v}}(\mathbf{x}, \omega) = \nabla \bar{p}(\mathbf{x}, \omega) \quad (2.4)$$

where $k = \omega/c$ is the wave number, $\bar{p}(\mathbf{x}, \omega)$ and $\bar{\mathbf{v}}(\mathbf{x}, \omega)$ are the complex magnitude spectrum of the acoustic pressure and velocity, respectively. In other words, they are the Fourier transforms of $p(\mathbf{x}, t)$ and $\mathbf{v}(\mathbf{x}, t)$, i.e., $\bar{p}(\mathbf{x}, \nu) = \int_{-\infty}^{\infty} p(\mathbf{x}, t) e^{-i\nu t} dt$ and $\bar{\mathbf{v}}(\mathbf{x}, \nu) = \int_{-\infty}^{\infty} \mathbf{v}(\mathbf{x}, t) e^{-i\nu t} dt$. It is worth noting that the traditional convention of choosing a harmonic time dependence in $e^{-i\omega t}$ results in a negative frequency $\nu = -\omega$ in the signal processing sense.

Equation (2.3) is an ordinary differential equation named Helmholtz equation.

Hereafter, the overbars will be omitted for the sake of convenience. Unless otherwise specified, frequency domain is assumed.

2.2 Directivity patterns

2.2.1 Simple multipole sources

Let (r, θ, ϕ) be spherical coordinates, where $r \geq 0$, $0 \leq \theta \leq \pi$ and $0 \leq \phi < 2\pi$ are, respectively, the radial coordinate, the zenith angle and the azimuth angle, as depicted in Fig. 2.1. Hence, the position vector can be written as $\mathbf{x} = r \sin \theta \cos \phi \mathbf{e}_x + r \sin \theta \sin \phi \mathbf{e}_y + r \cos \theta \mathbf{e}_z$, where \mathbf{e}_x , \mathbf{e}_y and \mathbf{e}_z are the unit vectors of the standard basis in three-dimensions.

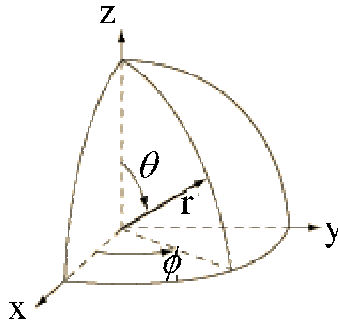


Figure 2.1: Spherical coordinates.

Now, consider a pulsating sphere of radius a centered at the origin and let v be the amplitude of the radial velocity at $r = a$, which is assumed to be constant over the sphere. Then, under free-field conditions, solution of Eq.(2.3) in spherical coordinates yields [58]

$$p(r) = -\frac{\iota\omega\rho Q_s}{4\pi r(1 - \iota ka)} e^{\iota k(r-a)} \quad (2.5)$$

where $r \geq a$ and $Q_s = 4\pi a^2 v$ is the volume velocity at a , also referred to as the source-strength function. It is worth noting that $-\iota\omega Q_s$ is the volume acceleration at a .

Equation (2.5) shows that a pulsating sphere in an unbounded medium gives rise to an outgoing spherically symmetric wave. In addition, the sound pressure magnitude decreases linearly with the distance r . Since the acoustic field does not depend on θ and ϕ , the pulsating sphere is an isotropic or omnidirectional source.

The pulsating sphere can be idealized as a point source if a is let to be very small but v very large, such that Q_s remains constant and ka can be neglected. Such a hypothetical source is called an acoustic monopole. If it is located at \mathbf{x}_s instead of at $r = 0$, Eq.(2.5) becomes

$$p(\mathbf{x}) = i\omega\rho Q_s G(\mathbf{x}, \mathbf{x}_s) \quad (2.6)$$

where

$$G(\mathbf{x}, \mathbf{x}_s) = -\frac{e^{ik|\mathbf{x}-\mathbf{x}_s|}}{4\pi|\mathbf{x}-\mathbf{x}_s|} \quad (2.7)$$

is the 3-D free-space Green's function¹ and $|\mathbf{x}-\mathbf{x}_s|$ is the radial distance from the source.

Sound fields other than omnidirectional can be obtained by superposing two or more monopoles. Consider two monopoles of opposite source-strengths $+Q_s$ and $-Q_s$, located at $\mathbf{x}_s + \mathbf{d}/2$ and $\mathbf{x}_s - \mathbf{d}/2$, respectively, as depicted in Fig. 2.2. Hence, the resulting sound pressure is

$$p(\mathbf{x}) = i\omega\rho Q_s G(\mathbf{x}, \mathbf{x}_s + \mathbf{d}/2) - i\omega\rho Q_s G(\mathbf{x}, \mathbf{x}_s - \mathbf{d}/2) \quad (2.8)$$

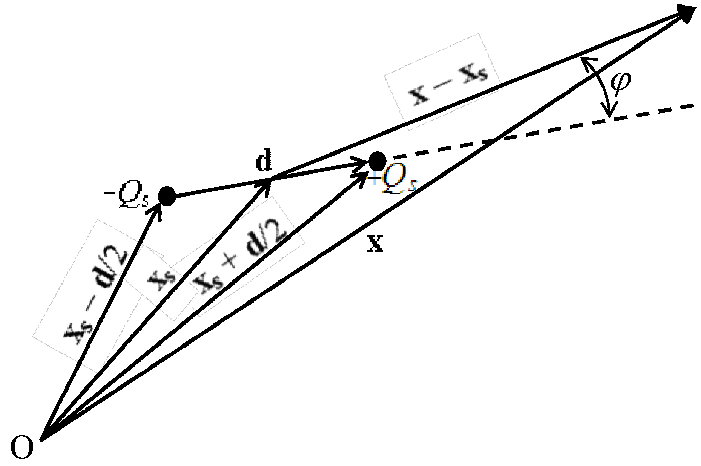


Figure 2.2: Acoustic dipole arbitrarily oriented modeled by two monopoles with source-strengths $+Q_s$ and $-Q_s$.

By assuming that $|\mathbf{d}|$ is vanishing small, an acoustic dipole is obtained. In this limit, $G(\mathbf{x}, \mathbf{x}_s \pm \mathbf{d}/2)$ can be approximated with a truncated Taylor series as $G(\mathbf{x}, \mathbf{x}_s) \pm (\mathbf{d}/2) \cdot \nabla_s G(\mathbf{x}, \mathbf{x}_s)$, where ∇_s denotes the gradient with respect to the source coordinates [58]. Then, Eq.(2.8) simplifies to

$$p(\mathbf{x}) = i\omega\rho Q_s \mathbf{d} \cdot \nabla_s G(\mathbf{x}, \mathbf{x}_s) \quad (2.9)$$

¹The Green's function so defined satisfies the inhomogeneous Helmholtz equation $\Delta G(\mathbf{x}, \mathbf{x}_s) + k^2 G(\mathbf{x}, \mathbf{x}_s) = \delta(\mathbf{x} - \mathbf{x}_s)$, where $\delta(\cdot)$ is the Dirac delta [59].

where

$$\nabla_s G(\mathbf{x}, \mathbf{x}_s) = \frac{dG(\mathbf{x}, \mathbf{x}_s)}{d|\mathbf{x} - \mathbf{x}_s|} \nabla_s |\mathbf{x} - \mathbf{x}_s| \quad (2.10)$$

and

$$\nabla_s |\mathbf{x} - \mathbf{x}_s| = -\frac{(\mathbf{x} - \mathbf{x}_s)}{|\mathbf{x} - \mathbf{x}_s|} \quad (2.11)$$

By using Eqs.(2.7), (2.10) and (2.11), Eq.(2.9) becomes

$$p(\mathbf{x}) = -\rho c k^2 |\mathbf{d}_m| \cos \varphi \left(1 + \frac{\iota}{k|\mathbf{x} - \mathbf{x}_s|} \right) \frac{e^{\iota k|\mathbf{x} - \mathbf{x}_s|}}{4\pi |\mathbf{x} - \mathbf{x}_s|} \quad (2.12)$$

where $\mathbf{d}_m \equiv Q_s \mathbf{d}$ is the dipole moment and φ is the angle between vectors \mathbf{d} and $\mathbf{x} - \mathbf{x}_s$.

Two monopoles with opposite source-strengths separated by an infinitesimal distance lead to a dipole. Analogously, two dipoles with opposite dipole moments separated by an infinitesimal distance lead to a quadrupole. Figure 2.3 shows the two basic types of quadrupoles: a longitudinal quadrupole on the left and a lateral quadrupole on the right, where $|\mathbf{d}|$ is vanishing small.

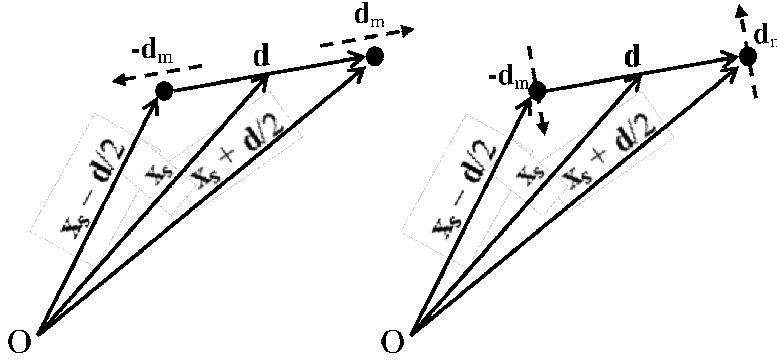


Figure 2.3: Longitudinal (on the left) and lateral (on the right) quadrupoles arbitrarily oriented modeled by two dipoles with moments \mathbf{d}_m and $-\mathbf{d}_m$.

Proceeding similarly as for the dipole, the quadrupole produces a sound pressure field given by

$$p(\mathbf{x}) = \iota \omega \rho (\mathbf{d}_m \cdot \nabla_s) (\mathbf{d} \cdot \nabla_s) G(\mathbf{x}, \mathbf{x}_s) \quad (2.13)$$

Consider a longitudinal quadrupole aligned along the z axis so that $\mathbf{d} = |\mathbf{d}| \mathbf{e}_z$, $\mathbf{d}_m = |\mathbf{d}_m| \mathbf{e}_z$ and $\mathbf{x}_s = z_s \mathbf{e}_z$. Then, Eq.(2.13) becomes

$$p(\mathbf{x}) = \iota\omega\rho|\mathbf{d}_m||\mathbf{d}|\frac{\partial^2 G(\mathbf{x}, \mathbf{x}_s)}{\partial z_s^2} \quad (2.14)$$

If $z_s = 0$, one has $|\mathbf{x} - \mathbf{x}_s| = r$ and $z = r \cos \theta$. Hence, evaluation of the partial derivatives of the Green's function in Eq.(2.14) yields (cf. [58])

$$p(r, \theta) = -\iota\rho ck^3|\mathbf{d}_m||\mathbf{d}|\left[(1 - 3\cos^2\theta)\left(\frac{\iota}{kr} - \frac{1}{k^2r^2} + \frac{1}{3}\right) - \frac{1}{3}\right]\frac{e^{\iota kr}}{4\pi r} \quad (2.15)$$

Similarly, for a lateral quadrupole with $\mathbf{d} = |\mathbf{d}|\mathbf{e}_y$, $\mathbf{d}_m = |\mathbf{d}_m|\mathbf{e}_x$ and $\mathbf{x}_s = x_s\mathbf{e}_x + y_s\mathbf{e}_y$, Eq.(2.13) becomes

$$p(\mathbf{x}) = \iota\omega\rho|\mathbf{d}_m||\mathbf{d}|\frac{\partial^2 G(\mathbf{x}, \mathbf{x}_s)}{\partial x_s \partial y_s} \quad (2.16)$$

If $x_s = y_s = 0$, one has $|\mathbf{x} - \mathbf{x}_s| = r$, $x = r \sin \theta \cos \phi$ and $y = r \sin \theta \sin \phi$. Hence, evaluation of the partial derivatives of the Green's function in Eq.(2.16) yields (cf. [58])

$$p(r, \theta, \phi) = -\iota\rho ck^3|\mathbf{d}_m||\mathbf{d}|\sin^2\theta \cos\phi \sin\phi \left(\frac{3}{k^2r^2} - 1 - \frac{3\iota}{kr}\right)\frac{e^{\iota kr}}{4\pi r} \quad (2.17)$$

Consider a sound source centered at the origin of the coordinate system depicted in Fig. 2.1. The directivity pattern of this source describes its acoustic field as a function of θ and ϕ for a given r , i.e., the directivity function of a sound source is its angular radiation pattern. Inspection of Eqs.(2.6), (2.12) and (2.17) reveals that the directivity patterns of the monopole, the dipole aligned along the z axis and the lateral quadrupole considered here are, respectively, a constant, $\cos \theta$ and $\sin^2 \theta \cos \phi \sin \phi$. These patterns are shown in Fig. 2.4, where they have been normalized to a unitary maximum pressure amplitude. The figure shape indicates the magnitude of the sound pressure, and the dark and light portions indicate a 180° phase difference. It is worth noting that the directivity patterns of these radiators do not depend on the distance and the frequency.

The angular radiation pattern of the longitudinal quadrupole is given by the term between square brackets in Eq.(2.15). Unlike the radiators presented in Fig. 2.4, the longitudinal quadrupole directivity depends on the non-dimensional parameter kr , i.e., it depends on the distance and the frequency. Figure 2.5 illustrates the directivity patterns of a longitudinal quadrupole aligned along the z axis for $kr = 0.2$, $kr = 2$, $kr = 20$ and very large kr (farfield). As before, the patterns have been normalized to a unitary maximum pressure amplitude with 0 phase. The figure shape

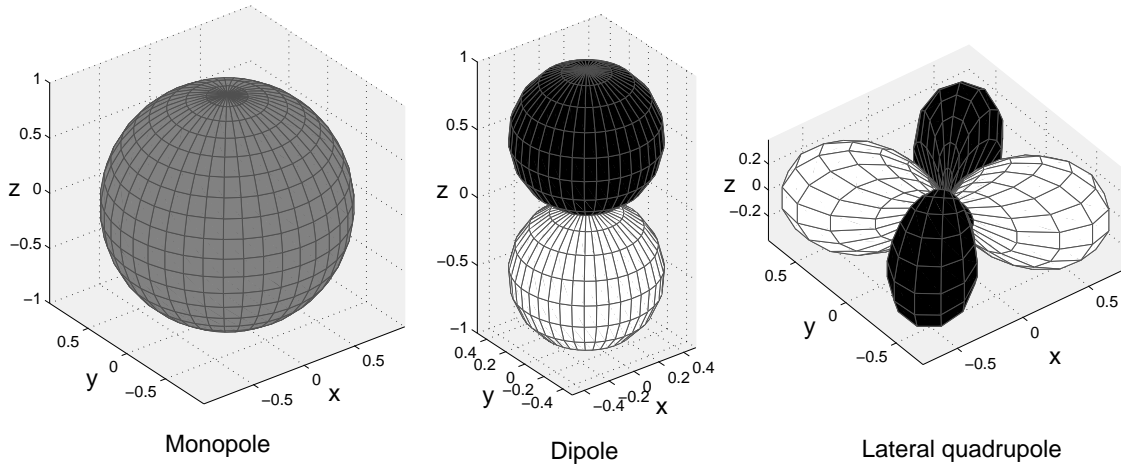


Figure 2.4: Directivity patterns of a monopole, a dipole and a lateral quadrupole. The figure shape indicates the magnitude of a normalized sound pressure, and the dark and light portions indicate a 180° phase difference.

indicates the magnitude of the sound pressure and the color gradient indicates its phase.

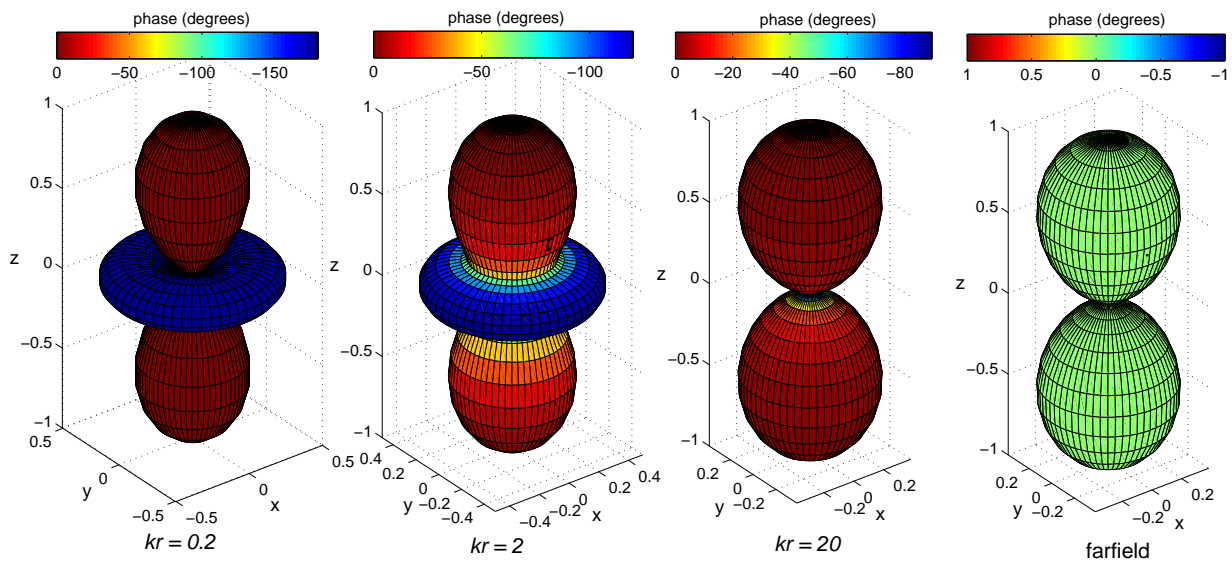


Figure 2.5: Directivity patterns of a longitudinal quadrupole evaluated at $kr = 0.2$, $kr = 2$, $kr = 20$ and under farfield condition. The figure shape indicates the magnitude of a normalized sound pressure and the color gradient indicates its phase.

The color gradient in Fig. 2.5 reveals that the directivity pattern is a complex-valued function that converges to the farfield directivity as kr increases. In fact, Fig. 2.4 illustrates very particular radiators whose directivities do not depend on kr . Unlike the monopole, the dipole and the lateral

quadrupole, the directivity patterns of most of the actual sound sources do depend on both distance and frequency. In addition, unlike the longitudinal quadrupole, the farfield directivity is generally a function of frequency. When the directivity pattern of a sound source is presented in a technical publication, it is understood that data were taken at the farfield. In the following section, the nearfield and farfield propagation are discussed.

2.2.2 Nearfield and farfield propagation

When dealing with sound radiation problems under free-field conditions, it is important to keep in mind the difference between nearfield and farfield propagation. For an arbitrary radiator, if the sound field is evaluated at a distance sufficiently large from the source, the sound pressure magnitude will decrease linearly with distance along a radial line connecting with the source, which characterizes the farfield propagation. Otherwise, one has nearfield propagation.

Equation (2.7) shows that the sound pressure magnitude produced by a monopole always decreases linearly with distance, so that there is no nearfield. On the other hand, the terms in brackets in Eqs.(2.12), (2.15) and (2.17) show that there is a nearfield pressure associated with the dipole and quadrupole. Since $k^{-1}r^{-2}$ and $k^{-2}r^{-3}$ tends to zero faster than r^{-1} as r increases, the nearfield terms vanish at a distance sufficiently large, as stated before. Then, under farfield condition, Eqs.(2.12), (2.15) and (2.17) simplify to

$$p(\mathbf{x}) = -\rho ck^2 |\mathbf{d}_m| \cos \varphi \frac{e^{\iota k |\mathbf{x} - \mathbf{x}_s|}}{4\pi |\mathbf{x} - \mathbf{x}_s|} \quad (2.18)$$

$$p(r, \theta) = \iota \rho ck^3 |\mathbf{d}_m| |\mathbf{d}| \cos^2 \theta \frac{e^{\iota kr}}{4\pi r} \quad (2.19)$$

and

$$p(r, \theta, \phi) = \iota \rho ck^3 |\mathbf{d}_m| |\mathbf{d}| \sin^2 \theta \cos \phi \sin \phi \frac{e^{\iota kr}}{4\pi r} \quad (2.20)$$

Many compact acoustical sources produce three-dimensional sound fields which can be conveniently represented in spherical coordinates in the same way as the simple multipole sources. Fortunately, Eq.(2.3) is separable in such a coordinate system so that application of the method of separation of variables leads to the general solution under free-field conditions (see appendix A.2)

$$p(r, \theta, \phi) = \sum_{n=0}^{\infty} \sum_{m=-n}^n A_{mn} h_n^{(1)}(kr) Y_n^m(\theta, \phi) \quad (2.21)$$

where A_{mn} is a constant, $h_n^{(1)}(\cdot)$ is the spherical Hankel function of the first kind and $Y_n^m(\cdot)$ is the spherical harmonic function that will be discussed in section 2.3.1.

Equation (2.21) shows that $h_n^{(1)}(\cdot)$ describes the radial propagation of each series term. Explicit expressions of this function for some n values are [60, 61]

$$\begin{aligned} h_0^{(1)}(x) &= -\iota \frac{e^{\iota x}}{x} \\ h_1^{(1)}(x) &= -\left(\frac{\iota}{x} + 1\right) \frac{e^{\iota x}}{x} \\ h_2^{(1)}(x) &= \left(-\frac{3\iota}{x^2} - \frac{3}{x} + \iota\right) \frac{e^{\iota x}}{x} \end{aligned} \quad (2.22)$$

For large arguments, the function $h_n^{(1)}(kr)$ approaches $(-\iota)^{n+1} e^{\iota kr} (kr)^{-1}$ [60, 61], so that each propagation term in Eq.(2.21) will decrease linearly with r , so does the sound pressure magnitude, as stated before. On the other hand, for small arguments, the function $h_n^{(1)}(kr)$ approaches $-\iota(kr)^{-n-1}(2n-1)!!$, where $(2n-1)!!$ is the double factorial of $(2n-1)$ [62, 61]. “This divergent behavior, customarily described as the ‘nearfield’, sets in when the argument kr becomes smaller than n . Hence, the nearfield extends further and further out for high n ; in fact at any r , no matter how large, nearfield behavior will be encountered if sufficiently large n values are included” [62].

Briefly, how far one must be from the source in order to ensure farfield propagation depends on the frequency and the complexity of the directivity pattern. The latter is represented by the largest n that must be retained in Eq.(2.21) in order to accurately describe the sound field, as it will be explained in section 2.3.1. As frequency increases and/or the directivity pattern becomes simpler, the nearfield effects take place closer to the source. However, it is worth noting that the directivity complexity of an actual source generally increases with frequency.

2.3 Subspaces for directivity representation

In this section, two distinct subspaces for directivity representation are described and discussed, namely, the subspace spanned by spherical harmonic functions and the subspace spanned by the acoustic radiation modes.

The angular dependence of the solution of the Helmholtz equation in spherical coordinates — Eq.(2.3) — is given by a linear combination of spherical harmonic functions (see Eq.(2.21)). Therefore, these functions constitute a natural basis for representation of sound source directivities and are applied to a wide range of sound radiation problems.

Acoustic radiation modes (also called simply radiation modes) are another class of functions that is of importance in sound radiation problems. Radiation modes constitute a set of independent surface velocity distributions and are a useful representation of vibration patterns when one is mainly interested in the sound field radiated by a vibrating structure. Such a modal decomposition is only a function of the frequency, the radiating structure geometry and the constraints the body is subjected to, i.e., it does not depend on the source of excitation and on the mass and stiffness of the structure, as it will be made clear later. In addition, radiation modes of some radiators (e.g., a continuous sphere) are frequency independent, whereas for some other radiators (e.g., a capped cylinder) they are claimed to present such a property [43].

In aiming to achieve a reduced representation of three-dimensional radiation patterns, subspaces spanned by a set of spherical harmonics or acoustic radiation modes (ARMs) have been widely used in the analysis of radiated sound fields, as said before. In the same way, these functions play a major role in this work. It is worth noting that only spherical harmonic decomposition has been used in studying the radiation from compact loudspeaker arrays, see [22, 21, 27, 26]; radiation modes have not yet been applied to loudspeaker arrays but planar ones, see [48]. Therefore, this section provides some background on such basis for directivity representation.

2.3.1 Spherical harmonics

As discussed in section 2.2.1, a directivity pattern is a complex-valued function evaluated over the sphere surface. Then, any directivity pattern with sufficient continuity properties can be expanded in a uniformly convergent double series of spherical harmonics due to the completeness property of these functions [60]. The complex-valued spherical harmonic functions are defined for $n \in \mathbb{N}$ and $m \in \mathbb{Z} : |m| \leq n$ by [60, 63]

$$Y_n^m(\theta, \phi) \equiv (-1)^m \sqrt{\frac{(2n+1)(n-m)!}{4\pi(n+m)!}} P_n^m(\cos\theta) e^{im\phi} \quad (2.23)$$

where $P_n^m(\cdot)$ is the associated Legendre function of the first kind. For $m > 0$, this function is related to the Legendre polynomial, $P_n(\cdot)$, by the formula [60]

$$P_n^m(x) = (1 - x^2)^{m/2} \frac{d^m P_n(x)}{dx^m} \quad (2.24)$$

For $m = 0$, one has $P_n^0(\cdot) = P_n(\cdot)$. In order to generate the functions for $m < 0$, the following expression can be used together with Eq.(2.24) [60]

$$P_n^{-m}(x) = (-1)^m \frac{(n - m)!}{(n + m)!} P_n^m(x) \quad (2.25)$$

In this work, n will be referred as the order of $Y_n^m(\cdot)$. It is worth noting that some authors refer to n as degree and to m as order. In addition, spherical harmonics as defined here contain the Cordon-Shortley phase factor $(-1)^m$ and are orthonormal over the spherical surface [60], i.e.,

$$\int_0^{2\pi} \int_0^\pi Y_n^m(\theta, \phi)^* Y_{n'}^{m'}(\theta, \phi) \sin \theta d\theta d\phi = \delta_{mm'} \delta_{nn'} \quad (2.26)$$

where the asterisk indicates complex conjugate and δ_{mn} is the Kronecker delta.

Figure 2.6 illustrates the complex-valued spherical harmonics up to order $n = 3$, where magnitude and phase are represented by figure shape and color gradient, respectively. Explicit expressions of $Y_n^m(\cdot)$ for some n and m values are [60, 61]

$$\begin{aligned} Y_0^0(\theta, \phi) &= \frac{1}{\sqrt{4\pi}} & Y_2^{-2}(\theta, \phi) &= \sqrt{\frac{5}{96\pi}} 3 \sin^2 \theta e^{-2i\phi} \\ Y_1^{-1}(\theta, \phi) &= \sqrt{\frac{3}{8\pi}} \sin \theta e^{-i\phi} & Y_2^{-1}(\theta, \phi) &= \sqrt{\frac{5}{24\pi}} 3 \sin \theta \cos \theta e^{-i\phi} \\ Y_1^0(\theta, \phi) &= \sqrt{\frac{3}{4\pi}} \cos \theta & Y_2^0(\theta, \phi) &= \sqrt{\frac{5}{4\pi}} \left(\frac{3}{2} \cos^2 \theta - \frac{1}{2} \right) \\ Y_1^1(\theta, \phi) &= -\sqrt{\frac{3}{8\pi}} \sin \theta e^{i\phi} & Y_2^1(\theta, \phi) &= -\sqrt{\frac{5}{24\pi}} 3 \sin \theta \cos \theta e^{i\phi} \\ & & Y_2^2(\theta, \phi) &= \sqrt{\frac{5}{96\pi}} 3 \sin^2 \theta e^{2i\phi} \end{aligned} \quad (2.27)$$

Alternatively, the angular dependence of the solution of the Helmholtz equation can be expressed by the real-valued spherical harmonic functions, $y_n^m(\cdot)$, instead of the complex-valued spherical harmonics defined in Eq.(2.23). The former are related to the latter by [64]

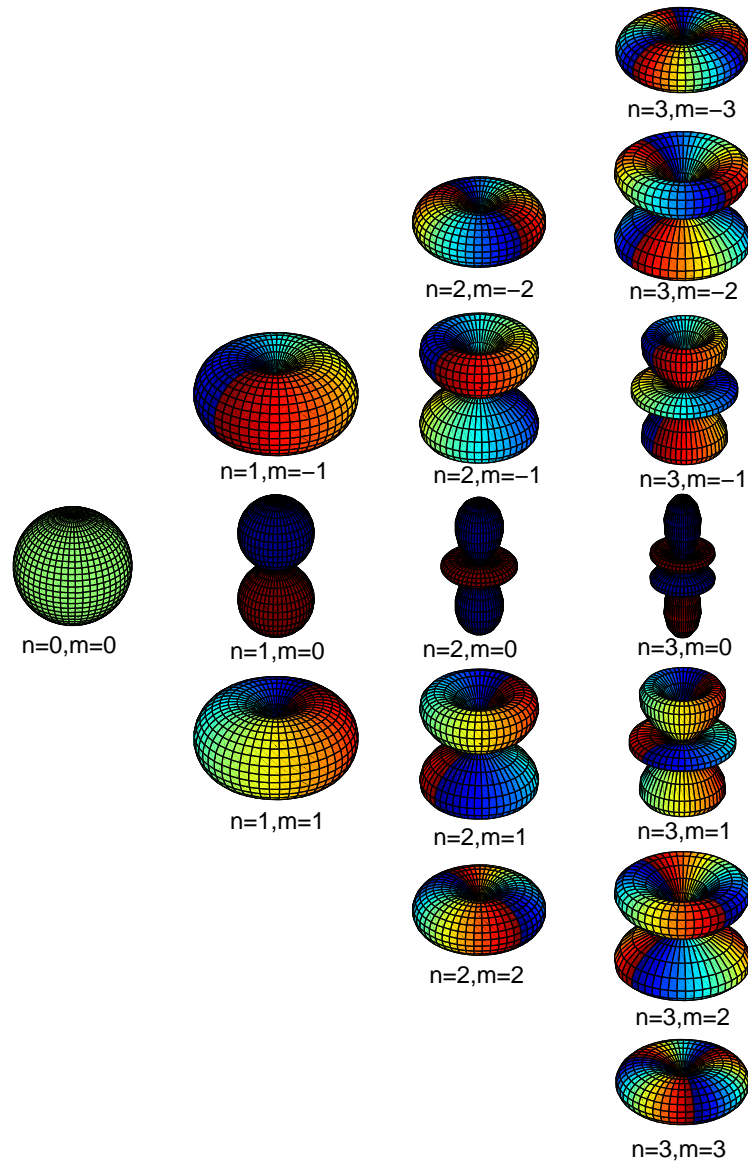


Figure 2.6: Complex-valued spherical harmonics up to order $n = 3$.

$$y_n^m(\theta, \phi) = \begin{cases} Y_n^m(\theta, \phi) & m = 0 \\ [(-1)^m Y_n^m(\theta, \phi) + Y_n^{-m}(\theta, \phi)] / (\sqrt{2}) & m > 0 \\ [(-1)^m Y_n^m(\theta, \phi) - Y_n^{-m}(\theta, \phi)] / (i\sqrt{2}) & m < 0 \end{cases} \quad (2.28)$$

In other words, since $Y_n^{-m}(\theta, \phi) = (-1)^m Y_n^m(\theta, \phi)^*$ [61], the functions $y_n^m(\cdot)$ are derived from the real and imaginary parts of the complex-valued spherical harmonics. Such functions are also orthonormal over the spherical surface.

Figure 2.7 illustrates the real-valued spherical harmonics up to order $n = 3$, where the dark and light portions indicate a 180° phase difference. Comparison of Figs. 2.7 and 2.6 and inspection of Eqs.(2.6), (2.12), (2.17), (2.27) and (2.28) reveal that real spherical harmonics of orders $n = 0$, $n = 1$ and $n = 2 : m \neq 0$ match the radiation patterns of the acoustic monopole, dipoles and lateral quadrupoles, respectively. On the other hand, $y_2^0(\cdot)$ and real spherical harmonics of higher orders are only similar to the longitudinal quadrupole, octupoles and so on; there is not an exact correspondence between them [61].

Function spaces spanned by complex or real-valued spherical harmonics of the same order n are linear subspaces that are invariant with respect to rigid rotation through spatial angles [65]. Then, a rotated spherical harmonic of order n can be written as a linear combination of spherical harmonics of order n . The rotation of the complex-valued spherical harmonics is described by [64]

$$Y_n^m(\theta', \phi') = \sum_{m'=-n}^n Y_n^{m'}(\theta, \phi) D_{m'm}^n(\alpha, \beta, \gamma) \quad (2.29)$$

where $0 \leq \alpha < 2\pi$, $0 \leq \beta \leq \pi$ and $0 \leq \gamma < 2\pi$ are the zyz Euler angles that relate the original coordinate system (θ, ϕ) to the rotated one (θ', ϕ') . Following [63], rotation matrices are

$$D_{m'm}^n(\alpha, \beta, \gamma) = e^{-im'\alpha} d_{m'm}^n(\beta) e^{-im\gamma} \quad (2.30)$$

where the functions $d_{m'm}^n(\cdot)$ are related to the Jacobi polynomials $J_n^{(m', m)}(\cdot)$ according to

$$d_{m'm}^n(\beta) = \sqrt{\frac{(n+m)!(n-m)!}{(n+m')!(n-m')!}} \left(\sin\frac{\beta}{2}\right)^{m-m'} \left(\cos\frac{\beta}{2}\right)^{m+m'} J_{n-m}^{(m-m', m+m')}(\cos\beta) \quad (2.31)$$

Similarly, the rotation of the real-valued spherical harmonics is described by [64]

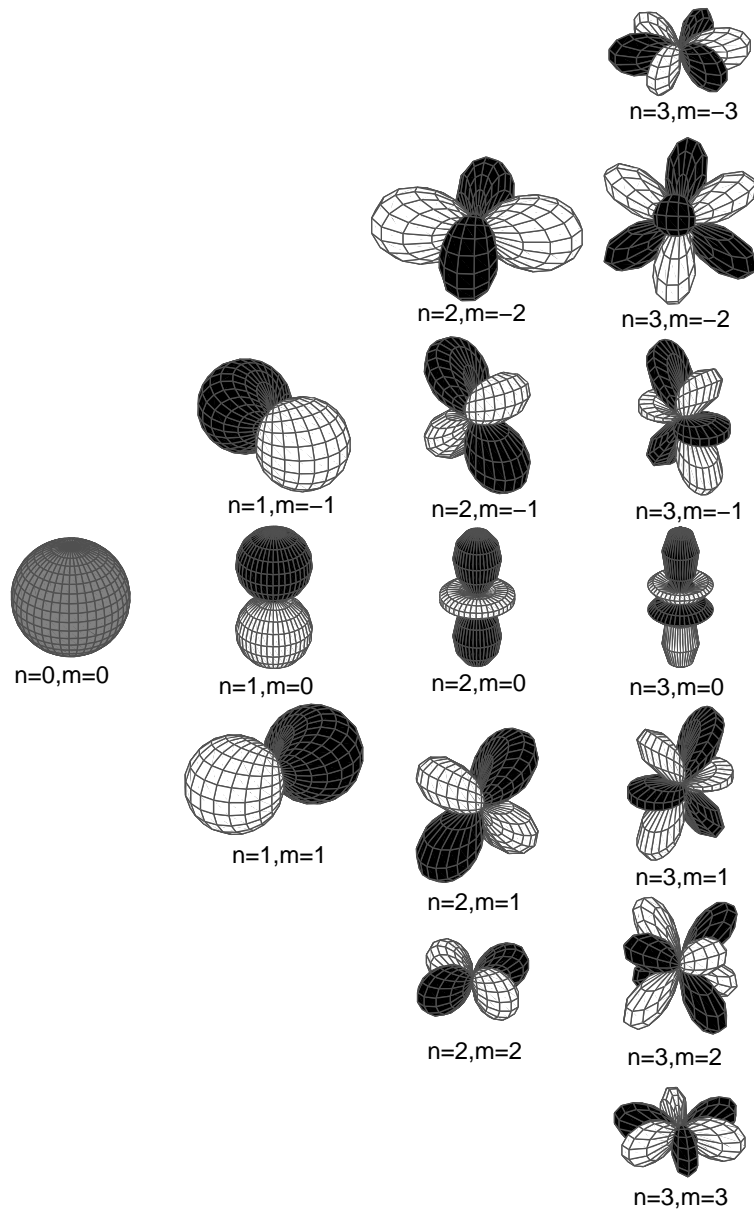


Figure 2.7: Real-valued spherical harmonics up to order $n = 3$.

$$y_n^0(\theta', \phi') = d_{00}^n(\beta)y_n^0(\theta, \phi) + 2^{-1/2} \sum_{m'=1}^n \left\{ \left[\cos(m'\alpha)y_n^{m'}(\theta, \phi) + \sin(m'\alpha)y_n^{-m'}(\theta, \phi) \right] \right. \\ \left. \left[(-1)^{m'} d_{m'0}^n(\beta) + d_{-m'0}^n(\beta) \right] \right\} \quad (2.32)$$

for $m = 0$,

$$y_n^m(\theta', \phi') = (-1)^m d_{0m}^n(\beta) \cos(m\gamma) \sqrt{2} y_n^0(\theta, \phi) + \\ \sum_{m'=1}^n \left\{ \left[(-1)^{m+m'} d_{m'm}^n(\beta) \cos(m\gamma + m'\alpha) + \right. \right. \\ \left. \left. (-1)^m d_{-m'm}^n(\beta) \cos(m\gamma - m'\alpha) \right] y_n^{m'}(\theta, \phi) + \right. \\ \left. \left[(-1)^{m+m'} d_{m'm}^n(\beta) \sin(m\gamma + m'\alpha) - \right. \right. \\ \left. \left. (-1)^m d_{-m'm}^n(\beta) \sin(m\gamma - m'\alpha) \right] y_n^{-m'}(\theta, \phi) \right\} \quad (2.33)$$

for $m > 0$ and

$$y_n^m(\theta', \phi') = (-1)^{m+1} d_{0m}^n(\beta) \sin(m\gamma) \sqrt{2} y_n^0(\theta, \phi) + \\ \sum_{m'=1}^n \left\{ \left[(-1)^{m+m'+1} d_{m'm}^n(\beta) \sin(m\gamma + m'\alpha) + \right. \right. \\ \left. \left. (-1)^{m+1} d_{-m'm}^n(\beta) \sin(m\gamma - m'\alpha) \right] y_n^{m'}(\theta, \phi) + \right. \\ \left. \left[(-1)^{m+m'} d_{m'm}^n(\beta) \cos(m\gamma + m'\alpha) - \right. \right. \\ \left. \left. (-1)^m d_{-m'm}^n(\beta) \cos(m\gamma - m'\alpha) \right] y_n^{-m'}(\theta, \phi) \right\} \quad (2.34)$$

for $m < 0$.

2.3.2 Acoustic radiation modes (ARMs)

The modal approach for representing the exterior radiation characteristics of vibrating structures has been used since the 1990's, see [42, 43, 44, 45, 40, 66, 47, 67, 46]. The expression ‘‘radiation mode’’ first appeared in [67]. In the same way as the structural modes widely used in solid

mechanics and vibration analysis [68], the acoustic radiation modes are real orthogonal functions describing surface velocity patterns. In addition, for a vibrating system with L degrees of freedom, these modal approaches both lead to a set of L linearly independent modes. On the other hand, unlike structural modes, radiation modes are defined so that they radiate sound energy independently, i.e., the total radiated sound power is given by a linear combination of the sound power produced by each mode. Then, in applications where one is mainly interested in the sound field, a reduced representation of the surface velocity can be achieved by neglecting the radiation modes which do not radiate efficiently.

Another advantage of radiation modes over structural modes is that, unlike the latter, the former do not depend on the mass and stiffness of the vibrating solid body, i.e., the material properties and thickness play no role in determining the radiation modes, which are only a function of the frequency, the body shape and the constraints it is subjected to, as it will be made clear later. In addition, radiation modes of some radiators (e.g., the continuous sphere) are frequency independent [43].

As far as a vibration system with a finite number of degrees of freedom is concerned, its radiation modes span an equally finite dimension subspace on which any radiation pattern that such a system is able to generate can be projected. Such a useful property does not hold for the spherical harmonic representation of the sound field produced by this same radiator. Actually, the real spherical harmonics are the radiation modes of the continuous sphere [40], i.e., the sphere which is able to assume any surface velocity pattern (infinite number of degrees of freedom). Therefore, spherical harmonics span an infinite dimension subspace, as can be verified by noting that the index n in Eq.(2.23) is unbounded. Hence, truncation error generally arises from the spherical harmonic decomposition, which can be dealt with by retaining a larger number of terms. Further details will be provided in section 3.1.

In the following, it will be shown how to obtain the radiation modes for a discrete structure with an arbitrary shape by accomplishing the eigenvalue analysis of a radiation operator.

Let Γ be a surface enclosing the sound source and \mathbf{n}_{out} be the unit normal pointing out of the volume containing the source. Then, the acoustic power W radiated by the source is [58]

$$W = \int_{\Gamma} \Re \left\{ \frac{1}{2} p^* \mathbf{v} \right\} \cdot \mathbf{n}_{\text{out}} d\Gamma \quad (2.35)$$

where p is the sound pressure, \mathbf{v} is the acoustic velocity and the asterisk indicates the complex conjugate.

The radiation efficiency σ of a vibrating structure is commonly defined as (see [44, 40, 66])

$$\sigma \equiv \frac{W}{\rho c S \langle |v_n(\mathbf{x}_s)|^2 \rangle} \quad (2.36)$$

where S is the effective area of the vibrating surface \mathbb{S} , v_n is the acoustic velocity normal to \mathbb{S} , $\mathbf{x}_s \in \mathbb{S}$ is a point on the radiator surface and $\langle \cdot \rangle$ is the spatial mean operator usually defined so that (see [40])

$$\langle |v_n(\mathbf{x}_s)|^2 \rangle = \frac{1}{2S} \int_{\mathbb{S}} |v_n(\mathbf{x}_s)|^2 d\mathbf{x}_s \quad (2.37)$$

For a vibrating structure with L degrees of freedom, the surface velocity can be represented as

$$v_n(\mathbf{x}_s) = \sum_{l=1}^L u_l \xi_l(\mathbf{x}_s) = \mathbf{u}^T \boldsymbol{\xi}(\mathbf{x}_s) \quad (2.38)$$

where \mathbf{u} is a column vector of velocity amplitude coefficients, $\boldsymbol{\xi}(\mathbf{x}_s)$ is a column vector containing an arbitrary complete set of orthogonal functions defined on the surface \mathbb{S} and the superscript T indicates the transpose.

Substitution of Eq.(2.38) into (2.37) yields

$$\langle |v_n(\mathbf{x}_s)|^2 \rangle = \mathbf{u}^H \mathbf{V} \mathbf{u} \quad (2.39)$$

where $\mathbf{V} = (2S)^{-1} \int_{\mathbb{S}} \boldsymbol{\xi}^*(\mathbf{x}_s) \boldsymbol{\xi}^T(\mathbf{x}_s) d\mathbf{x}_s$ is an $L \times L$ matrix, the superscript H indicates the complex conjugate transpose. Since $\boldsymbol{\xi}(\cdot)$ is a set of orthogonal functions, \mathbf{V} is a real positive diagonal matrix.

The calculation of the acoustic power radiated from a discrete structure generally leads to expressions of the form (cf. [43, 44, 45, 40, 66, 47])

$$W = \rho c S \mathbf{u}^H \mathbf{C} \mathbf{u} \quad (2.40)$$

where \mathbf{C} is an $L \times L$ real symmetric matrix [43, 45, 40] which couples the power radiated by the elements of \mathbf{u} .

Substitution of Eqs.(2.40) and (2.39) into (2.36) yields

$$\sigma(\mathbf{u}) = \frac{\mathbf{u}^H \mathbf{C} \mathbf{u}}{\mathbf{u}^H \mathbf{V} \mathbf{u}} \quad (2.41)$$

Notice that the radiation efficiency is in the form of the generalized Rayleigh quotient. Thus, the solution of the generalized eigenvalue problem $\mathbf{C}\boldsymbol{\psi} = \lambda\mathbf{V}\boldsymbol{\psi}$ leads to a set of L real orthogonal eigenvectors $\boldsymbol{\psi}_1, \boldsymbol{\psi}_2, \dots, \boldsymbol{\psi}_L$ corresponding to real eigenvalues, ordered as $\lambda_1 \geq \lambda_2 \geq \dots \geq \lambda_L$. These eigenvectors are the acoustic radiation modes (ARMs) and the eigenvalues are their radiation efficiency coefficients, i.e., $\sigma_l \equiv \sigma(\boldsymbol{\psi}_l) = \lambda_l$.

Let $\boldsymbol{\Psi}$ be an $L \times L$ modal matrix whose columns contain the radiation modes $\boldsymbol{\psi}_l$. Then, \mathbf{u} can be decomposed over such a basis, so that

$$\mathbf{u} = \boldsymbol{\Psi} \mathbf{c} \quad (2.42)$$

where \mathbf{c} is a column vector containing L nondimensional coefficients.

In addition, the generalized eigenvalue problem can be rewritten as

$$\mathbf{C}\boldsymbol{\Psi} = \mathbf{V}\boldsymbol{\Psi}\boldsymbol{\Lambda} \quad (2.43)$$

where $\boldsymbol{\Lambda}$ is an $L \times L$ diagonal matrix containing the eigenvalues λ .

Let the eigenvectors be normalized so that $\boldsymbol{\Psi}^T \mathbf{V} \boldsymbol{\Psi} = \mathbf{I}$, where \mathbf{I} is the identity matrix. Hence, substitution of Eqs.(2.42) and (2.43) into (2.40) yields

$$W = \rho c S \mathbf{c}^H \boldsymbol{\Lambda} \mathbf{c} = \rho c S \sum_{l=1}^L \sigma_l |c_l|^2 \quad (2.44)$$

Finally, substitution of Eqs.(2.42) and (2.43) into (2.41) leads to

$$\sigma = \frac{\mathbf{c}^H \boldsymbol{\Lambda} \mathbf{c}}{\mathbf{c}^H \mathbf{c}} = \frac{\sum_{l=1}^L \sigma_l |c_l|^2}{\sum_{l=1}^L |c_l|^2} \quad (2.45)$$

Inspection of Eqs.(2.44) and (2.45) reveals, respectively, that acoustic radiation modes radiate sound energy independently and that $\sigma_L \leq \sigma \leq \sigma_1$, i.e., an arbitrary velocity pattern cannot be either more efficient than the 1st mode, or less efficient than the L th mode. Hence, acoustic radiation modes allow to rank expansion terms by their radiation efficiencies, and to define a truncation

order from a required accuracy. Therefore, they improve surface velocity representation upon just using some arbitrary orthogonal basis $\xi(\cdot)$.

2.4 Spatial sound rendering using loudspeaker arrays

2.4.1 Theory

Let Γ_o and Γ_i be smooth closed surfaces defined so that Γ_o encloses Γ_i , as illustrated in Fig.2.8. Moreover, there are no sound sources and scatterers in the volume V between these surfaces, which will be called from now on “listening area”.

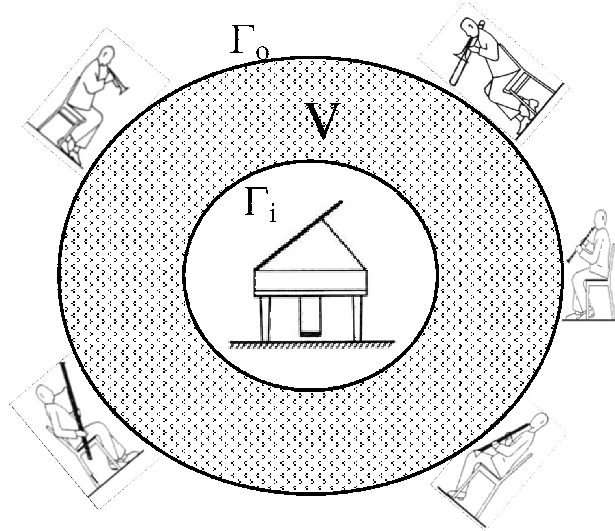


Figure 2.8: An acoustic domain (“listening area”), V , bounded by Γ_o and Γ_i , free of sound sources and scatterers.

Now, let Γ_p and Γ_v be the portions of the boundary on which, respectively, the acoustic pressure and velocity are specified. Hence, if $\Gamma = \Gamma_o \cup \Gamma_i$, one has $\Gamma_p \subset \Gamma$ and $\Gamma_v \subset \Gamma$, so that $\Gamma = \Gamma_p \cup \Gamma_v$, where $\Gamma_p \cap \Gamma_v = \emptyset$. Let $\gamma_p(\mathbf{x})$ and $\gamma_v(\mathbf{x})$ be, respectively, the sound pressure at Γ_p and the acoustic velocity at Γ_v normal to it pointing out to the exterior of V . The acoustic field on the boundary is due to the presence of acoustical sources outside V , which will be called “primary sources”. Then, the sound pressure in V is the solution of the following boundary value problem (refer to Eqs.(2.3) and (2.4)):

$$\begin{cases} \Delta p(\mathbf{x}) + k^2 p(\mathbf{x}) = 0 & \forall \mathbf{x} \in V \\ p(\mathbf{x}) = \gamma_p(\mathbf{x}) & \forall \mathbf{x} \in \Gamma_p \\ \frac{\partial p(\mathbf{x})}{\partial \mathbf{n}_{\text{out}}} = i\omega \rho \gamma_v(\mathbf{x}) & \forall \mathbf{x} \in \Gamma_v \end{cases} \quad (2.46)$$

where \mathbf{n}_{out} is the unit vector normal to Γ and pointing out to the exterior of V .

For all frequencies but the natural frequencies of the acoustical system, this boundary value problem has a unique solution [59], i.e., the sound field in V resulting from the primary sources and scatterers is entirely determined by the boundary conditions. Therefore, if the primary sources (and, eventually, the scatterers) are replaced by secondary sources (e.g., loudspeakers) that lead to the same pressure on the boundary as the original configuration did, the sound field produced by the secondary sources in the listening area will be exactly the same of that one generated by the primary sources. It is worth noting that $\gamma_p(\mathbf{x})$ and $\gamma_v(\mathbf{x})$ are complex-valued functions, so that their magnitude and phase must be considered.

The Green's representation of the solution of the problem (2.46) is given by the following expression, also known as Kirchhoff-Helmholtz integral [59]:

$$p(\mathbf{x}) = \int_{\Gamma} \left(p(\mathbf{x}_s) \frac{\partial G(\mathbf{x}, \mathbf{x}_s)}{\partial \mathbf{n}_{\text{out}}} - G(\mathbf{x}, \mathbf{x}_s) \frac{\partial p(\mathbf{x}_s)}{\partial \mathbf{n}_{\text{out}}} \right) d\Gamma \quad (2.47)$$

where $\mathbf{x} \in V$ and $\mathbf{x}_s \in \Gamma$. If $\mathbf{x} \in \mathbb{R}^3$, $G(\mathbf{x}, \mathbf{x}_s)$ is the 3-D free-space Green's function given in Eq.(2.7).

As discussed in section 2.2.1, the function $G(\mathbf{x}, \mathbf{x}_s)$ can be interpreted as the field of a monopole source placed at the point \mathbf{x}_s . Similarly, the directional derivative of $G(\mathbf{x}, \mathbf{x}_s)$ can be interpreted as the field of a dipole source placed at \mathbf{x}_s , whose main axis lies in the direction of \mathbf{n}_{out} . Then, Eq.(2.47) states that the sources and scatterers outside V can be replaced by monopoles and/or dipoles continuously distributed on the boundary Γ . It is worth noting that $p(\mathbf{x}_s)$ and its directional derivatives are not independent, the unknown function can be obtained by substituting the boundary conditions in Eq.(2.47) with \mathbf{x} on the boundary.

If the Helmholtz equation is separable in the chosen coordinate system, the method of separation of variables can be used to solve it. If so, such a solution can be used as an alternative to the Kirchhoff-Helmholtz integral. As stated before, the Helmholtz equation is separable in spherical coordinates and its general solution is (see appendix A)

$$p(r, \theta, \phi) = \sum_{n=0}^{\infty} \sum_{m=-n}^n (A_{mn} h_n^{(1)}(kr) + B_{mn} h_n^{(2)}(kr)) Y_n^m(\theta, \phi) \quad (2.48)$$

where A_{mn} and B_{mn} are constants to be determined from the boundary conditions; $h_n^{(2)}(\cdot)$ is the spherical Hankel function of the second kind. Since a harmonic time dependence of the form $e^{-i\omega t}$ has been assumed, $h_n^{(1)}(kr)$ and $h_n^{(2)}(kr)$ represent an outgoing wave and an incoming wave, respectively [61].

If Γ_o and Γ_i are concentric spherical surfaces, the series coefficients A_{mn} and B_{mn} can be obtained through the knowledge of either the acoustic pressure or the radial acoustic velocity at all points on the two concentric spheres.

The solution of the boundary value problem described by Eq.(2.46) is simplified if there are no sources and scatterers outside Γ_o or inside Γ_i . If so, one has an exterior problem or an interior problem, respectively, as depicted in Fig. 2.9. Then, the coefficients A_{mn} and B_{mn} are not independent of each other. For an exterior problem (free-field sound radiation), the outer sphere can be eliminated and $B_{mn} = 0$ in Eq.(2.48) due to the fact that there are no incoming waves. For an interior problem, the inner sphere can be eliminated and $A_{mn} = B_{mn}$ [62], so that Eq.(2.48) simplifies to

$$p(r, \theta, \phi) = \sum_{n=0}^{\infty} \sum_{m=-n}^n A_{mn} j_n(kr) Y_n^m(\theta, \phi) \quad (2.49)$$

where $j_n(x) = h_n^{(1)}(x) + h_n^{(2)}(x)$ is the spherical Bessel function of the first kind (see appendix A).

The primary source(s) (and, eventually, scatterers) generate(s) a 3-D acoustic field that can be recorded using a suitable arrangement of microphones. Then, the resulting multi-track recording can be reproduced by a set of loudspeakers operating at the same frequency range (secondary sources). Figure 2.10 depicts playback configurations concerning irradiation reproduction (interior problem) and radiation reproduction (exterior problem). Besides playback of a recorded sound field, the loudspeaker arrays can also be used to achieve spatial control of the acoustic field, for example, in real time performances. In addition, they can be used as improved sound enhancement systems that do not modify the spatial characteristics of the sound field produced by the primary sources. Similarly, loudspeaker arrays can be used in active noise control applications. Anyway, the problem of evaluating the electrical signal that will drive each loudspeaker must be undertaken.

In the following section, some of the most promising technologies for spatial sound rendering

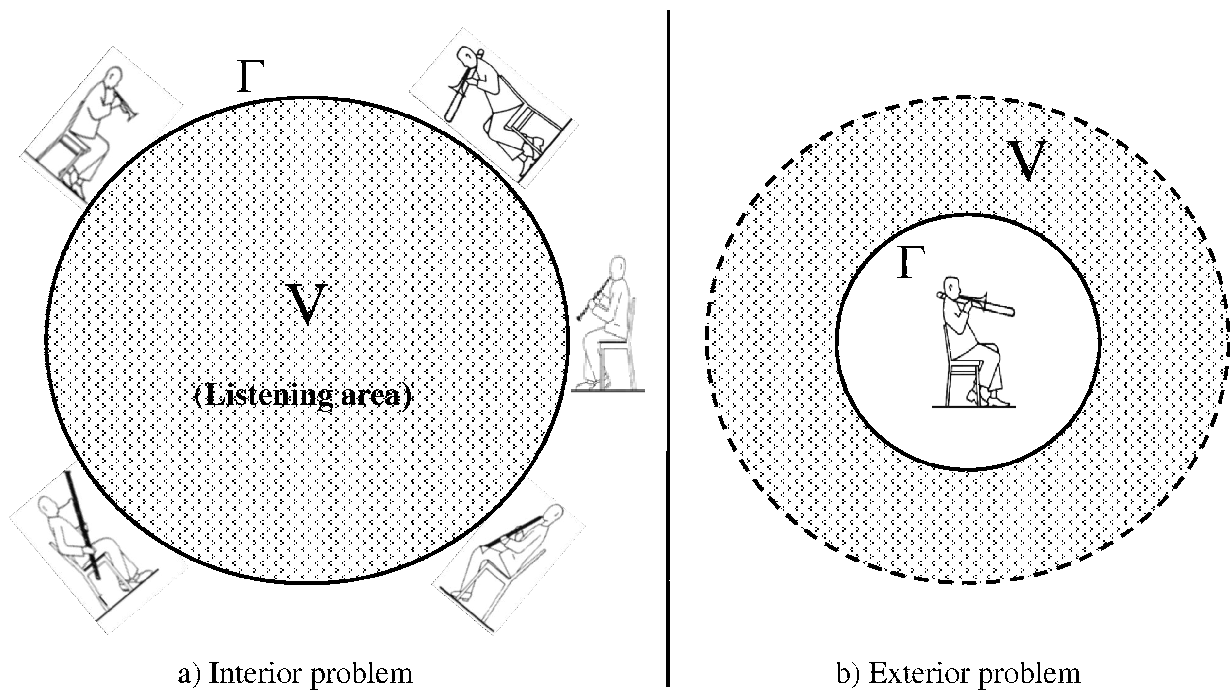


Figure 2.9: Boundary value problems: a) Interior problem: sound sources and scatterers outside the listening area; b) Exterior problem: free-field sound radiation.

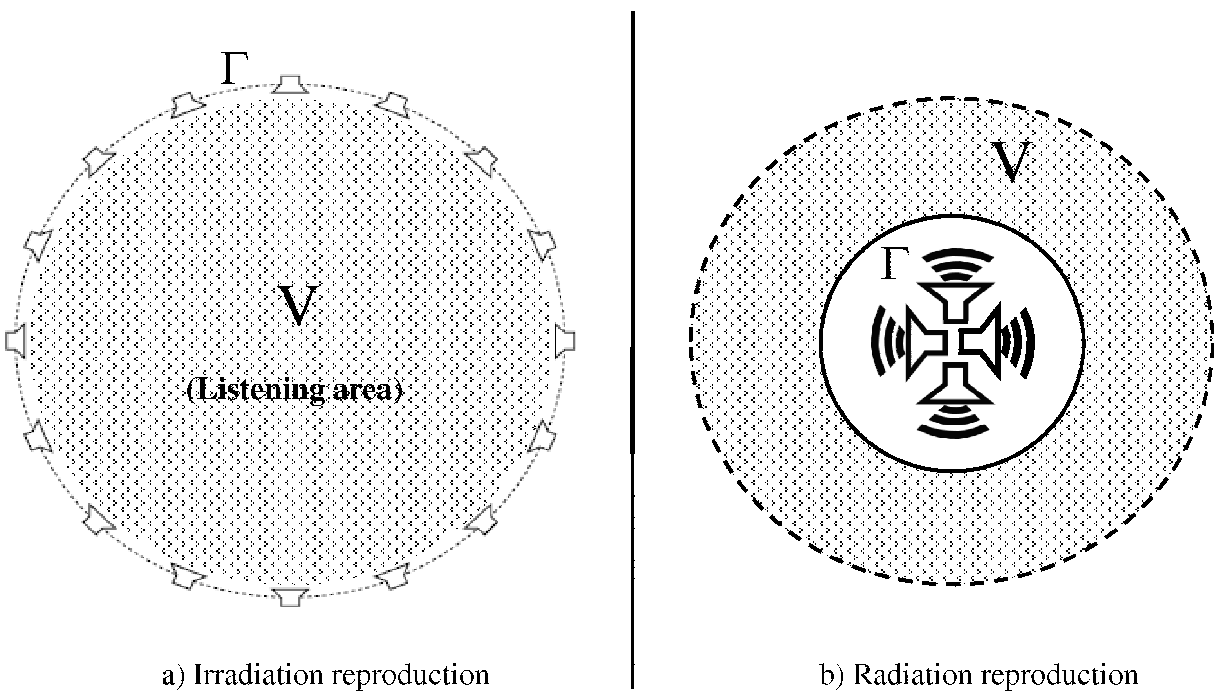


Figure 2.10: Synthesis or playback of an acoustic field: a) Irradiation reproduction: Ambisonics and Wave Field Synthesis; b) Radiation reproduction: compact loudspeaker array.

using loudspeaker arrays are introduced.

2.4.2 Spatial audio systems

The most of the spatial audio systems has been conceived for irradiation reproduction, which is illustrated on the left side of Fig. 2.10. The main characteristic of these systems is that many virtual sources located outside the listening area can be considered, so that the listeners are immersed in a complex sound scene. The stereophonic systems, comprising the conventional “surround” audio, are the most common irradiation reproduction systems. However, these systems present a reduced “sweet spot”, the rear channels are only for ambiance or special effects and they do not provide a stable position of the virtual sources, i.e., optimum listening is restricted to a small fraction of the listening area, and the virtual sources cannot be placed in any position of the 3-D space outside the listening area. There are more sophisticated systems that attempt to overcome these limitations, like Wave Field Synthesis (WFS) and Ambisonics, which will be briefly described in the following.

The WFS is a well established spatial audio rendering technique that potentially leads to an exact reproduction of the desired sound field within the whole listening area. It was first proposed by Berkhout in 1988 [69] and is based on the Kirchhoff-Helmholtz integral (Eq.(2.47)), so that the effect of primary sources is recreated by a continuous distribution of monopole and dipole sources on a closed surface around the listening area.

However, in actual WFS installations, the continuous distribution of secondary sources is replaced by a loudspeaker array with a finite number of transducers. This can be sought as a spatial sampling process, which leads to spatial aliasing artifacts that can degrade the system performance when the wavelength of the sound to be reproduced is small in comparison to the average distance between the secondary sources. Hence, a large number of densely placed loudspeakers must be used in order not to produce audible spatial aliasing artifacts, so that WFS remains a high cost spatial audio solution. Moreover, since WFS attempts to simulate the acoustic characteristics of a virtual space, the acoustics of the rendition space must be suppressed. However, the difficulties in predicting the interaction between the secondary sources and the room they are placed in make this problem complex to address. This can be dealt with by placing the whole system in an anechoic chamber, which would increase the system cost. For further details about the WFS, refer to [69, 4, 70, 71].

The Ambisonics is a spatial audio recording and rendering technique that aims to reproduce a desired sound field at the center of a loudspeaker setup. It was first proposed by Gerzon in

1973 [5] and is based on the spherical harmonic decomposition of the sound field, so that Eq.(2.49) is applied.

Like the WFS, the performance of the Ambisonics systems is limited by the number of loudspeakers. Since Eq.(2.49) represents an infinite sum, the series must be truncated to a given order $n \leq N$ which determines the minimum number of loudspeakers. In other words, the system performance is improved by reducing the truncation error, which can be dealt with by increasing the number of loudspeakers. The so-called B-format signal holds an Ambisonic signal of first order ($N = 1$), i.e., the sound information is encoded in four channels corresponding to the monopole and to the dipoles shown in Fig. 2.7. Systems with more channels are referred to Higher Order Ambisonics (HOA).

Nowadays, the HOA is an active area of research and development. The first Ambisonics Symposium was held in June 2009 at the IEM in Graz (Austria). For further details about the Ambisonics, refer to the symposium proceedings [72].

Unlike the irradiation reproduction, there are not many audio systems providing sound radiation control, which is illustrated on the right side of Fig. 2.10. As discussed in section 1.2, the most common radiation reproduction systems are the compact spherical loudspeaker arrays largely employed to obtain an approximate omnidirectional source in room acoustics measurements. Sound fields other than omnidirectional can be obtained by using a compact array of independently programmable loudspeakers. Compact spherical loudspeaker arrays for radiation control is a timely research field and some aspects concerning their electroacoustical behavior and practical implementation remain unclear. This work deals with such systems.

Chapter 3

Spherical Loudspeaker Array Modeling

3.1 Sound radiation

Sphere-like structures (e.g., dodecahedra and icosahedra) have been proposed for directivity synthesis by a compact loudspeaker array (see [25, 31, 22, 33, 26]) since their high symmetry is desirable when controlling sound fields in a three-dimensional space. For the same reason, the acoustic radiation from spherical sources can be evaluated analytically according to the expressions that will be developed in this chapter. It is worth noting that dodecahedra and icosahedra can be modeled as spheres for acoustic purposes.

Here, two different spherical sources are considered: the “continuous” sphere and the “discrete” sphere. The continuous sphere can assume any velocity distribution on its surface, i.e., it can oscillate continuously over its surface. On the other hand, the discrete sphere is a set of spherical caps mounted on a rigid sphere; each cap can oscillate independently with a constant radial velocity over its surface, so that the discrete sphere has a finite number of degrees of freedom equal to the number of caps.

3.1.1 Continuous sphere

The complex sound pressure amplitude outside a radiating sphere in the free-field condition is given by Eq.(2.21), and the complex radial velocity amplitude is (refer to appendix A.2)

$$v(r, \theta, \phi) = -\frac{t}{\rho c} \sum_{n=0}^{\infty} \sum_{m=-n}^n A_{mn} \frac{dh_n^{(1)}(kr)}{d(kr)} Y_n^m(\theta, \phi) \quad (3.1)$$

It has been demonstrated that the spherical harmonics are the acoustic radiation modes (ARMs) of the continuous sphere¹ [40]. Thus, substitution of the mn -th term of Eqs.(2.21) and (3.1) into (2.35) and (2.37) leads, respectively, to the radiated power and to the spatial mean-square velocity for the mn -th mode, i.e.,

$$W_{mn} = \frac{1}{2\rho c} \left(\frac{|A_{mn}|}{k} \right)^2 \quad (3.2)$$

and

$$\langle |v_{mn}(a, \theta, \phi)|^2 \rangle = \frac{1}{2S} \left(\frac{|A_{mn}|a}{\rho c} \right)^2 \frac{dh_n^{(1)}(ka)}{d(ka)} \frac{dh_n^{(2)}(ka)}{d(ka)} \quad (3.3)$$

where a is the sphere radius and $S = 4\pi a^2$.

Substitution of Eqs.(3.2) and (3.3) into (2.36) leads to the radiation efficiency of the mn -th mode (cf. [40])

$$\sigma_{mn} = \left((ka)^2 \frac{dh_n^{(1)}(ka)}{d(ka)} \frac{dh_n^{(2)}(ka)}{d(ka)} \right)^{-1} \quad (3.4)$$

where $mn = n^2 + n + 1 + m$ is used for linear indexing of the spherical harmonics.

Equation (3.4) shows that σ_{mn} does not depend on m and it is only a function of the non-dimensional parameter ka for spherical harmonics of a given order n . The radiation efficiencies for the first 49 radiation modes of the continuous sphere (spherical harmonics up to order $n = 6$) are presented in Fig. 3.1.

Figure 3.1 illustrates the grouping characteristic of the acoustic radiation modes discussed in [40]. The number of modes within each group is $2n+1$, i.e., 1 ($n = 0$), 3 ($n = 1$), 5 ($n = 2$), 7 ($n = 3$), 9 ($n = 4$), etc. It is shown that σ_{mn} increases with ka and decreases with n . Moreover, at low ka values, the radiation efficiency is strongly affected by n , so that simple directivity patterns (lower order spherical harmonics) radiate much more efficiently than complex ones. This result pinpoints the main difficulty concerning sound radiation reproduction in the low-frequency range: the sphere

¹It is worth noting that, in this work, the radiation modes are defined as surface velocity patterns, as in [40]. Some authors call “radiation mode” the surface velocity pattern and its corresponding farfield radiation pattern, or only the latter.

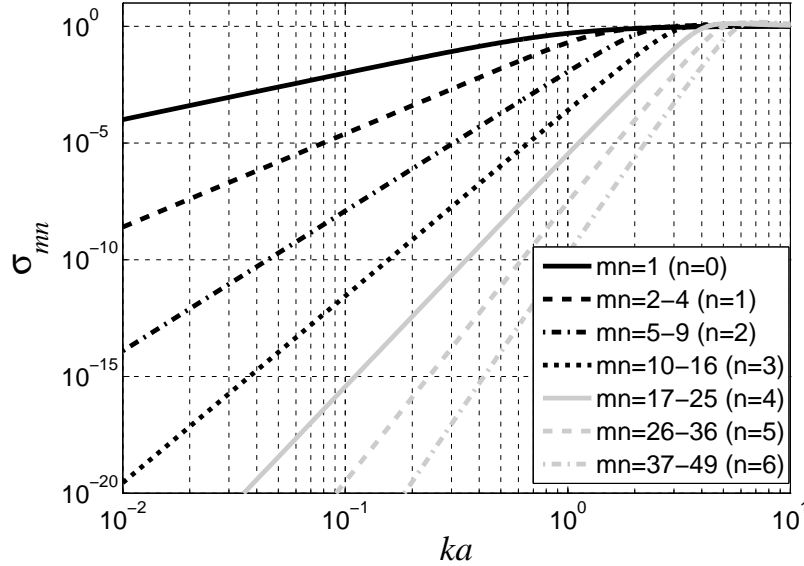


Figure 3.1: Radiation efficiencies of the first 49 acoustic radiation modes of the continuous sphere (spherical harmonics).

surface must present a huge velocity amplitude in order to produce complex directivity patterns with meaningful sound power levels. Besides technical constraints concerning large displacements of a real electroacoustic source, the linearized wave equation presented in section 2.1 does not describe properly the system dynamics for large displacements, so that a non-linear model must be used. It is worth noting that σ_{mn} can be increased over a given frequency range by increasing a . However, in practice, a larger sphere limits the radiation control in the high-frequency range, as it will become clear throughout this work.

3.1.2 Discrete sphere

The sound radiation from a loudspeaker mounted on a rigid sphere can be approximated by modeling the loudspeaker diaphragm as a spherical cap that oscillates with a constant radial velocity over its surface [49, 73, 33, 39, 26]. This model better approximates the actual loudspeaker sound field as the aperture angle of the cap is made smaller. In this work, a spherical loudspeaker array is modeled as a discrete sphere.

Figure 3.2 illustrates a spherical cap mounted on a rigid sphere, where (y, z) are global Cartesian coordinates, \mathbf{r}_c is the position vector of the center of the cap, \mathbf{r}_p is the position vector of a given but arbitrary point outside the sphere, θ_0 is the half aperture angle of the cap, θ_l is the zenith angle

in local coordinates and θ is the zenith angle in global coordinates. The position of the center of the cap defines the local coordinates so that \mathbf{r}_c corresponds to $\theta_l = 0$.

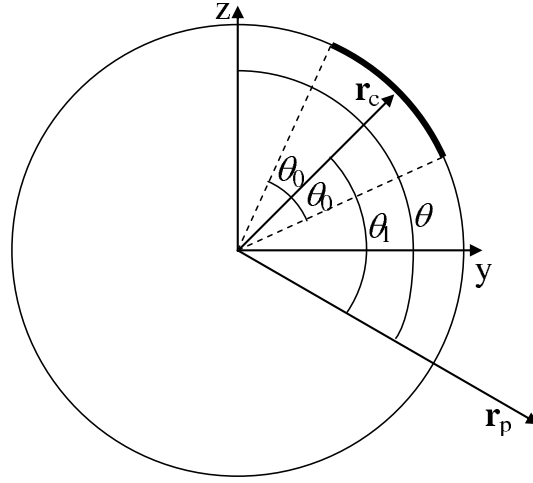


Figure 3.2: Spherical cap with aperture angle θ_0 mounted on a rigid sphere at \mathbf{r}_c .

Equations (2.21) and (3.1) describe the acoustic field. Now, let the cap oscillate with a constant radial velocity amplitude u_l over its surface, i.e., $\xi_l = 1$ over the cap surface or 0 otherwise (refer to Eq.(2.38)). Then,

$$v(a, \theta_l, \phi_l) = \begin{cases} u_l & \text{if } \theta_l \leq \theta_0 \\ 0 & \text{if } \theta_0 < \theta_l \leq \pi \end{cases} \quad (3.5)$$

By letting $r = a$ in Eq.(3.1), one has

$$v(a, \theta_l, \phi_l) = -\frac{\iota}{\rho c} \sum_{n=0}^{\infty} \sum_{m=-n}^n A_{mn} \frac{dh_n^{(1)}(ka)}{d(ka)} Y_n^m(\theta_l, \phi_l) \quad (3.6)$$

By using the orthonormality property of the spherical harmonics, multiplication of Eq.(3.6) by $Y_n^{m'}(\theta_l, \phi_l)^*$ and integration over the unit sphere yields

$$A_{mn} = \frac{\iota \rho c}{d(ka)} u_l \int_0^{2\pi} \int_0^{\theta_0} Y_n^m(\theta_l, \phi_l)^* \sin \theta_l d\theta_l d\phi_l \quad (3.7)$$

Let $\eta = \cos \theta_l$. Hence, by using Eq.(2.23),

$$\int_0^{2\pi} \int_0^{\theta_0} Y_n^m(\theta_l, \phi_l)^* \sin \theta_l d\theta_l d\phi_l = 2\pi \delta_{m0} \sqrt{\frac{2n+1}{4\pi}} \int_{\cos \theta_0}^1 P_n(\eta) d\eta \quad (3.8)$$

But, according to [60],

$$\int_{\eta_0}^1 P_n(\eta) d\eta = \begin{cases} \frac{1}{2n+1} \int_{\eta_0}^1 \left(\frac{dP_{n+1}(\eta)}{d\eta} - \frac{dP_{n-1}(\eta)}{d\eta} \right) d\eta & \text{if } n > 0 \\ \int_{\eta_0}^1 1 d\eta & \text{if } n = 0 \end{cases} \quad (3.9)$$

where $\eta_0 = \cos \theta_0$.

Substitution of Eq.(3.9) into (3.8) yields

$$\iint_{\Omega_l} Y_n^{m*} d\Omega = \delta_{m0} \sqrt{\frac{\pi}{2n+1}} \begin{cases} P_{n-1}(\eta_0) - P_{n+1}(\eta_0) & \text{if } n > 0 \\ 1 - \eta_0 & \text{if } n = 0 \end{cases} \quad (3.10)$$

where Ω_l is the angular sector containing the spherical cap and $d\Omega = \sin \theta_l d\theta_l d\phi_l$, so that $\iint_{\Omega_l} d\Omega = 2\pi(1 - \cos \theta_0)$ is the solid angle of the spherical cap.

Finally, substitution of Eq.(3.10) into (3.7) leads to (cf. [61])

$$A_{mn} = \frac{\iota \rho c u_l}{\frac{dh_n^{(1)}(ka)}{d(ka)}} \sqrt{\frac{\pi}{2n+1}} \delta_{m0} \begin{cases} P_{n-1}(\eta_0) - P_{n+1}(\eta_0) & \text{if } n > 0 \\ 1 - \eta_0 & \text{if } n = 0 \end{cases} \quad (3.11)$$

Notice that \mathbf{r}_c defines a symmetry axis. For this reason, $A_{mn} = 0$ if $m \neq 0$, since spherical harmonics with $m \neq 0$ do not present axial symmetry, as shown in Fig. 2.6. Hence, the sound pressure and the radial acoustic velocity produced by the cap become, respectively,

$$p_l(r, \theta_l, \phi_l) = \sum_{n=0}^{\infty} A_{0n} h_n^{(1)}(kr) Y_n^0(\theta_l, \phi_l) \quad (3.12)$$

and

$$v_l(r, \theta_l, \phi_l) = -\frac{\iota}{\rho c} \sum_{n=0}^{\infty} A_{0n} \frac{dh_n^{(1)}(kr)}{d(kr)} Y_n^0(\theta_l, \phi_l) \quad (3.13)$$

By letting $(\alpha_l, \beta_l, \gamma_l)$ be the zyz Euler angles that locate \mathbf{r}_c in the global coordinates system, substitution of Eq.(2.29) into (3.12) and (3.13) leads to

$$p_l(r, \theta, \phi) = \sum_{n=0}^{\infty} \sum_{m=-n}^n A_{0n} h_n^{(1)}(kr) Y_n^m(\theta, \phi) D_{m0}^n(\alpha_l, \beta_l, \gamma_l) \quad (3.14)$$

and

$$v_l(r, \theta, \phi) = -\frac{\iota}{\rho c} \sum_{n=0}^{\infty} \sum_{m=-n}^n A_{0n} \frac{dh_n^{(1)}(kr)}{d(kr)} Y_n^m(\theta, \phi) D_{m0}^n(\alpha_l, \beta_l, \gamma_l) \quad (3.15)$$

By superimposing the radiated fields from L caps with the same aperture angle and truncating the series so that $n \leq N$, the sound pressure and radial acoustic velocity generated by a spherical array are

$$p = \mathbf{u}^T \mathbf{B}^T \mathbf{Y} \quad (3.16)$$

and

$$v = \mathbf{u}^T \mathbf{E}^T \mathbf{Y} \quad (3.17)$$

where \mathbf{u} is a column vector containing the velocities of the L caps and \mathbf{Y} is a vector that contains $(N+1)^2$ spherical harmonics, so that $Y_i = Y_n^m$, with $i = n^2 + n + 1 + m$. \mathbf{B} and \mathbf{E} are $(N+1)^2 \times L$ matrices given by

$$B_{il} = \frac{1}{u_l} A_{0n} h_n^{(1)}(kr) D_{m0}^n(\alpha_l, \beta_l, \gamma_l) \quad (3.18)$$

and

$$E_{il} = -\frac{\iota}{\rho c u_l} A_{0n} \frac{dh_n^{(1)}(kr)}{d(kr)} D_{m0}^n(\alpha_l, \beta_l, \gamma_l) \quad (3.19)$$

Substitution of Eqs. (2.26), (3.16) and (3.17) into (2.35) leads to

$$W = \frac{r^2}{2} \mathbf{u}^T \Re \{ \mathbf{B}^H \mathbf{E} \} \mathbf{u} \quad (3.20)$$

Then, comparison of Eq.(2.40) with (3.20) yields

$$\mathbf{C} = \frac{r^2}{2\rho c S} \Re \{ \mathbf{B}^H \mathbf{E} \} \quad (3.21)$$

It is worth noting that \mathbf{C} is real and symmetric, as required. In addition, it does not depend on r , as expected (see appendix B).

Since it has been assumed that all spherical caps have the same area, the net vibration surface is $S = 2\pi a^2(1 - \cos \theta_0)L$. Thus, Eq.(2.39) becomes

$$\langle |v(a, \theta, \phi)|^2 \rangle = \frac{\mathbf{u}^H \mathbf{u}}{2L} \quad (3.22)$$

Comparison of Eq.(2.39) with (3.22) reveals that

$$\mathbf{V} = \frac{1}{2L} \mathbf{I} \quad (3.23)$$

where \mathbf{I} is the identity matrix.

Finally, the acoustic radiation modes of the discrete sphere and the corresponding radiation efficiencies can be obtained as described in section 2.3.2.

3.1.2.1 Convex regular polyhedra

The equations presented up to now can be used to predict the sound field radiated by a discrete sphere regardless of the positions of the spherical caps over the sphere. As far as radiation control in the full three-dimensional space is concerned, the loudspeakers must be distributed as symmetrically as possible over the spherical array frame in order not to favor any portion of the rendition space. Therefore, to distribute the spherical caps over the sphere according to a Platonic solid symmetry (i.e., the spatial orientation of each cap is made equal to the vector normal to a face of the polyhedron) presents great interest, as said before.

Figure 3.3 shows the five Platonic solids (convex regular polyhedra) and their midspheres. The midsphere of a polyhedron is a sphere which is tangent to every edge of the solid. The radius of the midsphere is called the midradius. It is worth noting that, for acoustic purposes, a Platonic solid can be approximated by a sphere whose radius, a , is the polyhedron's midradius.

The so-called dihedral angle of a Platonic solid is the interior angle between the planes of two adjacent faces. Then, it can be verified that the upper limit of θ_0 so that the spherical caps do not overlap each other is half the supplement of the dihedral angle. The dihedral angles are 70.5° , 90° , 109.5° , 116.6° and 138.2° for the tetrahedron, hexahedron, octahedron, dodecahedron and icosahedron, respectively [74]. Hence, the corresponding maximum θ_0 are 54.7° , 45° , 35.2° , 31.7° and 20.9° . Then, the ratio $2\pi a^2(1 - \cos \theta_0)L / (4\pi a^2)$ represents the available fraction of the spherical surface to mount the loudspeakers, namely, 84.4%, 87.9%, 73.1%, 89.5% and 65.8%,

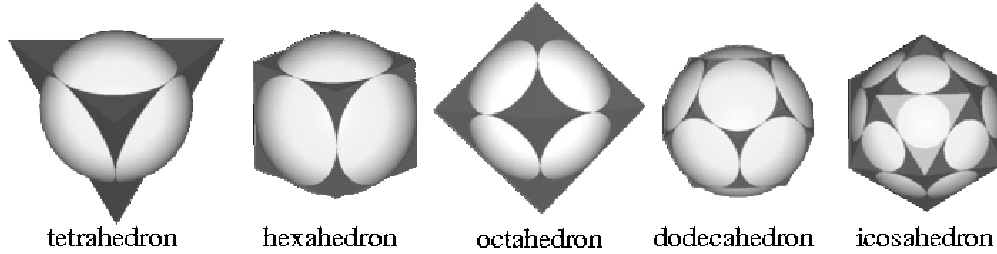


Figure 3.3: Convex regular polyhedra (Platonic solids) and their midspheres.

respectively. Therefore, among the Platonic solids having the same midradius a , the dodecahedron presents the largest surface area available for assembling the drivers, i.e., one can use larger drivers so that a higher sound power is obtained for a given a .

In order to obtain the acoustic radiation modes and their radiation efficiencies, the eigenvalue problem given by Eq.(2.43) must be solved, where \mathbf{C} and \mathbf{V} are given by Eqs.(3.21) and (3.23), respectively. These matrices depend on ka , θ_0 , L and on the Euler angles defining the position of each spherical cap on the sphere. The Cartesian coordinates of the center of each face of a Platonic solid and the corresponding Euler angle are given in appendix C.

Despite the fact that \mathbf{C} is a function of ka and θ_0 , it has been observed that the eigenvalue analysis leads to the same set of L orthogonal eigenvectors, Ψ , regardless of the ka and θ_0 values. Therefore, the results suggest that the acoustic radiation modes of a discrete sphere based on a Platonic solid do not depend on ka , as is the case for a continuous sphere². The modal matrix Ψ for each Platonic solid is presented in appendix C. It is worth noting that, in this work, the radiation modes are defined as surface velocity patterns. Some authors call “radiation mode” the surface velocity pattern and its corresponding farfield radiation pattern, or only the latter.

Unlike the modal matrix, the radiation efficiency of each radiation mode depends strongly on ka . Figures 3.4 to 3.8 show the radiation efficiency of the radiation modes (ARMs) of the discrete spheres based on the Platonic solids as a function of ka . For comparison, the radiation efficiency of the radiation modes of the continuous sphere (spherical harmonics) are also presented.

It can be noticed that the radiation modes of the discrete spheres present the grouping characteristic in the same way as the continuous sphere — each one of the Figs. 3.4 to 3.8 corresponds to a radiation group excepted for Fig. 3.7, which presents two radiation groups for the icosahedron.

²The frequency independence property of radiation modes does not hold for a general radiator geometry. However, a “nesting” property stating that the efficient radiation modes at frequency $\omega < \omega_{max}$ can be decomposed over the efficient radiation modes at ω_{max} is suggested in [43]. This property holds analytically for spherical, cylindrical and plane radiators (with infinite number of degrees of freedom), whereas it is a conjecture for some radiators other than these ones.

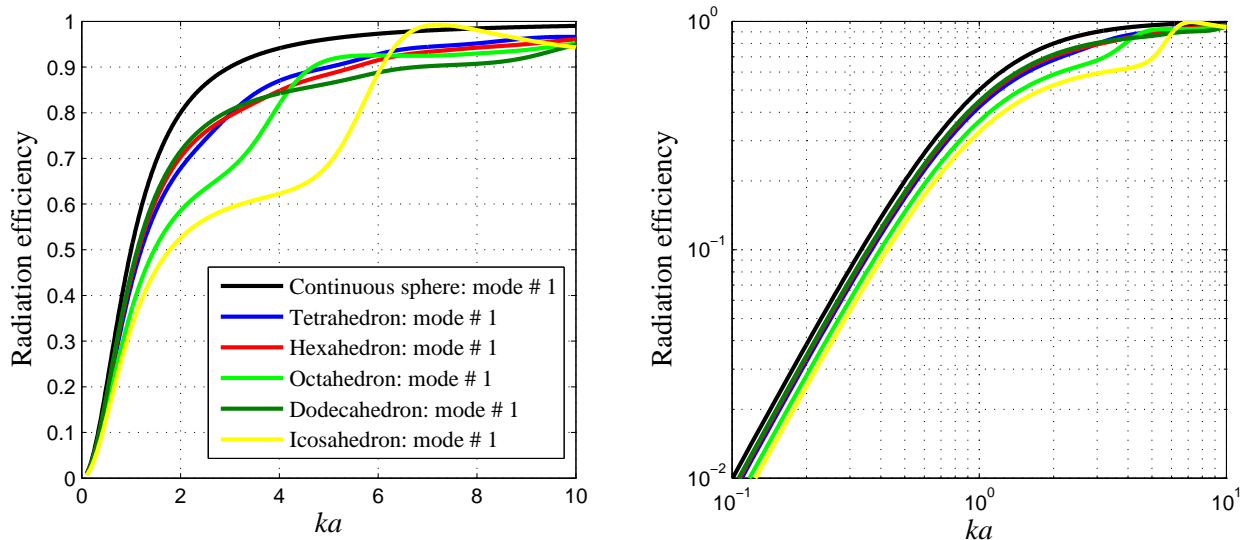


Figure 3.4: Radiation efficiency of the ARM # 1 of the continuous sphere and the discrete spheres based on the Platonic solids (linear scale on the left; logarithmic scale on the right).

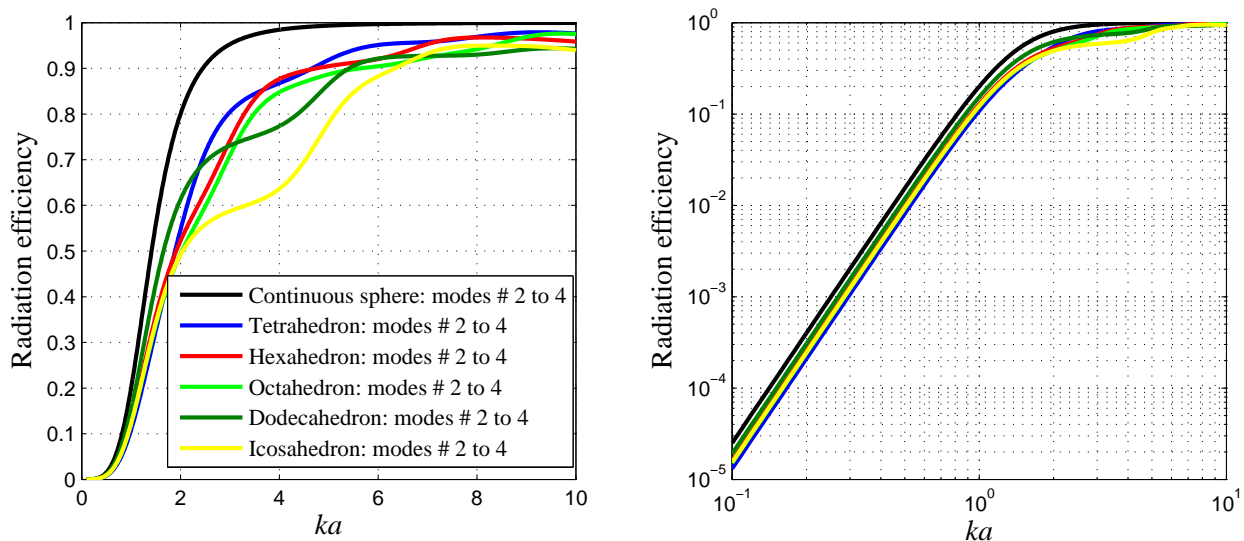


Figure 3.5: Radiation efficiency of the ARM # 2 to 4 of the continuous sphere and the discrete spheres based on the Platonic solids (linear scale on the left; logarithmic scale on the right).

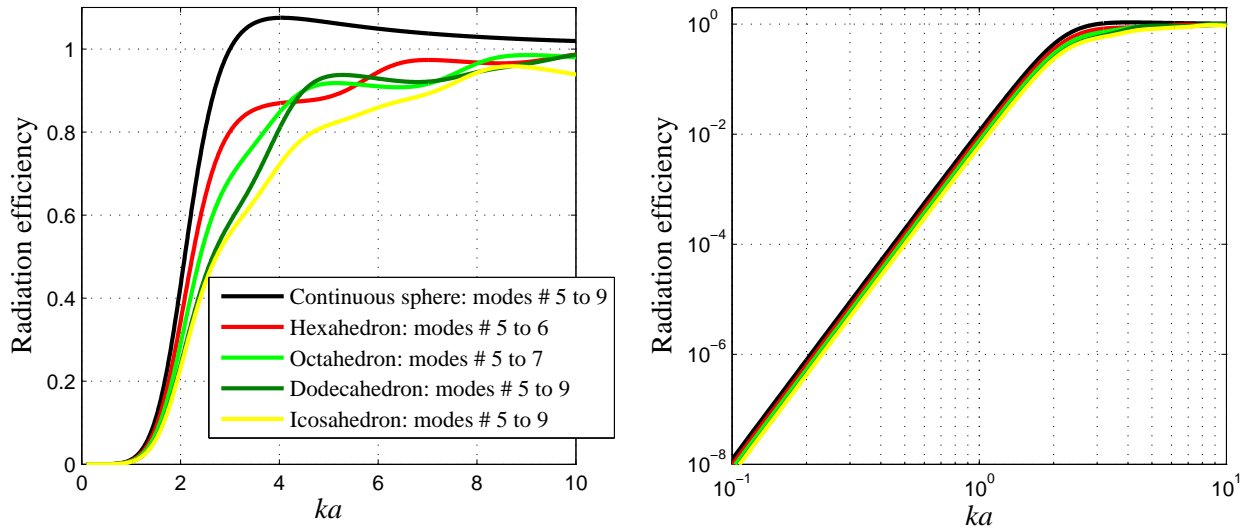


Figure 3.6: Radiation efficiency of the ARM # 5 to 9 of the continuous sphere, the dodecahedron-like sphere and the icosahedron-like sphere, as well as the ARM # 5 to 6 of the hexahedron-like sphere and the ARM # 5 to 7 of the octahedron-like sphere (linear scale on the left; logarithmic scale on the right).

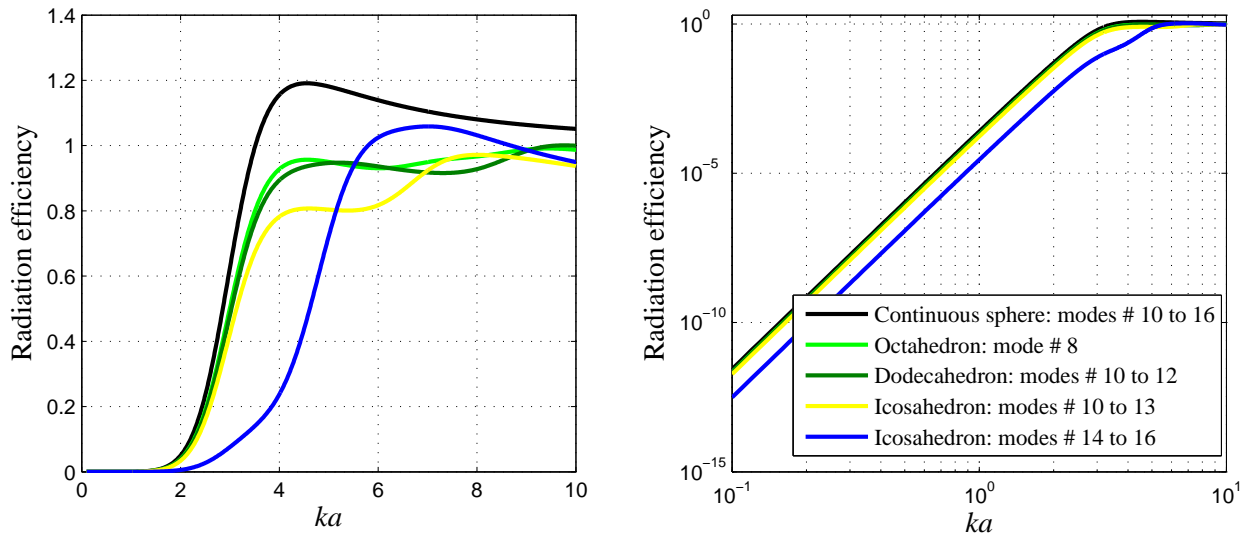


Figure 3.7: Radiation efficiency of the ARM # 10 to 16 of the continuous sphere, the ARM # 8 of the octahedron-like sphere, the ARM # 10 to 12 of the dodecahedron-like sphere and the ARM # 10 to 16 of the icosahedron-like sphere (linear scale on the left; logarithmic scale on the right).

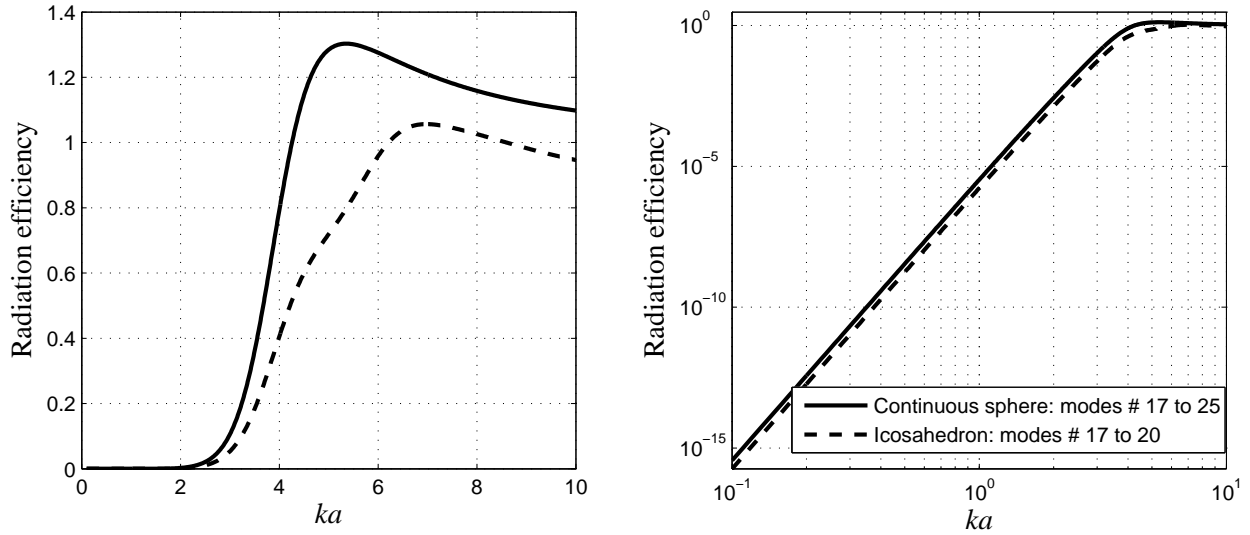


Figure 3.8: Radiation efficiency of the ARM # 17 to 25 of the continuous sphere and the ARM # 17 to 20 of the icosahedron-like sphere (linear scale on the left; logarithmic scale on the right).

In addition, it is shown that the continuous and discrete sphere curves present the same behavior at low ka values, so that the efficiency curves of the radiation groups are well discriminated. Therefore, the radiation modes have been arranged in descending order of their radiation efficiencies in the low ka range.

In order to better illustrate the relation between the acoustic behavior of the continuous and discrete spheres, the sound pressure patterns produced by some acoustic radiation modes of the discrete spheres based on the five Platonic solids are shown in Figs. 3.9 to 3.12. These directivity patterns have been evaluated on a spherical surface of radius $r = 10a$ for $ka = 0.1$. It has been assumed $\theta_0 = 54.7^\circ$, 45.0° , 35.2° , 31.7° and 20.9° for the tetrahedron, hexahedron, octahedron, dodecahedron and icosahedron, respectively. These θ_0 values correspond to the maximum values so that the spherical caps do not overlap each other. The series given by Eq.(3.14) has been truncated to order $N = 10$ and the medium properties assumed to be $c = 343\text{m/s}$ and $\rho = 1.21\text{kg/m}^3$.

Comparison of Figs. 3.9 to 3.12 with Fig. 2.7 reveals that the directivity patterns associated to the radiation modes of the discrete spheres match real spherical harmonic functions. Since the acoustic radiation modes are real modes, they lead to the real representation of spherical harmonics rather than the complex one.

Figure 3.13 shows the sound pressure patterns produced by the first acoustic radiation mode of the discrete spheres based on the five Platonic solids. Unlike the patterns presented in Fig. 3.9, these directivity patterns have been evaluated at $ka = 5$.

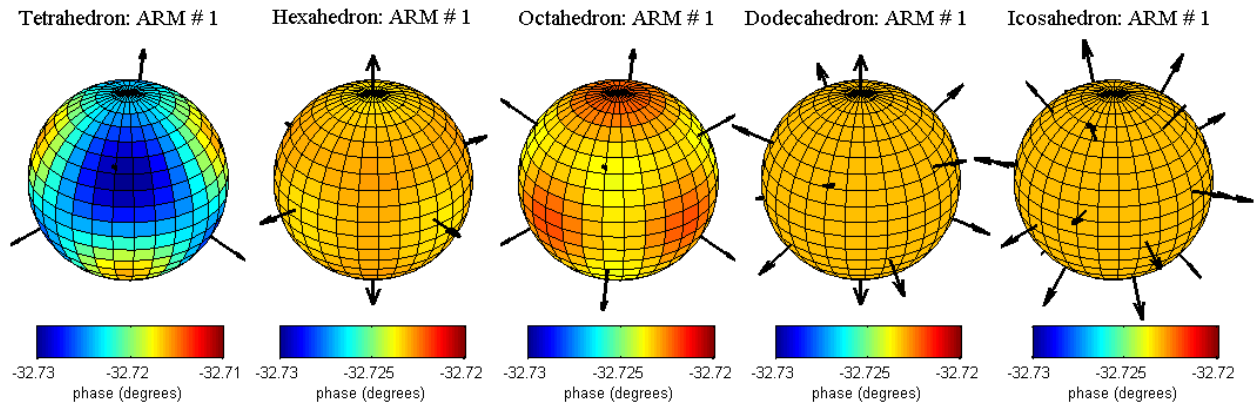


Figure 3.9: Sound pressure patterns corresponding to the ARM # 1 of the discrete spheres based on the five Platonic solids. Patterns obtained for $ka = 0.1$ at a distance $r = 10a$ from the sphere center.

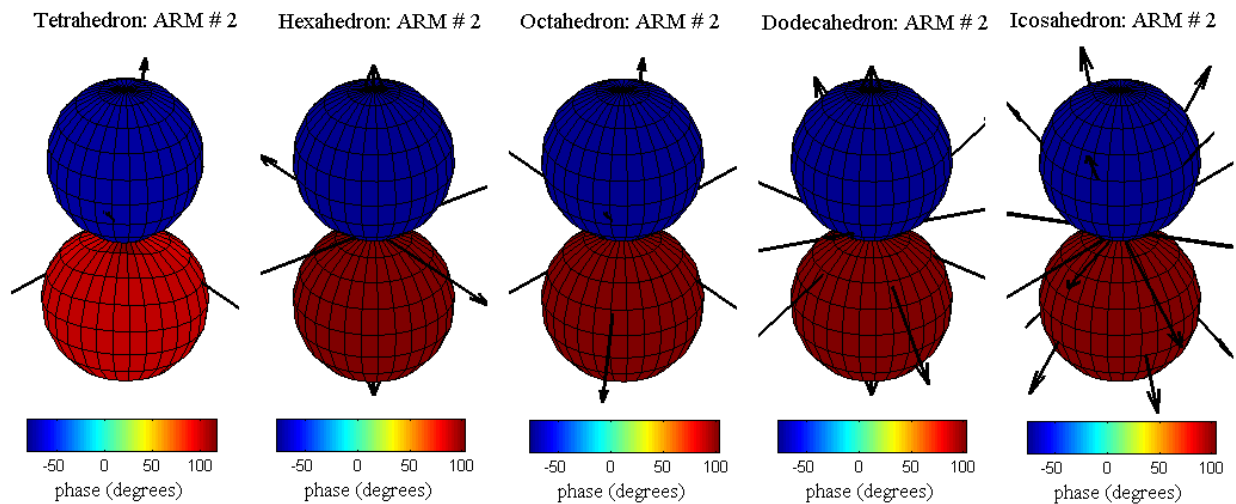


Figure 3.10: Sound pressure patterns corresponding to the ARM # 2 of the discrete spheres based on the five Platonic solids. Patterns obtained for $ka = 0.1$ at a distance $r = 10a$ from the sphere center.

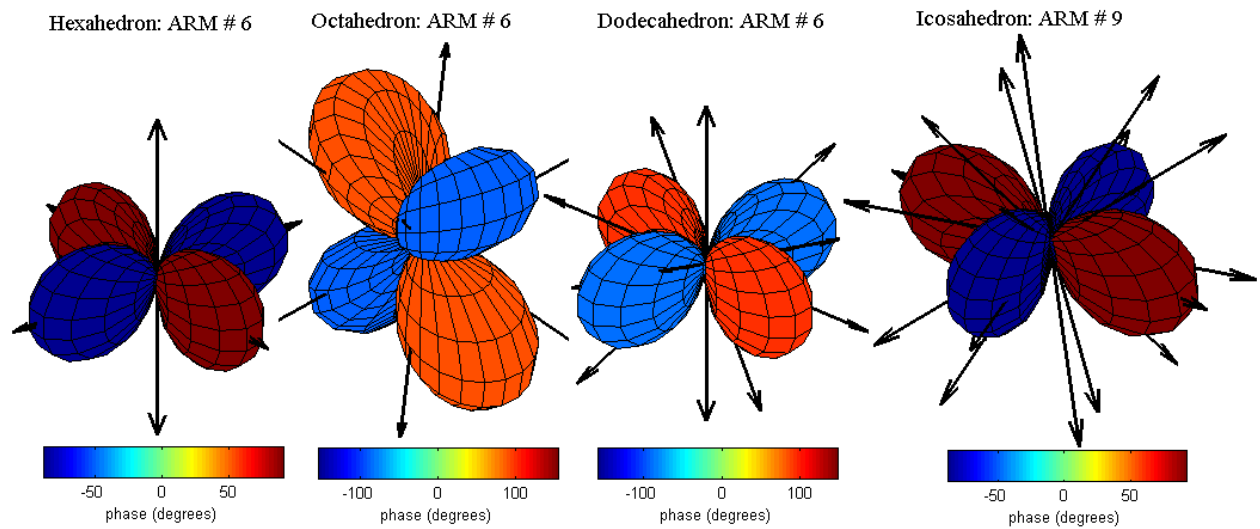


Figure 3.11: Sound pressure patterns corresponding to the ARM # 6 of the hexahedron-like, octahedron-like and dodecahedron-like spheres, as well as the ARM # 9 of the icosahedron-like sphere. Patterns obtained for $ka = 0.1$ at a distance $r = 10a$ from the sphere center.

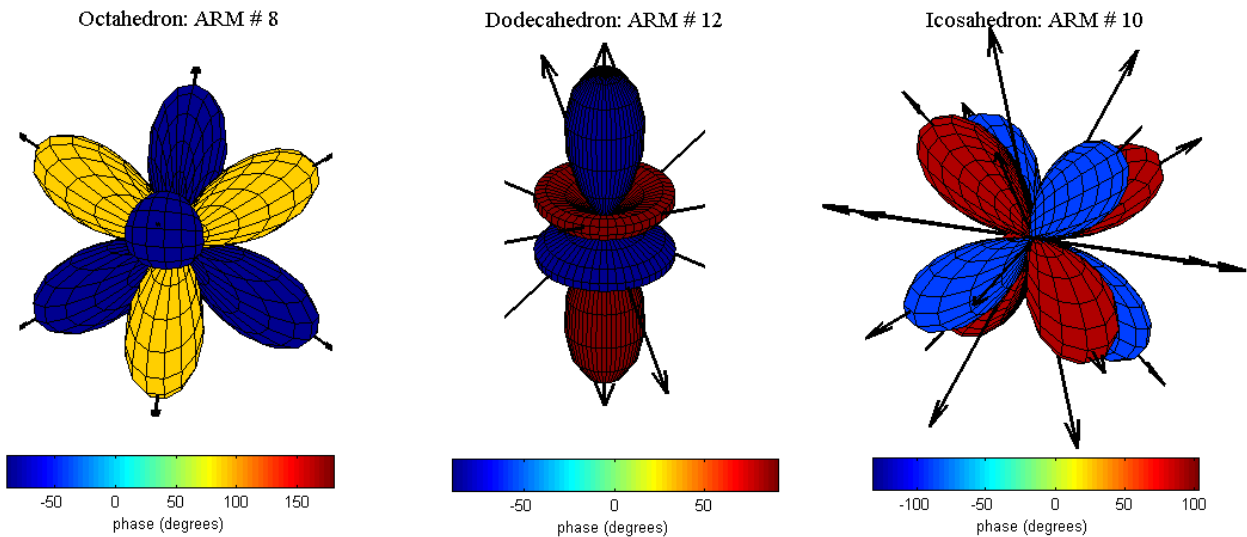


Figure 3.12: Sound pressure patterns corresponding to the ARM # 8 of the octahedron-like sphere, the ARM # 12 of the dodecahedron-like sphere and the ARM # 10 of the icosahedron-like sphere. Patterns obtained for $ka = 0.1$ at a distance $r = 10a$ from the sphere center.

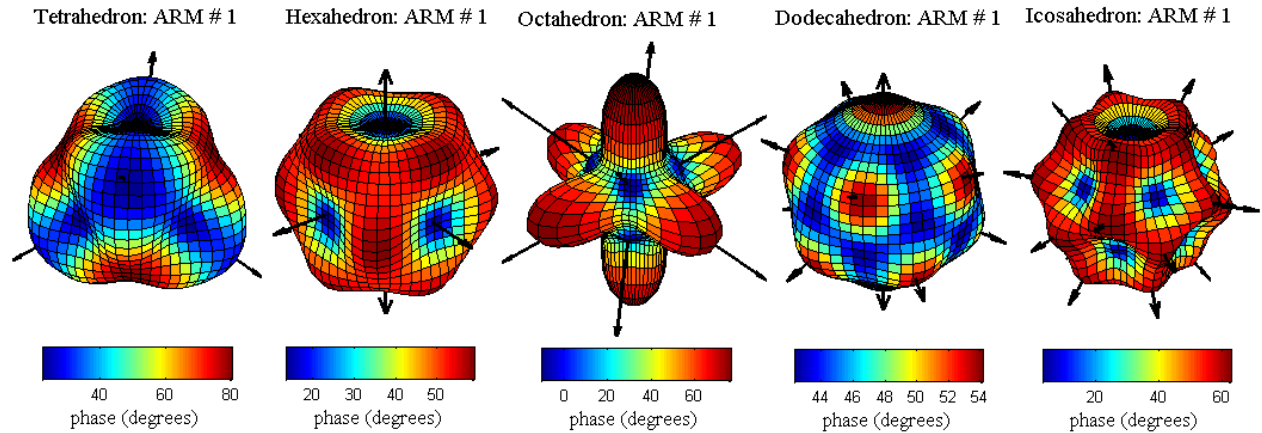


Figure 3.13: Sound pressure patterns corresponding to the ARM # 1 of the discrete spheres based on the five Platonic solids. Patterns obtained for $ka = 5$ at a distance $r = 10a$ from the sphere center.

Comparison of Figs. 2.7 and 3.13 shows that there are discrepancies between the radiated sound fields and the real spherical harmonics. This arises due to the fact that the radiation efficiency curves of the spherical harmonics become closer as ka increases (refer to Fig. 3.1), so that the higher order spherical harmonics excited by the discrete sphere contribute significantly to the resulting sound field. In other words, the radiated sound field is a linear combination of spherical harmonics of distinct orders rather than a pure spherical harmonic function. Since this phenomenon takes place due to the discretization of the radiation surface, it has been called “spatial aliasing” in the sound reproduction literature (cf. [71, 21, 52, 75]). Further details will be provided in section 4.2.

3.2 Electromechanical behavior

In this section, an electromechanical model of a compact loudspeaker array is presented. The theoretical development is divided into two subsections. In the first, the electrical and mechanical behavior of the array drivers is considered (here, only electrodynamic loudspeakers are concerned). Then, two different approaches for modeling the acoustic coupling between drivers are presented.

3.2.1 Electrodynamic loudspeakers

An electrodynamic loudspeaker can be modeled as a single degree-of-freedom (SDOF) mechanical system driven by electromagnetic and acoustic forces. The mass of the driver diaphragm assembly

M , the mechanical compliance of the driver suspension C and its mechanical resistance R provide, respectively, the inertial, the energy storage and the energy dissipation elements of the SDOF system. By assuming a harmonic time dependence of the form $e^{-i\omega t}$, application of the Newton's second law leads to

$$-i\omega M_l u_l + R_l u_l - \frac{1}{i\omega C_l} u_l = F_l^{(e)} + F_l^{(a)} \quad (3.24)$$

where the subscript l refers to the l -th loudspeaker of the array (L is the number of loudspeakers), u_l is its velocity, $F_l^{(e)}$ is the electromagnetic force and $F_l^{(a)}$ is the net acoustic force acting on the driver diaphragm.

Now, let B be the magnetic flux density in the driver air gap and l_e the length of the voice-coil conductor in the magnetic field, so that the diaphragm movement generates an induced voltage given by $B l_e u$. On the other hand, the electromagnetic force acting on the diaphragm due to the presence of an electrical current i in a magnetic field is given by $F^{(e)} = B l_e i$. Hence, application of the Kirchhoff's second law leads to

$$F_l^{(e)} = \frac{(B l_e)_l}{Z_l^{(e)}} (v_l - (B l_e)_l u_l) \quad (3.25)$$

where $(B l_e)_l$ is the force factor of the l -th loudspeaker unit, $Z_l^{(e)}$ is the clamped electrical impedance ($u_l = 0$) of its voice-coil and v_l is the voltage that feeds the l -th driver.

Many models have been proposed to evaluate $Z_l^{(e)}$. The simplest one considers it as an electrical resistance and is restricted to low-frequency analysis [76]. As frequency increases, the voice-coil inductance greatly affects its electrical impedance. In this work, following [77], the electrical part of the transduction system is modeled as a resistor in series with a lossy inductor, so that $Z_l^{(e)}$ is explicitly given by

$$Z_l^{(e)} = R_l^{(e)} + K_l (-i\omega)^{n_l} \quad (3.26)$$

where $R_l^{(e)}$ is the voice-coil resistance of the l -th driver and K_l and n_l are parameters of the lossy inductor model.

Substitution of Eq.(3.25) into (3.24) yields

$$\left(-i\omega M_l + R_l - \frac{1}{i\omega C_l} + \frac{(B l_e)_l^2}{Z_l^{(e)}} \right) u_l - F_l^{(a)} = b_l \quad (3.27)$$

where $b_l = (Z_l^{(e)})^{-1} (B l_e)_l v_l$ is the clamped electromagnetic force.

Equation (3.27) can be written in matrix notation as

$$\mathbf{G}\mathbf{u} - \mathbf{f}_a = \mathbf{b} \quad (3.28)$$

where \mathbf{G} is an $L \times L$ diagonal matrix whose entries are $g_l = -\iota\omega M_l + R_l - (\iota\omega C_l)^{-1} + (Z_l^{(e)})^{-1} (Bl_e)_l^2$, \mathbf{u} is an $L \times 1$ vector of velocity amplitude coefficients, \mathbf{f}_a is an $L \times 1$ vector of acoustic forces acting on the loudspeakers diaphragms and \mathbf{b} is an $L \times 1$ vector whose components are b_l .

In this section, algebraic expressions have been developed in order to evaluate \mathbf{G} . In the following, two distinct analytical models used to obtain \mathbf{f}_a are presented.

3.2.2 Acoustical coupling

Now, let $p_{ll'}^-$ and $p_{ll'}^+$ be the net sound pressures acting, respectively, on the inner and outer diaphragm surface of the l -th driver due to the movement of the l' -th driver. Then, the net acoustic force can be written as

$$F_l^{(a)} = \hat{S}_l \sum_{l'=1}^L (p_{ll'}^- - p_{ll'}^+) \quad (3.29)$$

where \hat{S}_l is the net surface area of the l -th loudspeaker unit.

Let \mathbf{S} be an $L \times L$ diagonal matrix containing \hat{S}_l in its entries. Then, Eq.(3.29) can be written in matrix notation as follows

$$\mathbf{f}_a = \mathbf{S} (\mathbf{Z}^- - \mathbf{Z}^+) \mathbf{S}\mathbf{u} \quad (3.30)$$

where \mathbf{Z}^- and \mathbf{Z}^+ are, respectively, the internal and external acoustic-impedance matrices ($L \times L$) which describe the acoustical coupling between the array drivers.

Finally, substitution of Eq.(3.30) into (3.28) leads to

$$(\mathbf{G} + \mathbf{S} (\mathbf{Z}^+ - \mathbf{Z}^-) \mathbf{S})\mathbf{u} = \mathbf{b} \quad (3.31)$$

As far as the enclosure design is concerned, two different approaches have been reported in literature. In the first approach, the drivers share a common hollow enclosure [31, 30] and, in the second, they have their own independent sealed cavities [31, 23]. In the latter, there will be no internal acoustic coupling so that \mathbf{Z}^- will be diagonal.

3.2.2.1 Lumped-parameter model

Let V_b be the net internal volume of the loudspeaker array. If the overall dimensions of the latter are much smaller than an acoustic wavelength and the energy dissipation is not taken into account, the enclosure behavior can be described by an acoustical compliance $C_b = V_b/\rho c^2$, i.e., a lumped-parameter element which stores energy, where ρ is the medium density and c is the sound speed [58]. Hence, the acoustic impedance associated with the volume V_b is $Z_b = (\omega C_b)^{-1}$ and the entries of the internal coupling matrix \mathbf{Z}^- becomes

$$Z_{ll'}^- = \frac{\rho c^2}{\omega V_b} \quad (3.32)$$

Equation (3.32) shows that $Z_{ll'}^-$ does not depend on the pair of drivers considered and it provides a simple and low computational cost way to evaluate the acoustic coupling between the loudspeakers in the array cavity. On the other hand, the external acoustic coupling cannot be so easily evaluated. Fortunately, the external acoustic force is small compared to the other forces acting on a loudspeaker diaphragm, so that it is not able to appreciably affect the system electromechanics. Therefore, the external acoustic coupling is neglected here and it is assumed that each loudspeaker behaves as a piston mounted on an infinite baffle as far as the external force acting on its diaphragm is concerned. The acoustic radiation impedance of a baffled-piston radiator is given by [58]

$$Z_{ll'}^+ = \frac{\rho c}{\pi r_l^2} \left(1 - \frac{J_1(2kr_l)}{kr_l} - i \frac{H_1(2kr_l)}{kr_l} \right) \delta_{ll'} \quad (3.33)$$

where r_l is the radius of the l -th piston, k is the wave number, $J_1(\cdot)$ is the Bessel function of first kind and order 1, $H_1(\cdot)$ is the Struve function of order 1 and $\delta_{ll'}$ is the Kronecker delta. At low frequencies, the main effect of this radiation impedance is to increase slightly the moving mass, whose value is therefore given as a corrected value (including radiation) in commercial data sheets.

If each transducer has an independent sealed cavity, the entries of the internal acoustic-impedance matrix become $Z_{ll}^- = \rho c^2(\omega V_b^{(l)})^{-1}$ and $Z_{ll'}^- = 0$ for $l \neq l'$, where $V_b^{(l)}$ is the net internal volume of the cavity of the l -th driver.

3.2.2.2 Distributed-parameter model

Similar to the exterior sound field, the interior field produced by a loudspeaker unit mounted on an empty rigid sphere can be approximated by modeling the loudspeaker diaphragm as a convex

spherical cap that oscillates with a constant radial velocity u_l over its surface. If so, the sound pressure inside the array's cavity is given by Eq.(A.22). The coefficients C_{mn} of the series are (compare to Eq.(3.11))

$$C_{mn} = \frac{\iota \rho c u_l}{\frac{dj_n(ka)}{d(ka)}} \sqrt{\frac{\pi}{2n+1}} \delta_{m0} \begin{cases} P_{n-1}(\eta_0) - P_{n+1}(\eta_0) & \text{if } n > 0 \\ 1 - \eta_0 & \text{if } n = 0 \end{cases} \quad (3.34)$$

In obtaining Eq.(3.34), it is assumed that the spherical cap center is placed at $\theta = 0$ (north pole), so that the problem becomes axisymmetric.

Equations (A.20), (3.11), (A.22) and (3.34) can be used to evaluate the external and internal sound pressure fields acting on each loudspeaker diaphragm due to its own vibration and to the vibration of the other loudspeakers. The net sound pressures $p_{ll'}^-$ and $p_{ll'}^+$ can be obtained by integrating Eqs.(A.22) and (A.20) over the surface of the l -th spherical cap and dividing this result by \hat{S}_l . Then, the entries of the acoustic-impedance matrices are given by

$$Z_{ll'}^\pm = \frac{1}{\hat{S}_l \hat{S}_{l'} u_{l'}} \int_0^{2\pi} \int_0^{\theta_l} p(a, \theta_l, \phi_l) a^2 \sin\theta_l d\theta_l d\phi_l \quad (3.35)$$

In the numerical implementation, the series given in Eqs.(A.20) and (A.22) must be truncated to order N so that $n \leq N$. It is worth noting that if $kr \ll 1$, the $Z_{ll'}^-$ calculated by the lumped-parameter and distributed-parameter models will lead to the same result.

3.3 Enclosure design

To define an optimum enclosure for a compact loudspeaker array with independently programmable transducers is not a simple task due to the fact that the drivers interact with each other in a complicated manner inside the cabinet. This problem can be addressed by providing each transducer with a sealed cavity in order to suppress the acoustical coupling, so that the electromechanical behavior of the compact array becomes easier to predict. However, this solution leads to a harder to build mechanical frame compared to the alternative solution of mounting the drivers on a common hollow enclosure. In addition, since the latter implies a larger cavity volume, one may conjecture that it leads to lower voltages for a given diaphragm velocity [31, 78, 79]. This section discusses and compares these two enclosure designs.

It is useful to consider two extreme cases concerning the relative movement of the transducers, but it must be kept in mind that any state in between can be achieved. In the first, all drivers vibrate with the same velocity magnitude and phase. In the second, the sum of the driver velocities is zero. As far as the spherical arrays presented in section 3.1.2.1 are concerned, the former corresponds to the first acoustic radiation mode, and the latter corresponds to anyone of the remaining radiation modes. This emerges from inspection of the modal matrices presented in Tabs. C.3 to C.7, which reveals that $\sum_{l=1}^L \Psi_{ll'} = 0$, for $l' = 2, 3, \dots, L$.

When all drivers vibrate in phase with the same velocity magnitude, inspection of Eqs.(3.31) and (3.32) shows that a common hollow cabinet provides each transducer with an additional mechanical compliance of $V_b(L\rho c^2 \hat{S}^2)^{-1}$, i.e., each transducer behaves as if it had been mounted on a sealed cavity with volume V_b/L . Therefore, the voltages evaluated using the lumped-parameter model remain unchanged whether the drivers have their own sealed cavities or share the same enclosure.

When the sum of the driver velocities is zero, the transducer displacements will not produce internal sound pressure fluctuation if they share a common cabinet, i.e., the entire cavity compliance is compensated by the opposite phase movement of the array's elements, which is equivalent to mount each driver on an independent cabinet with a huge volume. Therefore, to let the drivers share a common enclosure leads to lower voltages in the compliance-dominated region (low-frequency range) compared to providing each one of them with its own sealed cavity.

In both the extreme cases, if the drivers share a common cabinet, the acoustic modes of the spherical cavity will modify the system dynamics at discrete frequencies corresponding to the eigenfrequencies of such modes. Unlike the lumped-parameter model, this effect is predicted by the distributed-parameter model. The eigenfrequencies of a rigid spherical cavity are characterized by the singularities of the coefficients C_{mn} in Eq.(A.22). Inspection of Eq.(3.34) shows that such singularities take place at the zeros of the first derivative of $j_n(ka)$. Then, the lowest four eigenfrequencies correspond to the following ka values: 2.0816, 3.3421, 4.4934 and 5.9404.

As a numerical example, consider a compact spherical loudspeaker array with $L = 12$ drivers distributed on a sphere with radius $a = 0.075m$ according to the dodecahedron symmetry, so that the spatial orientation of each cap is made equal to the vector normal to a face of a dodecahedron. All drivers are supposed to be equal with the characteristics presented in the row "mean value" of Tab. 6.1. Since $a = 0.075m$ and $\hat{S} = 0.0012m^2$, the aperture angle of the spherical cap model is $\theta_0 = 15.1^\circ$. The two different enclosure designs discussed above are considered. In the first one, the drivers share the same spherical cavity with volume $V_b = (4/3)\pi a^3 = 1.8 \times 10^{-3}m^3$ and both the lumped- and the distributed-parameter model are used to compute the voltages. In the second,

each driver has its own independent sealed cavity with volume $V_b^{(l)} = V_b/12 = 1.4726 \times 10^{-4}m^3$ and the voltages are evaluated by the lumped-parameter model.

Frequency response functions (FRFs) between input diaphragm velocity and output voltage are shown in Fig. 3.14. For each FRF, the velocity and the voltage are taken on the same driver. These FRFs have been obtained by letting $\mathbf{u} = \psi_l$ in Eq.(3.28), where the acoustic radiation modes are given in Tab. (C.6). The medium properties have been assumed to be $c = 343m/s$ and $\rho = 1.21kg/m^3$. In addition, a truncation order $N = 29$ has been adopted when using the distributed-parameter model.

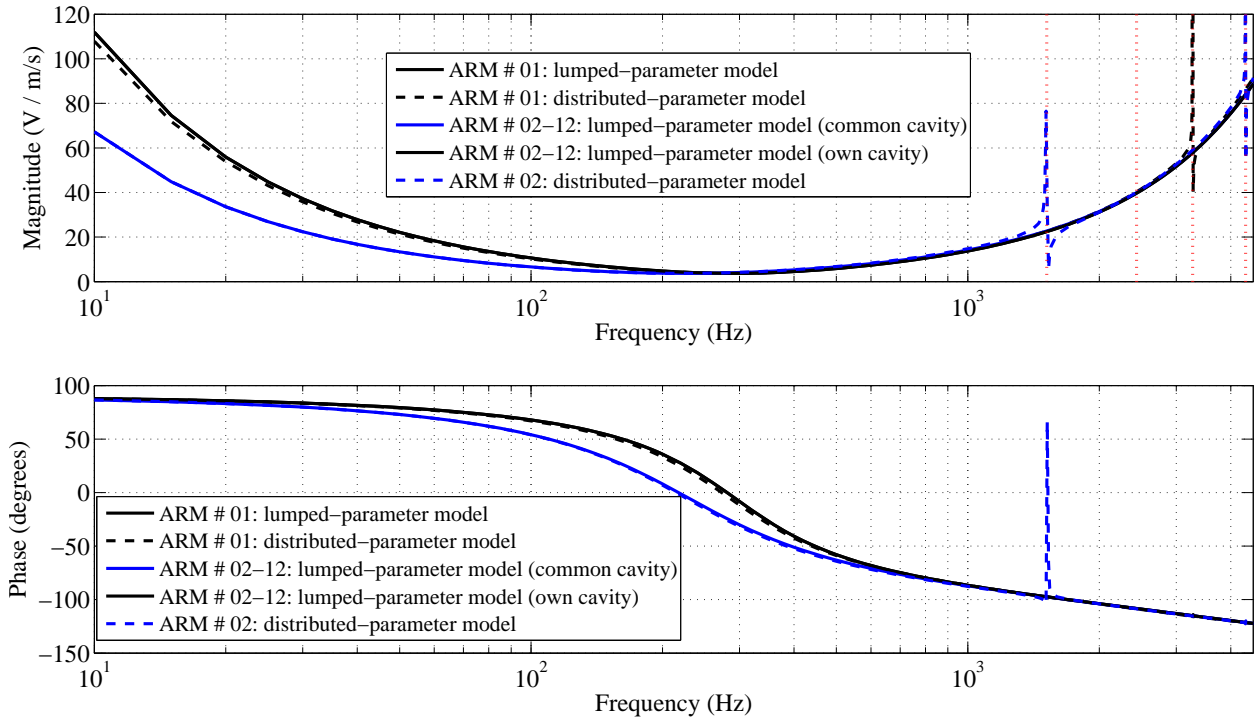


Figure 3.14: Frequency response functions between input diaphragm velocity and output voltage.

Since $a = 0.075m$, the eigenfrequencies of the spherical cavity are $1515Hz$, $2433Hz$, $3271Hz$ and $4324Hz$. The vertical dotted red lines in Fig. 3.14 indicate these frequencies. Comparison of the continuous black line with the dashed black line, as well as the continuous blue line with the dashed blue line show that the lumped- and the distributed-parameter model lead to the same curves, except for some singularities at the cavity eigenfrequencies, as discussed before.

As far as the first radiation mode is concerned, the cabinet provides each driver with an additional mechanical compliance of approximately $V_b(L\rho c^2\hat{S}^2)^{-1} \approx 7.31 \times 10^{-4}m/N$. This value is not much larger than the mechanical compliance $C = 4.75 \times 10^{-4}m/N$ of the driver suspension, so that the FRF magnitude increases in the compliance-dominated frequency range in comparison

with the remaining radiation modes. Moreover, if the cavity eigenfrequencies are neglected, to let the drivers share a common hollow enclosure will lead to the same electromechanical behavior as to provide each driver with its own sealed cavity, as expected.

It is worth noting that the theoretical FRFs presented in Fig. 3.14 do not depend on the choice of an active driver of the spherical array. Computation of the FRF will always lead to the same curve regardless of the considered active transducer.

No remarkable differences have been observed between the FRFs evaluated by the lumped- and the distributed-parameter model, except for frequencies corresponding to the natural frequencies of the spherical cavity. This suggests that driver voltages can be evaluated by using a simple lumped-parameter model for the enclosure, so that heavy calculations involved in the distributed-parameter modeling may be unnecessary. In fact, the two extreme cases shown in Fig. 3.14 do not represent a challenge to the acoustic coupling models presented in section 3.2.2. Since the statements presented in this section rely on the validity of the proposed theoretical models, a set of experiments must be accomplished in order to validate them. The accuracy of the proposed models is demonstrated by comparison with experimental results in chapter 6.

The radiation efficiency of the radiation modes has not yet been taken into account in the enclosure design discussion. Since a spherical array is supposed to produce an acoustic field rather than diaphragm vibration, radiation efficiency plays an important role. It has been stated that a reduction in the electrical signal power is achieved in the low-frequency range by letting the drivers share a common enclosure. However, one question remains unanswered: since the radiation efficiency drops rapidly with decreasing frequency (refer to Figs. 3.5 to 3.8), does this claimed voltage reduction take place in a frequency range in which the radiation efficiency values lead to meaningful sound power levels? If not, such an improvement is useless. In the following, an attempt is made to partially answer this question.

As said before, Fig. 3.14 was obtained by letting $\mathbf{u} = \psi_i$ in Eq.(3.28), where ψ_i is the i -th radiation mode. Then, $c_i = \delta_{il}$ in Eq.(2.44) so that these equations permit to evaluate the ratio between the voltage magnitude that feeds a given transducer of the array and the total sound power. Figure 3.15 shows this ratio for the dodecahedral source considered here for $i = 1, 2, 5$ and 12 . The voltages were taken at the most solicited driver of the array (driver # 01, refer to Tab. C.6) and computed by using the lumped-parameter model.

Comparison of the continuous with the dashed lines reveals that letting the drivers share a common cabinet reduces the voltages in a frequency range in which the radiation efficiency is too small, especially for the radiation modes # 5 and 12. A common cabinet is expected to provide

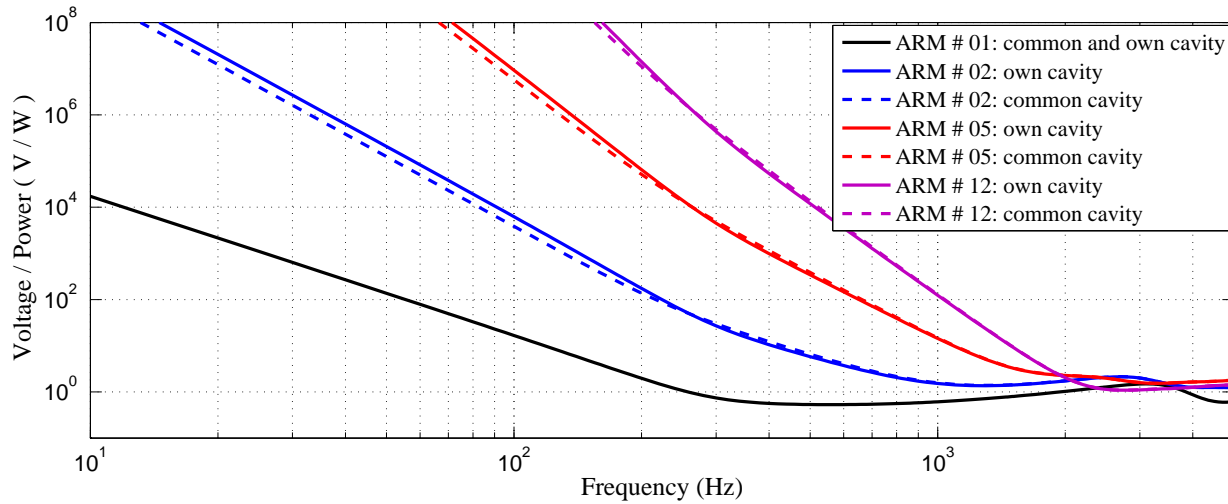


Figure 3.15: Ratio between the voltage magnitude that feeds the most solicited driver of the array (driver # 1) and the resulting sound power. Simulation results obtained for the acoustic radiation modes # 1, 2, 5 and 12.

some improvement only for the acoustic radiation modes # 2 to 4. Hence, the results presented here suggest that the enclosure design does not play a central role on the dynamic range of a compact loudspeaker array. Therefore, since a common cabinet is simpler to build and the models proposed in section 3.2 permit to predict the acoustical coupling inside the cavity, one may conclude that there is no reason to build a complicated frame in order to provide each driver with its own sealed cavity. In addition, it will be shown in chapter 6 that most of the cavity modes are damped in practice, so that they do not affect the loudspeaker dynamics.

Chapter 4

Synthesis and Reproduction of Directivity Patterns

A compact loudspeaker array with independently programmable transducers is an engineering solution aiming to realize the ambition of synthesizing and/or reproducing a given directivity pattern. In chapter 3, a theoretical model that predicts the radiation pattern of a spherical loudspeaker array from the knowledge of the driver velocities or voltages was proposed. In this chapter, the inverse problem is addressed. The task is to find optimum weights which must be applied to the array's elements in order to achieve the target directivity pattern.

First, the synthesis of an arbitrary pattern whose magnitude and phase are defined on a spherical surface enclosing the loudspeaker array is addressed by a weighted least-squares method. Next, this same approach is employed in order to synthesize pure spherical harmonic functions, i.e., the target directivity is a spherical harmonic. Finally, the problem of synthesizing only the magnitude of the directivity pattern (phase not concerned) is dealt with.

4.1 Synthesis of an arbitrary function

This section concerns the synthesis or reproduction of an arbitrary directivity pattern by a compact spherical loudspeaker array. The target pattern is a desired sound pressure distribution in (r_0, θ, ϕ) , where $r_0 > a$ is fixed but arbitrary, namely, the target pattern is defined on a spherical surface that encloses the loudspeaker array. The task is to find optimum weights which must be applied to each acoustic radiation mode in order to achieve the target directivity pattern.

Because the functions considered in this chapter are subjected to numerical processing, they must be sampled. Since these functions are defined on a spherical surface, the author has chosen to use a uniform angular grid given by $\theta_{\hat{t}} = \hat{t}\Delta\theta$ and $\phi_{\hat{p}} = \hat{p}\Delta\phi$, where $\hat{t} = 0, 1, \dots, N_t - 1$ and $\hat{p} = 0, 1, \dots, N_p - 1$; N_t and N_p are, respectively, the number of samples in the zenithal and azimuthal direction. Hence, $N_s = N_t N_p$ is the number of samples, $\Delta\theta = \pi/(N_t - 1)$ rad and $\Delta\phi = 2\pi/N_p$ rad. The sampled sphere so defined motivates the use of the following inner product:

$$[\mathbf{x}, \mathbf{y}] = \mathbf{y}^H \mathbf{W} \mathbf{x} \quad (4.1)$$

where $\mathbf{x}, \mathbf{y} \in \mathbb{C}^{N_s}$ and $\mathbf{W} \in \mathbb{R}_+^{N_s \times N_s}$. The matrix \mathbf{W} is diagonal and contains non-dimensional area weight factors that are determined by surface integration over appropriate sections of the sphere. Thus, the diagonal terms of \mathbf{W} , w_i , are

$$w_i = \begin{cases} \frac{1}{4\pi} \int_{\phi_{\hat{p}-\frac{\Delta\phi}{2}}^{\phi_{\hat{p}+\frac{\Delta\phi}{2}}} \int_0^{\theta_{\hat{t}}} \sin\theta d\theta d\phi = \frac{1}{N_p} \sin^2\left(\frac{\Delta\theta}{4}\right) & \text{if } \hat{t} = 0 \text{ or } \hat{t} = N_t - 1 \\ \frac{1}{4\pi} \int_{\phi_{\hat{p}-\frac{\Delta\phi}{2}}^{\phi_{\hat{p}+\frac{\Delta\phi}{2}}} \int_{\theta_{\hat{t}-\frac{\Delta\theta}{2}}^{\theta_{\hat{t}+\frac{\Delta\theta}{2}}} \sin\theta d\theta d\phi = \frac{\sin\theta_{\hat{t}}}{N_p} \sin\left(\frac{\Delta\theta}{2}\right) & \text{if } 1 \leq \hat{t} \leq N_t - 2 \end{cases} \quad (4.2)$$

where $i = \hat{p}N_t + \hat{t} + 1$.

Now, let \mathbf{Y}_s be a $(N + 1)^2 \times N_s$ matrix containing samples of the complex-valued spherical harmonics as rows (sampled version of the vector \mathbf{Y}), \mathbf{p} be a vector containing N_s samples of the sound pressure field produced by the spherical array at $r = r_0$ and \mathbf{p}_t be a vector containing N_s samples of the target directivity pattern. So, by referring to Eqs.(2.42) and (3.16), the following optimization problem can be formulated, which must be solved for each ka value for a given array geometry:

$$\min_{\mathbf{c}} \left\| \mathbf{Y}_s^T \mathbf{B} \Psi \mathbf{c} - \mathbf{p}_t \right\|_2 \quad (4.3)$$

where $\|\mathbf{x}\|_2 = [\mathbf{x}, \mathbf{x}]^{\frac{1}{2}}$ is the Euclidian norm and \mathbf{B} is evaluated at $r = r_0$.

This is a well-known convex optimization problem (weighted least-squares) whose solution is [80]

$$\mathbf{c}_{opt} = \left((\mathbf{Y}_s^T \mathbf{B} \Psi)^H \mathbf{W} (\mathbf{Y}_s^T \mathbf{B} \Psi) \right)^{-1} (\mathbf{Y}_s^T \mathbf{B} \Psi)^H \mathbf{W} \mathbf{p}_t \quad (4.4)$$

It is worth noting that the weight matrix \mathbf{W} must be used in order not to favor densely sampled regions on the sphere.

The voltages that must feed the drivers can be obtained by substituting Eqs.(4.4) and (2.42) into (3.28).

The optimization problem presented in expression (4.3) could be stated without using radiation modes. If so, optimization results are supposed to lead directly to the loudspeaker unit velocities. In this case, since the loudspeakers in the array usually present the same radiation efficiency, one must always deal with L independent channels regardless of ka . On the other hand, using radiation modes leads to a reduced number of channels due to the fact that some modes do not radiate sound energy at ka ranges that can be determined through inspection of their radiation efficiencies. Actually, the optimization problem over individual loudspeaker responses is ill-conditioned when the radiation modes of the array have very different efficiencies. This would lead to huge drive levels or require a regularization process, which is avoided when truncating the radiation mode expansion.

In addition, it has been shown in section 3.1.2.1 that radiation modes lead to spherical harmonic radiation patterns under some circumstances, so that the rotational properties of such functions can be used in order to rotate the radiation pattern with no need to evaluate Eq.(4.4) (further details on this subject will be provided in section 4.2). Finally, the radiation pattern of a radiation mode is generally more attractive than the radiation pattern of a loudspeaker unit. Thus, a single channel (radiation mode) is still useful in room acoustics and electroacoustic music applications, for example.

4.2 Synthesis of a spherical harmonic function

Linear combinations of spherical harmonics of the same order have been generally used as target patterns in directivity synthesis by compact loudspeaker arrays (cf. [22, 54, 26]). According to Zotter *et al.* (2007), it is possible to control spherical harmonics of order n provided that $n \leq \sqrt{L} - 1$, where L is the number of loudspeakers in the array. In addition, even if this rule of thumb is satisfied, the accuracy of spherical harmonic synthesis degrades as ka increases. In both cases, synthesis error is due to spatial aliasing. In the following, the synthesis of spherical harmonics by

spherical loudspeaker arrays is revisited within the framework of the acoustic radiation modes.

It is known that function spaces spanned by spherical harmonics of the same order n are linear subspaces that are invariant with respect to rigid rotation through spatial angles [65], refer to Eqs.(2.29) and (2.32) to (2.34). For example, if a given pattern is in the subspace generated only by harmonics of order $n = 3$, any rotation of this pattern also possesses a spherical harmonic expansion consisting only of harmonics of order $n = 3$. Then, if \mathbf{p}_t contains samples of a function in the subspace generated by spherical harmonics of order n , it can be expressed as $\mathbf{p}_t = (\mathbf{Y}_s^{(n)})^T \mathbf{q}_n$, where \mathbf{q}_n contains $2n+1$ complex coefficients and $\mathbf{Y}_s^{(n)}$ is an $2n+1 \times N_s$ matrix whose rows contain spherical harmonics of order n .

Now, let \mathbf{X}_n be an $L \times 2n + 1$ matrix containing the \mathbf{c}_{opt} associated with each one of the $2n + 1$ rows of $\mathbf{Y}_s^{(n)}$, namely, each column of \mathbf{X}_n is obtained by letting \mathbf{p}_t be a column of $(\mathbf{Y}_s^{(n)})^T$ in Eq.(4.4). Then, solution of problem (4.3) yields the following minimum root mean square error (RMSE):

$$\min_{\mathbf{c}}(\text{RMSE}) = \min_{\mathbf{c}} \left\| \mathbf{Y}_s^T \mathbf{B} \Psi \mathbf{c} - (\mathbf{Y}_s^{(n)})^T \mathbf{q}_n \right\|_2 = \left\| \left(\mathbf{Y}_s^T \mathbf{B} \Psi \mathbf{X}_n - (\mathbf{Y}_s^{(n)})^T \right) \mathbf{q}_n \right\|_2 \quad (4.5)$$

Equation (4.5) leads to the minimum RMSE for a given but arbitrary \mathbf{q}_n . Any function in the subspace spanned by spherical harmonics of order n can be represented by choosing a suitable \mathbf{q}_n . So, to let this vector be the optimization variable in an additional minimization or maximization of the RMSE given in Eq.(4.5) leads, respectively, to the easiest and hardest to synthesize directivity pattern in the considered subspace. If \mathbf{q}_n is normalized so that $\mathbf{q}_n^H \mathbf{q}_n = 1$, one has [22]

$$\min_{\mathbf{q}_n} \left\| \left(\mathbf{Y}_s^T \mathbf{B} \Psi \mathbf{X}_n - (\mathbf{Y}_s^{(n)})^T \right) \mathbf{q}_n \right\|_2 = \lambda_{\min} \quad (4.6)$$

and

$$\max_{\mathbf{q}_n} \left\| \left(\mathbf{Y}_s^T \mathbf{B} \Psi \mathbf{X}_n - (\mathbf{Y}_s^{(n)})^T \right) \mathbf{q}_n \right\|_2 = \lambda_{\max} \quad (4.7)$$

where λ_{\min} and λ_{\max} are the minimum and maximum singular values of $\mathbf{W}^{\frac{1}{2}}(\mathbf{Y}_s^T \mathbf{B} \Psi \mathbf{X}_n - (\mathbf{Y}_s^{(n)})^T)$, respectively.

Briefly, the maximum and minimum singular values of $\mathbf{W}^{\frac{1}{2}}(\mathbf{Y}_s^T \mathbf{B} \Psi \mathbf{X}_n - (\mathbf{Y}_s^{(n)})^T)$ provide, respectively, upper and lower mean square error bounds associated with the subspace spanned by spherical harmonics of order n . The directivity patterns associated with such bounds can be

determined by examining the right-singular vectors obtained in the singular value decomposition, which are the vectors \mathbf{q}_n corresponding to the singular values.

Figures 4.1 and 4.2 show the upper and lower bounds of the normalized RMSE — defined in Eq.(4.8) — computed as described in this section for different spherical arrays and spherical harmonic subspaces. In the same way as in section 3.1.2.1, the following values were used in the simulations: $N_s = 39 \times 20 = 780$, $c = 343m/s$, $\rho = 1.21kg/m^3$, $r_0 = 10a$ and $N = 10$. The five spherical array configurations corresponding to the Platonic solids were simulated. In Fig. 4.1, $\theta_0 = 15.1^\circ$ has been used for the tetrahedron, hexahedron, octahedron, dodecahedron and icosahedron. In Fig. 4.2, $\theta_0 = 54.7^\circ$, 45.0° , 35.2° , 31.7° and 20.9° have been used for the tetrahedron, hexahedron, octahedron, dodecahedron and icosahedron, respectively.

$$\text{Norm. RMSE} = \frac{\left\| \left(\mathbf{Y}_s^T \mathbf{B} \Psi \mathbf{X}_n - (\mathbf{Y}_s^{(n)})^T \right) \mathbf{q}_n \right\|_2}{\left\| (\mathbf{Y}_s^{(n)})^T \mathbf{q}_n \right\|_2} \quad (4.8)$$

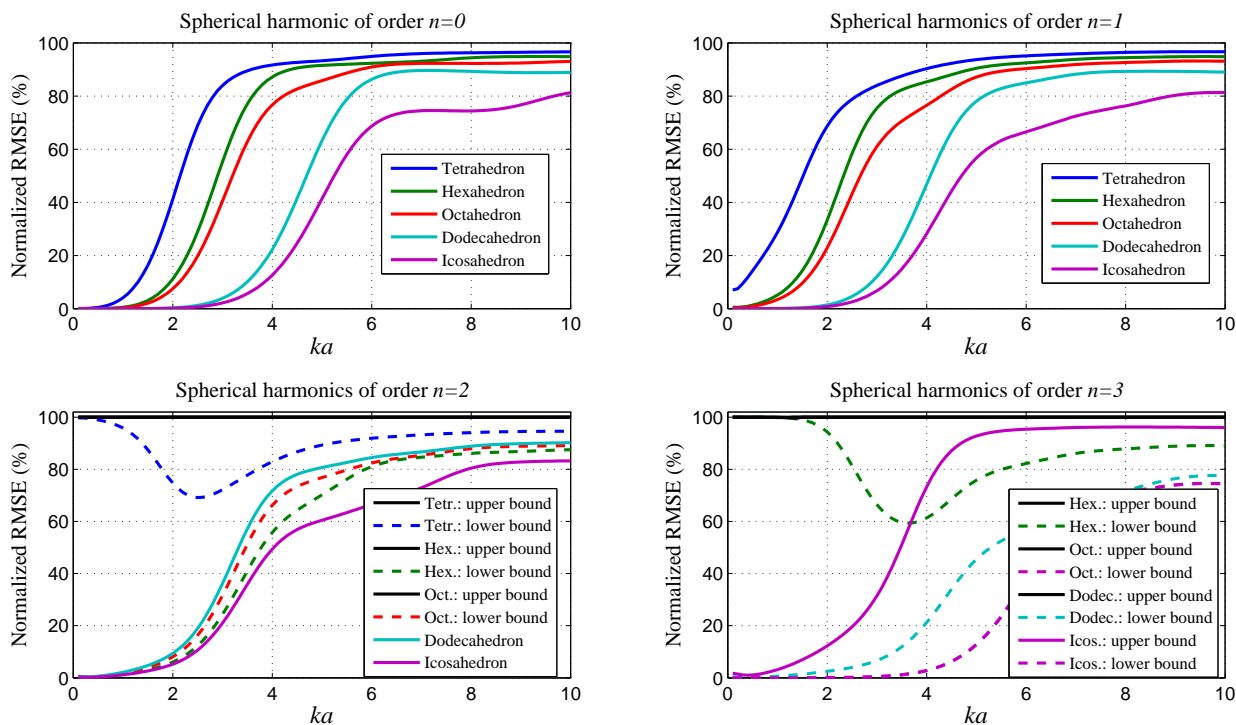


Figure 4.1: Upper and lower bounds of the normalized root mean square error (RMSE) achieved in the synthesis of functions in the subspaces spanned by spherical harmonics of orders 0, 1, 2 and 3. $\theta_0 = 15.1^\circ$ has been used for the tetrahedron, hexahedron, octahedron, dodecahedron and icosahedron.

The ability of a discrete sphere based on a Platonic solid to synthesize any pattern in a sub-

space spanned by spherical harmonics of order n is reduced as ka and n increase, as shown in Figs. 4.1 and 4.2. For each spherical array, only one curve is presented for $n = 0$ and $n = 1$ for the sake of clarity because computations have shown that upper and lower error bounds for each one of these subspaces are not distinguishable — the same is valid for $n = 2$ as far as the dodecahedron and the icosahedron are concerned. This means that a given directivity pattern in these subspaces can be freely rotated without affecting the RMSE. However, for $n = 3$ (and $n = 2$ for the tetrahedron, hexahedron and octahedron), the error is not uniformly distributed over the subspace, so that one has unachievable patterns and well synthesized patterns; both can be determined by examining the right-singular vectors obtained in the singular value decomposition, as said before. Figures 3.9 to 3.13 illustrate functions in the subspace spanned by spherical harmonics of the same order that lead to the lower error bound curves presented in Figs. 4.1 and 4.2.

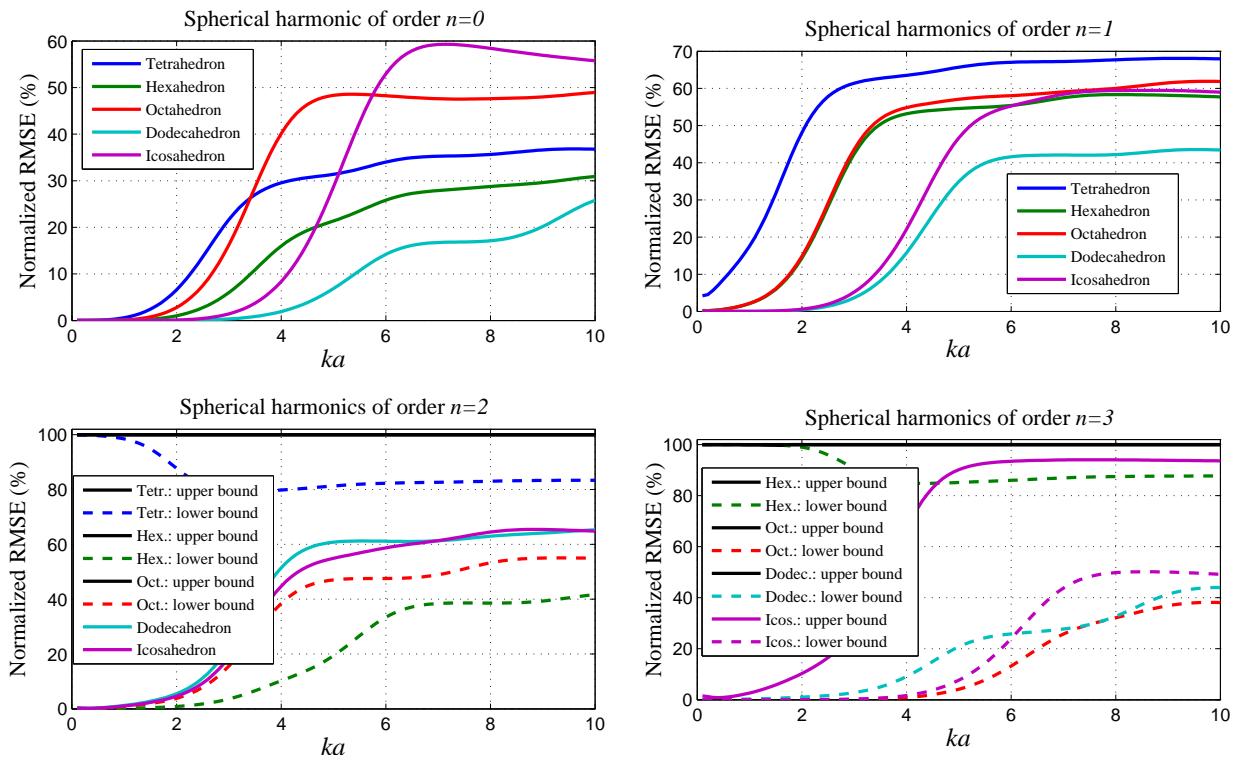


Figure 4.2: Upper and lower bounds of the normalized root mean square error (RMSE) achieved in the synthesis of functions in the subspaces spanned by spherical harmonics of orders 0, 1, 2 and 3. $\theta_0 = 54.7^\circ, 45.0^\circ, 35.2^\circ, 31.7^\circ$ and 20.9° have been used for the tetrahedron, hexahedron, octahedron, dodecahedron and icosahedron, respectively.

As a rule of thumb, it is not possible to synthesize a pure spherical harmonic function of order $n > \sqrt{L} - 1$ due to spatial aliasing, that is, the number of degrees of freedom of the discrete sphere is not large enough to match a high order spherical harmonic. However, high order spherical harmonics may co-exist with low order ones in the radiated field from a discrete sphere. This

phenomenon is also due to spatial aliasing and it takes place as ka increases, leading to synthesis error as shown in Figs. 4.1 and 4.2. Such a behavior can be explained by examining the radiation efficiencies of the spherical harmonic functions, which were presented in Fig. 3.1.

Figure 3.1 shows that the efficiency curves of the radiation groups are well discriminated in the low ka range, so that simple directivity patterns radiate much more efficiently than complex ones. Thus, even if the discrete sphere excites high order spherical harmonics due to spatial aliasing, they will not propagate to the farfield. Therefore, error in spherical harmonic synthesis is small at low ka values provided that r_0 is made sufficiently large. On the other hand, the efficiency curves of the spherical harmonics become closer as ka increases, so that spatial aliasing produces non-evanescent undesirable patterns in the sound field, leading to synthesis error.

In order to reduce the spatial aliasing artifacts that degrade the spherical harmonic synthesis at high frequencies, the sphere radius a can be made smaller. However, the low radiation efficiency at low ka values imposes a constraint on the directivity synthesis in the low frequency range, since high loudspeaker diaphragm displacements must be achieved in order to produce meaningful sound pressure levels. Then, the design of a spherical loudspeaker array for spherical harmonic synthesis must be a compromise between low and high frequency reproduction.

Figure 4.1 suggests that the RMSE decreases with increasing the number of loudspeakers in the array. However, because the same cap aperture angle $\theta_0 = 15.1^\circ$ was used in all spherical arrays, the available radiation surface of each polyhedron was not completely used. In Fig. 4.2, the cap aperture angle for each discrete sphere is chosen so that the available radiation surface is fully used. Therefore, Fig. 4.2 presents a better comparison between spherical arrays than Fig. 4.1.

Inspection of Fig. 4.2 reveals that the dodecahedron-like source leads to the smallest RMSE in the synthesis of functions in the subspaces spanned by spherical harmonics of orders $n = 0$ and $n = 1$. In addition, for $n = 2$, the icosahedron does not present a significant improvement over the dodecahedron. For $n \leq 3$, there are $(3 + 1)^2 = 16$ spherical harmonics, so that the dodecahedron (12 drivers) is not able to provide radiation control up to this order due to the spatial aliasing (although there is at least one pattern in the subspace $n = 3$ that is well synthesized, as indicated by the dodecahedron dashed line in Fig. 4.2). In this case, the icosahedron performs better.

When comparing spherical loudspeaker arrays with a given radius a , the position of the drivers on the sphere, the number of independently driven loudspeakers and the net radiation surface must be taken into account. In section 3.1.2.1, the available fraction of the source surface to mount the drivers for the spherical arrays based on the Platonic solids was presented. Among the Platonic solids, the dodecahedron presents the largest available radiation surface, so that it provides

the highest sound power level for a given velocity amplitude of the spherical caps. In addition, it leads to the smallest RMSE in the synthesis of a spherical harmonic of order $n = 0$. For these reasons, the omnidirectional sound sources are usually built according to the dodecahedron geometry.

Figure 4.2 shows that the ability of the icosahedron to synthesize an arbitrary function in the subspace $n = 3$ is limited to the low ka range. However, the radiation efficiencies of the icosahedron's radiation modes corresponding to the spherical harmonics of order $n = 3$ are very low in the low ka range, as shown in Fig. 3.7. In addition, the icosahedron presents the smallest available radiation surface. Then, the synthesis of functions in the subspace $n = 3$ by an icosahedron-like array is restricted to a narrow frequency range. Moreover, the extra eight channels that must be handled when using an icosahedron rather than a dodecahedron may be critical in real-time applications. Therefore, among the Platonic solids, the discrete sphere approach indicates that the dodecahedron is the best choice for sound directivity control in full 3-D space¹.

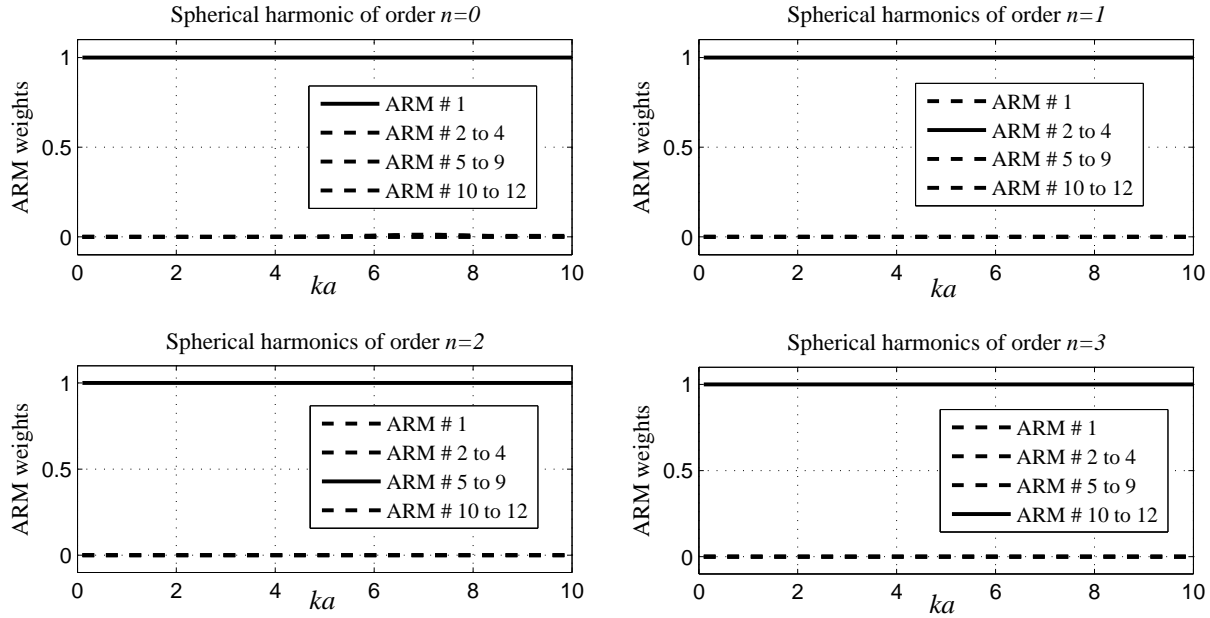


Figure 4.3: Normalized ARM weights for a dodecahedral source with $\theta_0 = 15.1^\circ$. These curves arise from the synthesis of a function in the subspace spanned by spherical harmonics of order n chosen so that it leads to the lowest RMSE.

As stated in Eq.(4.5), the vector containing the optimum weights that must be applied to each acoustic radiation mode of the spherical array is $\mathbf{c}_{opt} = \mathbf{X}_n \mathbf{q}_n$. Now, let the elements of \mathbf{c}_{opt} be grouped according to the radiation efficiencies of the corresponding radiation modes, which are shown in Figs. 3.4 to 3.8. Then, for a dodecahedral source, one has $\mathbf{c}_{opt}^T = [\mathbf{c}_0^T \mathbf{c}_1^T \mathbf{c}_2^T \mathbf{c}_3^T]$,

¹The discrete sphere model better approaches the actual sound field produced by a loudspeaker array as θ_0 is made smaller. Therefore, it is expected that the results presented in Fig.4.1 will be more accurate than the results presented in Fig. 4.2

where $\mathbf{c}_0 \in \mathbb{C}^{1 \times 1}$ is the contribution of the radiation mode # 1, $\mathbf{c}_1 \in \mathbb{C}^{3 \times 1}$ is the contribution of the radiation modes # 2 to 4, $\mathbf{c}_2 \in \mathbb{C}^{5 \times 1}$ is the contribution of the radiation modes # 5 to 9 and $\mathbf{c}_3 \in \mathbb{C}^{3 \times 1}$ is the contribution of the radiation modes # 10 to 12.

The scalar quantity $\sqrt{\mathbf{c}_i^H \mathbf{c}_i (\mathbf{c}_{opt}^H \mathbf{c}_{opt})^{-1}}$: $i = 0, 1, 2, 3$ can be used to evaluate the relative contribution of each radiation group to the synthesized pattern. In Fig. 4.3, these quantities are plotted against ka for a dodecahedral source with $\theta_0 = 15.1^\circ$. Each graph corresponds to a target directivity pattern, which is a function in the subspace spanned by spherical harmonics of order n that leads to the lower error bound shown in Fig. 4.1.

Figure 4.3 shows that only one radiation group is active for a given n , i.e., each radiation group is closely related to the subspace spanned by spherical harmonics of a given order. This result is consistent with the discussion in section 3.1.2.1.

4.3 Synthesis with desired magnitude response

In the previous sections of this chapter, both magnitude and phase of the target directivity pattern were taken into account in the cost function used to obtain optimum weights for the acoustic radiation modes of the spherical array. In addition, phase error and magnitude error were treated equally, which yielded a convex optimization problem that could be solved by a simple weighted least-squares method (refer to Eqs.(4.3) and (4.4)). However, this approach may lead to a sub-optimal solution if the importance of these errors are not equal. As discussed in section 1.3.3, it is expected that a spherical loudspeaker array will be able to better synthesize the perceptually relevant attributes of the sound field if the phase of the target pattern is excluded from the cost function.

It is worth noting that phase cannot be neglected if the target pattern is defined in the nearfield, i.e., r_0 must be made sufficiently large in order to ensure farfield propagation. In order to understand this, consider two nearfield directivity patterns with the same magnitude but with different phase at a given frequency. The two corresponding farfield directivity patterns will differ in magnitude due to the phase difference in the nearfield. Therefore, the phase must not be neglected if r_0 is in the nearfield.

At a given frequency, the directivity phase over the spherical surface defined by $r = r_0$ can be neglected, as discussed above. However, at a given but arbitrary point on this spherical surface, to neglect the phase spectrum may lead to audible phase distortion [81]. Throughout this section,

it will be shown how this problem can be somewhat handled.

The problem of synthesizing a directivity pattern with desired magnitude response has been addressed in the literature [37, 57, 23, 56, 32, 33, 82]. In this work, the cost function proposed in [57] is used, so that the optimization problem can be formulated as

$$\min_{\mathbf{c}} \left\| \left| \mathbf{Y}_s^T \mathbf{B} \Psi \mathbf{c} \right| - |\mathbf{p}_t| \right\|_2 \quad (4.9)$$

Unlike the problem stated in (4.3), this is a non-convex minimization problem called magnitude least-squares, which is studied in depth in [56]. This unconstrained minimization problem is equivalent to the following constrained one [57, 56]

$$\begin{aligned} & \underset{\mathbf{c}, \hat{\mathbf{p}}_t}{\text{minimize}} && \left\| \mathbf{Y}_s^T \mathbf{B} \Psi \mathbf{c} - \mathbf{P}_t \hat{\mathbf{p}}_t \right\|_2 \\ & \text{subject to} && (\text{diag}(\hat{\mathbf{p}}_t))^H \text{diag}(\hat{\mathbf{p}}_t) = \mathbf{I} \end{aligned} \quad (4.10)$$

where $\mathbf{P}_t = \text{diag}(|\mathbf{p}_t|)$ and $\hat{\mathbf{p}}_t \in \mathbb{C}^{N_s}$. The constraint ensures that $\hat{\mathbf{p}}_t$ provides only phase information.

Since phase is not concerned in (4.9), it makes intuitive sense using the phase of the target pattern as an optimization variable. Then, an optimum phase for the target pattern is searched in (4.10) so that the resulting target is now easier to synthesize in the traditional least-squares sense than the original target. A mathematical proof of the equivalence of (4.9) and (4.10) can be found in [56], as well as several different methods of solving it. However, a comparison between optimization with and without phase for radiation pattern synthesis has not been provided in the literature so far. Here, this task is accomplished by using a slightly modified version of the iterative variable exchange method for finding a local minimizer described in [56], which is presented below.

Problem (4.10) is not convex in the optimization variables \mathbf{c} and $\hat{\mathbf{p}}_t$. However, for fixed $\hat{\mathbf{p}}_t$, it is convex in \mathbf{c} and the solution is given in Eq.(4.4) by replacing \mathbf{p}_t with $\mathbf{P}_t \hat{\mathbf{p}}_t$. On the other hand, for fixed \mathbf{c} , the optimum $\hat{\mathbf{p}}_t$ is $e^{\angle \arg(\mathbf{Y}_s^T \mathbf{B} \Psi \mathbf{c})}$. This suggests a method to solve (4.10) in which $\hat{\mathbf{p}}_t$ is iteratively updated according to $\hat{\mathbf{p}}_t = e^{\angle \arg(\mathbf{Y}_s^T \mathbf{B} \Psi \mathbf{c})}$. The algorithm is summarized in Tab. 4.1.

This iterative method does not ensure optimality of the solution, but an example will be presented later in this chapter indicating that it performs better than the standard least-squares and provides good results as far as the directivity control by a compact spherical loudspeaker array is concerned. Its main advantage over the other methods proposed in [56] is that it is simple and easy to implement.

Table 4.1: Iterative variable exchange procedure to solve the magnitude least-squares problem.

<p>1) Choose convergence criteria ϵ</p> <p>2) Let $\hat{\mathbf{p}}_t^{(0)} = e^{\iota \arg(\mathbf{p}_t)}$</p> <p>3) Let $\mathbf{c} = \left((\mathbf{Y}_s^T \mathbf{B} \Psi)^H \mathbf{W} (\mathbf{Y}_s^T \mathbf{B} \Psi) \right)^{-1} (\mathbf{Y}_s^T \mathbf{B} \Psi)^H \mathbf{W} \mathbf{p}_t$</p> <p>4) Let $\hat{\mathbf{p}}_t^{(1)} = e^{\iota \arg(\mathbf{Y}_s^T \mathbf{B} \Psi \mathbf{c})}$</p> <p>5) Repeat while $\frac{\ \hat{\mathbf{p}}_t^{(1)} - \hat{\mathbf{p}}_t^{(0)}\ _2}{\ \hat{\mathbf{p}}_t^{(1)}\ _2} > \epsilon$</p> <p style="padding-left: 2em;">$\hat{\mathbf{p}}_t^{(0)} = \hat{\mathbf{p}}_t^{(1)}$</p> <p style="padding-left: 2em;">$\mathbf{c} = \left((\mathbf{Y}_s^T \mathbf{B} \Psi)^H \mathbf{W} (\mathbf{Y}_s^T \mathbf{B} \Psi) \right)^{-1} (\mathbf{Y}_s^T \mathbf{B} \Psi)^H \mathbf{W} \mathbf{p}_t \hat{\mathbf{p}}_t^{(1)}$</p> <p style="padding-left: 2em;">$\hat{\mathbf{p}}_t^{(1)} = e^{\iota \arg(\mathbf{Y}_s^T \mathbf{B} \Psi \mathbf{c})}$</p> <p>6) Optimal solution: $\mathbf{c}_{opt} = \mathbf{c}$ and $\hat{\mathbf{p}}_t^{(opt)} = \hat{\mathbf{p}}_t^{(1)}$</p>

The procedure described in Tab. 4.1 must be run for each ka value. Because the optimal results obtained for each ka value are not connected to each other, the phase spectrum of the synthesized sound pressure at a given but arbitrary point is expected to differ from the phase spectrum of the target sound pressure at this same point, which may give rise to audible phase distortion, as said before. Notice that if the phase of all elements of $\hat{\mathbf{p}}_t^{(opt)}$ are equally changed, the magnitude RMSE will remain unchanged and the phase of \mathbf{c}_{opt} will be changed by the same amount. Therefore, for each ka value, $\hat{\mathbf{p}}_t^{(opt)}$ and \mathbf{c}_{opt} can be redefined by multiplying them by an unit-modulus complex number so that the phase spectrum of the synthesized sound pressure at a chosen point will be exactly the same as the phase spectrum of the target sound pressure at the chosen point. Then, no phase distortion will take place at this point, which can be made to correspond to the main radiation direction (maximum sound pressure magnitude) of the target directivity pattern in a frequency range of interest.

In order to illustrate the ideas presented here and to compare the optimal solutions of the magnitude least-squares problem with the standard weighted least-squares problem, the directivity synthesis by a dodecahedral loudspeaker array with $\theta_0 = 15.1^\circ$ is considered. In the same way as in section 4.2, the following values were used in the simulations: $N_s = 39 \times 20 = 780$, $c = 343m/s$, $\rho = 1.21kg/m^3$ and $N = 10$. However, it was used $r_0 = 20a$ instead of $r_0 = 10a$ in order to ensure farfield propagation. The directivity of a single spherical cap mounted on a sphere was used as target pattern. The Euler angles used to define the position of this spherical cap on the sphere were $(0^\circ, 37.38^\circ, 0^\circ)$. Then, inspection of Tab. C.2 reveals that this position does not match any of the spherical caps of the dodecahedral source.

Figure 4.4 shows the normalized magnitude RMSE defined in Eq.(4.11), where \mathbf{c}_{opt} was obtained in the magnitude least-squares sense (phase not concerned) and in the standard weighted

least-squares sense (phase concerned). The target pattern and the synthesized patterns obtained by both methods for $ka = 2$, $ka = 3$ and $ka = 5$ are shown in Figs. 4.5 to 4.7, respectively.

$$\text{Norm. magnitude RMSE} = \frac{\| |\mathbf{Y}_s^T \mathbf{B} \Psi \mathbf{c}_{opt}| - |\mathbf{p}_t| \|_2}{\| |\mathbf{p}_t| \|_2} \quad (4.11)$$

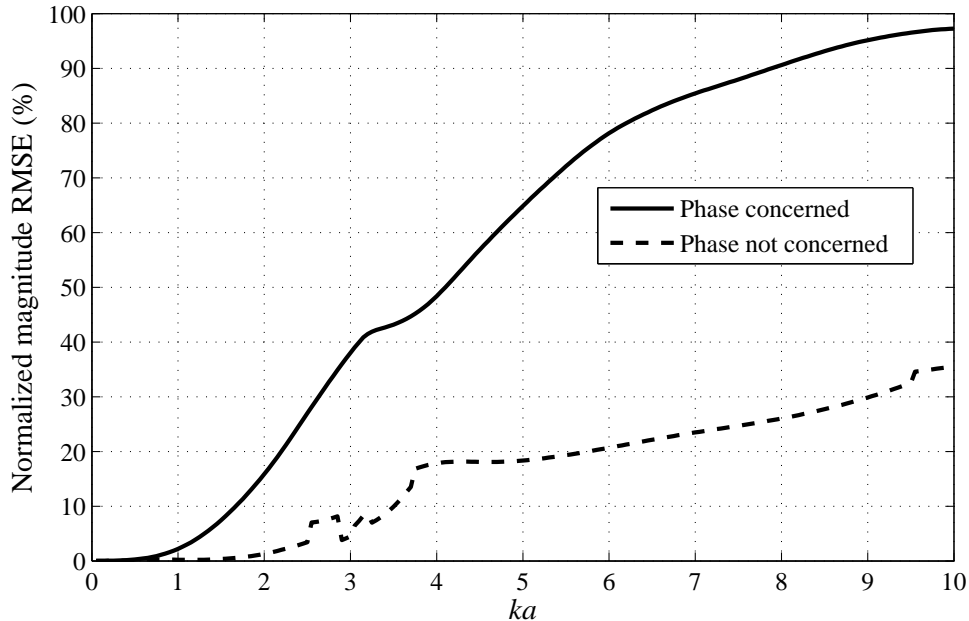


Figure 4.4: Synthesis of the farfield directivity of a spherical cap oriented according to the Euler angles $(0^0, 37.38^0, 0^0)$ by a dodecahedral source with $\theta_0 = 15.1^0$. Comparison between the normalized magnitude RMSE obtained by solving the standard weighted least-squares problem (phase concerned) and the magnitude least-squares problem (phase not concerned).

Figure 4.4 shows that the magnitude error can be drastically reduced if a cost function that does not take into account the phase error is used. Inspection of Figs. 4.5 and 4.6 reveals that magnitude synthesis is improved to the detriment of phase synthesis, as expected.

The standard least-squares gives rise to very low power radiation patterns for high ka values, as illustrated in Fig. 4.7. This can be clearly shown by comparing the optimum weights \mathbf{c}_{opt} obtained by the standard and the magnitude least-squares. Figure 4.8 shows the usual norm, $\sqrt{\mathbf{x}^H \mathbf{x}}$, of these vectors and the vector difference between them. The directivity patterns corresponding to the vector difference for $ka = 2, 3$ and 5 are shown in Fig. 4.9.

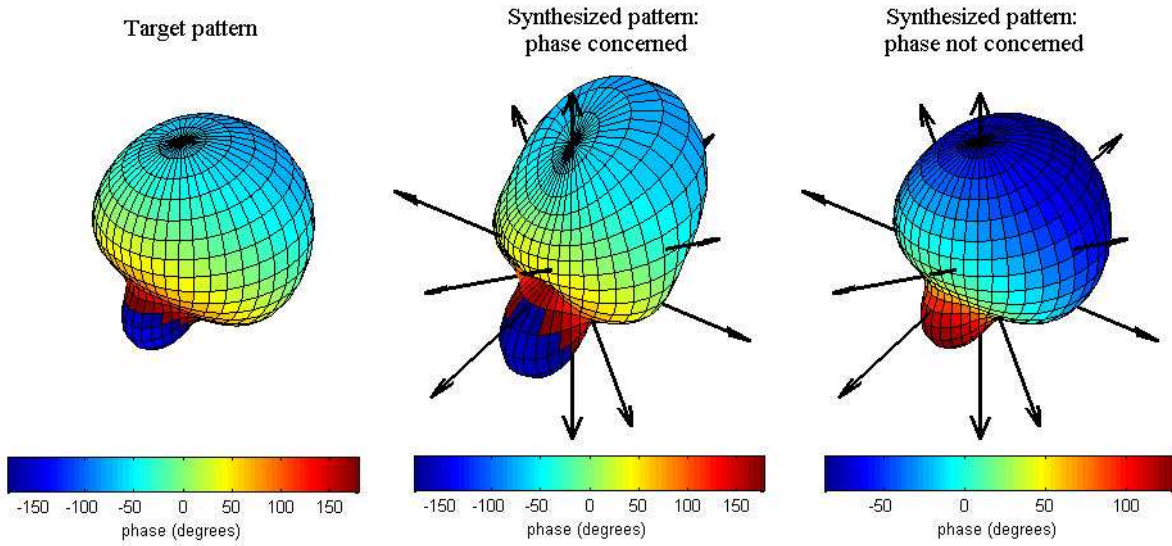


Figure 4.5: Synthesis of the farfield directivity of a spherical cap oriented according to the Euler angles $(0^0, 37.38^0, 0^0)$ by a dodecahedral source with $\theta_0 = 15.1^0$. Comparison between the target directivity pattern and the synthesized patterns obtained by solving the standard weighted least-squares problem (phase concerned) and the magnitude least-squares problem (phase not concerned) for $ka = 2$.

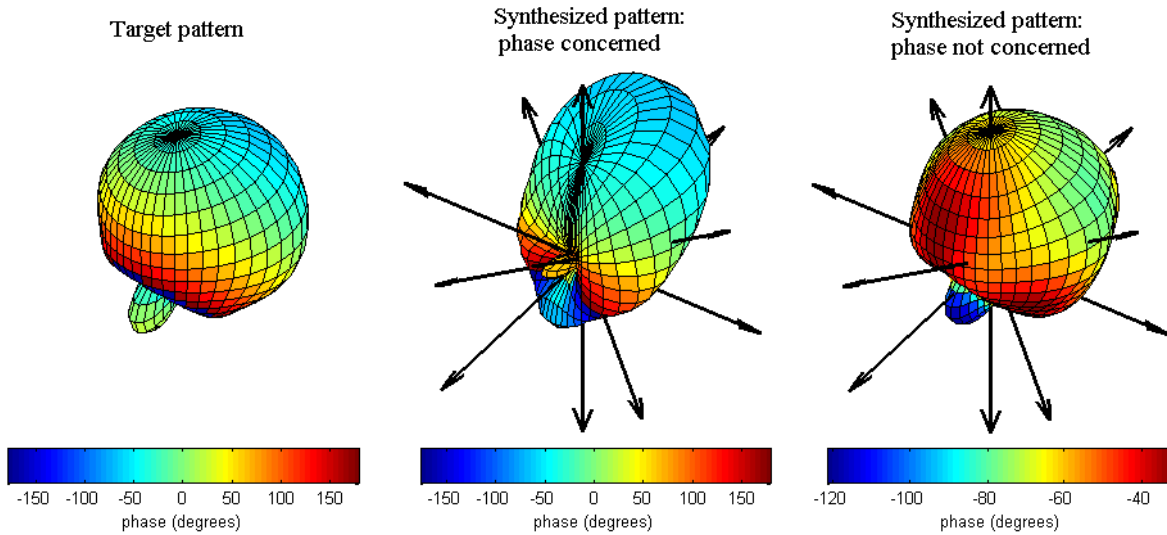


Figure 4.6: Synthesis of the farfield directivity of a spherical cap oriented according to the Euler angles $(0^0, 37.38^0, 0^0)$ by a dodecahedral source with $\theta_0 = 15.1^0$. Comparison between the target directivity pattern and the synthesized patterns obtained by solving the standard weighted least-squares problem (phase concerned) and the magnitude least-squares problem (phase not concerned) for $ka = 3$.

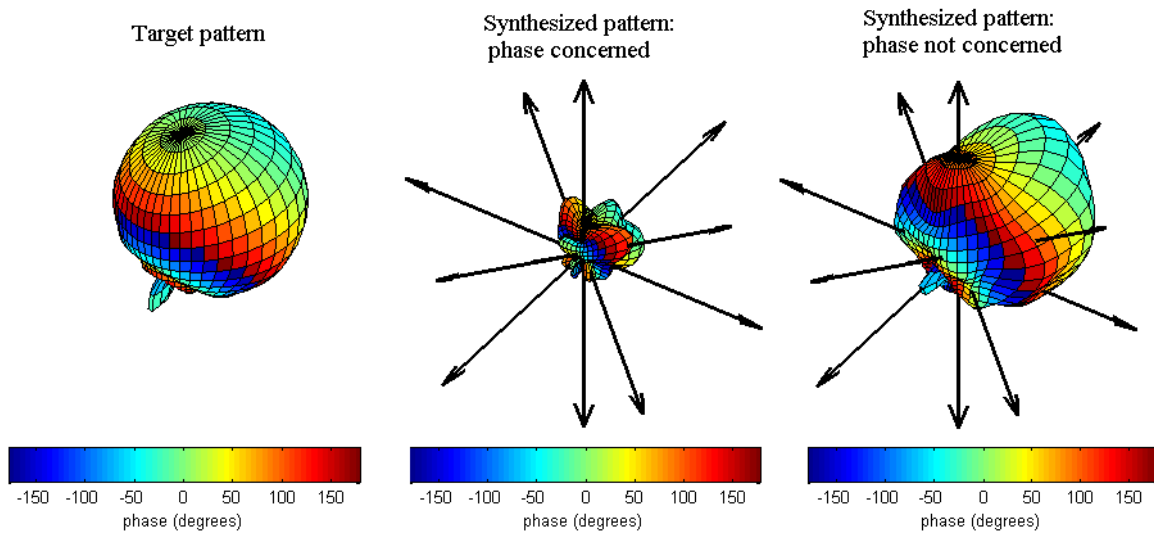


Figure 4.7: Synthesis of the farfield directivity of a spherical cap oriented according to the Euler angles $(0^0, 37.38^0, 0^0)$ by a dodecahedral source with $\theta_0 = 15.1^0$. Comparison between the target directivity pattern and the synthesized patterns obtained by solving the standard weighted least-squares problem (phase concerned) and the magnitude least-squares problem (phase not concerned) for $ka = 5$.

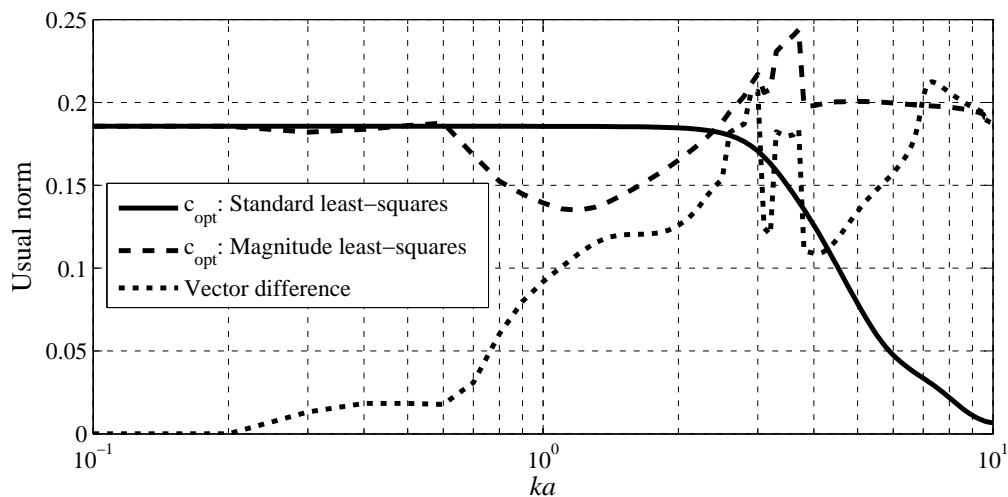


Figure 4.8: Synthesis of the farfield directivity of a spherical cap oriented according to the Euler angles $(0^0, 37.38^0, 0^0)$ by a dodecahedral source with $\theta_0 = 15.1^0$. Usual norm of \mathbf{c}_{opt} obtained by the standard and the magnitude least-squares, and of the vector difference between them.

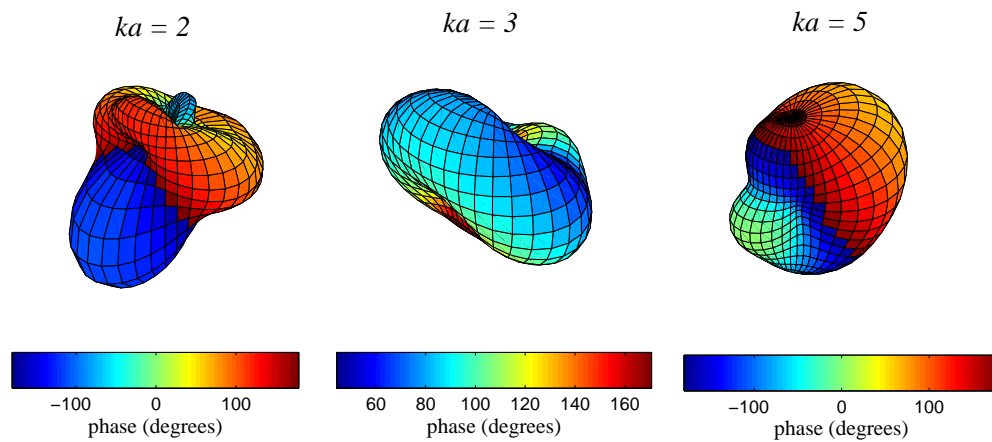


Figure 4.9: Synthesis of the farfield directivity of a spherical cap oriented according to the Euler angles $(0^0, 37.38^0, 0^0)$ by a dodecahedral source with $\theta_0 = 15.1^0$. Directivity patterns corresponding to the vector difference between the optimum weights \mathbf{c}_{opt} obtained by the standard and the magnitude least-squares.

Chapter 5

Equalization Filtering

In this chapter, the diffusion of a mono audio signal through a compact spherical loudspeaker array is considered. The mono signal provides the temporal attributes of the sound field produced by the spherical array, whereas its spatial characteristics are controlled by adjusting the gains associated to the multiple channels of the electroacoustic device, each one of them corresponding to an acoustic radiation mode of the spherical array.

First, the electroacoustical model of a spherical loudspeaker array presented in chapter 3 is revisited in order to derive a useful relation between the acoustic radiation modes of a discrete sphere and the electromechanical behavior of a hollow spherical loudspeaker array. Next, the signal processing chain to diffuse a mono signal through a hollow spherical array is presented. Since both the electromechanical response of the transducers and the radiation efficiency of the loudspeaker array depend on frequency, the system must be provided with a set of equalization filters in order to produce a flat frequency response. Two equalization approaches are presented and compared. In the first one, sound pressure equalization in a given radiation direction is provided. In the second approach, sound power equalization is provided. Finally, a numerical example is presented.

5.1 The electroacoustical modeling of spherical loudspeaker arrays revisited

The electromechanical modeling of a compact loudspeaker array was considered in section 3.2. It has been shown that the clamped electromagnetic force acting on a driver's membrane can be

related to the membrane velocity of the transducers according to Eq.(3.31). Assuming that all drivers of the array present the same electromechanical features and using the lumped-parameter model proposed in section 3.2.2.1 for drivers sharing a common cabinet, this equation simplifies to

$$\frac{Z^{(e)}(\omega)}{Bl_e} \left[\hat{g}(\omega) \mathbf{I} - \frac{\rho c^2}{i\omega V_b} \hat{S}^2 \mathbf{1} \right] \mathbf{u} = \mathbf{v} \quad (5.1)$$

where $\hat{g}(\omega) \equiv -i\omega M + R - (i\omega C)^{-1} + [Z^{(e)}(\omega)]^{-1} (Bl_e)^2 + Z^+(\omega) \hat{S}^2$, $\mathbf{1}$ is an $L \times L$ matrix of all 1's and \mathbf{v} is an $L \times 1$ vector containing the complex amplitude of the voltages that feed the transducers. By defining the functions $g(\omega) \equiv Z^{(e)}(\omega)(Bl_e)^{-1}\hat{g}(\omega)$ and $f(\omega) \equiv -Z^{(e)}(\omega)\rho c^2 \hat{S}^2 (i\omega V_b Bl_e)^{-1}$, Eq.(5.1) can be rewritten as

$$\mathbf{T}(\omega) \mathbf{u} = \mathbf{v} \quad (5.2)$$

where $\mathbf{T}(\omega) \equiv g(\omega)\mathbf{I} + f(\omega)\mathbf{1}$.

Now, let μ_l and ζ_l be, respectively, the l -th eigenvalue and eigenvector of \mathbf{T} , so that

$$\mathbf{T}(\omega) \zeta_l = \mu_l(\omega) \zeta_l \quad (5.3)$$

Substitution of the definition of \mathbf{T} into Eq.(5.3) yields

$$\mathbf{1} \zeta_l = \left[\frac{\mu_l(\omega) - g(\omega)}{f(\omega)} \right] \zeta_l \quad (5.4)$$

Inspection of Eq.(5.4) reveals that the term in brackets on the right side is the l -th eigenvalue of $\mathbf{1}$. In addition, comparison of Eqs.(5.3) and (5.4) shows that \mathbf{T} and $\mathbf{1}$ both possess the same set of eigenvectors $\zeta_1, \zeta_2, \dots, \zeta_L$. Because $\mathbf{1}$ is a constant matrix, its eigenvalues and eigenvectors are constant too, i.e., ζ_l and $[\mu_l(\omega) - g(\omega)][f(\omega)]^{-1}$ do not depend on frequency. The i -th row of Eq.(5.4) leads to

$$\frac{\mu_l(\omega) - g(\omega)}{f(\omega)} = \frac{\sum_{j=1}^L \zeta_{jl}}{\zeta_{il}} \quad (5.5)$$

where ζ_{jl} is the j -th element of the l -th eigenvector of \mathbf{T} .

Since the left side of Eq.(5.5) does not depend either on i or on j , admissible ζ_l must satisfy

one of the following conditions:

- $\zeta_{1l} = \zeta_{2l} = \dots = \zeta_{Ll}$;
- $\sum_{j=1}^L \zeta_{jl} = 0$.

Substitution of these expressions in Eq.(5.5) yields the eigenvalues of $\mathbf{1}$, namely,

$$\frac{\mu_l(\omega) - g(\omega)}{f(\omega)} = \begin{cases} L & \text{multiplicity } 1 \\ 0 & \text{multiplicity } L - 1 \end{cases} \quad (5.6)$$

Finally, the eigenvalues of \mathbf{T} are

$$\mu_l(\omega) = \begin{cases} Lf(\omega) + g(\omega) & \text{if } \zeta_{1l} = \zeta_{2l} = \dots = \zeta_{Ll} \\ g(\omega) & \text{if } \sum_{j=1}^L \zeta_{jl} = 0 \end{cases} \quad (5.7)$$

It is worth noting that \mathbf{T} describes the electromechanical behavior of any compact loudspeaker array regardless of its overall shape, provided that the drivers present the same electromechanical features and share a common cabinet.

A comparison between ζ_l and the acoustic radiation modes of the Platonic solids (refer to Tabs. C.3 to C.7) reveals that the latter, like the former, are eigenvectors of \mathbf{T} . Because neither the internal acoustic coupling between drivers nor their electromechanical characteristics are taken into account in deriving the radiation modes, this result can be explained by the highly symmetrical shape of the Platonic solids. The fact that the eigenvectors of $\mathbf{V}^{-1}\mathbf{C}$ (refer to Eq.(2.41)) are eigenvectors of \mathbf{T} greatly simplifies the design and implementation of equalization filters for a spherical loudspeaker array with internal acoustic coupling, as it will be shown in section 5.2.

5.2 Signal processing chain of a spherical loudspeaker array

Let $s_c(t)$ be the continuous-time audio signal one wants to diffuse through a spherical loudspeaker array with a directivity corresponding to an acoustic radiation mode of the array, i.e., $\mathbf{u}(\omega) = \mathbf{u}_l(\omega) = \boldsymbol{\psi}_l \bar{s}_c(\omega)$, where $\bar{s}_c(\omega)$ is the Fourier transform of $s_c(t)$. Assuming that the transducers share a common hollow cabinet and that the spherical array presents a Platonic solid shape, $\boldsymbol{\psi}_l$ is an eigenvector of \mathbf{T} , so that Eqs.(5.2) and (5.3) lead to

$$\mathbf{v}_l(\omega) = \mu_l(\omega)\boldsymbol{\psi}_l\bar{s}_c(\omega) \quad (5.8)$$

Equation (5.8) gives the voltages that must be fed to the array's transducers so that the surface vibration pattern corresponds to the l -th radiation mode. In addition, the caps' velocities present the same temporal characteristics as $s_c(t)$. A block diagram is shown in Fig. 5.1, where Ψ_{il} are the entries of the modal matrix, i.e., Ψ_{il} is the i -th element of the l -th radiation mode. It is worth noting that each element of the matrix $\boldsymbol{\Psi}$ is a real number.

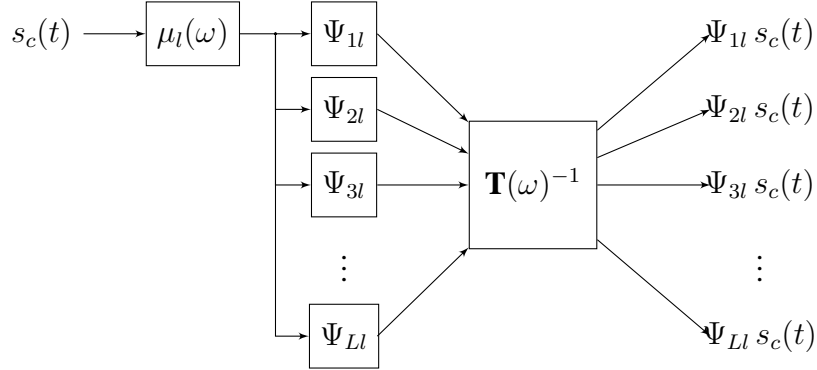


Figure 5.1: Block diagram representing the synthesis of the l -th acoustic radiation mode of a L -driver loudspeaker array.

Multiplication of the input signal by a set of L real numbers contained in $\boldsymbol{\psi}_l$ gives rise to the l -th radiation mode, as said before. The SISO (Single Input Single Output) system $\mu_l(\omega)$ plays the role of an equalization filter, which compensates for the non-flat frequency response of the electromechanical transducer. However, since radiation efficiency is highly dependent on frequency, additional equalization must be provided in order to take this into account. Let $\bar{e}_l(\omega)$ be a filter that comepasates both the electromechanical transducer response and the mechano-acoustical source response. Thus, for a complete equalized system, the voltages that must feed the drivers are given by

$$\mathbf{v}_l(\omega) = \bar{e}_l(\omega)\boldsymbol{\psi}_l\bar{s}_c(\omega) \quad (5.9)$$

In section 3.1.2, it has been shown that the sound pressure field produced by a spherical array is $p = \mathbf{u}^T \mathbf{B}^T \mathbf{Y}$ (refer to Eq.(3.16)). Hence, Eqs.(5.2) and (5.9) yield the sound pressure (after equalization) when the vibration pattern of the spherical array corresponds to its l -th radiation mode, namely,

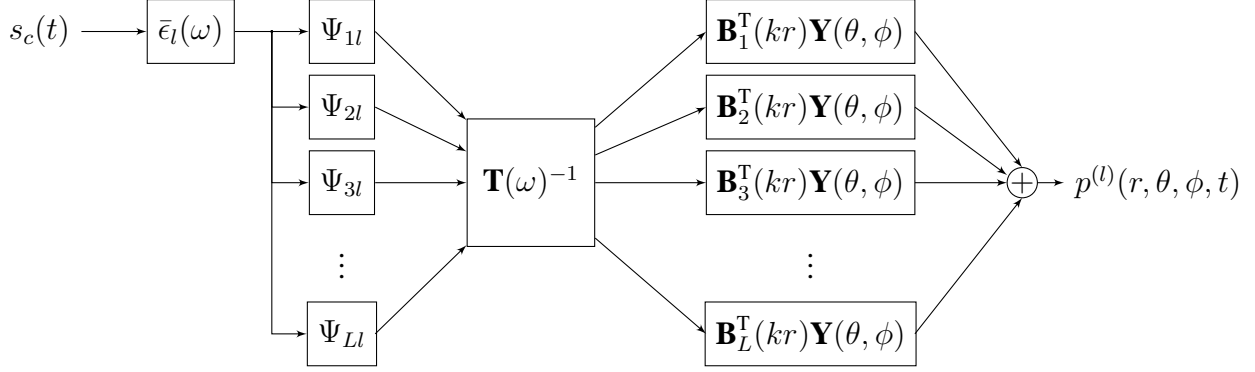


Figure 5.2: Block diagram representing the sound pressure field produced by the l -th acoustic radiation mode of a L -driver loudspeaker array after equalization.

$$\bar{p}^{(l)}(r, \theta, \phi, \omega) = \mathbf{Y}^T(\theta, \phi) \mathbf{B}(kr) \mathbf{T}(\omega)^{-1} \boldsymbol{\psi}_l \bar{\epsilon}_l(\omega) \bar{s}_c(\omega) \quad (5.10)$$

Figure 5.2 shows a block diagram, where \mathbf{B}_i is the i -th column of \mathbf{B} and the total system output is the sound pressure evaluated at (r, θ, ϕ) . The MIMO (Multiple Inputs Multiple Outputs) system $\mathbf{T}(\omega)^{-1}$ and the SISO systems $\mathbf{B}_i^T(kr)\mathbf{Y}(\theta, \phi)$ correspond to the physical system, namely, the transduction process and the sound radiation, respectively, whereas the SISO systems $\bar{\epsilon}_l(\omega)$ and Ψ_{il} must be implemented.

The systems $\bar{\epsilon}_l(\omega)$ and Ψ_{il} can be implemented on a DSP (Digital Signal Processing) chip or on a general-purpose computer¹. In both cases, a discrete-time representation of these systems must be derived. Because the entries of $\boldsymbol{\Psi}$ are real-valued constants, they can be easily dealt with. On the other hand, the digital realization of the filter $\bar{\epsilon}_l(\omega)$ is not so simple and it is considered below.

Let $\tilde{\epsilon}_l(t)$ be the impulse response of the continuous-time equalization filter — which is assumed to be an LTI (Linear Time-Invariant) system (refer to appendix D) — and $\epsilon_l[m]$ contain samples of $\tilde{\epsilon}_l(t)$ so that

$$\epsilon_l[m] = \tilde{\epsilon}_l(mT_s), \quad -\infty < m < \infty \quad (5.11)$$

where m is an integer and T_s is the sampling period. Hence, $\epsilon_l[m]$ is a discrete-time representation of $\tilde{\epsilon}_l(t)$. The inequality $|\omega T_s| < \pi$ must be satisfied in order not to produce aliasing distortion [8].

It is known that an LTI system whose frequency response can be written as a ratio of polyno-

¹The free software PD (Pure Data) can be mentioned as an example of a real-time environment for digital audio processing [83].

mials in $e^{i\omega T_s}$ satisfies a constant-coefficient difference equation (refer to appendix D), i.e., if

$$\bar{\epsilon}_l(\omega) = \frac{\sum_{j=0}^B b_j e^{i\omega j T_s}}{\sum_{j=0}^D d_j e^{i\omega j T_s}} \quad (5.12)$$

then,

$$\sum_{j=0}^D d_j y[m-j] = \sum_{j=0}^B b_j s[m-j] \quad (5.13)$$

where $s[m]$ contains samples of the input $s_c(t)$, $y[m] = \sum_{j=-\infty}^{\infty} s[j] \epsilon_l[m-j]$ contains samples of the output signal and b_j and d_j are constants. If $d_j = 0$ for $j \neq 0$, one has a so-called finite-duration impulse response (FIR) system; otherwise, one has an infinite-duration impulse response (IIR) system.

Inspection of Eq. (5.13) reveals that the system can be represented by structures consisting of an interconnection of the basic operations of addition, multiplication by a constant and delay. Hence, if the equalizer frequency response can be approximated by Eq.(5.12) with a relative small number of coefficients, the equalization filtering can be efficiently implemented in real-time with no need to explicitly evaluate the convolution sum or Fourier transforms.

In the following, two equalization schemes are presented to obtain $\bar{\epsilon}_l(\omega)$. The first one is based on the sound pressure response in a given radiation direction, and the second one is based on the sound power radiated by the spherical array. Then, for the reasons discussed above, $\bar{\epsilon}_l(\omega)$ is approximated by a rational polynomial function in $e^{i\omega T_s}$.

5.2.1 Sound pressure equalization

The sound pressure field produced by a spherical array when the driver tensions are weighted according to ψ_l and filtered by $\bar{\epsilon}_l(\omega)$ is given in Eq.(5.10).

Now, let $(\hat{r}, \hat{\theta}, \hat{\phi})$ be a given point in the acoustic domain and $H_l(\omega)$ be a frequency response function defined as

$$\begin{aligned} H_l(\omega) &\equiv \mathbf{Y}^T(\hat{\theta}, \hat{\phi}) \mathbf{B}(k\hat{r}) \mathbf{T}(\omega)^{-1} \psi_l \\ &= \mathbf{Y}^T(\hat{\theta}, \hat{\phi}) \mathbf{B}(k\hat{r}) \frac{1}{\mu_l(\omega)} \psi_l \end{aligned} \quad (5.14)$$

This is an LTI physical system. In addition, it is stable and causal. Assuming that $H_l(\omega)$

can be written as a rational function as shown in Eq.(5.12), it can be expressed as the product of a minimum-phase system and an all-pass system (refer to appendix D), so that

$$H_l(\omega) = H_l^{(min)}(\omega) H_l^{(ap)}(\omega) \quad (5.15)$$

where $H_l^{(min)}(\omega)$ is a minimum-phase system and $H_l^{(ap)}(\omega)$ is an all-pass system.

Comparison of Eqs.(5.10) and (5.14) shows that sound pressure equalization in the direction $(\hat{\theta}, \hat{\phi})$ could be achieved by letting $\bar{\epsilon}_l(\omega) = H_l(\omega)^{-1}$. However, this leads to a non-realizable equalizer since the inverse of $H_l^{(ap)}(\omega)$ is noncausal. Fortunately, for the problem considered in this work, it will be seen that $H_l^{(ap)}(\omega)$ is approximately a pure delay system, so that it does not provide phase distortion. Thus, a system with linear phase and no pressure magnitude distortion in the direction $(\hat{\theta}, \hat{\phi})$ can be obtained by letting

$$\epsilon_l(\omega) = \frac{1}{H_l^{(min)}(\omega)} \quad (5.16)$$

Since $\epsilon_l(\omega)$ is a minimum-phase system, the coefficients in Eq.(5.12) can be obtained by using a filter design method which approximates a given but arbitrary magnitude response.

5.2.2 Sound power equalization

The equalization scheme described in the previous section is limited to a given radiation direction. This can be dealt with by equalizing the sound power radiated by the array instead of the sound pressure in a given radiation direction.

Considering Fig. 5.2, the diaphragm velocities corresponding to the l -th ARM can be seen to be

$$\mathbf{u}(\omega) = \mathbf{T}(\omega)^{-1} \boldsymbol{\psi}_l \bar{\epsilon}_l(\omega) \bar{s}_c(\omega) = \boldsymbol{\psi}_l \frac{\bar{\epsilon}_l(\omega)}{\mu_l(\omega)} \bar{s}_c(\omega) \quad (5.17)$$

If the L transducers of the spherical array have the same diaphragm area, which are modeled as spherical caps, one has

$$S = 2\pi a^2 (1 - \cos \theta_0) L \quad (5.18)$$

If the acoustic radiation modes are normalized so that $\boldsymbol{\psi}_l^T \boldsymbol{\psi}_l = 2L$, substitution of Eq.(5.17) into (3.22) yields

$$\langle |v(a, \theta, \phi)|^2 \rangle = \frac{|\bar{\epsilon}_l(\omega)|^2}{|\mu_l(\omega)|^2} |\bar{s}_c(\omega)|^2 \quad (5.19)$$

Since $\sigma(\mathbf{u}) = \sigma(\boldsymbol{\psi}_l) = \sigma_l(\omega)$, substitution of Eqs.(5.18) and (5.19) into (2.36) leads to

$$W_l = \sigma_l(\omega) \rho c 2\pi a^2 (1 - \cos \theta_0) L \frac{|\bar{\epsilon}_l(\omega)|^2}{|\mu_l(\omega)|^2} |\bar{s}_c(\omega)|^2 \quad (5.20)$$

Finally, for a unitary gain, the magnitude response of the equalizer must be

$$|\bar{\epsilon}_l(\omega)| = \frac{|\mu_l(\omega)|}{\sqrt{\sigma_l(\omega) \rho c 2\pi a^2 (1 - \cos \theta_0) L}} \quad (5.21)$$

Since only magnitude response is concerned in Eq.(5.21), the coefficients in Eq.(5.12) can be obtained by using a filter design method which approximates a given but arbitrary magnitude response.

5.3 Numerical example: a dodecahedral loudspeaker array

In order to illustrate and to discuss the ideas presented in the previous sections, equalization filters for a hollow spherical array with $L = 12$ identical transducers are studied here.

As in section 3.3, the spherical caps (transducer diaphragm) are distributed on a sphere with radius $a = 0.075m$ according to the dodecahedron symmetry. The aperture angle of the caps under consideration is $\theta_0 = 15.1^\circ$ and the medium properties are assumed to be $c = 343m/s$ and $\rho = 1.21kg/m^3$. All transducers are supposed to be equal with the characteristics presented in the row “mean value” of Tab. 6.1.

Figure 5.3 shows the eigenvalues of $\mathbf{T}(\omega)$ given in Eq.(5.7), that is, the filters $\mu_l(\omega)$, $l = 1, 2, \dots, 12$, that compensates for the non-flat frequency response of the electromechanical transducers. For a dodecahedral source, the associated eigenvectors are the acoustic radiation modes, as discussed in section 5.1. In fact, Fig. 5.3 and the solid lines of Fig. 3.14 provide the same

information. Thus, for a discussion on the results presented in Fig. 5.3, the reader is referred to section 3.3.

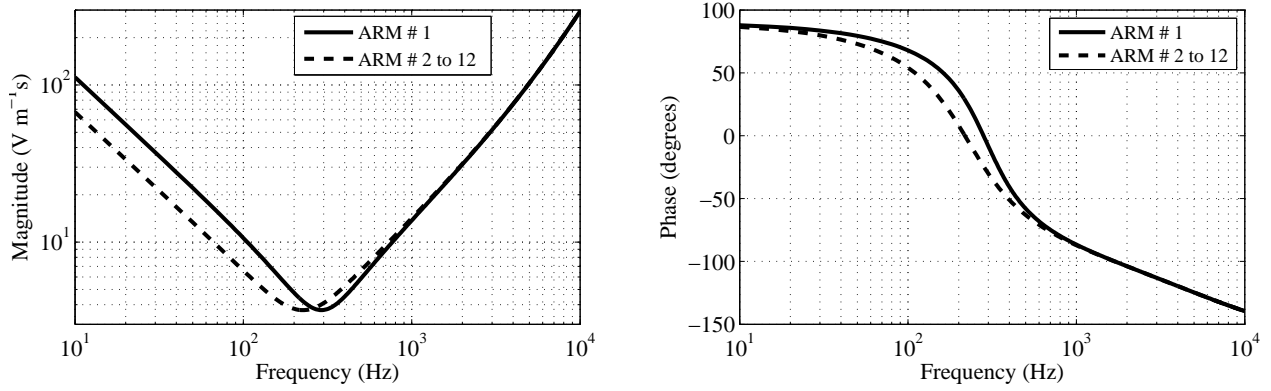


Figure 5.3: Filter $\mu_l(\omega)$, $l = 1, 2, \dots, 12$, that compensates for the non-flat frequency response of the electromechanical transducers of a hollow loudspeaker array with 12 identical drivers. The transducer features are given in the row “mean value” of Tab. 6.1.

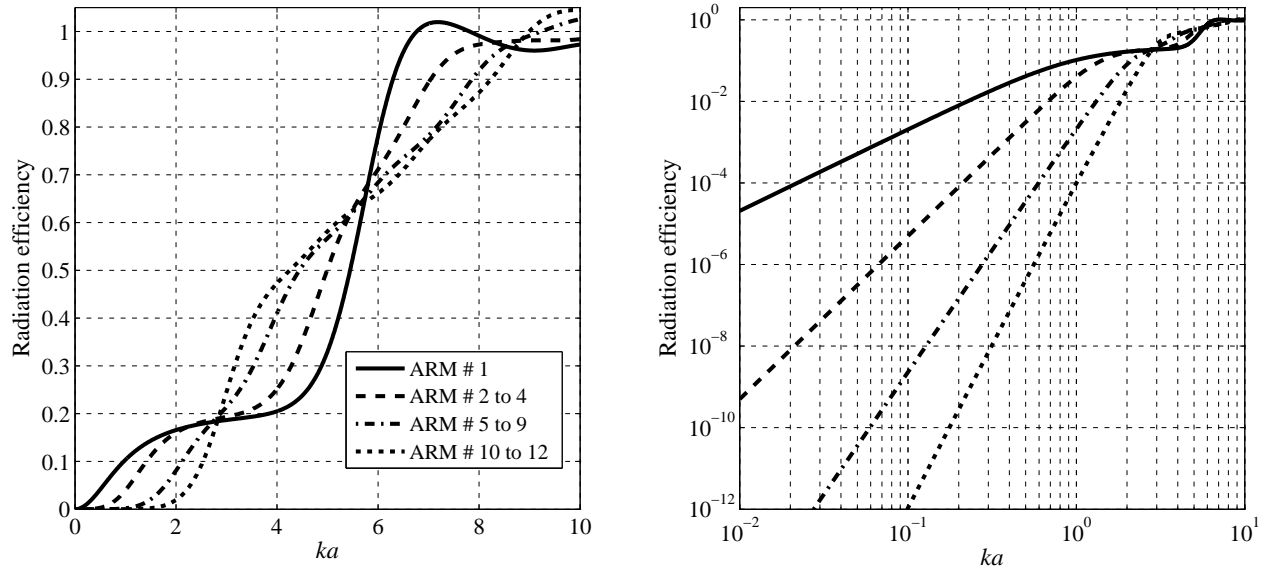


Figure 5.4: Radiation efficiency of the acoustic radiation modes of a dodecahedral source with $\theta_0 = 15.1^\circ$ (linear scale on the left; logarithmic scale on the right).

In order to evaluate $\mathbf{Y}^T(\hat{\theta}, \hat{\phi}) \mathbf{B}(k\hat{r})$ for use in Eq.(5.14) and the radiation efficiency for use in Eq.(5.21), the spherical harmonic series is truncated to order $n \leq 20$. The resulting radiation efficiency of the acoustic radiation modes of a dodecahedral source with $\theta_0 = 15.1^\circ$ is shown in Fig. 5.4. These radiation efficiencies for a dodecahedral source with $\theta_0 = 31.7^\circ$ are presented as dark green lines in Figs. 3.4 to 3.7. A comparison of these curves with Fig. 5.4 reveals that the radiation efficiency increases with θ_0 , as expected.

The value $\hat{r} = 0.75m$ is used to derive the sound pressure equalizers. In addition, the angular direction $(\hat{\theta}, \hat{\phi})$ is chosen so that it corresponds to the main radiation direction of the array in the low-frequency range. The log magnitude of the frequency response ($20 \log_{10} |\bar{\epsilon}_l(\omega)|$) of the sound pressure and sound power equalizers evaluated, respectively, by Eqs.(5.16) and (5.21) are shown in Figs.5.5 and 5.7. These curves have been multiplied by a constant so that the minimum value for the ARM # 1 corresponds to zero dB.

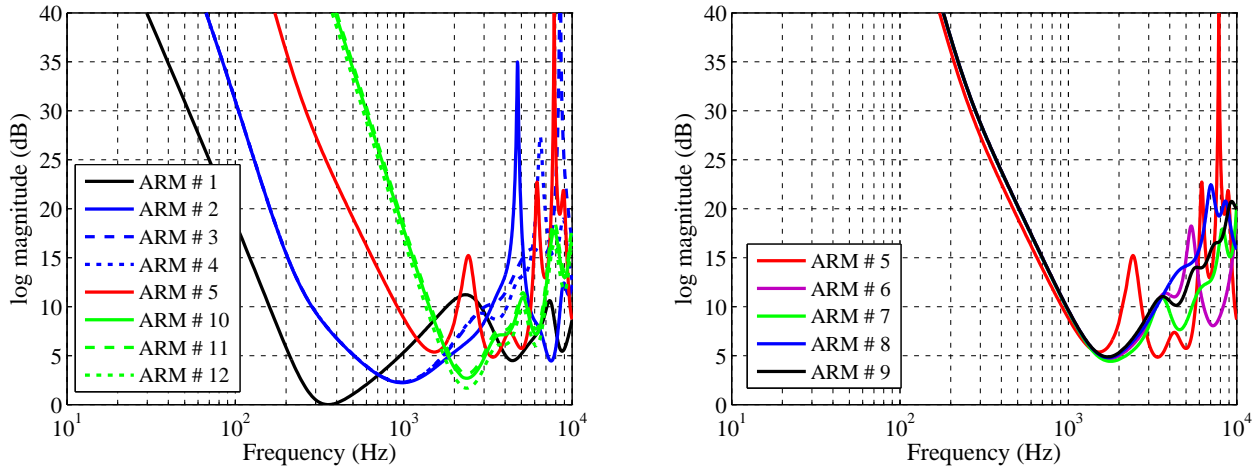


Figure 5.5: Frequency response (log magnitude) of the sound pressure equalizers for the acoustic radiation modes of a dodecahedral source.

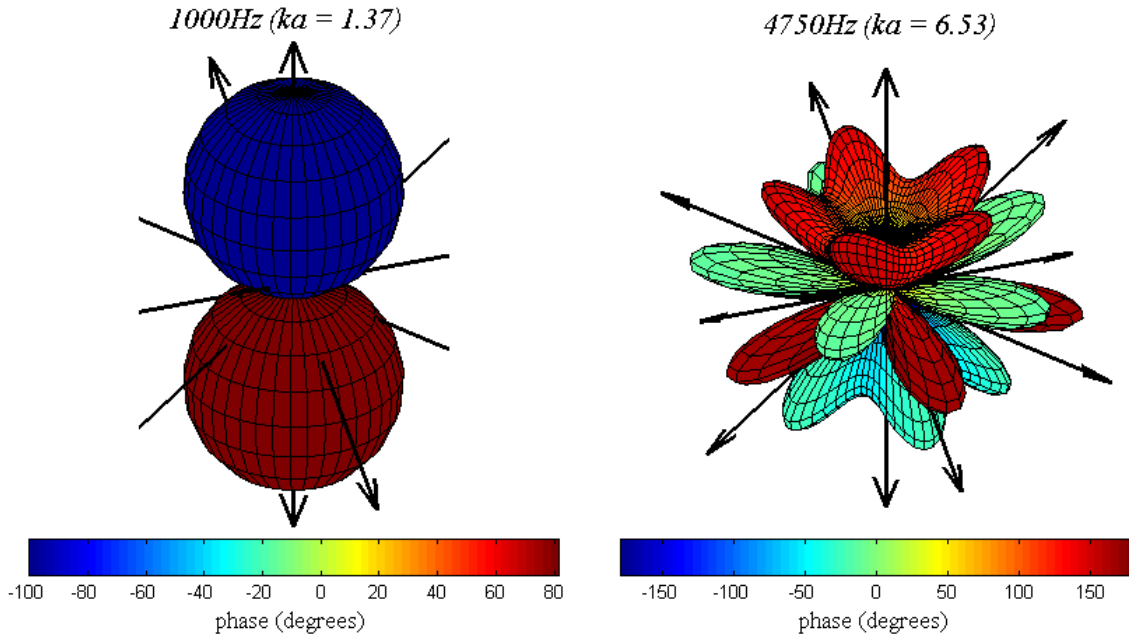


Figure 5.6: Radiation patterns at $1000Hz$ and $4750Hz$ corresponding to the ARM # 2 of a dodecahedral source with $a = 0.075m$ and $\theta_0 = 15.1^\circ$.

Since the directivity of the acoustic radiation modes becomes very complicated in the high-frequency range, it may happen that $(\hat{\theta}, \hat{\phi})$ matches a low pressure direction, leading to the sharp peaks shown in Fig.5.5. Figure 5.6 illustrates this fact, in which the radiation patterns for the ARM # 2 evaluated at $1000Hz$ and $4750Hz$ are presented. The radiation pattern is approximately a vertical dipole at $1000Hz$. In fact, in the low- and medium-frequency range, the maximum sound pressure value (main radiation direction) is achieved on the vertical axis passing through the loudspeakers located at the top and at the bottom of the spherical array, as shown on the left of Fig. 5.6. However, at $4750Hz$, this radiation direction corresponds to a low pressure region, so that a huge voltage should be applied to the drivers in order to provide sound pressure equalization at this point, as suggested by the high gain of the equalization filter at this frequency (refer to Fig. 5.5).

In order to eliminate the sharp peaks shown in Fig 5.5 — which can damage the drivers, lead to difficult to realize filters and do not make physical sense — the sound pressure equalizers can be derived by averaging the sound pressure values obtained for different points on the sphere of radius \hat{r} , instead of take only one point. However, because the radiation mode approach leads naturally to the sound power radiated by the source, sound power equalizers are a more attractive alternative. Figure 5.7 shows that using power equalizers completely eliminates the sharp peaks in the frequency response.

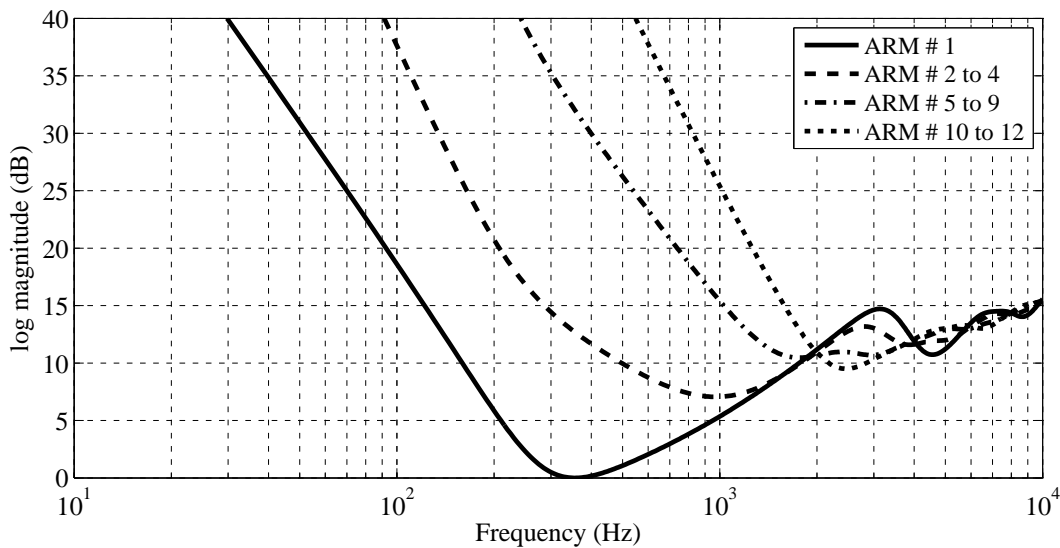


Figure 5.7: Frequency response (log magnitude) of the sound power equalizers for the acoustic radiation modes of a dodecahedral source.

On the other hand, because the directivity patterns of the radiation modes do not appreciably vary with frequency in the low-frequency range, there are no significant differences between the low-frequency response of the sound pressure and sound power equalizers, as shown in Figs. 5.5

and 5.7. Distinct normalization constants have been applied to the curves corresponding to the ARM # 1, so that they practically overlap. It is more difficult to produce a dipole with the same power of a monopole than with the same pressure at a given point. Therefore, the curves ARM # 2 to 12 in Fig. 5.5 present lower values than these curves in Fig. 5.7.

Figures 5.5 and 5.7 reveal that large gains must be applied to the input signal in the low-frequency range in order to compensate for the non-flat frequency response of the system, which can overload the drivers. This arises due to the electromechanical behavior and to the low radiation efficiency of the loudspeaker array, as shown in Figs. 5.3 and 5.4.

The four frequency-response curves shown in Fig. 5.7 become closer as frequency increases, so that they almost overlap above approximately $5kHz$. This is due to the fact that the radiation patterns of the radiation modes are very complex in the high-frequency range, so that the efficiency curves of the radiation groups are not as well discriminated as for lower frequencies (refer to Fig. 5.4). Since it is not meaningful to control such complex radiation patterns, only one active channel (radiation mode) can be used in the high-frequency range.

Besides the absence of sharp peaks in the frequency-response curve, sound power equalization presents another advantage over sound pressure equalization based on a single point, namely, the former can be achieved by using only 4 distinct filters, whereas the latter demands 12 distinct filters. This is due to the grouping characteristic of the radiation modes shown in Fig. 5.4.

The compensation filters can be approximated by rational polynomials in $e^{t\omega T_s}$ — refer to Eq.(5.12) — so that the corresponding constant-coefficient difference equations are obtained. Then, the equalizers can be implemented on a digital computer. The Matlab[®] filter design toolbox has been used to derive coefficients for discrete-time IIR filters that approximate the frequency-response magnitude of the sound power equalizers presented in Fig. 5.7.

Figure 5.8 shows the frequency response of the ideal theoretical filters evaluated by Eq.(5.21) and the approximated IIR filters obtained using the Matlab[®] filter design toolbox with $B = D = 9$ and $T_s = (44100)^{-1}s$. In deriving the IIR filters, each ideal filter has been divided by its minimum amplitude value so that the corresponding IIR filter provides at least a unitary gain. Since the ideal frequency response of the filters presents a large gain in the low-frequency range, equalization filtering can damage the drivers. Therefore, the low-frequency response of the equalizers has been ignored when evaluating the coefficients of the IIR filters.

Inspection of Eqs.(5.20) and (5.21) reveals that the quotient between each IIR filter and the associated ideal filter yields the characteristic sound power of the subset of channels corre-

sponding to a radiation group of the dodecahedral array. The characteristic sound power level — $10 \log_{10}(W/W_{ref})$ — is shown in Fig. 5.9, where W_{ref} has been chosen to equal the maximum value of the ARM # 1 curve.

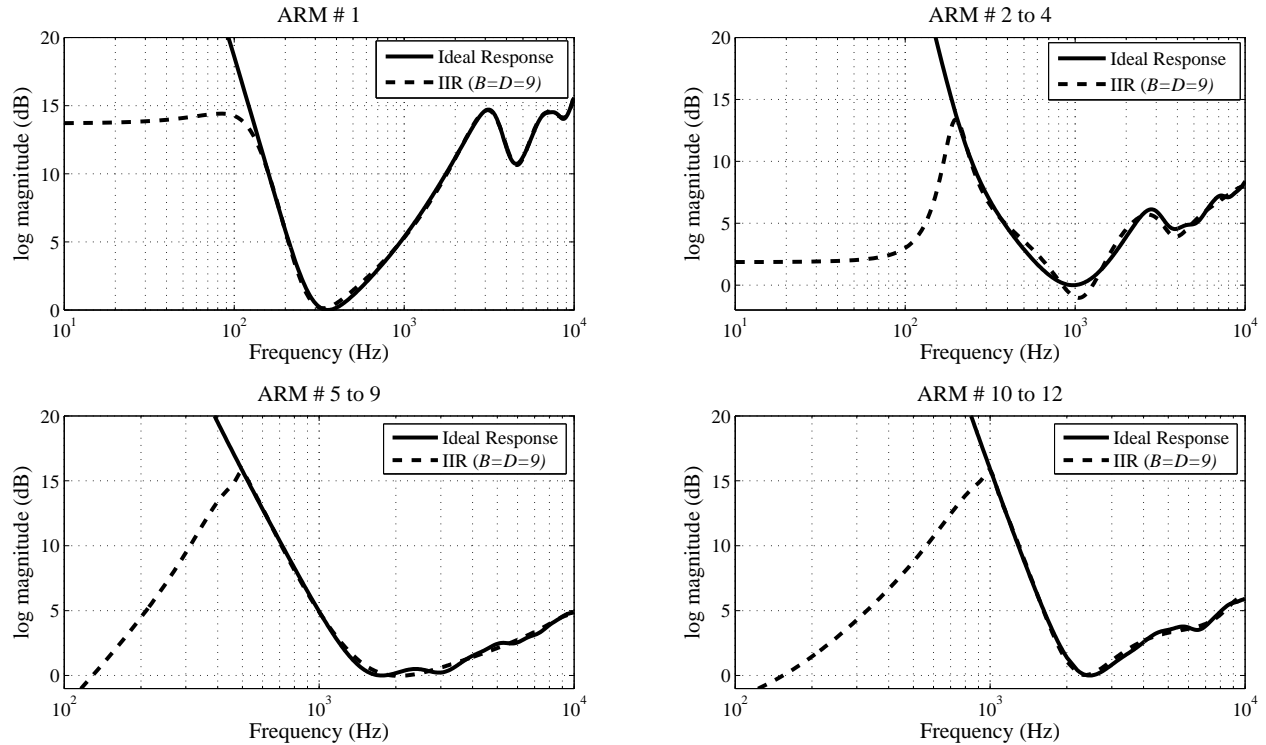


Figure 5.8: Frequency response (log magnitude) of the sound power equalizers for the acoustic radiation modes of a dodecahedral source. Solid curves: ideal theoretical filters; dashed curves: approximated IIR filters with $B = D = 9$.

Figure 5.9 shows that IIR filters with $B = D = 9$ provide fairly sound power equalization for the radiation groups of the dodecahedral source under consideration. Low-frequency equalization is not concerned for the sake of safety, as discussed before.

In order to establish whether or not the IIR power equalizers give rise to phase distortion, the sound pressure level (re $20 \mu Pa$) at $(\hat{r}, \hat{\theta}, \hat{\phi})$ is presented in Fig. 5.10 for the ARM # 1, 2, 5 and 10, i.e., the curves are given by the product of $H_l(\omega)$ and the corresponding IIR compensation filter, for $l = 1, 2, 5$ and 10.

The phase response of the sound pressure is approximately linear regardless of the considered channel, as shown on the right in Fig. 5.10; the phase is wrapped between 0^0 and 1080^0 for the sake of readability. Therefore, the presence of sound power compensation filters, at least in the radiation direction $(\hat{\theta}, \hat{\phi})$, does not lead to phase distortion, as mentioned in the last paragraphs of section 5.2.1.

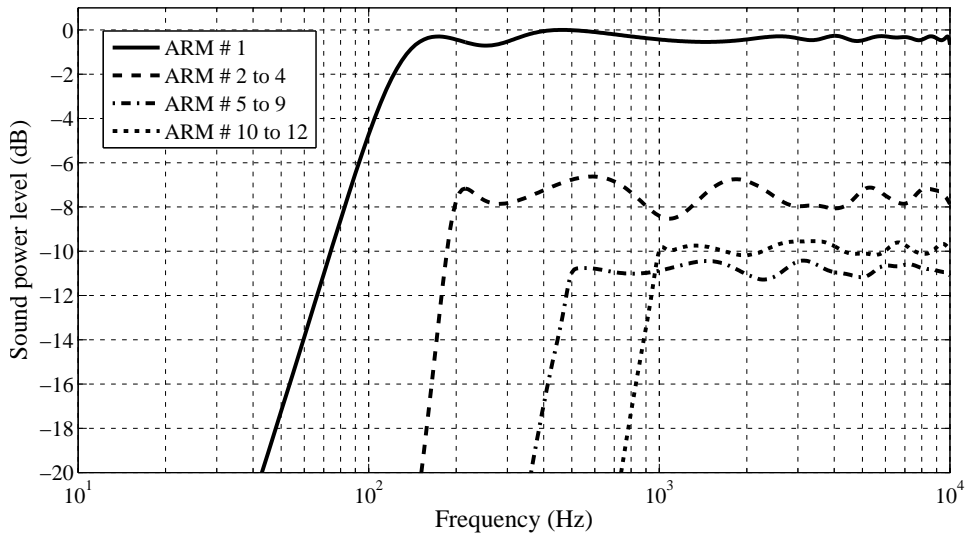


Figure 5.9: Sound power level of the equalized acoustic radiation modes of a dodecahedral source. The ideal sound power equalization filters have been approximated by IIR filters with $B = D = 9$.

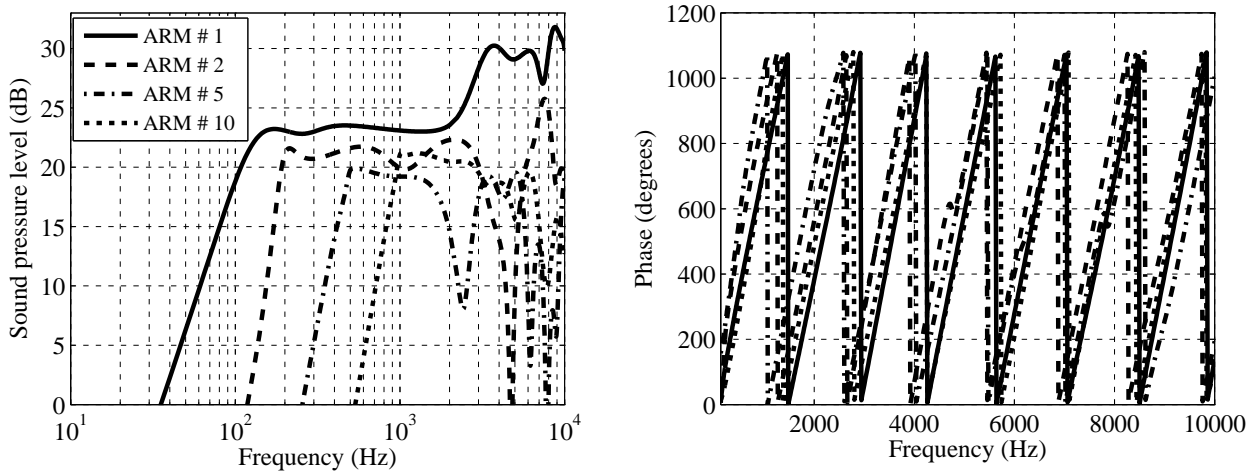


Figure 5.10: Sound pressure response at $(\hat{r}, \hat{\theta}, \hat{\phi})$ for some acoustic radiation modes of the dodecahedral array with IIR sound power equalizers.

Chapter 6

Experimental Evaluation

In the previous chapters, theoretical and computational aspects concerning compact spherical loudspeaker arrays for radiation control were considered. Most of the results and discussions presented up to now are based on the validity of the theoretical models proposed in chapter 3. In order to experimentally validate them, a spherical array prototype has been designed, built and subjected to a series of measurements. In this chapter, the experimental results are presented and compared to the prediction models. All the experimental work reported here was carried out at the Laboratory of Mechanics and Acoustics of the National Center for Scientific Research (UPR-7051, CNRS, Marseille, France) from may 2009 to july 2009.

The first section is devoted to the description of the spherical array prototype. The second section deals with the identification of the parameters to be used in the electrodynamic loudspeaker model described in section 3.2.1 for each individual transducer of the prototype. Next, an analysis of the electromechanical behavior of the prototype based on surface vibration pattern measurements is presented, including the effects of the acoustic coupling inside the array frame. Finally, sound radiation patterns of the prototype obtained from directivity measurements in an anechoic chamber are presented.

6.1 Prototype description

The main source parameters determining the angular radiation pattern of a spherical array are: the position of each loudspeaker on the array, the number of transducers L , the sphere radius a and the radiation patterns of the individual drivers. In addition, the radiated sound power is affected by the

array enclosure design, as discussed in section 3.3. In the following, the effects of these parameters on the sound field are briefly reviewed in order to justify the values used in the prototype described here.

If the spherical array is intended to provide radiation control in a full 3-D space, the drivers must be distributed as symmetrically as possible over the sphere surface. For the same reason, ideally identical drivers should be used. Therefore, L transducers of a given type are usually mounted on the sphere surface according to a Platonic solid geometry. Then, one may have $L = 4$ (tetrahedron), $L = 6$ (hexahedron), $L = 8$ (octahedron), $L = 12$ (dodecahedron) or $L = 20$ (icosahedron) drivers. It is easy to realize that the complexity of the controllable radiation patterns increases with L , as well as the computational cost and the overall system complexity.

Among the Platonic solids having the same midradius a , the dodecahedron presents the largest surface area available for assembling the drivers, i.e., one can use larger drivers so that a higher sound power is obtained for a given a , as shown in section 3.1.2.1. Furthermore, using a dodecahedron leads to a smaller error when synthesizing the monopole and the dipoles, whereas higher order spherical harmonics are better synthesized by the icosahedron (refer to Fig. 4.2).

For the reasons stated above, a dodecahedron-like array has been considered as a good compromise between complexity of the controllable radiation patterns, system complexity and sound power. Figure 6.1 shows pictures of the prototype studied here, a 12-driver spherical array.

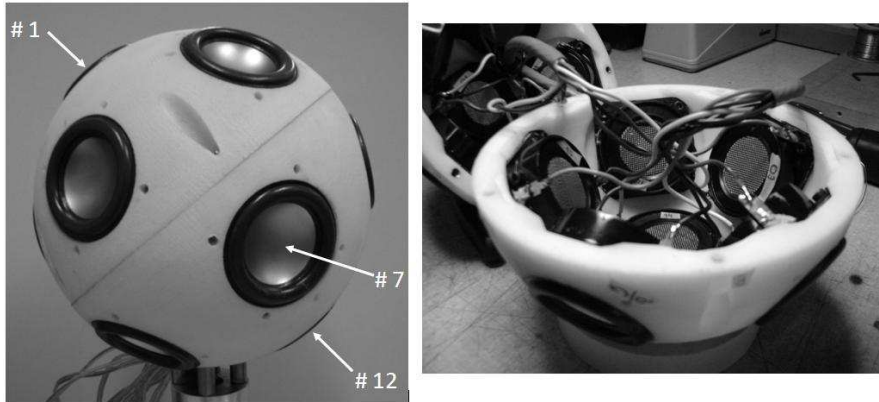


Figure 6.1: Spherical array prototype with $L = 12$ independently programmable transducers mounted on a hollow sphere with outer radius $a = 0.075m$ and inner radius $a_i = 0.060m$.

In section 4.2, it was shown that the ability in controlling sound directivity by using a spherical array with a given L degrades as the non-dimensional parameter ka increases. Hence, high frequency control can be improved by decreasing a . However, this leads to a smaller radiating surface so that sound power is reduced. This is critical in the low-frequency range due to the very

low radiation efficiency of the source at low ka values. Therefore, the choice of a is a trade-off between low and high frequency sound reproduction. The prototype presented in this work has $a = 0.075m$ and the nominal diameter of the drivers is $0.051m$. In addition, the inner sphere radius is $a_i = 0.060m$.

The radiation patterns of the individual loudspeakers mounted on a rigid sphere are not usually available to be taken into account in the design phase. The frequency responses of the drivers and their variability can be used as a criteria for choosing suitable transducers. However, the latter information is not usually provided by the loudspeaker manufacturers, so that the designer must be experienced in order to be able to use the drivers variability as a choice criteria. The alternative adopted in this work was to simulate the frequency responses of the spherical array, as described in section 3.2, with some different drivers by using the electromechanical parameters presented in the manufacturers' data sheets. In addition, compact drivers that are easy to handle and do not occupy much space of the sphere cavity have been considered to be better. The prototype presented here uses Aurasound® NSW2-326-8A drivers (nominal diameter: $0.051m$; cone material: titanium).

As said in section 3.3, to let the drivers share a common empty cabinet leads to an easier to build mechanical frame and to slightly lower voltages in the low-frequency range. Therefore, the prototype presents an empty spherical frame, which has been manufactured by stereolithography. Moreover, this design choice permits to evaluate experimentally the acoustic coupling model proposed in section 3.2. However, it is expected that some natural frequencies of the cavity will lead to undesirable effects on the electromechanical behavior of the system.

6.2 Parameter estimation of the electrodynamic loudspeaker model

According to the electrodynamic loudspeaker model presented in section 3.2, the l -th driver unit of a loudspeaker array can be characterized by the following parameters: M_l , C_l , R_l , $(Bl_e)_l$, $R_l^{(e)}$, K_l , n_l and \hat{S}_l . Many identification methods have been proposed to estimate them. Most of these methods are based on electrical impedance measurements at the voice-coil terminals of the driver. In this work, an identification method developed by Dr. Philippe Herzog (co-advisor of this PhD work) has been used for evaluating each transducer of the spherical array prototype. The parameters identification is based on accurate measurements of the electrical impedance of the driver, and on an iterative process which alternates the identification of electrical impedance and mechanical resonance, each through an analytic LMS identification, until the overall residue is low enough.

The resonance frequency shifts observed when applying a set of mechanical perturbations (added masses and compliances) are then used in an LMS estimation of the speaker compliance, mass and effective surface [84]. Briefly, the method estimates the model parameters from a set of electrical impedance measurements obtained with the driver operating under different conditions and it has been successfully applied to a wide range of loudspeaker types.

All parameters mentioned above can be estimated by measuring directly the diaphragm diameter in order to obtain \hat{S}_l and by making two electrical impedance measurements. In the first, the driver is mounted on a baffle of any size or with no baffle and, in the second, the driver is mounted on an unlined closed test box of a known volume.

For small drivers, the direct measurement method is not expected to provide accurate results for \hat{S}_l due to the proportionally large surface area of the driver suspension. A better estimative is obtained if an additional impedance measurement is taken. In this case, the driver is mounted on a baffle or with no baffle (as in the first impedance measurement) and a known test mass is attached to the driver diaphragm. In addition, the C_l estimation can also be improved by making an extra impedance measurement with the driver mounted on an unlined closed test box of volume other than the previous one.

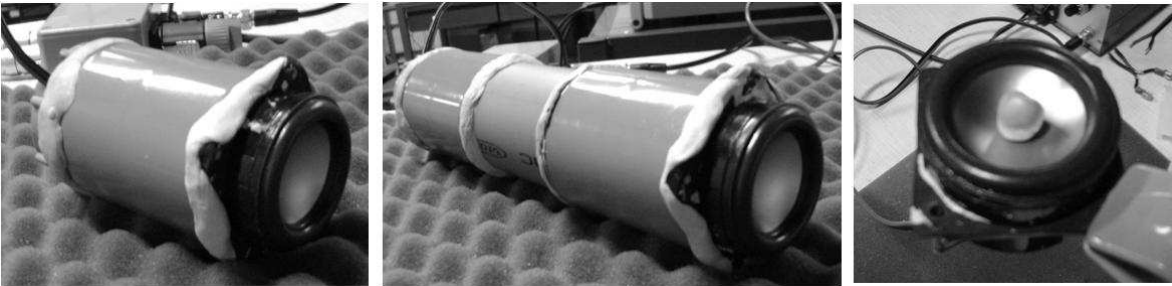


Figure 6.2: Experimental set-up for the electrical impedance measurements.

The model parameters for each driver unit to be used in the spherical array prototype have been estimated from a set of seven electrical impedance measurements taken with the driver operating under the following conditions:

- Suspended driver (with no baffle);
- Driver mounted at the open side of open-closed tubes of volumes $(V_{t1}, V_{t2}) = (1.5, 3.3) \times 10^{-4}m^3$ and diameter $0.050m$ (refer to the pictures on the left and on the middle of Fig. 6.2);
- Suspended driver with attached masses of $(M_{t1}, M_{t2}, M_{t3}, M_{t4}) = (0.9, 1.4, 2.3, 2.8) \times 10^{-3}kg$ (refer to the picture on the right of Fig. 6.2).

Since it is difficult to adjust the attached masses on the diaphragm surface of such small drivers, four impedance measurements with four distinct masses have been taken in order to achieve a somewhat average result.

Table 6.1: Estimated parameters of the 12 Aurasound® NSW2-326-8A drivers used in the spherical array prototype.

	$M(kg)$	$C(m/N)$	$R(N.s/m)$	$Bl_e(T.m)$	$R^{(e)}(\Omega)$	K	n	$\hat{S}(m^2)$
Driver #01	1.10×10^{-3}	4.22×10^{-4}	0.25	3.16	6.51	7.61×10^{-4}	0.87	1.18×10^{-3}
Driver #02	1.04×10^{-3}	4.95×10^{-4}	0.26	3.20	6.32	7.34×10^{-4}	0.88	1.18×10^{-3}
Driver #03	1.23×10^{-3}	4.10×10^{-4}	0.27	3.36	6.16	8.19×10^{-4}	0.86	1.30×10^{-3}
Driver #04	1.13×10^{-3}	5.37×10^{-4}	0.31	3.28	6.29	6.79×10^{-4}	0.89	1.26×10^{-3}
Driver #05	1.06×10^{-3}	4.62×10^{-4}	0.26	3.16	6.34	6.31×10^{-4}	0.89	1.21×10^{-3}
Driver #06	1.03×10^{-3}	5.50×10^{-4}	0.25	2.99	6.11	8.48×10^{-4}	0.85	1.20×10^{-3}
Driver #07	1.10×10^{-3}	4.60×10^{-4}	0.32	3.23	6.41	7.71×10^{-4}	0.88	1.19×10^{-3}
Driver #08	1.09×10^{-3}	4.48×10^{-4}	0.31	3.20	6.25	8.68×10^{-4}	0.86	1.22×10^{-3}
Driver #09	1.09×10^{-3}	5.32×10^{-4}	0.27	3.11	6.30	7.80×10^{-4}	0.86	1.20×10^{-3}
Driver #10	1.15×10^{-3}	4.16×10^{-4}	0.30	3.17	6.28	8.84×10^{-4}	0.85	1.23×10^{-3}
Driver #11	1.03×10^{-3}	5.20×10^{-4}	0.24	3.05	6.36	9.73×10^{-4}	0.84	1.11×10^{-3}
Driver #12	1.03×10^{-3}	4.53×10^{-4}	0.25	2.96	6.26	9.42×10^{-4}	0.84	1.15×10^{-3}
Mean value	1.09×10^{-3}	4.75×10^{-4}	0.27	3.16	6.30	8.07×10^{-4}	0.86	1.20×10^{-3}
Standard deviation	0.06×10^{-3}	0.50×10^{-4}	0.03	0.12	0.10	1.02×10^{-4}	0.02	0.05×10^{-3}

Table 6.1 presents the estimated parameters of the 12 drivers of the spherical array prototype. It can be noticed that parameter variability seems to be significant, especially for C , R and K , which may have effects on the radiation pattern.

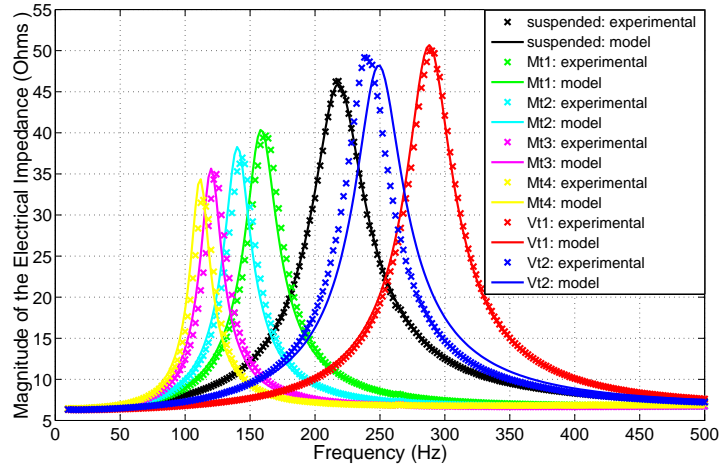


Figure 6.3: Theoretical and experimental electrical impedance of the driver #11 under the following operation conditions: suspended driver, driver mounted at open-closed tubes of volumes $V_{t1} = 1.5 \times 10^{-4}m^3$ and $V_{t2} = 3.3 \times 10^{-4}m^3$, suspended driver with attached masses of $(M_{t1}, M_{t2}, M_{t3}, M_{t4}) = (0.9, 1.4, 2.3, 2.8) \times 10^{-3}kg$.

Figure 6.3 shows the electrical impedance magnitude of driver #11 operating under the seven

conditions described before. The discontinuous lines present experimental results that have been used to estimate the parameters of the model developed in section 3.2. The continuous lines present the curves obtained by using such a model with $F^{(a)} = 0$ and the estimated parameters of the driver #11¹. Except for a small deviation when the driver is mounted on the tube of volume V_{t2} , the loudspeaker model fits very well the measured data in the low- and medium-frequency ranges. It is worth noting that good agreement has also been found for the other 11 drivers used in the array prototype.

The curves labeled “suspended” in Fig. 6.3 are plotted in Fig. 6.4 for the driver #08, but in a wider frequency range and with phase response included. A small disturbance around 1600Hz can be noticed in the experimental curve. Beyond this value, the theoretical phase response deviates from the experimental data. This behavior has also been observed on the other array drivers and it is due to the non-rigid body motion of the diaphragm suspension assembly, as it will be discussed in the next section.

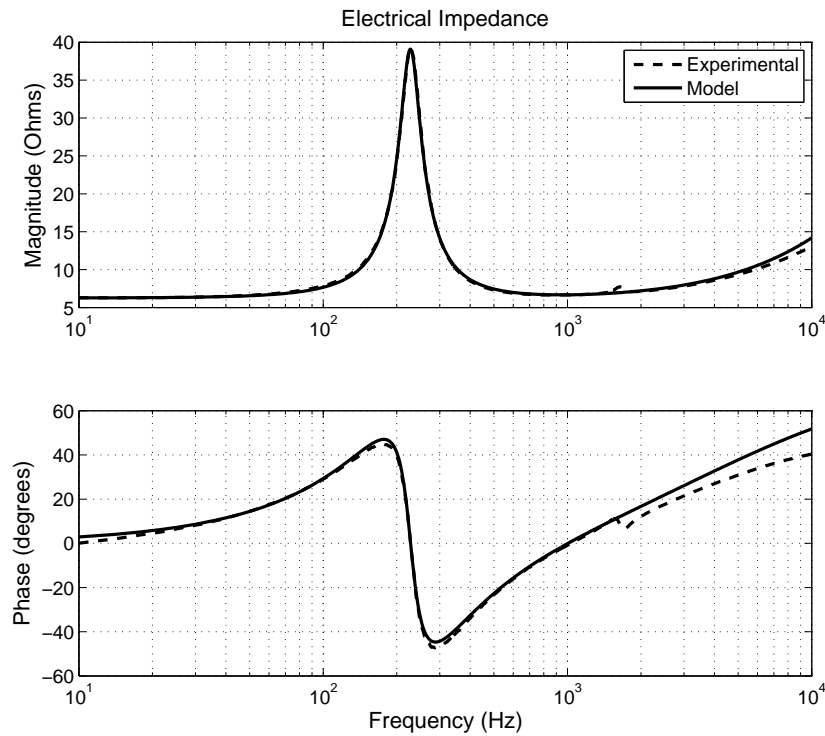


Figure 6.4: Theoretical and experimental electrical impedance of a suspended driver unit (driver #08) for use in the spherical array prototype.

¹In fact, the imaginary part of $F^{(a)}/u$ is an inertance that was assimilated into M in Tab. 6.1. Therefore, only the real part of $F^{(a)}/u$ is actually neglected.

6.3 Electromechanical behavior

Results of electrical impedance (v/i) and diaphragm velocity/voltage (u/v) measurements can be used to experimentally evaluate the electromechanical behavior of a loudspeaker unit. The former are used to estimate the electroacoustic parameters that describe the driver low-frequency response, as discussed in the previous section. The latter permit to identify vibration patterns other than rigid body motion which potentially affect the sound radiation. This section deals with diaphragm velocity/voltage measurements.

As far as a compact loudspeaker array for radiation control is concerned, the experimental analysis becomes more complicated, especially when the drivers share a common cabinet. If so, since the acoustic coupling between drivers affects the overall electromechanical behavior of the array, it must be somehow evaluated. It is worth noting that coupling effects depend on phase and magnitude relations between transducers, i.e., on the radiation pattern one aims to achieve.

In the following, the experimental procedures used to investigate the electromechanics of the spherical array prototype are described and the results are presented. First, the individual loudspeaker units are considered. Then, their interaction when operating together in the spherical array is investigated.

6.3.1 Experimental procedures

The following methods can be used to experimentally characterize vibroacoustic sources:

- Vibrational methods: vibration sensors such as accelerometers are placed on the radiating body surface in order to directly measure its vibration;
- Acoustical methods: microphones are used to measure the acoustic field around the source, so that backpropagation yields the body vibration;
- Optical methods: laser beams are used to measure the vibration of a target surface.

For surface measurements of light structures like loudspeaker membranes, vibrational methods do not provide good results because the sensor mass greatly affect the system dynamics. Then, non-contact (no mass loading) methods such as acoustical and optical methods are more suitable. Besides surface velocity, acoustical methods lead to a description of the sound field, but have

the shortcoming of requiring the knowledge of a radiation operator and the solution of an inverse problem [85]. Hence, since the radiated field is not important to investigate the electromechanical behavior of loudspeakers, optical methods were used to measure the surface vibration of the loudspeakers employed in the spherical array prototype.

The frequency response functions (FRF) between input voltage and output velocities of points on the driver diaphragm and suspension (under the “suspended” driver condition) have been measured using a scanning laser Doppler vibrometer (Polytec® PSV-400). The left side of Fig. 6.5 illustrates the measurement grid. Since the driver suspension presents a vibration pattern more complicated than the diaphragm itself, a finer mesh in the radial direction has been used over the driver suspension.

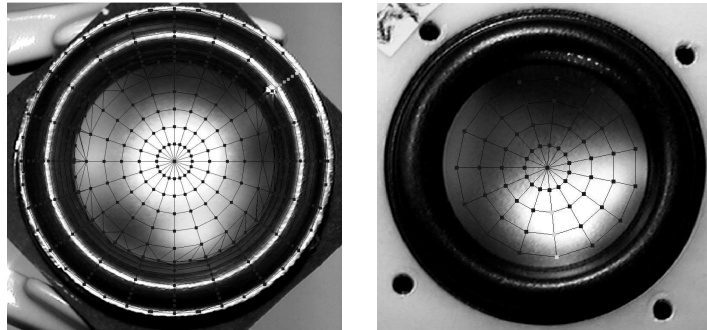


Figure 6.5: Laser scanning grid points on the driver vibrating surface. On the left, driver is suspended and both diaphragm and suspension velocities are measured. On the right, driver is mounted on the spherical array prototype and only the diaphragm velocity is measured.

In order to investigate the interaction between drivers, a set of additional FRF measurements has been carried out with the drivers mounted on the hollow sphere. However, unlike the previous measurements, the input voltage and the output velocity have been taken at different drivers of the spherical array, as summarized in Tab. 6.2, where each driver number corresponds to a position in the array depicted on the left of Fig. 6.1. Here, only points on the driver diaphragm are considered, as shown on the right side of Fig. 6.5.

Table 6.2: Measurement configurations for evaluating the interaction between drivers mounted on the spherical array prototype. Each driver number corresponds to a position in the array shown in Fig. 6.1.

Configuration	Active drivers	Input	Output
1	#7	#7	#7
2	#1	#1	#7
3	#1 and #12 out of phase	#1	#7
4	#1–12 in phase	#7	#7

In Tab. 6.2, the “active drivers” column contains the numbers of the active transducers, which are fed with the same magnitude signal. The column “input” contains the number of the transducer in which the input voltage is taken. The column “output” contains the number of the transducer in which the output velocity is taken. It is worth mentioning that all passive drivers were operating in a closed-circuit configuration during the experiments, but not connected to an amplifier.

For all configurations shown in Tab. 6.2, the FRF output is the surface velocity of a point at the diaphragm of the driver #7. In config. 1, only transducer #7 is driven, so that the FRF input is its voltage. This configuration permits to evaluate the effects of the passive radiators (inactive drivers) and the sphere volume on the electromechanics of the active driver.

Only driver #1 is active in config. 2. Hence, the FRF input is its voltage. Since the FRF output is the velocity of an undriven transducer (driver #7), such a configuration leads to the evaluation of the acoustic coupling inside of the array frame.

It is expected that the acoustic coupling will lead to two main effects. First, the dynamic response of each driver will change in the compliance-dominated (low-frequency) region due to the sound pressure fluctuations inside the sphere induced by the driver displacements. Second, the acoustic modes of the spherical cavity will modify the system dynamics at discrete frequencies corresponding to the eigenfrequencies associated to these modes. Both effects are expected to appear in config. 2. Configuration 3 is an attempt to isolate the second effect. One has two active drivers fed by signals having the same magnitude, but in phase opposition. Then, internal sound pressure fluctuation will occur only if cavity modes are present, otherwise the measured FRF will be zero.

Finally, all drivers are active in config. 4 and fed by the same signal (magnitude and phase). Hence, ideally, it does not matter which driver(s) is(are) considered to obtain the FRF. Such a configuration leads to an approximately omnidirectional sound field and this is considered here in order to emphasize the differences between the behavior of an omnidirectional source and a directivity controlled source. The results are presented in the following.

6.3.2 Results and discussion

Figure 6.6 shows the measured surface velocity of the diaphragm suspension assembly of the driver #7 plotted against the radial coordinate. Such a pattern has been measured at 1616Hz with the driver under the “suspended” condition. The laser scanning points are illustrated on the left of Fig. 6.5. Then, it can be noticed that the first 7 circles in Fig. 6.6 are points on the driver diaphragm

and circles 8 to 16 are points on the driver suspension. The results have been normalized and, since the vibration pattern is practically axisymmetric, averaged over the circumferences shown in Fig. 6.5.

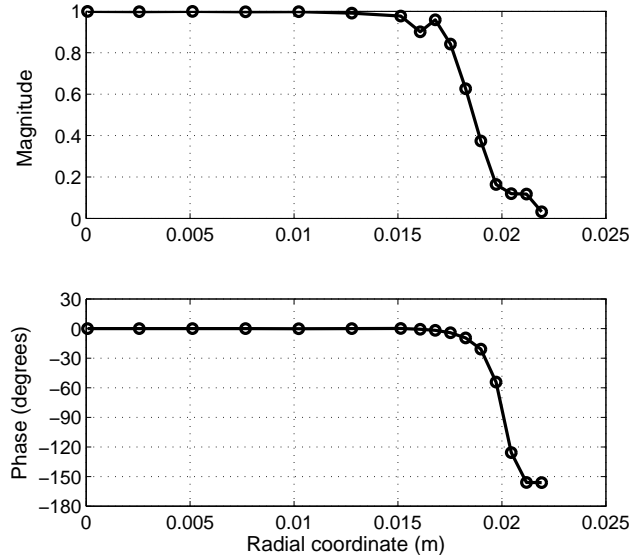


Figure 6.6: Measured vibration pattern of the diaphragm (first 7 inner circles) and suspension (circles 8 to 16) of a suspended driver for use in the spherical array prototype. This pattern has been measured at the frequency of $1616Hz$ and the grid points are illustrated on the left of Fig. 6.5. The results have been normalized and averaged over the circumferences shown in such a figure.

At frequencies below approximately $1500Hz$, diaphragm and suspension oscillate in phase and the vibration amplitude is nearly constant over the diaphragm surface and over the inner portion of the suspension surface, so that rigid motion assumption is justified. As frequency increases, the driver diaphragm still behaves as a rigid body. However, the suspension vibration becomes more complex and its overall phase does not match the phase of the diaphragm motion. Near $1616Hz$, the inner and outer borders of the suspension vibrate practically in opposite phase, as shown in Fig. 6.6. A previous work (refer to [84]) concerning loudspeakers has shown that the finite stiffness of the membrane may allow such a resonance, which leads to the perturbation in the electrical impedance shown in Fig. 6.4.

The suspension of any driver of the array presents the behavior described above. Since the suspension surface of the Aurasound® NSW2-326-8A drivers is proportionally large, it is understandable that its vibration affects the electrical impedance.

Now, the acoustic coupling effects that take place when drivers are mounted on the spherical array prototype are investigated. Such effects are evaluated by considering the FRFs described in Tab. 6.2. Unless otherwise stated, each experimental FRF presented in the next figures is the area-

weighted average of the FRFs measured on the 61 points shown on the right side of Fig. 6.5. It is worth noting that one has checked that the surface velocity is approximately uniform over the diaphragm surface.

In all simulations, the medium properties have been assumed to be $c = 343m/s$ and $\rho = 1.21kg/m^3$. In addition, a truncation order $N = 29$ has been adopted when using the distributed-parameter model described in section 3.2.2.2.

Figure 6.7 shows the theoretical and experimental FRFs corresponding to config. 1 (refer to Tab. 6.2). In addition, the FRF for a “suspended” driver is presented in order to show the effect of the sphere volume on the system response. This experimental FRF is the area-weighted average of the FRFs measured at the points on the driver diaphragm shown on the left side of Fig. 6.5. Theoretical results have been computed using both the lumped and the distributed-parameter (continuous) models to evaluate the acoustic coupling (refer to section 3.2.2). The distributed-parameter model assumes that the array cavity is an ideal sphere of radius $a = 0.075m$, i.e., the effects of the presence of driver elements and cables inside of the spherical cavity on the system response are not taken into account. It is expected that such effects can be considered in an overall sense by applying a correction factor to the spherical cavity volume when using the lumped-parameter approach. Hence, in this work, the cavity volume value to be used in Eq.(3.32) is $V_b = (CF)(\frac{4}{3}\pi a^3)$, where CF is a correction factor that can be obtained by trial and error.

For frequencies lower than approximately $1300Hz$, the curves presented in Fig. 6.7 almost superimpose. Since driver #7 is the only active driver of the array, the spherical cavity provides an additional mechanical compliance of approximately $V_b(\rho c^2 \hat{S}_2^2)^{-1} \approx 0.01m/N$ if $CF = 1$. This value is much larger than the mechanical compliance C of the driver suspension. Therefore, the spherical cavity does not affect the system response in the low frequency range, as shown in the figure.

However, the distributed-parameter model leads to some singularities due to the acoustic cavity modes. The lowest 4 eigenfrequencies of a rigid spherical cavity correspond to the following ka values: 2.0816, 3.3421, 4.4934 and 5.9404. Thus, for $a = 0.075m$, one has $1515Hz$, $2433Hz$, $3271Hz$ and $4324Hz$. Nevertheless, comparison of the 2 experimental curves reveals that only the first cavity mode affects the experimental FRF. This suggests that higher order modes are much more damped, probably due to a mismatch between the modal shape and the arrangement of the loudspeaker frames inside the cavity. Moreover, the mechanical behavior of the membrane becomes more and more dominated by its mass inertia as frequency increases. Coincidentally, the first eigenfrequency is very close to the high frequency limit beyond which the inner and outer borders of the driver suspension no longer oscillate in phase.

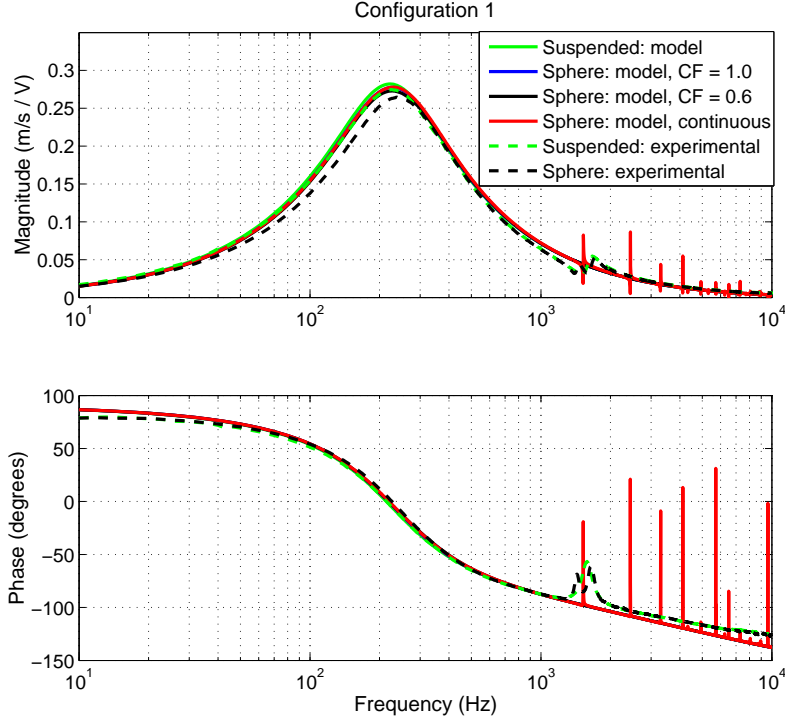


Figure 6.7: Theoretical and experimental FRFs corresponding to the config. 1 described in Tab. 6.2 and to a “suspended” driver. Each experimental FRF is the area-weighted average of FRFs measured on the driver diaphragm surface.

Figure 6.8 shows the theoretical and experimental FRFs corresponding to config. 2. Here, the diaphragm velocity is measured on a passive driver, so that its movement is only due to acoustic coupling effects. Therefore, unlike in config. 1, changes in the cavity volume have a great influence on the FRF. Therefore, a correction factor $CF = 0.6$ has been used in order to approximate the experimental result by the lumped-parameter model in the compliance-dominated frequency range. When no correction factor is applied ($CF = 1$), the lumped-parameter model leads to the same result that the continuous model, except at the cavity eigenfrequencies discussed before, as expected. It can be noticed that the experimental driver response is greatly affected near the first cavity eigenfrequency. Since higher order cavity modes are damped in practice, the measured diaphragm velocity of the passive driver is zero in the mass-dominated frequency range.

Figure 6.9 shows the theoretical and experimental magnitude responses corresponding to config. 3. Since the active drivers (#1 and #12) are fed by electrical signals of the same magnitude but in phase opposition, the diaphragm velocity of the passive driver (#7) is non-zero only at frequencies close to the cavity eigenfrequencies that are not attenuated, namely, 1515Hz for the array prototype considered here. Therefore, the lumped-parameter model is not able to produce a non-zero frequency response regardless of the correction factor CF . On the other hand, the first cavity

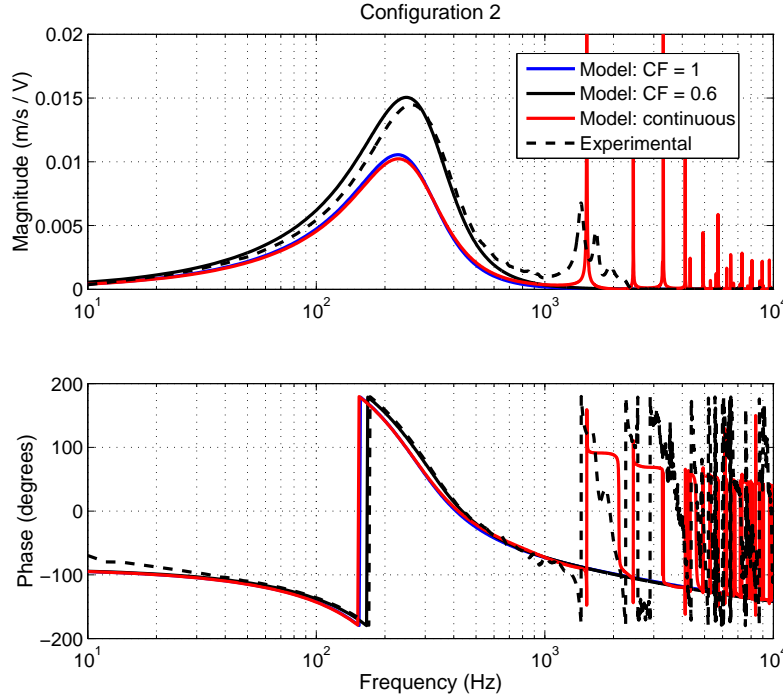


Figure 6.8: Theoretical and experimental FRFs corresponding to the config. 2 described in Tab. 6.2. The experimental FRF is the area-weighted average of FRFs measured on the driver diaphragm surface.

eigenfrequency emerges in the simulation results using the distributed-parameter model. Experimental data indeed shows that the cavity resonance cannot be neglected in this situation, although its effect is disturbed by the mechanical resonance of the loudspeaker suspension, which occurs at a frequency very close to the first acoustical resonance of the cavity.

The theoretical and experimental FRFs corresponding to config. 4 are shown in Fig. 6.10. Like config. 2, the application of the correction factor $CF = 0.6$ improves the lumped-parameter model results in the compliance-dominated frequency range. If the variability between the array drivers is neglected, they will vibrate with the same velocity magnitude and phase. If so, the spherical cavity provides each driver with an additional mechanical compliance of approximately $V_b(L\rho c^2\hat{S}^2)^{-1} \approx 7.31 \times 10^{-4}m/N$ if $CF = 1$, i.e., each transducer behaves as if it was mounted on a sealed cavity with volume V_b/L . This value is not much larger than the mechanical compliance C of the driver suspension, so that the FRF magnitude peak is shifted to the right in Fig. 6.10 in comparison with Fig. 6.7. As far as an omnidirectional spherical array is concerned, if the cavity eigenfrequencies and the transducers variability are neglected, to let the drivers share a common hollow enclosure will lead to the same electroacoustical behavior as to provide each driver with its own sealed cavity. Therefore, the enclosure design for omnidirectional sources is much simpler

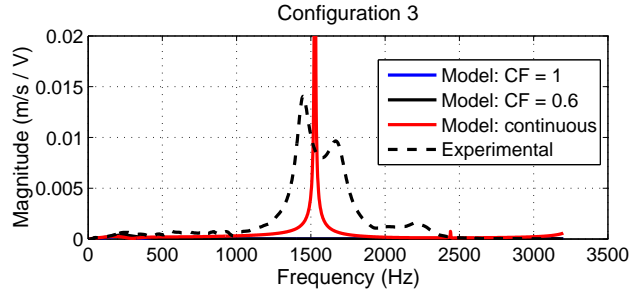


Figure 6.9: Theoretical and experimental FRFs corresponding to the config. 3 described in Tab. 6.2. The experimental FRF is the area-weighted average of FRFs measured on the driver diaphragm surface.

than for directivity controlled sources.

It is worth commenting on the apparently large volume correction used here in order to adjust the lumped-parameter model, i.e., $CF = 0.6$. Notice that this factor is applied to the volume of a sphere whose radius is the outer radius of the dodecahedral array prototype ($a = 0.075m$). Since this volume is not the empty volume of the prototype cabinet, CF does not possess a strict physical sense. If the thickness of the spherical frame was taken into account in the definition of CF (its inner radius is $a_i = 0.060m$), a correction factor of $0.6(a/a_i)^3 = 1.17$ would lead to the same theoretical results presented in this section, which is not a reasonable number because it is expected that the presence of wires inside the cavity will reduce, instead of increase the empty volume. As a matter of fact, inspection of the Aurasound[®] NSW2-326-8A driver geometry and its assembling on the spherical frame reveals that the cavity volume is increased by an approximate amount of $2.5 \times 10^{-5}m^3$ due to each driver. Then, if the spherical frame thickness and the driver shape were taken into account in defining CF , a correction factor of $(0.6 \times 4\pi a^3/3)/(12 \times 2.5 \times 10^{-5} + 4\pi a_i^3/3) = 0.88$ would result. By considering the wires inside the cavity, this value will increase a little so that the “optimum” volume corresponding to the $CF = 0.6$ curves presented in this section does not deviate much from the actual empty volume of the prototype cabinet, which corroborates the theory.

On the other hand, since the distributed-parameter model assumes that the loudspeaker array cabinet is a perfect sphere, a sphere radius rather than a volume must be provided. Choosing a sphere radius that yielded the actual cabinet volume would lead to good results in the compliance-dominated frequency range, similar to the lumped-parameter model. However, the interest in using the distributed-parameter model is that it takes into account the higher order cavity modes. Due to the fact that the actual cabinet is not a perfect sphere, it is not possible to ensure that using a sphere radius corresponding to the actual cabinet volume will lead to accurate cavity eigenfrequency re-

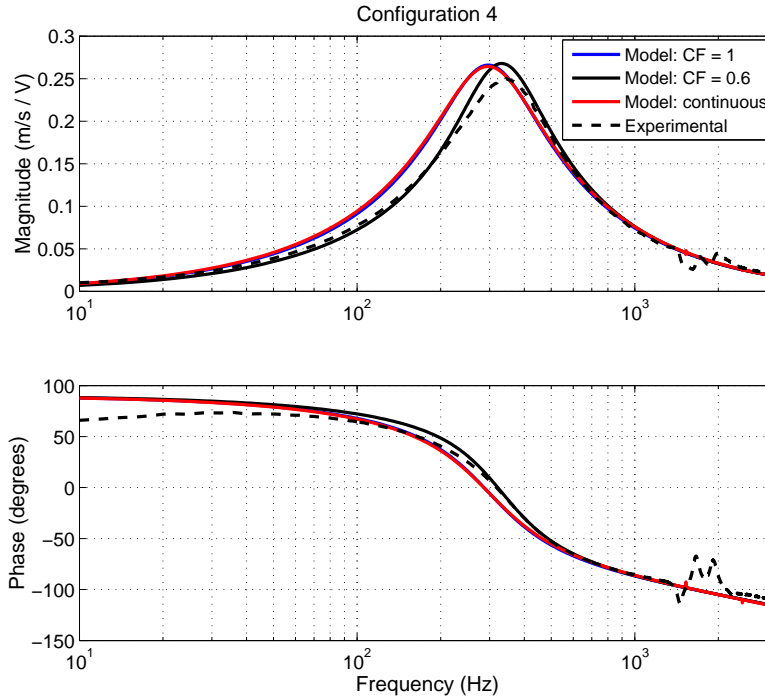


Figure 6.10: Theoretical and experimental FRFs corresponding to the config. 4 described in Tab. 6.2. The experimental FRF is the area-weighted average of FRFs measured on the driver diaphragm surface.

sults. Hence, for the sake of convenience, the outer radius of the dodecahedral array prototype was used in the distributed-parameter model results presented in this section. Finally, the adopted definition of CF permits to compare the lumped-parameter to the distributed-parameter model in the compliance-dominated frequency range by letting $CF = 1$, so that it is justified.

As shown in Figs. 6.7, 6.8, 6.9 and 6.10, the electromechanical models presented in this work are not able to accurately predict the response of a transducer of the array prototype in the frequency range approximately from 1.2 to $2kHz$. For the other frequencies, the corrected lumped-parameter model can be used to evaluate the frequency response. The discrepancies between experimental and theoretical results over this frequency range are due to the superposition of two effects: the actual non-spherical sound field inside the prototype cavity (which includes damping, actual driver geometry and wires) and the non-rigid body motion of the drivers suspension. The latter can be taken into account by modeling the actual vibration pattern of the driver suspension, whereas a complex enclosure model should be used in order to take the former into account. However, since it is not yet known how these effects influence the sound radiation pattern, the pertinence of developing such an improved model could be questioned in practice. As far as the cavity model is concerned, the results presented here show that the response of a passive driver is harder to predict

than the response of an active driver. However, one may conjecture that the passive drivers of a spherical array do not contribute as much as the active drivers to the radiated sound field, so that the development of a complex cavity model would not be justified. This hypothesis should be tested in a future work.

6.4 Sound radiation

The sound radiation prediction model described in section 3.1.2 assimilates each driver membrane of the spherical array as a convex spherical cap that oscillates with a constant radial velocity amplitude across its surface. However, the membrane of the Aurasound® NSW2-326-8A driver is a concave spherical cap rather than a convex one. Since direct radiator loudspeakers with convex and concave membranes present different radiation patterns in the high-frequency range [50, 51], it is not expected that the proposed method will be able to predict the sound radiation from the spherical loudspeaker array prototype for all frequencies. Moreover, the diaphragm suspension assembly of each driver is assumed to be a rigid body in the sound radiation model, which is not a good assumption for all frequencies of interest, as shown in the previous section. Then, additional error is introduced due to the uneven deformation of the driver suspension.

In order to evaluate the effects of the non-ideal geometry and vibration of the transducers on the radiation pattern, the sound directivity of the spherical array prototype operating under distinct conditions was measured in an anechoic chamber. In the following, the experimental set-up is briefly described and measurement data are presented and compared to simulation results. Since it was shown in section 6.3 that only the first cavity mode affects the vibration of the drivers' membranes, for the sake of simplicity, the author has decided to take the internal acoustic coupling into account by using the lumped-parameter model presented in section 3.2.2.1, i.e., the high-order cavity modes are neglected in the theoretical results presented here.

6.4.1 Experimental procedures

Figure 6.11 shows the experimental set-up for the directivity measurements. The driver and microphone labels are indicated in Fig. 6.12. The loudspeaker array prototype was mounted at the center of a circular microphone array with radius $r_0 = 0.70m$ and with $N_t = 28$ transducers equally spaced, so that the angular spacing between consecutive microphones is approximately $\Delta\theta = 6.7^\circ$. The antenna was attached to an automatic turntable whose rotation axis passes through the center of

the loudspeaker array prototype. Measurements were taken at $N_p = 49$ different antenna positions with an angular spacing between consecutive positions of approximately $\Delta\phi = 7.0^\circ$, except for spacing between positions 1 and 49, in which $\Delta\phi = 24.0^\circ$ was used due to mechanical constraints.



Figure 6.11: Experimental set-up for the directivity measurements at the large anechoic chamber of the Laboratory of Mechanics and Acoustics of the National Center for Scientific Research (UPR-7051, CNRS, Marseille, France).

Condenser microphones with Panasonic® electret capsules and omnidirectional characteristics were used. Because of the low cost and small size of these microphones, a large number of them could be dealt with and a relatively non-diffracting antenna could be obtained in a simple way. The calibration was performed in January 2010 at the LMA large anechoic chamber by using a commercial pistonphone (B&K type 4231) with the microphones mounted on the circular frame. The resulting microphone sensitivities are presented in Tab. 6.3 .

For each microphone and antenna position, an FRF between input driver voltage and output sound pressure at the microphone position was measured. White noise at a sampling rate of 44100Hz was used as the input signal. Then, the experimental set-up led to a total of $N_t N_p = 1372$ samples of the radiation pattern. Many directivity patterns were measured corresponding to different combinations of magnitude and phase of the driver voltages. For each directivity measurement run, the FRF input was taken at a specific driver of the loudspeaker array.

In the first set of experiments, only one driver was made active through application of a

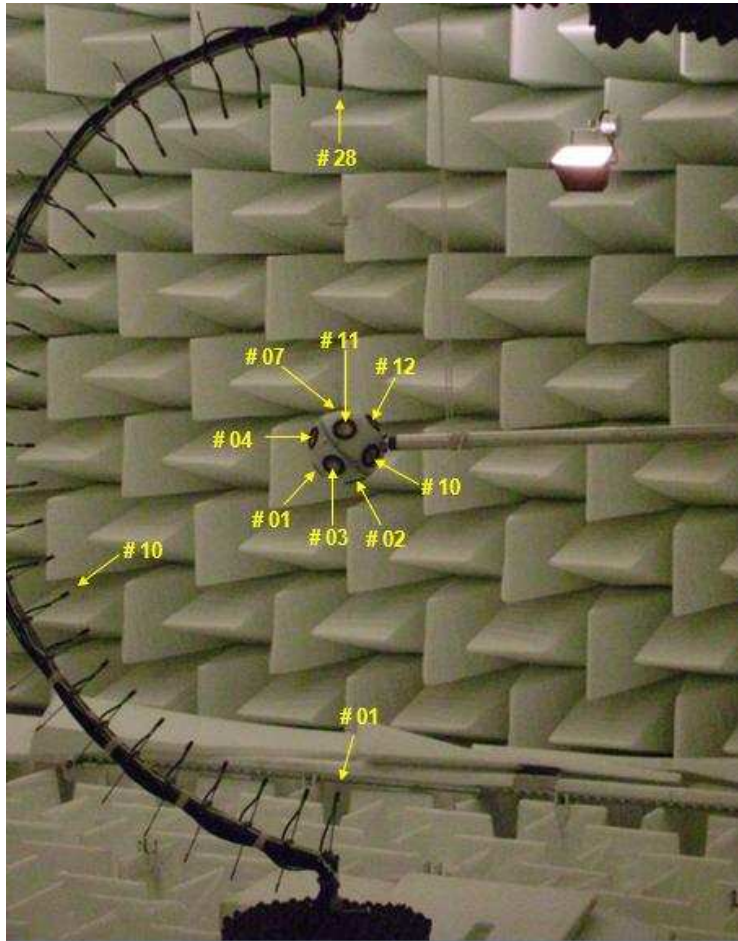


Figure 6.12: Experimental set-up for the directivity measurements with the driver and microphone labels indicated.

voltage of $0.93V_{rms}$ in order to approximately obtain the radiation pattern of each one of the 12 drivers mounted on the sphere. It is worth noting that the other (passive) drivers may also contribute to the resulting sound field due to the acoustic coupling. Therefore, it is not rigorous to state that the resulting directivity data corresponds to the radiation pattern of a single driver mounted on a sphere.

Next, voltages proportional to the values presented in each column of the Tab. C.6 were applied to the array drivers in order to obtain the directivity patterns of each one of the 12 acoustic radiation modes of the spherical array. The largest voltage value was $0.93V_{rms}$, corresponding to driver #01 and ARM #05. Finally, directivity patterns corresponding to linear combinations of radiation modes in a same radiation group were measured.

For the sake of clarity, only a few results considered as the most relevant by the author are presented here, namely, some FRF magnitude curves at a given microphone position and some

Table 6.3: Sensitivities of the electret microphones used in the directivity measurements; calibration performed in january 2010.

Microphone	Sensitivity (mV/Pa)	Microphone	Sensitivity (mV/Pa)
#01	25.8	#15	22.9
#02	25.8	#16	26.3
#03	27.5	#17	18.6
#04	24.6	#18	32.1
#05	23.9	#19	26.9
#06	18.5	#20	28.3
#07	23.6	#21	22.8
#08	20.4	#22	22.3
#09	27.5	#23	24.4
#10	35.5	#24	23.7
#11	25.7	#25	17.8
#12	31.9	#26	24.6
#13	20.0	#27	24.7
#14	19.8	#28	21.4

directivity patterns at given frequencies. The former are summarized in Tab. 6.4.

Table 6.4: Measurement configurations for evaluating some FRFs between an input driver voltage and an output sound pressure taken at the mic #10. The antenna is positioned so that mic #10 is approximately in front of the driver #01.

Configuration	Active drivers	Input
1	#01	#01
2	#12	#12
3	#04	#04
4	#10	#10
5	ARM #01	#01
6	ARM #02	#12
7	ARM #05	#12

Finally, it is worth mentioning that all passive drivers were connected to amplifiers during the experiments, so that they were operating in a closed-circuit configuration.

6.4.2 Results and discussion

Figures 6.13 and 6.14 present the magnitude of the FRFs corresponding, respectively, to the configurations #1 to #4 and #5 to #7 described in Tab. 6.4. The sound pressure is taken at the mic #10. The antenna is positioned so that mic #10 is approximately in front of the driver #01, which is approximately the situation represented in Fig. 6.12.

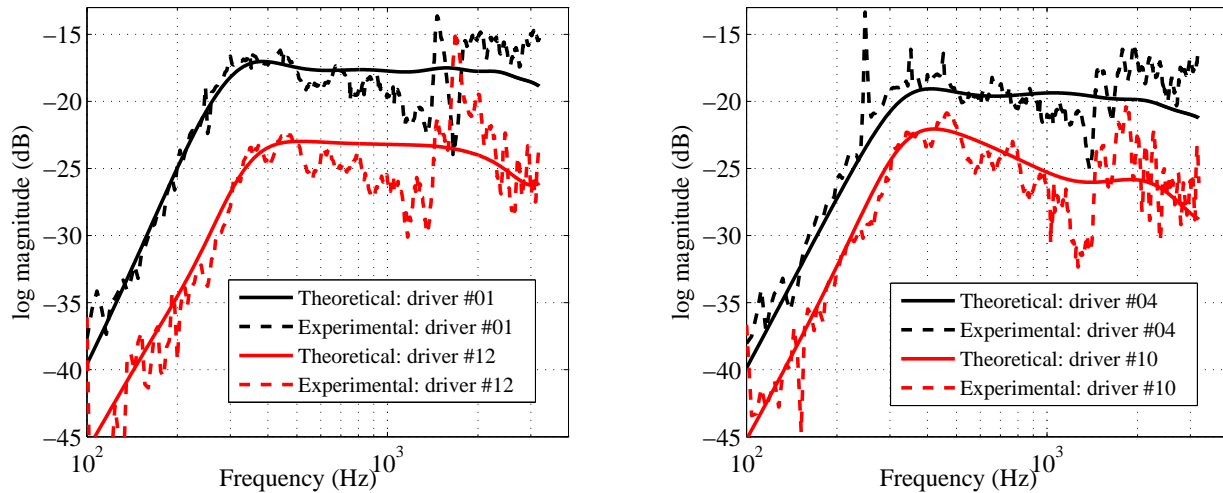


Figure 6.13: Theoretical and experimental FRFs corresponding to the configurations #1 to #4 shown in Tab. 6.4.

Comparison of Figs. 6.12 and 6.13 reveals that the FRF magnitude decreases as the angle between the microphone position and the symmetry axis of the active driver increases, as expected. This is due to the acoustical shadowing produced by the sphere and to the radiation pattern of a single driver, in which the main radiation direction is the driver symmetry axis.

Figure 6.14 shows that, in the low-frequency range, the FRF magnitude decreases with increasing the complexity of the acoustic radiation mode. This is due to the fact that, at low frequencies, the radiation efficiency decreases as the radiation mode complexity increases, as shown in Fig. 5.4.

The theoretical results present good agreement with the experimental data in the low-frequency range, as shown in Figs. 6.13 and 6.14. However, as frequency increases, the theoretical model is no longer able to predict the actual sound pressure spectrum at a given measurement point. It is worth noting that the experimental curves present a remarkable behavior change around 1600 Hz , which is due to the uneven diaphragm deformation shown in Fig. 6.6 and to the first cavity mode. As a matter of fact, since the mechanical resonance of the driver suspension occurs at a frequency very close to the first cavity eigenfrequency, it is not possible to determine their individual contributions to the discrepancy observed in the corresponding frequency range between sound pressure simulation results and sound pressure experimental data.

Figures 6.15 to 6.28 show the theoretical and experimental directivity patterns corresponding to some acoustic radiation modes of the dodecahedral array prototype for specific frequencies. Notice that one sector of grid points is missing in the directivity plots, which is due to the mechanical constraints mentioned in section 6.4.1. Simulation results match fairly well the experimental data

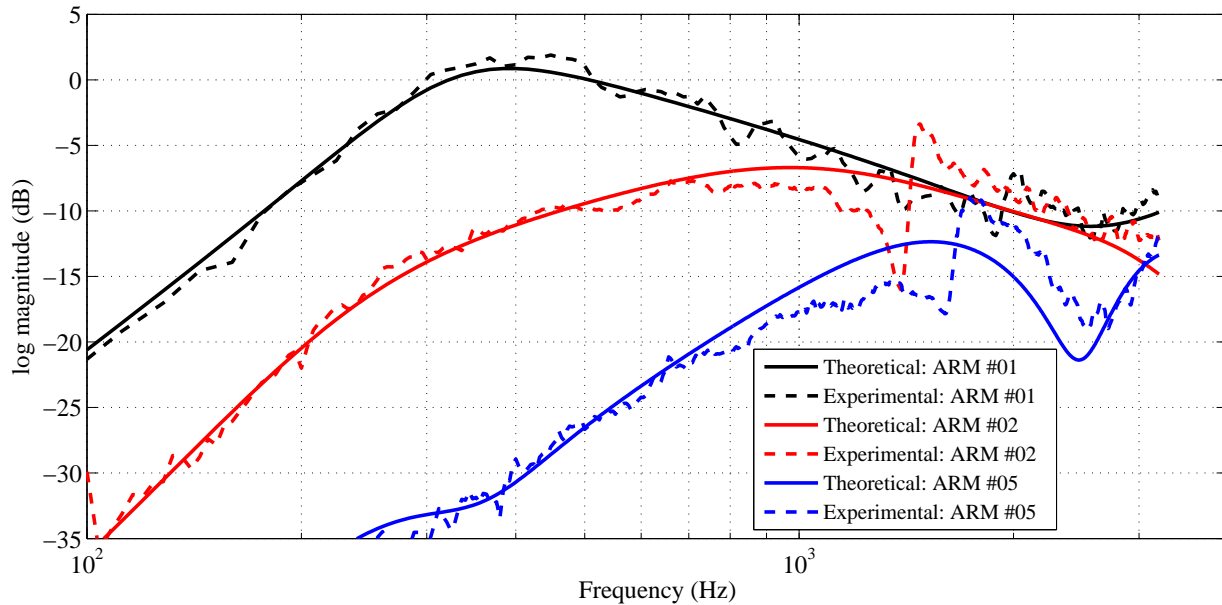


Figure 6.14: Theoretical and experimental FRFs corresponding to the configurations #5 to #7 shown in Tab. 6.4.

(notice that the FRF magnitude is presented in linear scale), although inspection of the latter reveals that the variation of the FRF magnitude over the zenith angle — unlike over the azimuthal angle — is not as smooth as the theoretical results. This can be due to a calibration problem between the microphones of the circular antenna. Notice that each microphone corresponds to a zenith angle.

Despite the fact that the radiation model is not able to predict the sound pressure spectrum at a given point for high frequencies, Figs. 6.18, 6.22, 6.26 and 6.28 reveal a fairly good correspondence between simulation results and experimental data as far as the overall directivity pattern is concerned. This indicates that the velocity magnitude and phase relations between distinct drivers are more important than the vibration pattern of each individual driver membrane to the resulting directivity pattern.

For frequencies higher than approximately 1000 Hz , there are some perturbations on the experimental directivity patterns near the poles, as shown in Figs. 6.17, 6.18, 6.20, 6.26 and 6.28. This is probably due to wave reflections from the frame on which the microphone antenna is mounted.

As discussed in sections 3.1.2.1 and 4.2, the directivity patterns associated to the radiation modes of a dodecahedral loudspeaker match real-valued spherical harmonic functions for low ka values. If this condition is satisfied, a pure spherical harmonic pattern with an angular orientation other than that produced by a single radiation mode can be obtained by making a linear combination of the radiation modes within the corresponding radiation group. For example, it is possible to

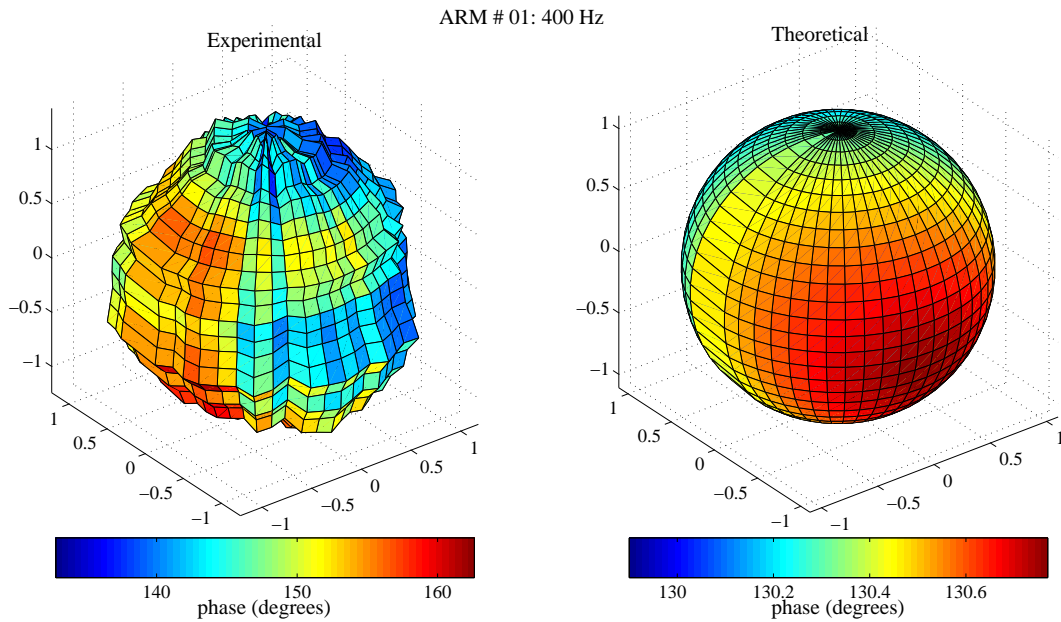


Figure 6.15: Theoretical and experimental directivity pattern for the ARM #01 at 400Hz.

synthesize a rotated dipole with any axis orientation by choosing a proper combination of the radiation modes #02 to #04. The weights to be applied to each radiation mode can be evaluated from the zyz Euler angles describing the desired rotation by using Eqs.(2.32), (2.33) or (2.34).

Figures 6.29 and 6.30 show, respectively, a rotated dipole and a rotated lateral quadrupole obtained using the equations cited above. Again, there is fair agreement between the experimental and theoretical results. It is worth mentioning that several additional rotated patterns obtained from different combinations of orthogonal dipoles (ARM #02 to #04) or real-valued spherical harmonics of order 2 (ARM #05 to #09) have been measured and the results have always revealed a fair agreement. Hence, the dodecahedral loudspeaker prototype described in this work can be used to produce directivity patterns that can be electronically rotated. It is expected that this could be done in real-time, which may find applications in electroacoustic music.

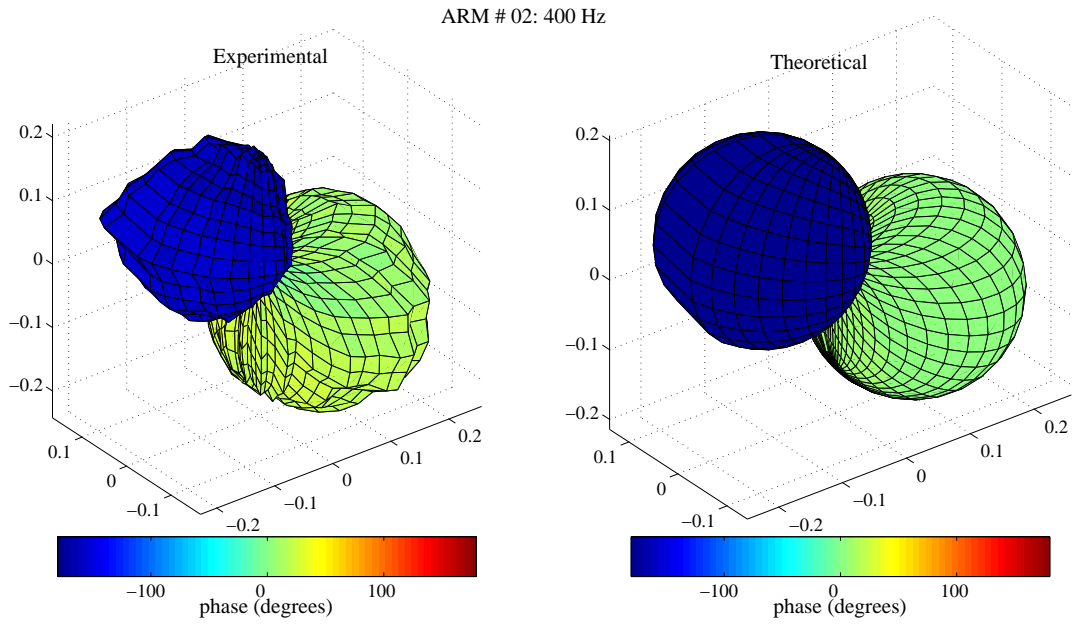


Figure 6.16: Theoretical and experimental directivity pattern for the ARM #02 at $400Hz$.

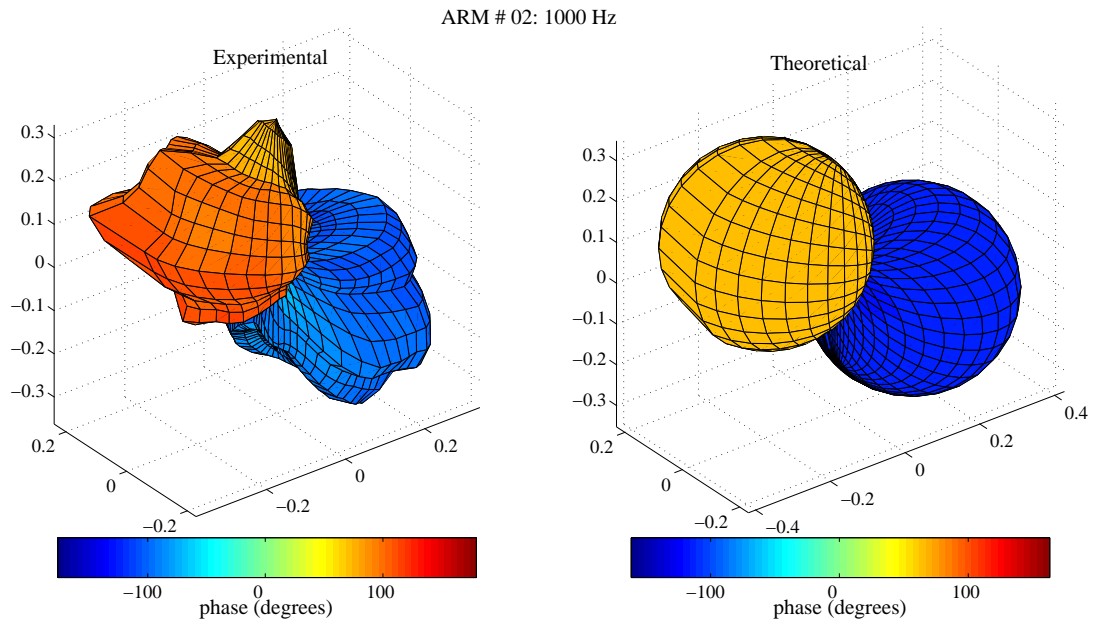


Figure 6.17: Theoretical and experimental directivity pattern for the ARM #02 at $1000Hz$.

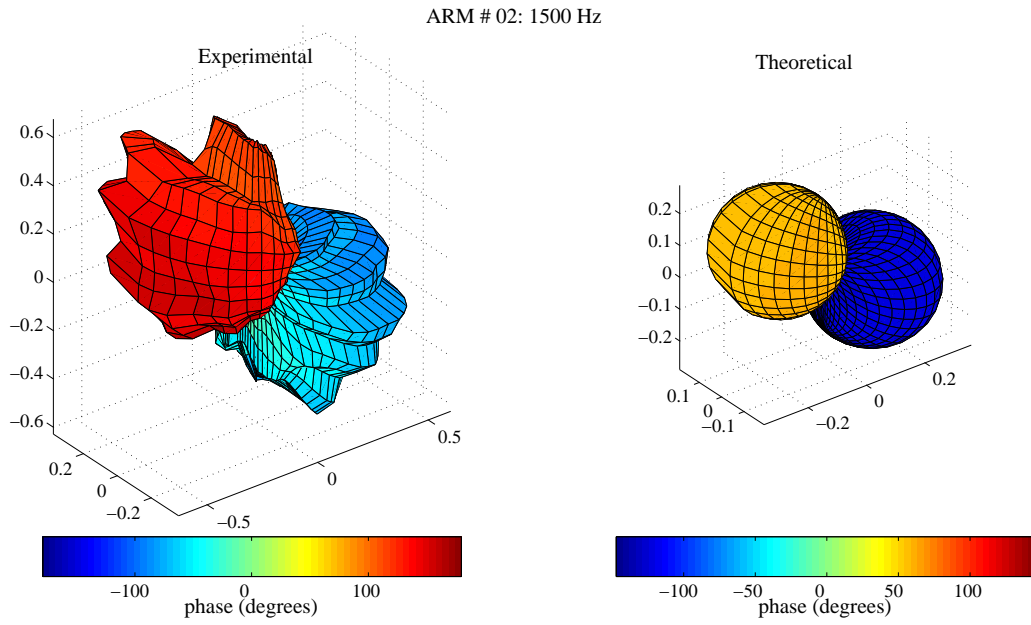


Figure 6.18: Theoretical and experimental directivity pattern for the ARM #02 at 1500 Hz.

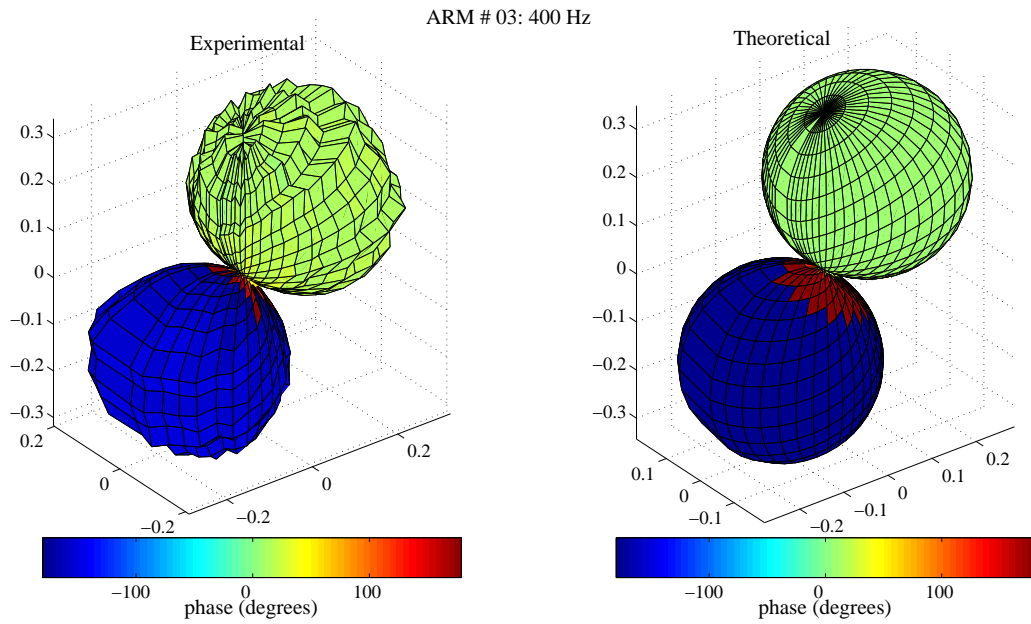


Figure 6.19: Theoretical and experimental directivity pattern for the ARM #03 at 400 Hz.

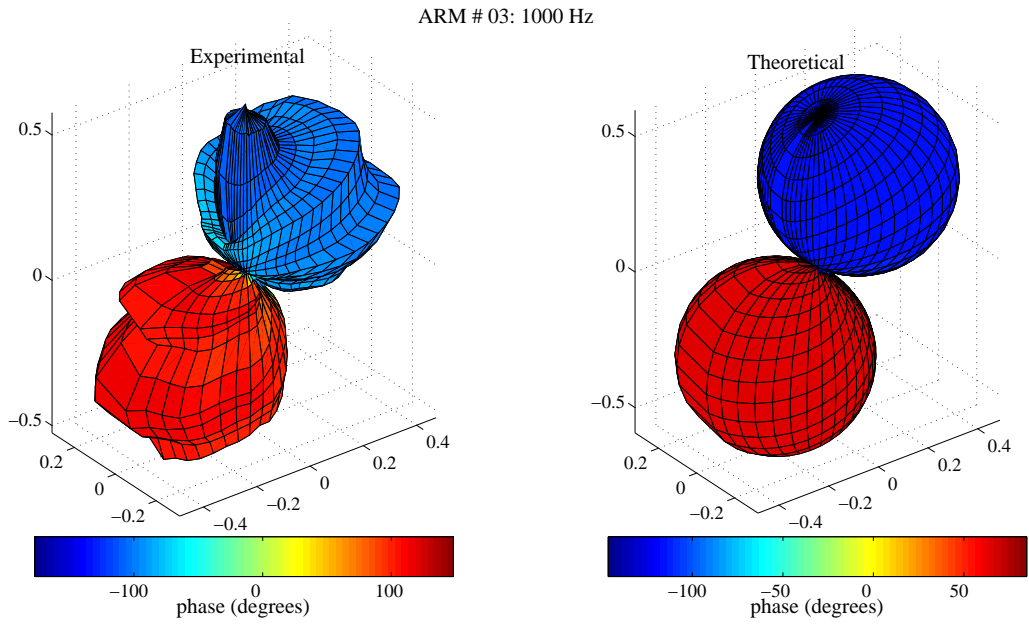


Figure 6.20: Theoretical and experimental directivity pattern for the ARM #03 at $1000Hz$.

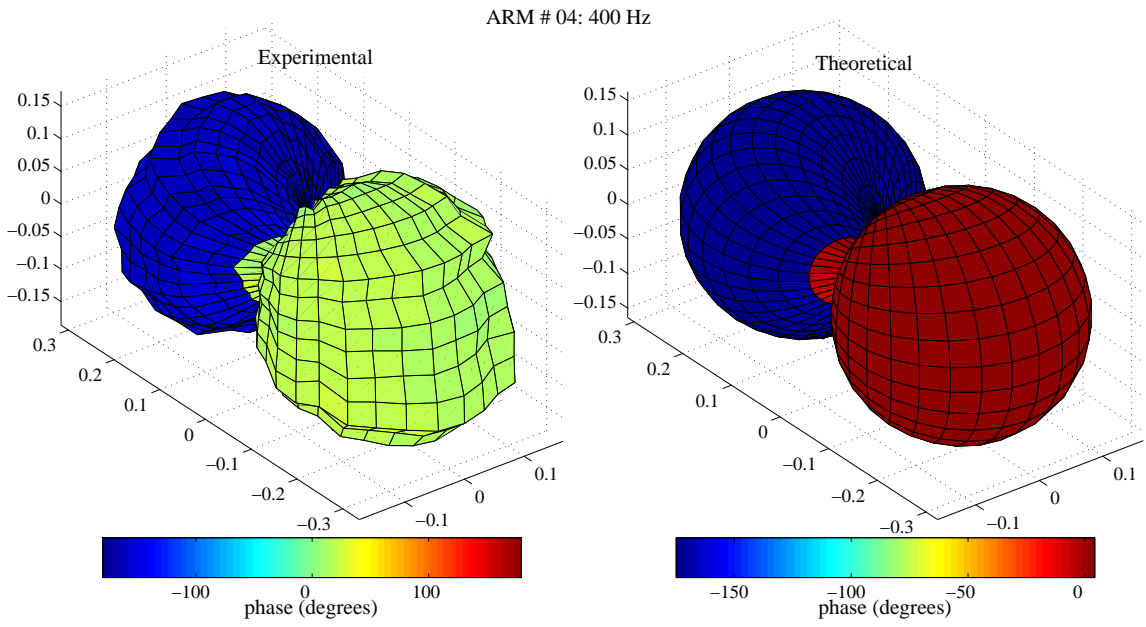


Figure 6.21: Theoretical and experimental directivity pattern for the ARM #04 at $400Hz$.

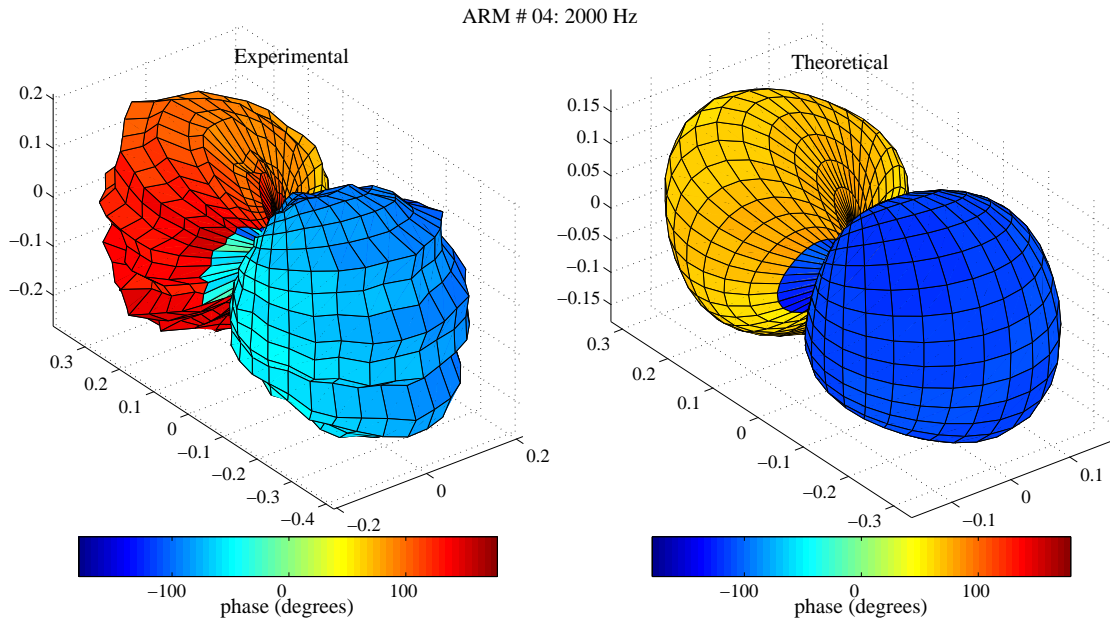


Figure 6.22: Theoretical and experimental directivity pattern for the ARM #04 at $2000Hz$.

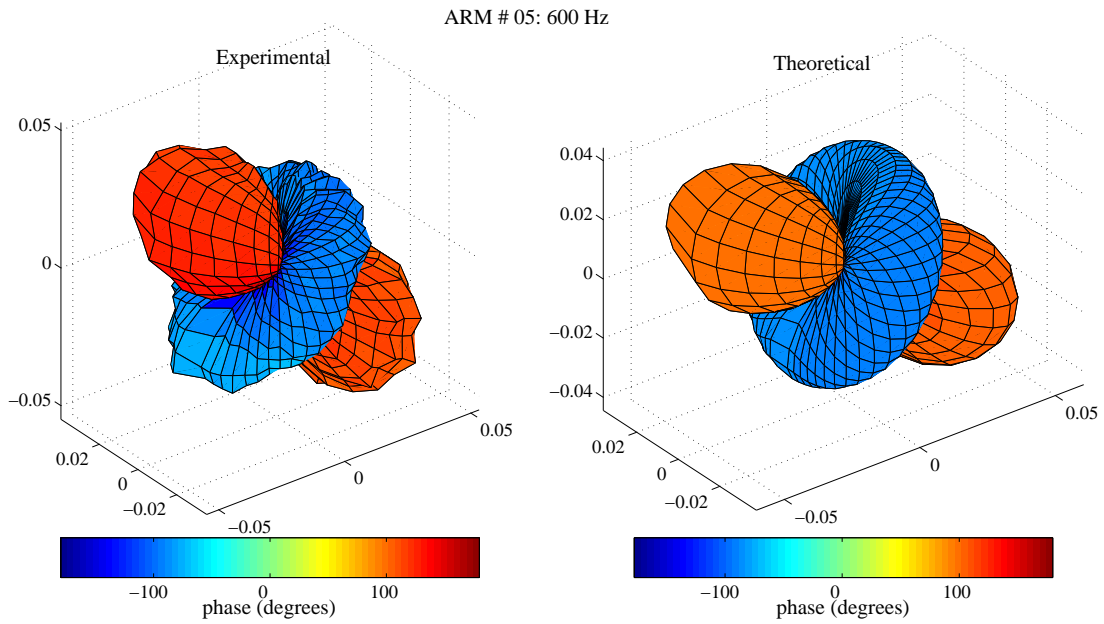


Figure 6.23: Theoretical and experimental directivity pattern for the ARM #05 at $600Hz$.

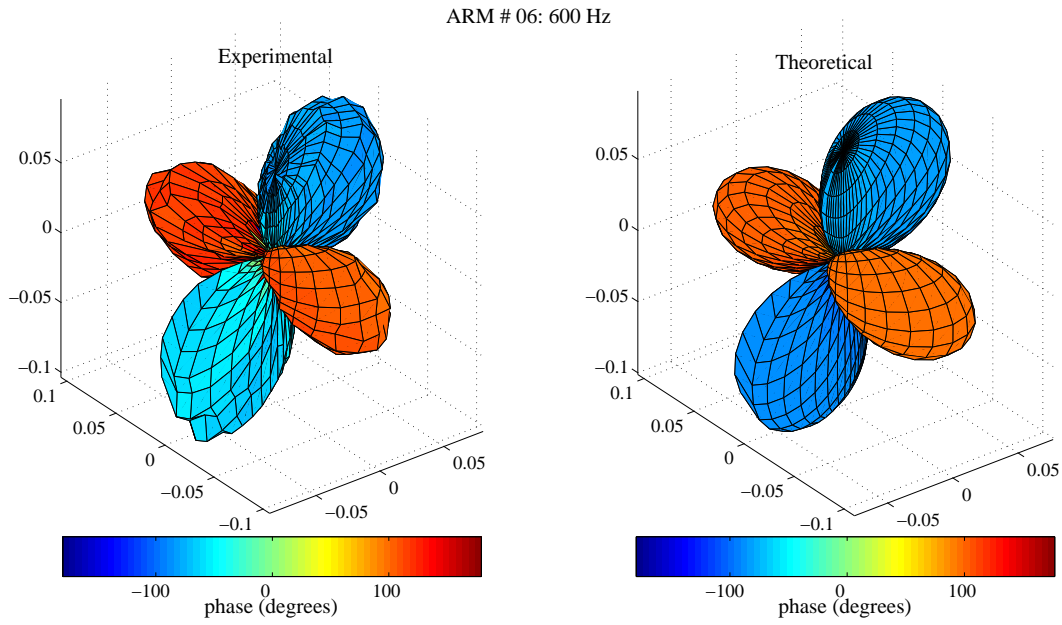


Figure 6.24: Theoretical and experimental directivity pattern for the ARM #06 at $600Hz$.

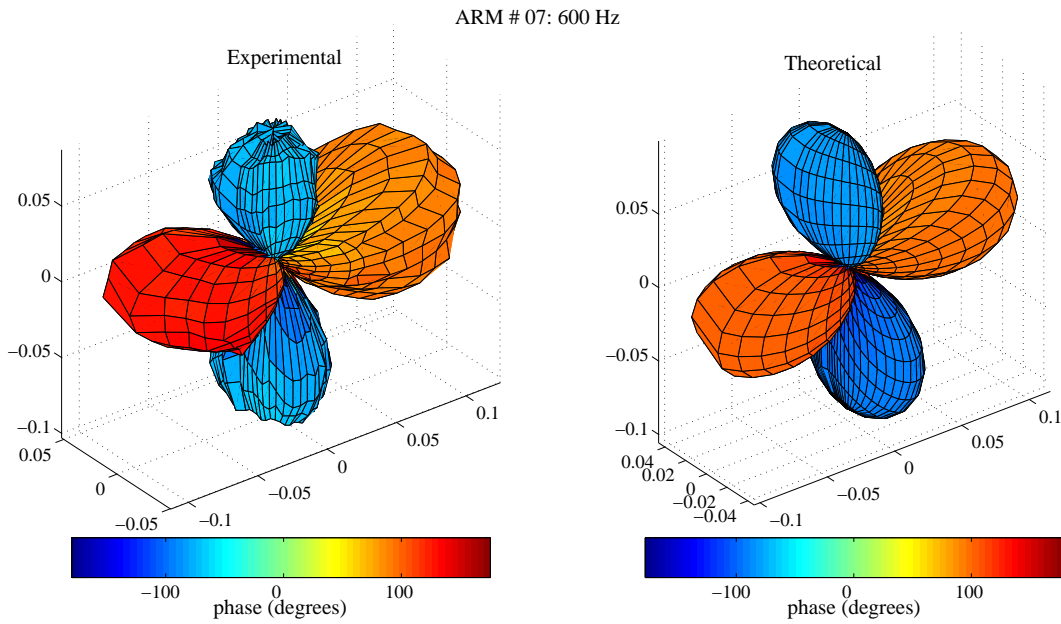


Figure 6.25: Theoretical and experimental directivity pattern for the ARM #07 at $600Hz$.

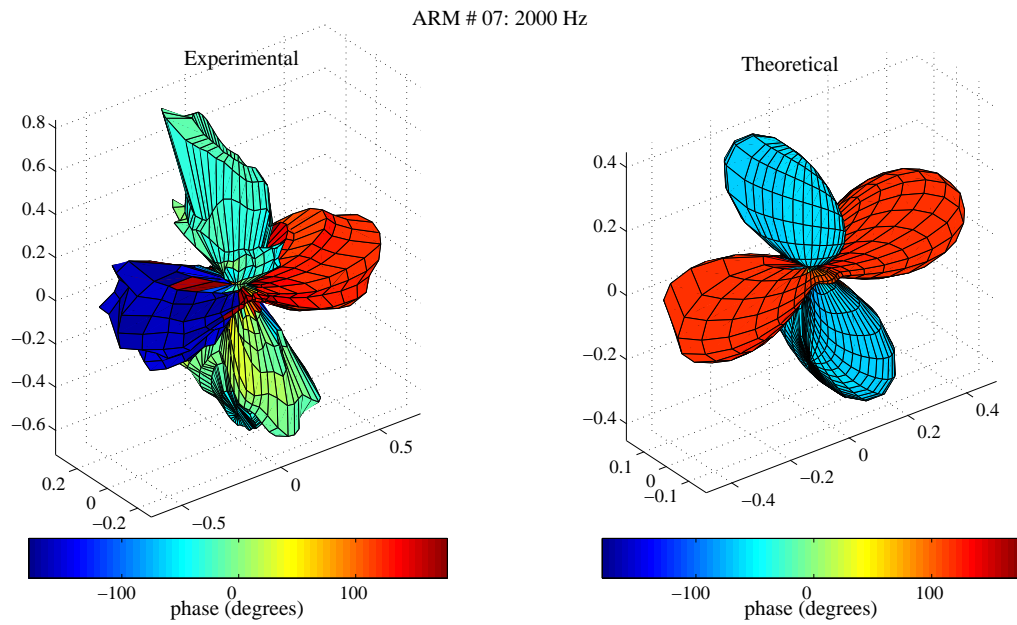


Figure 6.26: Theoretical and experimental directivity pattern for the ARM #07 at $2000Hz$.

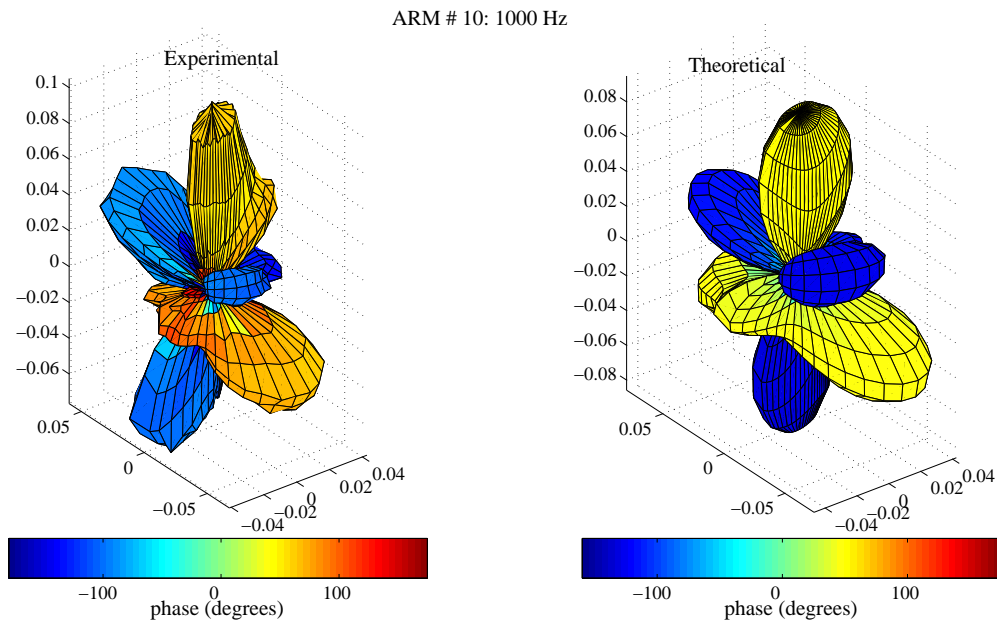


Figure 6.27: Theoretical and experimental directivity pattern for the ARM #10 at $1000Hz$.

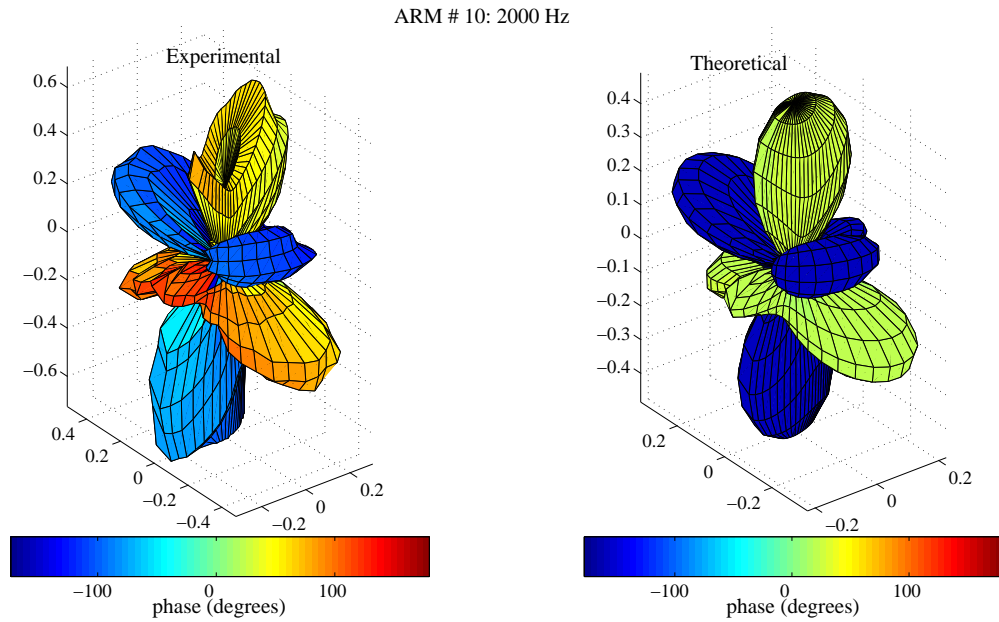


Figure 6.28: Theoretical and experimental directivity pattern for the ARM #10 at $2000H z$.

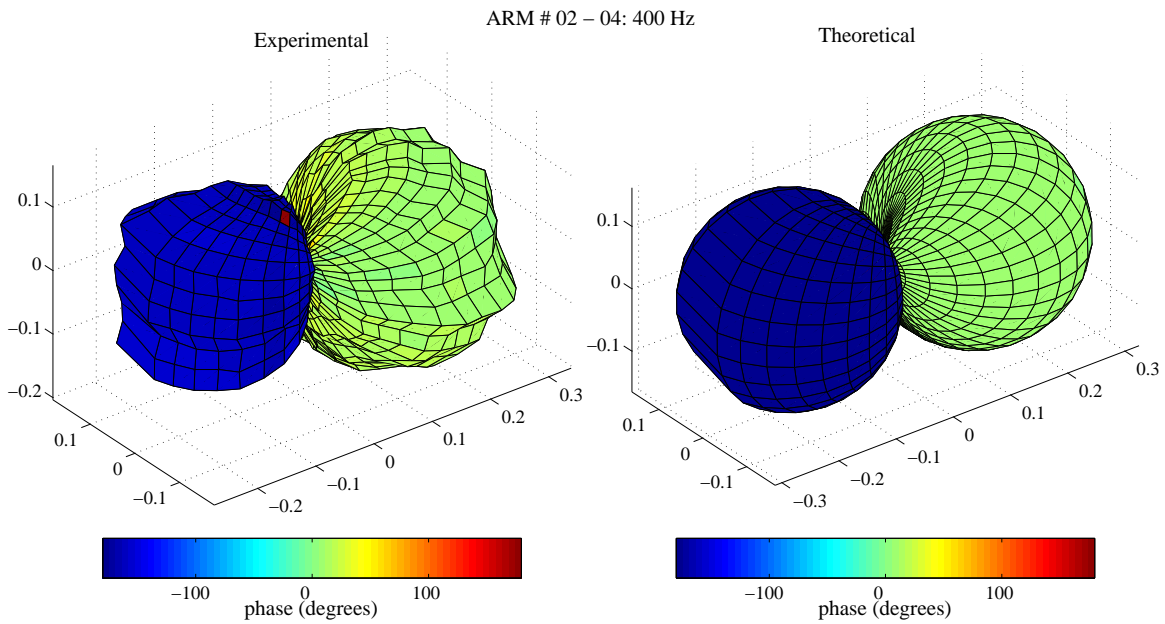


Figure 6.29: Theoretical and experimental directivity pattern at $400H z$ corresponding to a rotated dipole obtained from a linear combination of the ARM #02 to #04.

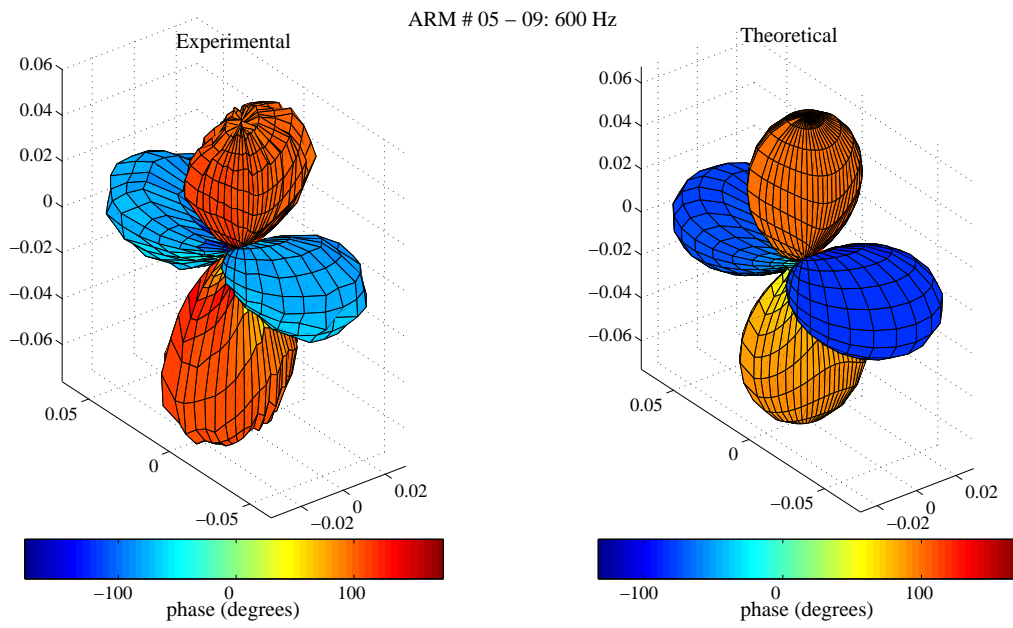


Figure 6.30: Theoretical and experimental directivity pattern at 600 Hz corresponding to a rotated lateral quadrupole obtained from a linear combination of the ARM #05 to #09.

Chapter 7

Conclusion

As stated in chapter 1, the main contributions of this thesis are:

- The characterization of an improved basis for directivity representation, namely, the acoustic radiation modes discussed in sections 2.3.2 and 3.1.2;
- The investigation of the electromechanical behavior of compact loudspeaker arrays. This was provided through the development of the electromechanical models presented in section 3.2, which were experimentally validated from laser Doppler vibrometry measurements in section 6.3;
- The comparative analysis of distinct optimization criteria to derive the signals that must feed the drivers in order to reproduce a given directivity pattern. In section 4.3 of this work, the standard least-squares (phase concerned) was compared to the magnitude least-squares (phase not concerned). The latter was shown to perform better.

In the following, these topics are summarized and suggestions for further work are presented.

7.1 Directivity representation

In this work, acoustic radiation modes were applied to sound field synthesis by a spherical loudspeaker array. As described in section 3.1.2, the transducer array was modeled as a discrete sphere, i.e., a rigid sphere on which a set of independent spherical caps is mounted. Analytical expressions

were presented to evaluate the radiated field, the radiation efficiency and the acoustic radiation modes of spherical arrays. In addition, the spherical cap approach was experimentally validated through directivity measurements of a spherical array prototype performed in an anechoic chamber, as shown in section 6.4.

It was shown in section 3.1.2.1 that the radiation efficiency of a spherical array decreases as the complexity of the radiation mode increases and with decreasing frequencies. Low radiation efficiency means that high loudspeaker diaphragm displacements must be achieved in order to produce meaningful sound pressure levels. It is worth noting that increasing the number of loudspeakers does not significantly improve the radiation efficiency at low frequencies, since even a continuous sphere does not radiate efficiently at low frequencies.

The farfield radiation pattern of each radiation mode of a discrete sphere matches a real low-order spherical harmonic at low frequencies. However, this does not occur as frequency increases, when high-order spherical harmonics start to propagate to the farfield, so that radiation modes lead rather to a combination of many spherical harmonics of distinct orders.

Using radiation modes to describe the array directivity presents several advantages over spherical harmonics. Unlike the latter, the former constitute a finite set of vectors that spans a subspace on which any radiation pattern the array is able to reproduce can be projected. Furthermore, the eigenvalue analysis that must be carried out in order to obtain the radiation modes leads also to the radiation efficiencies of the modes, i.e., the low-frequency constraints in sound reproduction by a spherical array are naturally evaluated. In addition, these modes radiate sound energy independently, so that the total sound power is given by summing the individual contributions of each mode. Radiation modes also lead to a reduced number of active channels due to the fact that some modes do not radiate sound energy at some frequency ranges that can be determined through inspection of their radiation efficiencies. Thus, it is useless to take such modes into account and so this approach avoids overloading the loudspeakers. Finally, radiation modes are not restricted to spherical shapes. So, it is expected that most of the ideas presented here can be extended to non-spherical loudspeaker arrays and will allow to take into account the actual vibration pattern and shape of the loudspeakers.

Therefore, to provide the array with preprogrammed surface velocity distributions corresponding to its acoustic radiation modes is a better control strategy than using spherical harmonics as elementary directivities.

7.2 Electromechanical behavior of spherical loudspeaker arrays

In section 3.2, two electromechanical models of a compact loudspeaker array for radiation control were presented: a lumped-parameter model and a distributed-parameter model. Both take into account the acoustic coupling between drivers and can be used to compute the diaphragm velocities of the array elements from the voltages that feed them and vice versa. In order to evaluate the accuracy of the proposed models, a compact spherical array prototype with 12 drivers was subjected to electrical impedance and LDV surface velocity measurements, as discussed in sections 6.2 and 6.3, respectively. Since the spherical array prototype presents a hollow spherical cavity on which the transducers are mounted, the acoustic coupling effects could be experimentally investigated.

In the lumped-parameter model, the enclosure is modeled as an acoustic compliance and, in the distributed-parameter model, the cavity is assumed to be a perfect rigid sphere so that the analytical solution of the Helmholtz equation in spherical coordinates can be used. The latter, unlike the former, takes into account the acoustic modes of the spherical cavity that affect the system response as frequency increases. Therefore, the distributed-parameter model leads to singularities at frequencies corresponding to the spherical cavity eigenfrequencies. However, experimental results demonstrated that only the first cavity eigenfrequency (approximately 1.5 kHz) affects the system behavior, so that one may conclude that higher order cavity modes have a negligible contribution to the membrane velocity.

On the other hand, it was observed that the results obtained by both the distributed-parameter and the lumped-parameter models do not match the experimental data in the compliance-dominated frequency range. This is due to the presence of wires and driver components inside the cavity, so that the actual cavity shape deviates from the ideal sphere. However, this could be dealt with by applying a correction factor to the spherical cavity volume when using the lumped-parameter model. In fact, the corrected lumped-parameter model presented good agreement with experimental data, except for the frequency range approximately from 1.2 to 2 kHz, which comprises the first cavity eigenfrequency. In addition, the discrepancy between the corrected lumped-parameter model results and the experimental data in this frequency range is also due to the fact that the inner and outer borders of the driver suspension vibrate practically in opposite phase near 1.6 kHz.

It was shown that the electromechanical behavior of the array prototype cannot be completely described by assuming that the diaphragm suspension assembly of each driver is a rigid body. In addition, the non-spherical geometry of the enclosure complicates the internal sound field near the first cavity eigenfrequency. Coincidentally, for the spherical array prototype studied in this work, the mechanical resonance of the driver suspension occurs at a frequency very close to the first acoustical

resonance of the cavity. Therefore, it was not possible to determine their individual contributions to the discrepancy observed in the corresponding frequency range between sound pressure simulation results and sound pressure experimental data, which was presented in section 6.4.2. Anyway, theoretical results can be improved by using a flexible driver membrane model and by taking into account the uneven suspension deformation. On the other hand, the effects of the acoustical resonance of the cavity can be reduced by working on the enclosure design, e.g., by adding an acoustic absorbent material in the cavity.

The combined use of radiation modes and the proposed electromechanical models led to a simple way to compare the performance of the two different enclosure designs that have been described in the literature, namely, drivers sharing a common hollow cavity and each driver with its own sealed cavity. Simulation results for a specific spherical array indicated that the former does not provide a relevant reduction in the voltages that feed the drivers in the operating frequency range. Nevertheless, a common enclosure is easier to build, the acoustical coupling can be predicted by the electromechanical models proposed in this work, and the experimental results revealed that only the first cavity resonance affects the system dynamics (this effect can be reduced, as discussed above). Hence, one may conclude that there is no reason to build a complicated mechanical frame in order to provide each driver with its own sealed cavity.

Finally, it was shown in chapter 5 that the acoustic radiation modes of a Platonic shaped loudspeaker are the eigenvectors of the transduction matrix for drivers sharing a common cabinet, which greatly simplifies the equalization filter design.

7.3 Optimization criteria

The capability of Platonic shaped loudspeakers in reproducing spherical harmonic patterns was evaluated in the least-squares sense in chapter 4. The design of a spherical loudspeaker array for spherical harmonic synthesis must be a compromise between low and high frequency reproduction: at high frequencies, spatial aliasing artifacts degrade the spherical harmonic synthesis, which can be dealt with by decreasing the radius of the spherical array. On the other hand, at low frequencies one has the low radiation efficiency problem, which can be dealt with by increasing the radius of the spherical array.

Among the Platonic solids having the same midradius, the dodecahedron presents the largest surface area available for assembling the drivers, therefore yielding a higher sound power for a given midradius. Furthermore, it was shown that using a dodecahedral source leads to a smaller

error when synthesizing the monopole and the dipole. Thus, the dodecahedral loudspeaker presents the best compromise between complexity of the controllable radiation patterns, number of channels and sound power. It is worth noting that the only benefit of using an icosahedron is to provide control over some spherical harmonics of order $n = 3$ within a very limited frequency range. No improvement either in the sound power level or in the synthesis error for low-order spherical harmonics is achieved.

An example of directivity synthesis in which the target pattern is not a spherical harmonic was provided in section 4.3. Two different cost functions were used and compared: the standard RSME (phase concerned) and the magnitude RMSE (phase not concerned). It was shown that excluding the phase error of the cost function greatly reduces the magnitude error in directivity synthesis, which increases significantly the application of loudspeaker arrays toward high frequencies. This reveals that the relation between the phase and magnitude spatial distributions depends largely on the radiating body characteristics, so that magnitude synthesis does not yield phase synthesis and vice versa. Finally, it is worth noting that phase can be neglected only in farfield synthesis.

7.4 Further research

As discussed in section 3.1.2.1, it was observed that the acoustic radiation modes of a Platonic solid loudspeaker do not depend on frequency, which is a very useful result because it leads to a basis for directivity representation that can be used for all frequencies and possesses the advantages summarized in section 7.1. However, this result has not been rigorously proved. In fact, the frequency independence property for radiation modes is not required. For the frequency range of interest, it is sufficient that the efficient radiation modes at any frequency can be decomposed over the efficient radiation modes obtained for the maximum frequency of interest. Such a “nesting” property holds analytically for spherical, cylindrical and plane radiators (with infinite number of degrees of freedom), whereas it is a conjecture for some radiators other than these ones [43]. Then, further research concerning the “nesting” property of the radiation modes of spherical loudspeaker arrays would help to evaluate the applicability of such a basis to different radiating bodies and to sampling strategies over the sphere other than Platonic.

In the electromechanical loudspeaker models proposed in this work, the membrane suspension assembly is assumed to be rigid. This is one of the main shortcomings of these models, which would benefit from the development of a multi-degree-of-freedom approach describing the mechanical behavior of the driver membrane and suspension.

It was shown in section 6.3 that the driver response is affected by the first cavity mode for frequencies close to the corresponding eigenfrequency. Then, alternative enclosure designs including, for example, an acoustic absorbent material can be investigated in order to minimize the effects of cavity resonances on the loudspeaker array performance.

Finally, the magnitude error in the directivity synthesis is greatly reduced by excluding the phase error of the cost function, as shown in section 4.3. This suggests that using a cost function based on a psychoacoustic metric rather than on the physical characteristics of the sound field may significantly increase the realism of the synthesized pattern. Therefore, the directivity synthesis by a compact loudspeaker array would benefit from further research on the perceptual features of directivity patterns.

Bibliography

- [1] J. Meyer, *Acoustics and the Performance of Music: Manual for Acousticians, Audio Engineers, Musicians, Architects and Musical Instrument Makers*. New York: Springer-Verlag, 5th ed., 2009.
- [2] F. Otondo, “Recent spatialisation trends in electroacoustic music,” in *Proceedings of the Electroacoustic Music Studies Conference*, (Leicester, UK), June 2007.
- [3] M. Trochimczyk, “From circles to nets: on the signification of spatial sound imagery in new music,” *Computer Music Journal*, vol. 25, no. 4, pp. 39–56, 2001.
- [4] A. J. Berkhout, D. de Vries, and P. Vogel, “Acoustic control by wave field synthesis,” *Journal of the Acoustical Society of America*, vol. 93, pp. 2764–2778, May 1993.
- [5] M. A. Gerzon, “Periphony: with-height sound reproduction,” *Journal of the Audio Engineering Society*, vol. 21, pp. 2–10, Jan. 1973.
- [6] J. Blauert, *Spatial Hearing: The Psychophysics of Human Sound Localization*. London: MIT Press, 1997.
- [7] E. Zwicker and H. Fastl, *Psychoacoustics — Facts and Models*. New York: Springer-Verlag, 3rd ed., 2007.
- [8] A. V. Oppenheim, R. W. Schaffer, and J. R. Buck, *Discrete-Time Signal Processing*. New Jersey: Prentice-Hall, Inc., 2nd ed., 1999.
- [9] F. Otondo and J. H. Rindel, “New method for the directional representation of musical instruments in auralizations,” in *Proceedings of the International Computer Music Conference*, (Göteborg, Sweden), pp. 248–251, Sept. 2002.
- [10] F. Otondo and J. H. Rindel, “The influence of the directivity of musical instruments in a room,” *Acta Acustica united with Acustica*, vol. 90, pp. 1178–1184, Nov. 2004.

- [11] F. Otondo, J. H. Rindel, and C. L. Christensen, “Directional patterns and recordings of musical instruments in auralizations,” in *Proceedings of the MOSART workshop on Current Research Directions in Computer Music*, (Barcelona, Spain), pp. 230–232, Nov. 2001.
- [12] O. Warusfel, P. Derogis, and R. Caussé, “Radiation synthesis with digitally controlled loudspeakers,” in *Proceedings of the 103rd Audio Engineering Society Convention*, (New York), Sept. 1997. paper number 4577.
- [13] G. Weinreich, “Directional tone color,” *Journal of the Acoustical Society of America*, vol. 101, pp. 2338–2346, Apr. 1997.
- [14] N. H. Fletcher and T. D. Rossing, *The Physics of Musical Instruments*. New York: Springer-Verlag, 2nd ed., 1998.
- [15] S. Hosoe, T. Nishino, K. Itou, and K. Takeda, “Measurement of head-related transfer functions in the proximal region,” in *Proceedings of the Forum Acusticum*, (Budapest, Hungary), 2005.
- [16] T. W. Leishman, S. Rollins, and H. M. Smith, “An experimental evaluation of regular polyhedron loudspeakers as omnidirectional sources of sound,” *Journal of the Acoustical Society of America*, vol. 120, pp. 1411–1422, Sept. 2006.
- [17] V. Tarnow, “Sound radiation from loudspeaker system with the symmetry of the Platonic solids,” Technical Review 04/1974, Brüel & Kjaer, 1974.
- [18] W. Weise, “Investigation of the anisotropy of hemi-dodecahedron noise source radiation,” *Journal of Sound and Vibration*, vol. 270, pp. 137–147, Feb. 2004.
- [19] R. Caussé, J. F. Bresciani, and O. Warusfel, “Radiation of musical instruments and control of reproduction with loudspeakers,” in *Proceedings of the International Symposium on Musical Acoustics*, (Tokyo), 1992.
- [20] P. Derogis, R. Caussé, and O. Warusfel, “On the reproduction of directivity patterns using multi-loudspeaker sources,” in *Proceedings of the International Symposium on Musical Acoustics*, (Dourdan, France), pp. 387–392, 1995.
- [21] O. Warusfel and N. Misdariis, “Directivity synthesis with a 3D array of loudspeakers: application for stage performance,” in *Proceedings of the COST G-6 Conference on Digital Audio Effects (DAFX-01)*, (Limerick, Ireland), Dec. 2001.
- [22] P. Kassakian and D. Wessel, “Characterization of spherical loudspeaker arrays,” in *Proceedings of the 117th Audio Engineering Society Convention*, (San Francisco, CA, USA), Oct. 2004. Paper number 6283.

- [23] P. Kassakian and D. Wessel, “Design of low-order filters for radiation synthesis,” in *Proceedings of the 115th Audio Engineering Society Convention*, (New York), Oct. 2003. Paper number 5925.
- [24] T. Kridel, “Ball of sound: spherical loudspeaker arrays could help create a more realistic audio experience in theatres and concert halls,” *Pro AV magazine*, pp. 94–95, Aug. 2006.
- [25] R. Avizienis, A. Freed, P. Kassakian, and D. Wessel, “A compact 120 independent element spherical loudspeaker array with programmable radiation patterns,” in *Proceedings of the 120th Audio Engineering Society Convention*, (Paris), May 2006. Paper number 6783.
- [26] F. Zotter, A. Sontacchi, and R. Höldrich, “Modeling a spherical loudspeaker system as multipole source,” in *Proceedings of the 33rd German Annual Conference on Acoustics*, (Stuttgart), Mar. 2007.
- [27] F. Zotter and R. Höldrich, “Modeling radiation synthesis with spherical loudspeaker arrays,” in *Proceedings of the 19th International Congress on Acoustics*, (Madrid), Sept. 2007.
- [28] H. Pomberger, *Angular and radial directivity control for spherical loudspeaker arrays*. Master’s project, University of Music and Performing Arts, Institute of Electronic Music and Acoustics, Graz, Austria, 2008.
- [29] F. Zotter, H. Pomberger, and A. Schmeder, “Efficient directivity pattern control for spherical loudspeaker arrays,” in *Proceedings of the 2nd ASA–EAA Joint Conference*, (Paris), pp. 4229–4234, June 2008.
- [30] F. Zotter and A. Sontacchi, “Icosahedral loudspeaker array,” IEM Report 39/07, Institute of Electronic Music and Acoustics, Graz, Austria, Jan. 2007.
- [31] G. K. Behler, “Sound source for the measurement of room impulse responses for auralisation,” in *Proceedings of the 19th International Congress on Acoustics*, (Madrid), Sept. 2007.
- [32] M. Pollow, *Variable directivity of dodecahedron loudspeakers*. Master’s thesis, Institute of Technical Acoustics, Aachen, Germany, 2007.
- [33] M. Pollow and G. K. Behler, “Variable directivity for Platonic sound sources based on spherical harmonics optimization,” *Acta Acustica united with Acustica*, vol. 95, pp. 1082–1092, Nov. 2009.
- [34] P. R. Cook, G. Essl, G. Tzanetakis, and D. Trueman, “N>>2: Multi-speaker display systems for virtual reality and spatial audio projection,” in *Proceedings of the International Conference on Auditory Display*, (Glasgow), Nov. 1998.

- [35] D. Trueman, C. Bahn, and P. R. Cook, “Alternative voices for electronic sound: spherical speakers and sensor-speaker arrays (SenSAs),” in *Proceedings of the International Computer Music Conference*, (Berlin), Aug. 2000.
- [36] D. Trueman, P. Cook, S. Smallwood, and G. Wang, “PLOrk: the Princeton laptop orchestra, year 1,” in *Proceedings of the International Computer Music Conference*, (New Orleans), Nov. 2006.
- [37] M. Bédard and A. Berry, “Development of a directivity-controlled piezoelectric transducer for sound reproduction,” *Journal of Sound and Vibration*, vol. 311, pp. 1271–1285, 2008.
- [38] A. Freed, A. Schmeder, and F. Zotter, “Applications of environmental sensing for spherical loudspeaker arrays,” in *Proceedings of the 10th IASTED International Conference on Signal and Image Processing*, (Kailua-Kona, Hawaii, USA), Aug. 2008. Paper 623-136.
- [39] B. Rafaely, “Spherical loudspeaker array for local active control of sound,” *Journal of the Acoustical Society of America*, vol. 125, pp. 3006–3017, May 2009.
- [40] K. A. Cunefare, M. N. Currey, M. E. Johnson, and S. J. Elliott, “The radiation efficiency grouping of free-space acoustic radiation modes,” *Journal of the Acoustical Society of America*, vol. 109, pp. 203–215, Jan. 2001.
- [41] L. L. Beranek, *Acoustics*. New York: Acoustical Society of America, 1993.
- [42] G. V. Borgiotti, “The power radiated by a vibrating body in an acoustic fluid and its determination from boundary measurements,” *Journal of the Acoustical Society of America*, vol. 88, pp. 1884–1893, Oct. 1990.
- [43] G. V. Borgiotti and K. E. Jones, “Frequency independence property of radiation spatial filters,” *Journal of the Acoustical Society of America*, vol. 96, pp. 3516–3524, Dec. 1994.
- [44] K. A. Cunefare, “The minimum multimodal radiation efficiency of baffled finite beams,” *Journal of the Acoustical Society of America*, vol. 90, pp. 2521–2529, Nov. 1991.
- [45] K. A. Cunefare and M. N. Currey, “On the exterior acoustic radiation modes of structures,” *Journal of the Acoustical Society of America*, vol. 96, pp. 2302–2312, Oct. 1994.
- [46] A. Sarkissian, “Acoustic radiation from finite structures,” *Journal of the Acoustical Society of America*, vol. 90, pp. 574–578, July 1991.
- [47] S. J. Elliott and M. E. Johnson, “Radiation modes and the active control of sound power,” *Journal of the Acoustical Society of America*, vol. 94, pp. 2194–2204, Oct. 1993.

- [48] Y. Wen, W.-S. Gan, and J. Yang, “Application of radiation mode in desired sound field generation using loudspeaker array,” in *Proceedings of the IEEE International Symposium on Circuits and Systems*, vol. 4, (Kobe, Japan), pp. 3139–3142, May 2005.
- [49] P. S. Meyer and J. D. Meyer, “Multi acoustic prediction program (MAPP): recent results,” tech. rep. presented at the Institute of Acoustics (Stratford upon Avon, UK), Meyer Sound Laboratories Inc., Nov. 2000.
- [50] N. Quaegebeur and A. Chaigne, “On the influence of the geometry on radiation for electrodynamic loudspeakers,” in *Proceedings of the 120th Audio Engineering Society Convention*, (Paris), May 2006. Paper number 6775.
- [51] H. Suzuki and J. Tichy, “Sound radiation from convex and concave domes in an infinite baffle,” *Journal of the Acoustical Society of America*, vol. 69, pp. 41–49, Jan. 1981.
- [52] F. Zotter, *Analysis and synthesis of sound-radiation with spherical arrays*. PhD dissertation, University of Music and Performing Arts, Institute of Electronic Music and Acoustics, Graz, Austria, 2009.
- [53] F. Zotter, A. Schmeder, and M. Noisternig, “Crosstalk cancellation for spherical loudspeaker arrays,” in *Proceedings of the 34th German Annual Conference on Acoustics*, (Dresden), Mar. 2008.
- [54] O. Warusfel and N. Misdariis, “Sound source radiation synthesis: from stage performance to domestic rendering,” in *Proceedings of the 116th Audio Engineering Society Convention*, (Berlin), May 2004. paper number 6018.
- [55] M. Vorländer, *Auralization: Fundamentals of Acoustics, Modelling, Simulation, Algorithms and Acoustic Virtual Reality*. Berlin: Springer-Verlag, 1st ed., 2008.
- [56] P. W. Kassakian, *Convex approximation and optimization with applications in magnitude filter design and radiation pattern synthesis*. PhD thesis, University of California, Berkeley, May 2006.
- [57] P. Kassakian, “Magnitude least-squares fitting via semidefinite programming with applications to beamforming and multidimensional filter design,” in *Proceedings of the IEEE International Conference on Acoustics, Speech, and Signal Processing*, (Philadelphia, USA), Mar. 2005.
- [58] A. D. Pierce, *Acoustics: An Introduction to Its Physical Principles and Applications*. Melville, NY: Acoustical Society of America, 1994.

- [59] P. J. T. Filippi, A. Bergassoli, D. Habault, and J. P. Lefebvre, *Acoustics: Basic Physics, Theory and Methods*, ch. 2, pp. 41–88. Academic Press, 1st ed., 1999.
- [60] G. B. Arfken and H. J. Weber, *Mathematical Methods for Physicists*. Harcourt/Academic Press, 5th ed., 2001.
- [61] E. G. Williams, *Fourier Acoustics: Sound Radiation and Nearfield Acoustical Holography*, ch. 6, pp. 183–234. Academic Press, 1999.
- [62] G. Weinreich and E. B. Arnold, “Method for measuring acoustic radiation fields,” *Journal of the Acoustical Society of America*, vol. 68, pp. 404–411, Aug. 1980.
- [63] L. C. Biedenharn and J. D. Louck, *Angular Momentum in Quantum Physics: Theory and Application*, ch. 3, pp. 29–179. Massachusetts: Addison-Wesley, 1981.
- [64] Z. Su and P. Coppens, “Rotation of real spherical harmonics,” *Acta Crystallographica Section A*, vol. A50, pp. 636–643, 1994.
- [65] M. Kazhdan, T. Funkhouser, and S. Rusinkiewicz, “Rotation invariant spherical harmonic representation of 3D shape descriptors,” in *Proceedings of the Eurographics Symposium on Geometry Processing*, (Aachen, Germany), pp. 156–164, June 2003.
- [66] M. N. Currey and K. A. Cunefare, “The radiation modes of baffled finite plates,” *Journal of the Acoustical Society of America*, vol. 98, pp. 1570–1580, Sept. 1995.
- [67] D. M. Photiadis, “The relationship of singular value decomposition to wave-vector filtering in sound radiation problems,” *Journal of the Acoustical Society of America*, vol. 88, pp. 1152–1159, Aug. 1990.
- [68] R. R. Craig Jr., *Structural Dynamics: An Introduction to Computer Methods*. Wiley, 1981.
- [69] A. J. Berkhout, “A holographic approach to acoustic control,” *Journal of the Audio Engineering Society*, vol. 36, pp. 977–995, Dec. 1988.
- [70] S. Spors and R. Rabenstein, “Spatial aliasing artifacts produced by linear and circular loudspeaker arrays used for wave field synthesis,” in *Proceedings of the 120th Audio Engineering Society Convention*, (Paris), May 2006. paper number 6711.
- [71] S. Spors, R. Rabenstein, and J. Ahrens, “The theory of wave field synthesis revisited,” in *Proceedings of the 124th Audio Engineering Society Convention*, (Amsterdam), May 2008. Paper number 7358.

- [72] *Proceedings of the Ambisonics Symposium*, (Graz), Institute of Electronic Music and Acoustics, June 2009.
- [73] P. M. Morse and K. U. Ingard, *Theoretical Acoustics*. Princeton: McGraw-Hill, Inc., 1968.
- [74] H. S. M. Coxeter, *Introduction to Geometry*. John Wiley & Sons, 2nd ed., 1969.
- [75] F. Zotter and M. Noisternig, “Near- and farfield beamforming using spherical loudspeaker arrays,” in *Proceedings of the 3rd Congress of the Alps Adria Acoustics Association*, (Graz, Austria), Sept. 2007.
- [76] R. H. Small, “Direct-radiator loudspeaker system analysis,” *Journal of the Audio Engineering Society*, vol. 20, pp. 383–395, June 1972.
- [77] W. M. Leach, Jr., “Loudspeaker voice-coil inductance losses: circuit models, parameter estimation, and effect on frequency response,” *Journal of the Audio Engineering Society*, vol. 50, pp. 442–450, June 2002.
- [78] R. H. Small, “Closed-box loudspeaker systems: analysis,” *Journal of the Audio Engineering Society*, vol. 20, pp. 798–808, Dec. 1972.
- [79] R. H. Small, “Closed-box loudspeaker systems: synthesis,” *Journal of the Audio Engineering Society*, vol. 21, pp. 11–18, Jan. 1973.
- [80] S. Boyd and L. Vandenberghe, *Convex Optimization*. Cambridge, United Kingdom: Cambridge University Press, sixth printing ed., 2008.
- [81] R. Greenfield and M. Hawksford, “The audibility of loudspeaker phase distortion,” in *Proceedings of the 88th Audio Engineering Society Convention*, (Montreux), Mar. 1990. Paper number 2927.
- [82] F. Wang, V. Balakrishnan, P. Zhou, J. Chen, R. Yang, and C. Frank, “Optimal array pattern synthesis using semidefinite programming,” *IEEE Transactions on Signal Processing*, vol. 51, pp. 1172–1183, May 2003.
- [83] M. Puckette, *The Theory and Technique of Electronic Music*. World Scientific Publishing Co., 2007.
- [84] J. C. Le Roux, *The electrodynamic loudspeaker: determination of the low-frequency electroacoustic parameters and modelisation of the suspension*. PhD dissertation, Maine University, Le Mans, France, 1994. In french.

- [85] J. D. Maynard, E. G. Williams, and Y. Lee, “Nearfield acoustic holography: I. Theory of generalized holography and the development of NAH,” *Journal of the Acoustical Society of America*, vol. 78, pp. 1395–1413, Oct. 1985.
- [86] M. Abramowitz and I. A. Stegun, *Handbook of Mathematical Functions with Formulas, Graphs, and Mathematical Tables*. USA: National Bureau of Standards, tenth printing ed., 1972.

Appendix A

Wave Equation in Spherical Coordinates

A.1 General solution

Here, a general solution for the wave equation in spherical coordinates is developed. Hence, the Laplace operator becomes [73]

$$\Delta(\cdot) \equiv \frac{1}{r^2} \frac{\partial}{\partial r} \left(r^2 \frac{\partial(\cdot)}{\partial r} \right) + \frac{1}{r^2 \sin \theta} \frac{\partial}{\partial \theta} \left(\sin \theta \frac{\partial(\cdot)}{\partial \theta} \right) + \frac{1}{r^2 \sin^2 \theta} \frac{\partial^2(\cdot)}{\partial \phi^2} \quad (\text{A.1})$$

where r is the radial coordinate, θ is the zenith angle and ϕ is the azimuth angle.

Substitution of Eq.(A.1) into (2.3) yields to

$$\frac{1}{r^2} \frac{\partial}{\partial r} \left(r^2 \frac{\partial p}{\partial r} \right) + \frac{1}{r^2 \sin \theta} \frac{\partial}{\partial \theta} \left(\sin \theta \frac{\partial p}{\partial \theta} \right) + \frac{1}{r^2 \sin^2 \theta} \frac{\partial^2 p}{\partial \phi^2} + k^2 p = 0 \quad (\text{A.2})$$

Equation (A.2) is separable. Hence, its solution is

$$p(r, \theta, \phi) = R(r) \Theta(\theta) \Phi(\phi) \quad (\text{A.3})$$

Substitution of Eq.(A.3) into (A.2) leads to

$$\frac{1}{R} \frac{d}{dr} \left(r^2 \frac{dR}{dr} \right) + \frac{1}{\Theta \sin \theta} \frac{d}{d\theta} \left(\sin \theta \frac{d\Theta}{d\theta} \right) + \frac{1}{\Phi \sin^2 \theta} \frac{d^2 \Phi}{d\phi^2} + k^2 r^2 = 0 \quad (\text{A.4})$$

By separating the variables, Eq.(A.4) yields to three ordinary differential equations:

$$\frac{1}{\Phi} \frac{d^2\Phi}{d\phi^2} = -m^2 \quad (\text{A.5})$$

$$\frac{\sin\theta}{\Theta} \frac{d}{d\theta} \left(\sin\theta \frac{d\Theta}{d\theta} \right) + n(n+1) \sin^2\theta = m^2 \quad (\text{A.6})$$

$$\frac{1}{R} \frac{d}{dr} \left(r^2 \frac{dR}{dr} \right) + k^2 r^2 = n(n+1) \quad (\text{A.7})$$

where m and n are constants.

The general solution to Eq.(A.5) can be easily shown to be

$$\Phi(\phi) = \Phi_1 e^{\iota m \phi} + \Phi_2 e^{-\iota m \phi} \quad (\text{A.8})$$

where Φ_1 and Φ_2 are constants. Since the relation $\Phi(\phi) = \Phi(\phi + 2\pi l)$ must be satisfied in order to provide continuity and periodicity of $\Phi(\phi)$ (where l is an integer), m must be an integer.

To solve Eq.(A.6), let $\eta = \cos\theta$. Then, it becomes

$$(1 - \eta^2) \frac{d^2\Theta}{d\eta^2} - 2\eta \frac{d\Theta}{d\eta} + \left(n(n+1) - \frac{m^2}{1 - \eta^2} \right) \Theta = 0 \quad (\text{A.9})$$

Equation (A.9) is an associated Legendre equation whose general solution is [86]

$$\Theta(\theta) = \Theta_1 P_n^m(\cos\theta) + \Theta_2 Q_n^m(\cos\theta) \quad (\text{A.10})$$

where Θ_1 and Θ_2 are constants; $P_n^m(\cdot)$ and $Q_n^m(\cdot)$ are the Legendre functions of the first and second kind, respectively. Since $Q_n^m(\eta)$ are not finite at the poles where $\eta = \pm 1$, $\Theta_2 = 0$. $P_n^m(\eta)$ diverges at $\eta = 1$ unless n is restricted to be an integer. In addition, when n is an integer then $P_n^m(\eta) = 0$ if $m > n$ [61].

Equations (A.8) and (A.10) show that the angular dependence of the solution to Eq.(A.2) is conveniently described by spherical harmonic functions (refer to section 2.3.1).

Finally, Eq.(A.7) will be solved. Let $x = kr$ and $y = \sqrt{kr}R$. Then, Eq.(A.7) becomes

$$x^2 \frac{d^2 y}{dx^2} + x \frac{dy}{dx} + \left(x^2 - \left(n + \frac{1}{2} \right)^2 \right) y = 0 \quad (\text{A.11})$$

Equation (A.11) is a Bessel equation. Then, the general solution to Eq.(A.7) is [86]

$$R(r) = \frac{1}{\sqrt{kr}} \left(R_1 J_{n+\frac{1}{2}}(kr) + R_2 Y_{n+\frac{1}{2}}(kr) \right) \quad (\text{A.12})$$

where R_1 and R_2 are constants; $J_n(\cdot)$ and $Y_n(\cdot)$ are the Bessel functions of the first and second kind, respectively.

Equation (A.12) can be more properly written in terms of the spherical Bessel functions of the first and second kind, which are respectively defined as [86]

$$j_n(x) \equiv \sqrt{\frac{\pi}{2x}} J_{n+\frac{1}{2}}(x) \quad (\text{A.13})$$

$$y_n(x) \equiv \sqrt{\frac{\pi}{2x}} Y_{n+\frac{1}{2}}(x) \quad (\text{A.14})$$

Thus, Eq.(A.12) can be rewritten as

$$R(r) = R_1 j_n(kr) + R_2 y_n(kr) \quad (\text{A.15})$$

Alternatively, the solution can be written as

$$R(r) = R_1 h_n^{(1)}(kr) + R_2 h_n^{(2)}(kr) \quad (\text{A.16})$$

where $h_n^{(1)}(\cdot)$ and $h_n^{(2)}(\cdot)$ are the spherical Hankel functions of the first and second kind (also called spherical Bessel functions of the third kind), respectively, which are defined as [86]

$$h_n^{(1)}(x) \equiv j_n(x) + \iota y_n(x) \quad (\text{A.17})$$

$$h_n^{(2)}(x) \equiv j_n(x) - \iota y_n(x) \quad (\text{A.18})$$

It is worth noting that the constants R_1 and R_2 presented in Eqs.(A.12), (A.15) and (A.16) are different.

Since a time dependence of the form $e^{-i\omega t}$ has been assumed (refer to section 2.1), $h_n^{(1)}(kr)$ and $h_n^{(2)}(kr)$ represent an outgoing wave and an incoming wave, respectively.

The general solution to Eq.(A.2) is obtained by substituting Eqs.(A.8), (A.10), (A.16) and (2.23) into (A.3), so that

$$p(r, \theta, \phi) = \sum_{n=0}^{\infty} \sum_{m=-n}^n (A_{mn} h_n^{(1)}(kr) + B_{mn} h_n^{(2)}(kr)) Y_n^m(\theta, \phi) \quad (\text{A.19})$$

where A_{mn} and B_{mn} are constants to be determined from the boundary conditions.

A.2 Exterior and interior problems

Equation (A.19) is simplified if there are no sources and scatterers outside an imaginary surface enclosing the sources or inside an imaginary surface surrounded by the sources. If so, one has an exterior problem or an interior problem, respectively. Then, the coefficients A_{mn} and B_{mn} are not independent of each other.

For an exterior problem (free-field sound radiation), since there are not incoming waves, $B_{mn} = 0$ so that Eq.(A.19) simplifies to

$$p(r, \theta, \phi) = \sum_{n=0}^{\infty} \sum_{m=-n}^n A_{mn} h_n^{(1)}(kr) Y_n^m(\theta, \phi) \quad (\text{A.20})$$

Substitution of Eq.(A.20) into (2.4) yields to the following expression for the radial component of the acoustic velocity v :

$$v(r, \theta, \phi) = -\frac{i}{\rho c} \sum_{n=0}^{\infty} \sum_{m=-n}^n A_{mn} \frac{dh_n^{(1)}(kr)}{d(kr)} Y_n^m(\theta, \phi) \quad (\text{A.21})$$

For an interior problem, since the $y_n(\cdot)$ functions are not finite at the origin [61], $A_{mn} = B_{mn}$ so that Eq.(A.19) simplifies to

$$p(r, \theta, \phi) = \sum_{n=0}^{\infty} \sum_{m=-n}^n C_{mn} j_n(kr) Y_n^m(\theta, \phi) \quad (\text{A.22})$$

Substitution of Eq.(A.22) into (2.4) yields to the following expression for the radial component of the acoustic velocity:

$$v(r, \theta, \phi) = -\frac{t}{\rho c} \sum_{n=0}^{\infty} \sum_{m=-n}^n C_{mn} \frac{dj_n(kr)}{d(kr)} Y_n^m(\theta, \phi) \quad (\text{A.23})$$

Appendix B

Properties of the Coupling Matrix for the Discrete Sphere

The matrix that couples the power radiated by the spherical caps of a discrete sphere is given by Eq.(3.21). Each term of such a matrix is

$$C_{ll'} = \frac{r^2}{2\rho c S} \Re \left\{ \sum_{i=1}^{(N+1)^2} B_{il}^* E_{il'} \right\} \quad (\text{B.1})$$

By using Eqs.(3.18) and (3.19), one has

$$\sum_{i=1}^{(N+1)^2} B_{il}^* E_{il'} = \frac{1}{u_l u_{l'}} \sum_{n=0}^N -\frac{\iota}{\rho c} |A_{0n}|^2 h_n^{(1)}(kr)^* \frac{dh_n^{(1)}(kr)}{d(kr)} \chi_{ll'}^n \quad (\text{B.2})$$

where

$$\begin{aligned} \chi_{ll'}^n &= \sum_{m=-n}^n D_{m0}^n(\alpha_l, \beta_l, \gamma_l)^* D_{m0}^n(\alpha_{l'}, \beta_{l'}, \gamma_{l'}) \\ &= d_{00}^n(\beta_l) d_{00}^n(\beta_{l'}) + \sum_{m=1}^n 2d_{m0}^n(\beta_l) d_{m0}^n(\beta_{l'}) \cos(m(\alpha_l - \alpha_{l'})) \end{aligned} \quad (\text{B.3})$$

is real and $\chi_{ll'}^n = \chi_{l'l}^n$.

It can be shown that

$$\Re \left\{ -\iota h_n^{(1)}(kr) \frac{dh_n^{(1)}(kr)}{d(kr)} \right\} = \frac{1}{(kr)^2} \quad (\text{B.4})$$

Since $S = 2\pi a^2(1 - \cos \theta_0)L$, substitution of Eqs.(B.2) and (B.4) into (B.1) leads to

$$C_{ll'} = (4\pi L(1 - \cos \theta_0)(\rho c)^2(ka)^2 u_l u_{l'})^{-1} \sum_{n=0}^N |A_{0n}|^2 \chi_{ll'}^n \quad (\text{B.5})$$

It can be verified that \mathbf{C} is symmetric and that it does not depend on r . In addition, substitution of Eq.(3.11) into (B.5) reveals that \mathbf{C} does not depend on c and ρ either.

Appendix C

Convex Regular Polyhedra

Table C.1 presents some basic properties of Platonic solids [74]. The dihedral angle is the interior angle between any two face planes.

Table C.1: Basic properties of Platonic solids.

Polyhedron	number of faces	number of vertices	dihedral angle (degrees)
Tetrahedron	4	4	70.53
Hexahedron	6	8	90.00
Octahedron	8	6	109.47
Dodecahedron	12	20	116.57
Icosahedron	20	12	138.19

Table C.2 presents the Cartesian coordinates of the center of each face of a Platonic solid and the corresponding Euler angle.

The modal matrices containing the acoustic radiation modes of the discrete spheres based on the Platonic solids are presented in Tabs. C.3 to C.7. The modal matrices have been normalized so that $\Psi^T \mathbf{V} \Psi = \mathbf{I}$.

Table C.2: Cartesian coordinates and Euler angles of the center of the polyhedrons' faces.

Polyhedron	Cartesian coordinates	Euler angles (degrees)
Tetrahedron	(+1, +1, +1)	(45, 54.74, 0)
	(-1, -1, +1)	(225, 54.74, 0)
	(-1, +1, -1)	(135, 125.64, 0)
	(+1, -1, -1)	(315, 125.64, 0)
Hexahedron	(-1, 0, 0)	(180, 90, 0)
	(+1, 0, 0)	(0, 90, 0)
	(0, -1, 0)	(270, 90, 0)
	(0, +1, 0)	(90, 90, 0)
	(0, 0, -1)	(0, 180, 0)
	(0, 0, +1)	(0, 0, 0)
Octahedron	(+1, +1, +1)	(45, 54.74, 0)
	(+1, +1, -1)	(45, 125.26, 0)
	(+1, -1, +1)	(315, 54.74, 0)
	(+1, -1, -1)	(315, 125.26, 0)
	(-1, +1, +1)	(135, 54.74, 0)
	(-1, +1, -1)	(135, 125.26, 0)
	(-1, -1, +1)	(225, 54.74, 0)
	(-1, -1, -1)	(225, 125.26, 0)
Dodecahedron	(0, 0, +1)	(0, 0, 0)
	(0.8944, 0, 0.4472)	(0, 63.43, 0)
	(0.2764, 0.8507, 0.4472)	(72, 63.43, 0)
	(-0.7236, 0.5257, 0.4472)	(144, 63.43, 0)
	(-0.7236, -0.5257, 0.4472)	(216, 63.43, 0)
	(0.2764, -0.8507, 0.4472)	(288, 63.43, 0)
	(-0.8944, 0, -0.4472)	(180, 116.57, 0)
	(-0.2764, -0.8507, -0.4472)	(252, 116.57, 0)
	(0.7236, -0.5257, -0.4472)	(324, 116.57, 0)
	(0.7236, 0.5257, -0.4472)	(36, 116.57, 0)
	(-0.2764, 0.8507, -0.4472)	(108, 116.57, 0)
	(0, 0, -1)	(0, 180, 0)
Icosahedron	(2, 0, 2.618)	(0, 37.38, 0)
	(0.618, 1.9021, 2.618)	(72, 37.38, 0)
	(-1.618, 1.1756, 2.618)	(144, 37.38, 0)
	(-1.618, -1.1756, 2.618)	(216, 37.38, 0)
	(0.618, -1.9021, 2.618)	(288, 37.38, 0)
	(-2, 0, -2.618)	(180, 142.62, 0)
	(-0.618, -1.9021, -2.618)	(252, 142.62, 0)
	(1.618, -1.1756, -2.618)	(324, 142.62, 0)
	(1.618, 1.1756, -2.618)	(36, 142.62, 0)
	(-0.618, 1.9021, -2.618)	(108, 142.62, 0)
	(3.2361, 0, 0.618)	(0, 79.19, 0)
	(1, 3.0777, 0.618)	(72, 79.19, 0)
	(-2.618, 1.9021, 0.618)	(144, 79.19, 0)
	(-2.618, -1.9021, 0.618)	(216, 79.19, 0)
	(1, -3.0777, 0.618)	(288, 79.19, 0)
	(-3.2361, 0, -0.618)	(180, 100.81, 0)
	(-1, -3.0777, -0.618)	(252, 100.81, 0)
	(2.618, -1.9021, -0.618)	(324, 100.81, 0)
	(2.618, 1.9021, -0.618)	(36, 100.81, 0)
	(-1, 3.0777, -0.618)	(108, 100.81, 0)

Table C.3: Modal matrix (Ψ) of the tetrahedron.

1.4142	1.4142	1.4142	1.4142
1.4142	1.4142	-1.4142	-1.4142
1.4142	-1.4142	-1.4142	1.4142
1.4142	-1.4142	1.4142	-1.4142

Table C.4: Modal matrix (Ψ) of the hexahedron.

1.4140	0	-2.4495	0	-1.0001	1.7321
1.4140	0	2.4495	0	-1.0001	1.7321
1.4140	0	0	-2.4495	-1.0001	-1.7321
1.4140	0	0	2.4495	-1.0001	-1.7321
1.4140	-2.4495	0	0	2.0002	0
1.4140	2.4495	0	0	2.0002	0

Table C.5: Modal matrix (Ψ) of the octahedron.

1.4142	1.4142	1.4142	1.4142	1.4142	-1.4142	1.4142	1.4142
1.4142	-1.4142	1.4142	1.4142	1.4142	1.4142	-1.4142	-1.4142
1.4142	1.4142	1.4142	-1.4142	-1.4142	1.4142	1.4142	-1.4142
1.4142	-1.4142	1.4142	-1.4142	-1.4142	-1.4142	-1.4142	1.4142
1.4142	1.4142	-1.4142	1.4142	-1.4142	-1.4142	-1.4142	-1.4142
1.4142	-1.4142	-1.4142	1.4142	-1.4142	1.4142	1.4142	1.4142
1.4142	1.4142	-1.4142	-1.4142	1.4142	1.4142	-1.4142	1.4142
1.4142	-1.4142	-1.4142	-1.4142	1.4142	-1.4142	1.4142	-1.4142

Table C.6: Modal matrix (Ψ) of the dodecahedron.

1.4143	2.4495	0	0	3.1623	0	0	0	0	0	0	2.4495
1.4143	1.0954	2.1908	0	-0.6325	2.1908	2.1908	0	2.1908	0	0	-1.0954
1.4143	1.0954	0.6770	2.0835	-0.6325	-1.7725	0.6770	2.0835	-1.2879	-1.7725	-1.2879	-1.0954
1.4143	1.0954	-1.7725	1.2879	-0.6325	0.6770	-1.7725	1.2879	2.0835	0.6770	2.0835	-1.0954
1.4143	1.0954	-1.7725	-1.2879	-0.6325	0.6770	-1.7725	-1.2879	-2.0835	0.6770	-2.0835	-1.0954
1.4143	1.0954	0.6770	-2.0835	-0.6325	-1.7725	0.6770	-2.0835	1.2879	-1.7725	1.2879	-1.0954
1.4143	-1.0954	-2.1908	0	-0.6325	2.1908	2.1908	0	0	-2.1908	0	1.0954
1.4143	-1.0954	-0.6770	-2.0835	-0.6325	-1.7725	0.6770	2.0835	-1.2879	1.7725	1.2879	1.0954
1.4143	-1.0954	1.7725	-1.2879	-0.6325	0.6770	-1.7725	1.2879	2.0835	-0.6770	-2.0835	1.0954
1.4143	-1.0954	1.7725	1.2879	-0.6325	0.6770	-1.7725	-1.2879	-2.0835	-0.6770	2.0835	1.0954
1.4143	-1.0954	-0.6770	2.0835	-0.6325	-1.7725	0.6770	-2.0835	1.2879	1.7725	-1.2879	1.0954
1.4143	-2.4495	0	0	3.1623	0	0	0	0	0	0	-2.4495

Table C.7: Modal matrix (Ψ) of the icosahedron.

1.4142	1.9465	1.3876	-0.5346	0.6396	1.1520	0.2540	2.8232	0.4785	-0.1943	1.5769	1.4764	-1.8154	1.6549	-1.6157	-0.8066	2.6696	0.1015	0.8545	0.3639
1.4142	1.9465	0.9371	1.1545	-0.1266	-0.9052	-2.4518	1.7621	0.2200	-0.0397	-1.4157	2.3503	0.6858	-2.3936	0.0581	0.5169	-1.5961	-2.0087	-1.1491	0.3118
1.4142	1.9465	-0.8084	1.2480	0.0879	-3.1250	-0.1607	0.0132	0.4477	-2.2049	-0.3177	-0.6950	1.5982	2.1274	0.3627	-1.1587	0.5979	2.6482	-0.7419	0.2814
1.4142	1.9465	-1.4368	-0.3831	-2.1933	-1.0402	1.5333	-0.5978	1.1828	0.2739	-1.3947	-2.2778	-0.8898	-1.1392	-1.8040	-1.2033	-0.2743	-1.4798	2.1131	1.1270
1.4142	1.9465	-0.0796	-1.4849	-1.5385	0.7446	1.9591	1.2660	-1.2797	2.1651	1.5511	-0.8539	0.4212	-0.3748	1.3972	1.9767	-1.3972	0.7388	-1.0765	-2.0840
1.4142	-1.9465	-1.3876	0.5346	0.6396	1.1520	0.2540	2.8232	0.4785	0.1943	-1.5769	-1.4764	1.8155	-1.6549	1.6157	0.8066	2.6696	0.1015	0.8546	0.3639
1.4142	-1.9465	-0.9371	-1.1545	-0.1266	-0.9052	-2.4518	1.7621	0.2200	0.0397	1.4157	-2.3503	-0.6858	2.3936	-0.0581	-0.5169	-1.5961	-2.0087	-1.1491	0.3118
1.4142	-1.9465	0.8084	-1.2480	0.0879	-3.1250	-0.1607	0.0132	0.4477	2.2049	0.3177	0.6950	-1.5982	-2.1274	-0.3627	-1.1587	0.5979	2.6482	-0.7419	0.2814
1.4142	-1.9465	1.4368	0.3831	-2.1933	-1.0402	1.5333	-0.5978	1.1828	-0.2739	1.3947	2.2778	0.8898	1.1392	1.8039	1.2033	-0.2743	-1.4798	2.1131	1.1270
1.4142	-1.9465	0.0796	1.4849	-1.5385	0.7446	1.9591	1.2660	-1.2797	-2.1651	-1.5511	0.8539	-0.4212	0.3748	-1.3972	-1.9767	-1.3972	0.7388	-1.0765	-2.0840
1.4142	0.4596	2.2452	-0.8649	2.3046	1.3126	0.7467	-0.2049	1.5382	-2.1253	-0.1354	-1.4964	-1.1070	-0.9322	2.1576	-0.6899	-2.3460	1.0669	0.5166	1.0444
1.4142	0.4596	1.5164	1.8680	-0.8540	1.0678	-2.5451	-1.0742	-0.7062	2.3993	-1.2593	-0.7814	0.2172	1.5700	1.1231	-1.5079	-0.0754	1.2677	2.1857	-1.2688
1.4142	0.4596	-1.3080	2.0194	2.4077	-1.1796	0.7577	-1.1511	-0.9550	-0.2342	2.8104	-0.0725	0.2040	-1.2241	0.9348	-1.9046	0.6746	-1.8079	0.5200	-2.0015
1.4142	0.4596	-2.3248	-0.6199	-0.7427	1.3402	-0.2651	-1.8770	2.0147	0.0399	-1.2334	1.5489	-2.0194	0.7947	2.2739	-0.4448	1.3479	-0.4275	-2.4077	-0.4513
1.4142	0.4596	-0.1288	-2.4026	0.0152	0.6328	0.1717	-0.9594	-2.9410	-0.0796	-0.1823	0.8014	2.7052	0.3223	0.2955	-2.4102	0.3990	-0.0993	-0.8146	2.6772
1.4142	-0.4596	-2.2452	0.8649	2.3046	1.3126	0.7467	-0.2049	1.5382	2.1253	0.1354	1.4964	1.1070	0.9322	-2.1576	0.6899	-2.3460	1.0669	0.5166	1.0444
1.4142	-0.4596	-1.5164	-1.8680	-0.8540	1.0678	-2.5451	-1.0742	-0.7062	-2.3993	1.2593	0.7814	-0.2172	-1.5700	-1.1231	1.5079	-0.0754	1.2677	2.1857	-1.2688
1.4142	-0.4596	1.3080	-2.0194	2.4077	-1.1796	0.7577	-1.1511	-0.9550	0.2342	-2.8104	0.0725	-0.2040	1.2241	-0.9348	1.9046	0.6746	-1.8079	0.5200	-2.0015
1.4142	-0.4596	2.3248	0.6199	-0.7427	1.3402	-0.2651	-1.8770	2.0147	-0.0399	1.2334	-1.5489	2.0194	-0.7947	-2.2739	0.4448	1.3479	-0.4275	-2.4077	-0.4513
1.4142	-0.4596	0.1288	2.4026	0.0152	0.6328	0.1717	-0.9594	-2.9410	0.0796	0.1823	-0.8014	-2.7052	-0.3223	-0.2955	2.4101	0.3990	-0.0993	-0.8146	2.6772

Appendix D

Discrete-Time LTI Systems

This appendix presents some basic concepts concerning discrete-time LTI (Linear Time-Invariant) systems that have been taken from [8], to which the reader may refer for an in-depth discussion.

A discrete-time signal is a sequence of numbers that can be obtained, for instance, by sampling a continuous-time signal. Let T_s be the sampling period and $x_c(t)$ be a continuous-time signal. Thus, a discrete-time representation of $x_c(t)$ is given by $x[n] = x_c(nT_s)$, where n is an integer in the range $-\infty < n < \infty$.

A discrete-time system $T\{\cdot\}$ is an operator applied to $x[n]$ that gives rise to a discrete-time signal $y[n]$, i.e., $y[n] = T\{x[n]\}$, where $x[n]$ is the system input and $y[n]$ is the system output. Because this system possesses one input and one output, it is called a SISO (Single Input Single Output) system. A block diagram representation of a SISO system is shown in Fig. D.1.

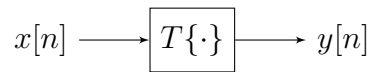


Figure D.1: Block diagram representation of a discrete-time SISO system.

The so-called linear systems satisfy the principle of superposition. Let $\sum_j x_j[n]$ be the input of a SISO system and c_j be a constant. Then, the system is linear if and only if

$$T \left\{ \sum_j c_j x_j[n] \right\} = \sum_j c_j T \{ x_j[n] \} \quad (\text{D.1})$$

In addition, the system will be time-invariant if a time shift in the input produces the same

shift in the output. In other words, if $y[n] = T\{x[n]\}$, the system will be time-invariant provided that $y[n - n_0] = T\{x[n - n_0]\}$, for all n_0 .

Besides linearity and time-invariance, the following properties of systems are also of importance:

- **Causality:** a system is causal if the output depends only on past and current inputs, but not on future inputs;
- **Stability:** a system is stable in the BIBO (Bounded-Input Bounded-Output) sense if and only if every bounded input produces a bounded output.

This work deals with LTI systems. An LTI system has a useful property, namely, it is completely characterized by its impulse response $h[n]$. Then, if $h[n]$ is known, the system response to any input can be evaluated by

$$y[n] = \sum_{j=-\infty}^{\infty} x[j]h[n - j] \quad (\text{D.2})$$

Equation (D.2) is called the convolution sum and is also represented by $y[n] = x[n] * h[n]$.

An LTI system is stable if and only if $\sum_{j=-\infty}^{\infty} |h[j]| < \infty$. In addition, it is causal if $h[n] = 0$ for $n < 0$. If the impulse response has a finite number of nonzero samples, the system is called a FIR (Finite-duration Impulse Response) system. Otherwise, it is called an IIR (Infinite-duration Impulse Response) system.

Let z be a complex variable. The z -transform of a sequence $x[n]$ is defined as

$$X(z) = \sum_{n=-\infty}^{\infty} x[n]z^{-n} \quad (\text{D.3})$$

The convolution property states that $Y(z) = H(z)X(z)$, where the z -transform of the impulse response of an LTI system is referred to as the system function. Since the z -transform of a sequence constitutes a unique pair, any LTI system is completely characterized by its system function (assuming that the series in Eq.(D.3) converges).

It is known that an LTI system whose z -transform of the impulse response can be written as a ratio of polynomials in z^{-1} satisfies a constant-coefficient difference equation, i.e., if

$$H(z) = \frac{Y(z)}{X(z)} = \frac{\sum_{j=0}^B b_j z^{-j}}{\sum_{j=0}^D d_j z^{-j}} \quad (\text{D.4})$$

then

$$\sum_{j=0}^D d_j y[n-j] = \sum_{j=0}^B b_j x[n-j] \quad (\text{D.5})$$

where b_j and d_j are constants, $x[n]$ is the system input and $y[n]$ is the system output. Equation (D.5) is a D th-order linear constant-coefficient difference equation that leads to the system output with no need to explicitly evaluate the convolution sum or to deal with z -transforms.

If z in Eq.(D.3) is replaced by $e^{j\omega T_s}$, the z -transform reduces to the Fourier transform, where ν is the angular frequency and $|\nu T_s| < \pi$ in order to avoid aliasing. The frequency response of a LTI system is the Fourier transform of the impulse response. In general, knowledge of the magnitude of the frequency response does not provide any information about the phase of the frequency response. However, for the so-called minimum-phase systems, the frequency-response magnitude specifies the phase uniquely, and the frequency-response phase specifies the magnitude to within a scale factor. A minimum-phase system is stable, causal and possess a rational system function, i.e., $H_{\min}(z)$ can be written in the form presented in Eq.(D.4). Moreover, the inverse system of a minimum-phase system — a system with system function $H_{\min}(z)^{-1}$ — is also stable and causal.

A nonminimum-phase LTI system that presents a rational system function can be represented as the cascade combination of a minimum-phase system and an all-pass system. The latter is a system for which the frequency-response magnitude is a constant. Hence,

$$H(z) = H_{\min}(z)H_{\text{ap}}(z) \quad (\text{D.6})$$

where $H_{\text{ap}}(z)$ is the system function of the corresponding all-pass system.

Now, consider a stable and causal LTI system described by a rational function $H_d(z)$. Assume that this system presents an undesirable frequency response so that it distorts the input signal. The original signal can be recovered by processing the distorted signal with a compensating system. Perfect compensation will be achieved if the system function of the compensating system is $H_d(z)^{-1}$. However, if the compensating system is required to be stable and causal, perfect compensation will be achieved only if $H_d(z)$ is a minimum-phase system. If not, application of Eq.(D.6) yields

$$H_d(z) = H_{\min}^{(d)}(z)H_{\text{ap}}^{(d)}(z) \quad (\text{D.7})$$

The functions $H_d(z)$ and $H_{\min}^{(d)}(z)$ present the same frequency-response magnitude. Letting the compensation filter be $[H_{\min}^{(d)}(z)]^{-1}$, the resulting function that relates the original signal and the recovered one is

$$H_{\min}^{(d)}(z)H_{\text{ap}}^{(d)}(z)\frac{1}{H_{\min}^{(d)}(z)} = H_{\text{ap}}^{(d)}(z) \quad (\text{D.8})$$

Then, the frequency-response magnitude is exactly compensated, whereas the phase response is modified according to $H_{\text{ap}}^{(d)}(e^{j\nu T_s})$ so that phase distortion takes place. However, if $H_{\text{ap}}^{(d)}(e^{j\nu T_s})$ is a linear-phase system, i.e., if

$$H_{\text{ap}}^{(d)}(e^{j\nu T_s}) = e^{-j\nu T_s n_d} \quad (\text{D.9})$$

then the effect of this system is a simple time shift of n_d samples, which corresponds to introduce a delay of $T_s n_d$. Therefore, an all-pass system with a linear phase response is acceptable in many applications.

Appendix E

Author's Publications

In the following, a full list of publications this thesis has contributed with is provided.

Conference papers:

- PASQUAL, A. M., ARRUDA, J. R. F., and HERZOG, P. Digital equalization filters for a spherical loudspeaker array. In *Proceedings of the Ambisonics Symposium* (Graz, Austria, June 2009), pp. 1–7;
- PASQUAL, A. M., ARRUDA, J. R., and HERZOG, P. Effects of enclosure design on the directivity synthesis by spherical loudspeaker arrays. In *Proceedings of the 2nd ASA–EAA Joint Conference* (Paris, 2008), pp. 4235–4240;
- PASQUAL, A. M., ARRUDA, J. R., and HERZOG, P. Optimal array pattern synthesis with desired magnitude response. In *Proceedings of the 2nd ASA–EAA Joint Conference* (Paris, 2008), pp. 4597–4602;
- PASQUAL, A. M., ARRUDA, J. R. F., and HERZOG, P. Remarks on the design of spherical loudspeaker arrays for directivity synthesis. In *Proceedings of the V National Congress of Mechanical Engineering* (Salvador, Brazil, Aug. 2008), pp. 1–10.

Journal articles:

- PASQUAL, A. M., ARRUDA, J. R. F., and HERZOG, P. Application of acoustic radiation modes in the directivity control by a spherical loudspeaker array. *Acta Acustica united with Acustica* 96, 1 (2010), pp. 32–42;

- PASQUAL, A. M., HERZOG, P., and ARRUDA, J. R. F. Theoretical and experimental analysis of the electromechanical behavior of a spherical loudspeaker array for radiation control. *Journal of the Acoustical Society of America*. (Under review).